

2021

## Forward & Off-Forward Parton Distributions From Lattice Qcd

Colin Paul Egerer

*William & Mary - Arts & Sciences*, [cegerer@jlab.org](mailto:cegerer@jlab.org)

Follow this and additional works at: <https://scholarworks.wm.edu/etd>



Part of the [Physics Commons](#)

---

### Recommended Citation

Egerer, Colin Paul, "Forward & Off-Forward Parton Distributions From Lattice Qcd" (2021). *Dissertations, Theses, and Masters Projects*. William & Mary. Paper 1638386798.

<https://scholarworks.wm.edu/etd/1638386798>

This Dissertation is brought to you for free and open access by the Theses, Dissertations, & Master Projects at W&M ScholarWorks. It has been accepted for inclusion in Dissertations, Theses, and Masters Projects by an authorized administrator of W&M ScholarWorks. For more information, please contact [scholarworks@wm.edu](mailto:scholarworks@wm.edu).

Forward & Off-Forward Parton Distributions from Lattice QCD

Colin Paul Egerer

Ann Arbor, Michigan

Master of Science, College of William & Mary, 2017  
Bachelor of Science, University of Wisconsin La-Crosse, 2015

A Dissertation presented to the Graduate Faculty  
of The College of William & Mary in Candidacy for the Degree of  
Doctor of Philosophy

Department of Physics

College of William & Mary  
August 2021

©2021  
Colin Paul Egerer  
All rights reserved.

## APPROVAL PAGE

This Dissertation is submitted in partial fulfillment of  
the requirements for the degree of

Doctor of Philosophy



---

Colin Paul Egerer

Approved by the Committee June 2021



---

Committee Co-Chair

David Richards, Adjunct Professor, Physics  
College of William & Mary



---

Committee Co-Chair

Konstantinos Orginos, Calkins-Ritter Professor, Physics  
College of William & Mary



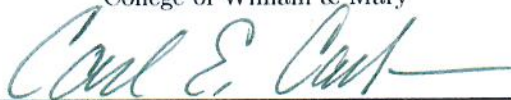
---

David Armstrong, Chancellor Professor, Physics  
College of William & Mary



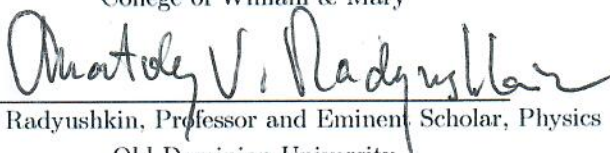
---

Jozef Dudek, Sallie Gertrude Smoot Spears Associate Professor, Physics  
College of William & Mary



---

Carl Carlson, Class of 1962 Professor, Emeritus, Physics  
College of William & Mary



---

Anatoly Radyushkin, Professor and Eminent Scholar, Physics  
Old Dominion University

## ABSTRACT

The interpretation of (semi-)inclusive and certain exclusive scattering processes relies on the factorization of hard parton level cross sections from long-range and non-perturbative parton correlations. The familiar Parton Distribution Functions (PDFs) and Generalized Parton Distributions quantify the non-perturbative dynamics in these situations and address a number of key questions surrounding the structure of hadrons. A certain class of matrix elements accessible in lattice QCD, so called Lattice Cross Sections, have been shown to factorize into these collinear distributions in a manner akin to the factorization of hadronic cross sections. In the short-distance regime, matrix elements of space-like separated two-current operators and parton bilinears can be expressed as the convolution of perturbative coefficient functions and the PDFs. Matrix elements of this type are isolated in the pion and nucleon, each offering a glimpse of the unpolarized valence quark content of these phenomenologically important hadronic states. The calculations within the nucleon represent the first application of the distillation spatial smearing paradigm to the collinear structure of hadrons, and is found to offer higher precision data compared to similar calculations in the literature. A novel method to obtain PDFs from these lattice data, while simultaneously controlling systematic effects, is developed and applied to the nucleon dataset. The coordinate space factorization of space-like separated parton bilinears has also recently been extended to include Generalized Parton Distributions. Preliminary results in off-forward nucleon matrix elements using distillation are explored.

## TABLE OF CONTENTS

Acknowledgments . . . . .	v
Dedication . . . . .	vi
List of Tables . . . . .	vii
List of Figures . . . . .	ix
CHAPTER	1
1 Invitation . . . . .	2
2 Quantum Chromodynamics . . . . .	5
2.1 Hadron Structure and Parton Distributions . . . . .	10
2.1.1 Generalized Parton Distributions . . . . .	13
2.1.2 Parton Distribution Functions . . . . .	15
2.2 Deep Inelastic Scattering . . . . .	17
2.2.1 The Parton Model . . . . .	22
2.2.2 PDFs from Structure Functions . . . . .	24
2.3 Lattice QCD . . . . .	27
2.3.1 Euclidean Lattice Field Theory . . . . .	29
2.3.2 Fermions on the Lattice . . . . .	32
2.3.3 Gluons & Wilson’s Gauge Action . . . . .	37
2.3.4 Symanzik Improvement . . . . .	39
2.3.5 Lattice Observables & the Equivalence with Statistical Mechanics . . . . .	42
2.4 Numerical Techniques of Lattice QCD . . . . .	45

3	Nucleon Matrix Elements & Excited-State Effects . . . . .	55
3.1	Excited-State Contributions to Nucleon Isovector Charges . . . . .	57
3.1.1	Computational Methodology . . . . .	58
3.1.2	Interpolator Constructions . . . . .	59
3.1.3	Correlator Behavior & Matrix Elements . . . . .	62
3.1.4	Results . . . . .	68
3.2	High-Momentum Matrix Elements with Distillation . . . . .	74
3.2.1	A Modified Distillation Space . . . . .	76
3.2.2	Demonstration of Efficacy . . . . .	79
3.2.3	Towards Matrix Elements at High Momentum . . . . .	86
3.2.4	Closing Remarks . . . . .	95
4	Coordinate-Space Factorizable Matrix Elements . . . . .	101
4.1	Quasi-Distributions . . . . .	104
4.2	Lattice Cross Sections . . . . .	107
4.2.1	Two-Current Correlations . . . . .	108
4.2.2	Wilson Line Operator . . . . .	118
4.3	Pion Ioffe-time Pseudo-Structure Functions . . . . .	122
4.3.1	Vector-Axial Currents and $f_{q_v/\pi}(x)$ . . . . .	127
4.3.2	Numerical Implementation . . . . .	131
4.4	Unpolarized Nucleon Ioffe-time Pseudo-Distributions with Distillation . . . . .	134
4.5	Closing Remarks . . . . .	140
5	Extraction of Parton Distributions from LQCD . . . . .	141
5.1	Regularization Through Model Ansätze . . . . .	142

5.1.1	Phenomenology . . . . .	143
5.1.2	Jacobi Polynomials . . . . .	147
5.2	Pion Valence PDF from	
	Ioffe-time Pseudo-Structure Functions . . . . .	148
5.2.1	Discussion of $f_{q_v/\pi}(x)$ Results . . . . .	153
5.2.2	Comparison with Experiment . . . . .	155
5.2.3	Stability of the NLO Matching Kernel . . . . .	157
5.2.4	Areas for Improvement in Two-current LCSs . . . . .	158
5.3	Unpolarized Nucleon PDFs from Ioffe-time	
	Pseudo-Distributions . . . . .	160
5.3.1	PDF Extractions from ITDs . . . . .	163
5.3.2	Direct Extraction of PDFs from Reduced Pseudo-ITDs . . . . .	166
5.3.3	Nucleon PDFs from Reduced Pseudo-ITDs Parameterized with	
	Jacobi Polynomials . . . . .	171
5.3.4	On the Numerical Consistency with DGLAP . . . . .	187
6	Generalized Ioffe-time Pseudo-Distributions . . . . .	196
6.1	Numerical Implementation . . . . .	198
6.2	Outlook . . . . .	201
7	Conclusion and Outlook . . . . .	203
APPENDIX A		
	Euclidean Space Relations . . . . .	206
A.1	The Pauli-Dirac Representation . . . . .	207
A.2	Completeness . . . . .	207
APPENDIX B		
	Gell-Mann Matrices . . . . .	208



APPENDIX C	
Grassmann Numbers . . . . .	209
Bibliography . . . . .	214

## ACKNOWLEDGMENTS

As a budding graduate student I was often struck by the enormity of nuclear physics and how to effectively make contributions to the field. My earliest role models in how to navigate this were Raza Sufian and Joe Karpie. Their mentorship as early career scientists has left a tremendous impact on my ability to think critically and passionately pursue research. Although the enormity of nuclear physics will likely remain, I am confident I can continue to tackle the subject head on. My sanity through this process is owed to the many phone calls and periods of relaxation with family and friends.

My chief foray into the software architectures underpinning lattice QCD was the development of the two-current matrix elements featured herein. I would be remiss if I did not thank Robert Edwards for the countless hours of dialog and suggestions given in pursuit of this goal. The occasional humor hiding amongst the many thousands of lines of QDP++ often provided the nugget of morale needed to push through an evening of debugging. I must also thank Bálint J6o whose contributions have supported not only my research, but the success of the HadStruc Collaboration and lattice community at large.

I am indebted to Jo Dudek for establishing my initial connection to research at Jefferson Lab. Despite not being one of his advisees, Jo stepped beyond his responsibilities to ensure I had the means to pursue my curiosity of nuclear theory through the lens of lattice QCD.

In the past couple years I have found myself in roles of increasing responsibility, each presenting unique challenges and requiring more from me as a scientist and a collaborator. Many of these are due to charges, occasionally indirectly, from Kostas Orginos. Your encouragement to independently take on objectives beneficial to our collaboration and manage project workflows has contributed immensely to my confidence and passion for our shared fields of research.

Above all, I am most thankful for the many valuable years spent under the guidance of David Richards. Your mentorship and teachings were and remain one of patience and open-mindedness. You have helped instill in me a valuable combination of independence and humility. I am honored to continue our professional collaboration. In this journey called graduate school I truly feel I have had the pleasure of knowing what it means to have stood on the shoulders of giants.

To my parents Nancy and Tom, their parents, and my brother Kyle.  
From counting cones to scrawling digits on a number scroll, you labored relentlessly to  
foster my curiosity.

## LIST OF TABLES

3.1	Kinematic factors arising from the traces appearing in the spectral representation of the three-point function (3.13) in the forward-limit. Each factor is the result of applying $\Gamma_{\alpha\beta}^{3\text{pt}}$ as described in the text for each possible Dirac structure of the external current. . . . .	67
3.2	Results of simultaneous fits to the two-point and three-point correlators with $\gamma_3\gamma_5$ insertion. The distilled interpolators were constructed from 64 eigenvectors. . . . .	73
3.3	Results of simultaneous fits to the two-point and three-point correlators with $\gamma_1\gamma_2$ insertion. The distilled interpolators were constructed from 64 eigenvectors. . . . .	73
3.4	Lattice ensembles utilized in the phased distillation proof of principle calculations. The rank of the distillation space $R_{\mathcal{D}}$ and distinct source positions $N_{\text{srcs}}$ per configuration are also indicated. The choice of $R_{\mathcal{D}} = 64$ in both cases is justified in the Appendix of [85]. . . . .	81
3.5	Renormalized isovector charges determined at rest and in boosted frames. The comparatively large correlated $\chi^2/\text{d.o.f}$ for each $g_{\Gamma}^{u-d}$ in the $ap_z = 8\pi/L$ frame can be traced to the large fluctuations of the corresponding two-point correlator (cf. Fig. 3.10), which suffers from few measurements to constrain the needed energies and overlaps. . . . .	95
4.1	Leading-order coordinate space matrix elements resulting from the scalar operators presented in Eq. 4.14 - 4.18. The Dirac structure of each current, and the prefactor of each current-current pair are indicated. Powers of the invariant interval $z^2$ are included to ensure each leading-order kernel has the same Ioffe-time dependence where possible. . . . .	116
4.2	Parameters for each gauge ensemble used in this work: lattice spacing, pion mass, spatial and temporal sizes, and number of configurations used. . . .	123

5.1	(Upper panel) Fit parameters of the $z$ -expansion fit in Eq. 5.10 where ellipses are placeholders for the correction terms in the $z$ -expansion fit, which all have the same $\lambda_i$ and $\chi^2/\text{d.o.f.}$ (Lower panel) Alternative corrections supplementing the $z$ -expansion fit of $T_1^\pi(\nu, z^2)$ . The alternate coefficients $b_k$ are seen to be sub-leading relative to the adopted fit, and the $z$ -expansion parameters are unaltered. . . . .	151
5.2	(Top panel) Results for $f_{q_v/\pi}(x, \mu_0^2)$ using two- and three-parameter phenomenological ansätze convolved with the NLO matching kernel (4.53) at an initial scale of $\mu_0 = 2$ GeV. The systematic uncertainty of each PDF fit parameter set is obtained by a 10% variation of $\alpha_s$ from the nominal three-flavor $\alpha_s(2 \text{ GeV}) \simeq 0.303$ value taken from LHAPDF6 [148]. (Bottom panel) Results of a leading order three-parameter fit to $T_1^\pi(\nu, z^2)$ computed on the $a127m417L$ ensemble [119], with the PDF parameterized at an initial scale $\mu_0 = 1$ GeV. The $z$ -expansion was not implemented in this LO analysis, so errors are statistical only and no corrections have been implemented. . . . .	153
5.3	Unpolarized nucleon valence and plus quark PDF parameters obtained from performing uncorrelated cosine/sine transform fits to the real/imaginary component of the matched ITD at 2 GeV in $\overline{\text{MS}}$ . Results for the plus quark PDF are only shown for $N_{\text{param}} = 2$ , where the smooth polynomial $P(x) = 1$ , as higher numbers of parameters led to uncontrolled fits. The uncorrelated figure of merit is also shown. . . . .	165
5.4	Unpolarized nucleon valence and plus quark PDF parameters obtained from type- $K$ fits to the real/imaginary component of $\mathfrak{M}(\nu, z^2)$ . . . . .	168
5.5	Various Jacobi polynomial fits to the real and imaginary components of the unpolarized reduced pseudo-ITD for $z/a \leq 12$ . Each column represents distinct orders of truncation in the Jacobi polynomial expansions to the leading-twist, discretization, twist-4 and twist-6 corrections. The real and imaginary component fits were found to have the highest likelihoods of describing the data with truncation orders $\{4, 1, 3, 2\}_v$ and $\{3, 3, 1, 0\}_+$ , respectively. The dramatic effect even a single discretization term has on each fit is shown in the columns $\{4, 0, 3, 2\}_v$ and $\{3, 0, 1, 0\}_+$ . . . . .	181

## LIST OF FIGURES

2.1	A generic parton correlation function with momentum assignments. . . . .	11
2.2	(a) The leading contribution to the DVCS process. (b) A representative diagram contributing to the exclusive deeply virtual meson production channel. In each the blue/green blob denotes the non-perturbative off-forward parton bilinear encapsulated by GPDs, and the orange a meson distribution amplitude. . . . .	14
2.3	(a) The DIS amplitude to lowest-order in electromagnetism. (b) The leading parton model approximation of DIS involves the highly virtual photon scattering from an individual quark within the hadron. (c) A higher-order correction to the parton model ultimately responsible for the scaling violations observed in the structure functions associated with the hadronic tensor. . . . .	18
2.4	Cut-diagram notation for the hadronic tensor in deep inelastic scattering. The cut through the hadronic blob denotes a sum and integral over final states. . . . .	20
2.5	The spread of experimental data used in a recent global analysis by the CT collaboration [36]. . . . .	25
2.6	Unpolarized proton PDFs determined by the MMHT collaboration via a global analysis of lepton-hadron and hadron-hadron data, where the perturbative hard coefficient functions and partonic cross sections are truncated at NNLO. The PDFs determined at $Q^2 = 10 \text{ GeV}^2$ are shown at left, while those at $Q^2 = 10^4 \text{ GeV}^2$ given at the right. Details of the extraction are contained in Ref. [37]. . . . .	26
2.7	Unpolarized proton PDFs determined by the NNPDF collaboration via a global analysis of lepton-hadron and hadron-hadron data, where the perturbative hard coefficient functions and partonic cross sections are truncated at NNLO. The PDFs determined at $Q^2 = 10 \text{ GeV}^2$ are shown at left, while those at $Q^2 = 10^4 \text{ GeV}^2$ given at the right. Details of the extraction are contained in Ref. [38]. . . . .	27

2.8	Two dimensional time slices of a hypercubic Euclidean lattice. The coordinate space propagation of a three quark interpolator is shown with the red/green/blue directional lines, a plaquette with filled red, and a generic gauge invariant loop in orange. Directional gauge links are also shown in cyan. . . . .	36
2.9	Illustration of the plaquette sum appearing in the discretization of the field strength tensor $\hat{G}_{\mu\nu}$ . . . . .	41
2.10	Wick contractions to realize a light-quark baryon two-point function (left) and the square of its variance (right). The correlation function variance induces Wick contractions that may be ordered into three light-quark mesons. Additional contraction permutations omitted for brevity. . . . .	46
2.11	Pictorial representation of the factorization of a baryon two-point correlation function. Perambulators are shown in green and elementals as gray ovals. . . . .	52
3.1	Pictorial representation of the factorization of a baryon three-point correlation function with a local current insertion of Dirac structure $\Gamma$ . Perambulators are shown in green, elementals as gray ovals, and a generalized perambulator in red. . . . .	63
3.2	Nucleon effective mass when using Jacobi-SS (purple) and distilled interpolators constructed from 32 (left) and 64 (right) eigenvectors. The distilled interpolators ${}^2S_S^{\frac{1}{2}^+}$ (blue), $\hat{\mathcal{P}}_3$ (green), and $\hat{\mathcal{P}}_7$ (red) demonstrate a plateau in the effective mass as early as $t_{\text{sep}} = 6$ , but the statistical uncertainty is comparable to that of the Jacobi-SS when 32 eigenvectors are used. Considerable improvement in statistics is seen for the case of 64 eigenvectors. . . . .	69
3.3	Effective $\hat{g}_A^{u-d}$ using the Jacobi-SS (upper-left), $N^2S_S^{\frac{1}{2}^+}$ (upper-right), $\hat{\mathcal{P}}_3$ (lower-left), and $\hat{\mathcal{P}}_7$ (lower-right) distilled interpolators with $\mathcal{R}_{\mathcal{D}} = 64$ . The bands are the ratio of the simultaneous fits (3.17) & (3.16) with $T_{\text{fit}}^{2\text{pt}}/a \in [2, 16]$ and $\tau_{\text{fit}}/a \in [2, T^{3\text{pt}} - 2]$ , and error estimated via jackknife resampling. The figure of merit for each simultaneous fit is also shown. . . . .	72
3.4	Effective $\hat{g}_T^{u-d}$ using the Jacobi-SS (upper-left), $N^2S_S^{\frac{1}{2}^+}$ (upper-right), $\hat{\mathcal{P}}_3$ (lower-left), and $\hat{\mathcal{P}}_7$ (lower-right) distilled interpolators with $\mathcal{R}_{\mathcal{D}} = 64$ . The bands are the ratio of the simultaneous fits (3.17) & (3.16) with $T_{\text{fit}}^{2\text{pt}}/a \in [2, 16]$ and $\tau_{\text{fit}}/a \in [2, T^{3\text{pt}} - 2]$ , and error estimated via jackknife resampling. The figure of merit for each simultaneous fit is also shown. . . . .	74
3.5	Distinct Wick contraction topologies required to evaluate a light-quark baryon two-point correlation function. . . . .	77

- 3.6 Qualitative momentum space overlaps following modification of a computed eigenvector basis. Translation invariance is expressly violated for all but Panel 1, nullifying computational gains with Panels 2-4 were translation symmetry preserved. . . . . 78
- 3.7 The left-hand (a) and right-hand (b) plots show the effective energies for the nucleon obtained on the  $a094m358$  ensemble, using the spatially-local, non-relativistic interpolator  $N^2S_S\frac{1}{2}^+$  subduced into the  $G_{1g}$  and  $E_1$  irreps of  $O_h^D$  and  $Dic_4$ , respectively. Panel (a) results from standard eigenvectors and panel (b) from  $\vec{\zeta}_1$ -phased eigenvectors. Data are shown for points where the signal-noise ratios are  $\geq 1.35$  (a) and  $\geq 2$  (b), and are shifted horizontally for legibility. The bands show the two-state fits to the correlators, where the dark regions indicate data included in the fits. The dashed lines are energies expected from the continuum dispersion relation. . . . . 82
- 3.8 The ground-state nucleon principal correlators rescaled as  $\lambda_0 e^{E_0(T-T_0)}$  for the  $a094m358$  ensemble using projected interpolators within each momentum channel obtained from  $\mathcal{B}_{\vec{p}=\vec{0}}^{[7]}$  and  $\mathcal{B}_{\vec{p}\neq\vec{0}}^{[16]}$ . The left-hand and right-hand panels are obtained from the unphased and  $\vec{\zeta}_1$ -phased eigenvectors, respectively. The ground-state principal correlator from the unphased  $\mathcal{B}_{\vec{p}=\vec{0}}$  basis is shown for reference (blue). In each case, data are shown for signal-to-noise ratios  $\geq 2$ . The bands show the two-exponential fits of Eq. 2.75, with data excluded from the fits in gray. . . . . 83
- 3.9 The ground-state nucleon dispersion relation for the  $a094m358$  ensemble, together with expectations from the continuum (blue) and free lattice scalar (purple) dispersion relations. Energies without the use of phasing are shown in magenta for the  $N^2S_S\frac{1}{2}^+$  operator, and orange for the variational analyses using the bases  $\mathcal{B}_{\vec{p}=\vec{0}}^{[7]}$ ,  $\mathcal{B}_{\vec{p}\neq\vec{0}}^{[16]}$ . The squares and triangles are results from the variational analyses of  $\vec{\zeta}_1$  and  $\vec{\zeta}_2$  phased eigenvectors. A subsequent GEVP of a purely local basis (red), demonstrates the phase factors do not invalidate the group theory used to construct our operators. The energies for  $ap_z = 4(2\pi/L)$ , where each phase and unphased eigenvectors were used, are shown in the inset plot. The lower panel emphasizes the differences between each method by normalizing each with respect to the continuum dispersion relation. . . . . 85



3.10	Nucleon effective energies for the $a094m278$ ensemble using a projected interpolator obtained from the $\mathcal{B}_{\vec{p}=\vec{0}}^{[7]}$ and $\mathcal{B}_{\vec{p}\neq\vec{0}}^{[16]}$ bases subduced into the relevant little group, together with continuum expectations (dashed), and 2-state fits (bands), where in each case the darker region denotes the time series included in the fit. No phasing was used to extract the ground-state nucleon energy for lattice momenta $ap_z \in \mathbb{Z}_5$ , while $ap_z = 4(2\pi/L)$ was also determined with $\vec{\zeta}_2$ -phasing (3.24). In the case of $ap_z = 4(2\pi/L)$ , the results with and without phased eigenvectors are shown as the green and red points respectively, clearly demonstrating the need for phasing. Data shifted for legibility, and shown for signal-to-noise ratios greater than 1.35. . . . .	87
3.11	Renormalized $R_S(T, \tau)$ and $g_S^{u-d}$ for momenta $ap_z = 0$ (upper-left), $ap_z = (2\pi/L)$ (upper-right), $ap_z = 4 \times (2\pi/L)$ without phasing (lower-left), and $ap_z = 4 \times (2\pi/L)$ with $\vec{\zeta}_2$ -phasing (lower-right). Variationally improved operators were used within each momentum channel, with $T_{\text{fit}}^{\text{max}} = 16, 16, 7, 12$ respectively. . . . .	90
3.12	Rest-frame renormalized $R_{V_4}(T, \tau)$ and $g_{V_4}^{u-d}$ (left), and $R_{\gamma_3\gamma_5}(T, \tau)$ and $g_{A_3}^{u-d}$ (right). A variationally improved operator was used in these determinations.	91
3.13	Renormalized $R_{V_\mu}(T, \tau)$ and $g_{V_\mu}^{u-d}$ determined from $\gamma_3$ (left panel) and $\gamma_4$ (right panel) insertions. External nucleon momentum according to $ap_z = (2\pi/L)$ (upper), $ap_z = 4(2\pi/L)$ without phasing (middle), $ap_z = 4(2\pi/L)$ with $\vec{\zeta}_2$ -phasing (lower). Variationally improved operators were used within each momentum channel. . . . .	98
3.14	Renormalized $R_{A_\mu}(T, \tau)$ and $g_{A_\mu}^{u-d}$ determined from $\gamma_3\gamma_5$ (left panel) and $\gamma_4\gamma_5$ (right panel) insertions. External nucleon momentum according to $ap_z = (2\pi/L)$ (upper), $ap_z = 4(2\pi/L)$ without phasing (middle), $ap_z = 4(2\pi/L)$ with $\vec{\zeta}_2$ -phasing (lower). Variationally improved operators were used within each momentum channel. . . . .	99
3.15	Renormalized $R_{T_{12}}(T, \tau)$ and $g_{T_{12}}^{u-d}$ for momenta $ap_z = 0$ (upper-left), $ap_z = (2\pi/L)$ (upper-right), $ap_z = 4(2\pi/L)$ without phasing (lower-left), and $ap_z = 4(2\pi/L)$ with $\vec{\zeta}_2$ -phasing (lower-right). Variationally improved operators were used within each momentum channel. . . . .	100
4.1	Recent isovector unpolarized (left), helicity (center), and transversity (right) PDFs obtained by the ETM collaboration using the quasi-distribution formalism [97]. The momentum fraction $x$ -dependence is obtained from the LaMET procedure. A strong dependence on the hadron's momentum is evident. . . . .	107

4.2	Lowest order Feynman diagrams contributing to the quark partonic matching coefficient. Each current is spatially separated by $z$ . The current insertions are denoted as red dashed lines with a potential open Dirac index indicated. . . . .	113
4.3	Wick contraction topologies resulting from two current correlators with each current conserving flavor. The use of flavor changing currents cancels all but contractions (a) and (d), while the latter is canceled by an isovector construction. . . . .	125
4.4	Diagrammatic construction of the pion four-point function built from a modified sequential source (black) and a time-local auxiliary heavy quark propagator (red). This setup admits correlation of currents with arbitrary Lorentz structure and separation independent of the costly Dirac inversions. . . . .	127
4.5	Representative matrix element extractions for $z = 3a$ and increasing pion boosts on the ensembles $a94m278$ (left) and $a94m358$ (right). The leading time dependence has been removed to expose the asymptotic plateau in the data. The $p = 1.25, 1.65$ GeV data have been rescaled by factors of 5 and 25, respectively, to illustrate the rapid deterioration of the matrix element signals as the pion momentum is increased. . . . .	132
4.6	The Ioffe-time pseudo-structure function $T_1^\pi(\nu, z^2)$ computed on the $a94m278$ ( $\circ$ ), $a94m358$ ( $\square$ ), $a127m413$ ( $\star$ ), and $a127m413L$ ( $\triangle$ ) ensembles. In the small- $z$ regime $T_1^\pi(\nu, z^2)$ factorizes into the valence quark PDF of the pion $f_{q_v/\pi}(x)$ . . . . .	134
4.7	The factorization of a baryonic three-point with the non-local space-like operator $\hat{\mathcal{O}}_{\text{WL}}^{[\gamma_4]}(z, \tau)$ . Distillation splits this correlation function into reusable elementals (blue), perambulators (green) and generalized perambulators (red) of the form in Eq. 4.61. . . . .	136
4.8	Real (above) and imaginary (below) summation data $R(p_3, z_3; T)$ for $\{p_3, z_3/a\} = (0.82 \text{ GeV}, 10), (1.24 \text{ GeV}, 9), (2.47 \text{ GeV}, 4)$ from left to right, together with the linear fit (4.63) applied for different time series. The slope of each linear fit yields the bare matrix element, which is seen to be consistently determined for varied fitting windows. Slight tension in the $(2.47 \text{ GeV}, 4)$ extracted matrix element is observed as the fitting window is altered. Although minor, this stems from the poorly determined $T/a = 12, 14$ data. . . . .	137
4.9	The real (left) and imaginary (right) component of the unpolarized reduced pseudo-ITD on the $a94m358$ ensemble with Wilson like extents $z/a < 13$ . . . . .	139

5.1	Simultaneous and correlated $z$ -expansion fit to the $T_1^\pi(\nu, z^2)$ Ioffe-time pseudo-structure function computed on the $a94m278$ ( $\circ$ ), $a94m358$ ( $\square$ ), $a127m413$ ( $\star$ ), and $a127m413L$ ( $\triangle$ ) ensembles. The indigo band is $T_1^\pi(\nu)$ in the continuum limit, having removed the lattice effects parameterized by the $b_i$ coefficients in Eq. 5.10. The $\rho_k$ covariances are used to determine the $T_1^\pi(\nu)$ errorband. The outer dark cyan band is the result of combining the $T_1^\pi(\nu)$ statistical uncertainties in quadrature with the systematic $b_i$ uncertainties.	150
5.2	(a) The pion valence quark distribution obtained from fitting the convolution of the NLO matching kernel (4.53) and two- and three-parameter PDF ansätze to the $T_1^\pi(\nu)$ ITD obtained from the $z$ -expansion fit (5.10). The two- and three-parameter PDFs are obtained from the NLO matching at an initial scale $\mu_0^2 = 4 \text{ GeV}^2$ , and are given in red and green respectively. The same PDF obtained from a three-parameter LO matching of the $a127m413L$ $T_1^\pi(\nu, z^2)$ at $\mu_0^2 = 1 \text{ GeV}^2$ is given in cyan - error is omitted for clarity, but may be found in Ref. [119]. (b) Comparison of $T_1^\pi(\nu)$ with reconstructions from the PDF fits for $4 < \nu < 5$ .	154
5.3	The $x f_{q_v/\pi}(x, \mu^2)$ distributions evolved to the scale $\mu^2 = 27 \text{ GeV}^2$ . The PDFs resulting from the two- and three-parameter NLO analyses of the $T_1^\pi(\nu)$ ITD are shown in red and green, respectively. The three-parameter PDF obtained from the LO analysis of $T_1^\pi(\nu, z^2)$ on the $a127m413L$ ensemble is given in cyan. This evolution scale was chosen to facilitate a direct comparison with a LO analysis [152] of the E615 pionic Drell-Yan data (blue points), and a re-analysis [159] accounting for the emission of soft gluons [156] (orange points).	156
5.4	(a) The convolution of the $K^{(1,0)}$ kernel with model PDFs. (b) The convolution of the $K^{(1,1)}$ kernel with model PDFs. Note the green and black model PDFs are precisely the PDF results obtained from the above global analysis of the $T_1^\pi(\nu)$ ITD using the NLO matching kernel. The respective agreement between the green and black $K^{(1,0)}$ and $K^{(1,1)}$ convolutions reiterates $T_1^\pi(\nu, z^2)$ data at larger values of $\nu$ are needed to discriminate these PDF parameterizations.	157
5.5	The $T_g^\pi(\nu, z^2)$ pseudo-structure function obtained on the $a127m413$ ensemble by averaging $\gamma_x \gamma_x$ and $\gamma_y \gamma_y$ two-current combinations. Lack of a clear functional trend together with a floating normalization of $f_{q_v/\pi}(x)$ accessible from these current combinations, limits a global analysis with the vector-axial currents.	159

5.6	Convolutions needed to evolve (upper) and match (lower) the reduced pseudo-ITD to a common scale of 2 GeV in $\overline{\text{MS}}$ . The real and imaginary convolutions are shown at the left and right, respectively. The NLO prefactor $\alpha_s C_F/2\pi$ is included in these data, but omitted from the labels for clarity. The convolutions were performed up to $z/a = 16$ , but data for $z/a > 9$ are generally noisy and not shown. . . . .	163
5.7	The real (left) and imaginary (right) components of the unpolarized ITD at a scale of 2 GeV in $\overline{\text{MS}}$ obtained from the matching relation (5.15) applied to polynomial fits of the reduced pseudo-ITD data. Data is shown for Wilson line extents $z/a \leq 12$ - Wilson lines of $z/a > 12$ are considerably uncertain, and thus excluded from our ensuing analysis. . . . .	164
5.8	(a) Real component of the matched ITD at $\mu = 2$ GeV in $\overline{\text{MS}}$ fit by cosine transforms of two- and three-parameter model PDFs (Eq. 5.5). Data have been fit for $z/a \leq 12$ , and correlations have been neglected. The resulting PDF parameters and figure of merit are gathered in Tab. 5.3. (b) The two- and three-parameter PDF parameterizations are compared with four phenomenological determinations (noted in text) at the same scale. . . . .	165
5.9	(a) Imaginary component of the matched ITD at $\mu = 2$ GeV in $\overline{\text{MS}}$ fit by a sine transform of a two-parameter model PDF (Eq. 5.6). Data has been fit for $z/a \leq 12$ , and correlations have been neglected. The resulting PDF parameters and figure of merit are gathered in Tab. 5.3. (b) The two-parameter PDF parameterization is compared with four phenomenological determinations (noted in text) at the same scale. . . . .	166
5.10	Two-parameter valence (a) and plus (b) quark PDFs resulting from type- $C$ (red) and type- $K$ (indigo) fits to the unpolarized nucleon ITD and reduced pseudo-ITD, respectively. The direct matching fits are consistent with the cosine/sine transform of the model PDF fit to the ITD. . . . .	168
5.11	(a) Real component of the matched ITD at $\mu = 2$ GeV in $\overline{\text{MS}}$ fit by the cosine transform of a two-parameter model PDF (5.5). Data has been fit for $z/a \leq 12$ and <i>data correlations have been incorporated</i> . The fit clearly misses each point of the ITD. The derived CJ15 ITD at the same scale is shown for reference. (b) The same as panel (a), but with focus given to the small- $\nu$ region. The correlated two-parameter fit is seen to deviate appreciably from the precise small- $\nu$ data. . . . .	170
5.12	Data covariance in the real (left) and imaginary (right) components of the matched ITD at 2 GeV, normalized according to $\text{Cov}_{ij}/\sqrt{\text{Cov}_{ii}\text{Cov}_{jj}}$ . Within each lattice momentum block, entries are ordered in ascending Wilson line lengths. . . . .	171

5.13	The eight lowest-order $\sigma_{0,n}^{(\alpha,\beta)}$ (left) and $\eta_{0,n}^{(\alpha,\beta)}$ (right) polynomials for an arbitrarily chosen basis $\alpha = 0.125$ and $\beta = 2.85$ . Each polynomial features an extremum in a range of Ioffe-time accessible in our lattice calculation, and asymptotically approaches zero for $\nu \rightarrow \infty$ . . . . .	174
5.14	Parameter covariances in Jacobi polynomial fits with $[n_{lt}, n_{az}, n_{t4}, n_{t6}] = [6342]$ to the real (left) and imaginary (right) components of the unpolarized reduced pseudo-ITD for $z/a \leq 12$ . Entries are normalized according to $\text{Cov}_{ij}/\sqrt{\text{Cov}_{ii}\text{Cov}_{jj}}$ . . . . .	179
5.15	Fit to the real component of the unpolarized reduced pseudo-ITD where the leading-twist, discretization, twist-4, and twist-6 corrections have been expanded in Jacobi polynomials up to order $\{n_{lt}, n_{az}, n_{t4}, n_{t6}\}_v = \{4, 1, 3, 2\}_v$ . Starting from the upper left panel and traversing horizontally, the leading-twist plus corrections are shown for each $z/a \leq 12$ . . . . .	182
5.16	Parameter covariances of the optimal Jacobi polynomial fits to the real (a) and imaginary (b) component of the unpolarized reduced pseudo-ITD for $z/a \leq 12$ with truncation orders $\{n_{lt}, n_{az}, n_{t4}, n_{t6}\}_v = \{4, 1, 3, 2\}_v$ and $\{n_{lt}, n_{az}, n_{t4}, n_{t6}\}_+ = \{3, 3, 1, 0\}_+$ , respectively. Entries are normalized according to $\text{Cov}_{ij}/\sqrt{\text{Cov}_{ii}\text{Cov}_{jj}}$ . . . . .	183
5.17	(a) The real component of the leading-twist ITD (purple) at 2 GeV derived from the Jacobi polynomial expansion of the reduced pseudo-ITD for $z/a \leq 12$ with $\{n_{lt}, n_{az}, n_{t4}, n_{t6}\}_v = \{4, 1, 3, 2\}_v$ . The result is compared with the uncorrelated 2-parameter phenomenological form of Eq. 5.5 shown in red. (b) The valence quark leading-twist PDF (purple) obtained from the $\{n_{lt}, n_{az}, n_{t4}, n_{t6}\}_v = \{4, 1, 3, 2\}_v$ Jacobi polynomial expansion of the reduced pseudo-ITD. The $a/z$ (orange), twist-4 (brown), and twist-6 (navy) $x$ -space distributions are also shown and seen to be sub-leading. The distributions are compared with the uncorrelated 2-parameter phenomenological fit of Eq. 5.5 (red), as well as an NLO global analyses of CJ15 [132] and JAM20 [160], and the NNLO analyses of MSTW [161] and NNPDF [38] at the same scale. . . . .	184
5.18	Fit to the imaginary component of the unpolarized reduced pseudo-ITD where the leading-twist, discretization, twist-4, and twist-6 corrections have been expanded in Jacobi polynomials up to order $\{n_{lt}, n_{az}, n_{t4}, n_{t6}\}_+ = \{3, 3, 1, 0\}_+$ . Starting from the upper left panel and traversing horizontally, the leading-twist plus corrections are shown for each $z/a \leq 12$ . . . . .	185

5.19	(a) The imaginary component of the leading-twist ITD (purple) at 2 GeV derived from the Jacobi polynomial expansion of the reduced pseudo-ITD for $z/a \leq 12$ with $\{n_{lt}, n_{az}, n_{t4}, n_{t6}\}_+ = \{3, 3, 1, 0\}_+$ . The result is compared with the uncorrelated 2-parameter phenomenological form of Eq. 5.6 shown in red. (b) The plus quark leading-twist PDF (purple) obtained from the $\{n_{lt}, n_{az}, n_{t4}, n_{t6}\}_+ = \{3, 3, 1, 0\}_+$ Jacobi polynomial expansion of the reduced pseudo-ITD. The $a/z$ (orange) and twist-4 (brown) $x$ -space distributions are also shown and seen to be sub-leading. The distributions are compared with the uncorrelated 2-parameter phenomenological fit of Eq. 5.6 (red), as well as the NLO global analyses of CJ15 [132] and JAM20 [160], and the NNLO analyses of MSTW [161] and NNPDF [38] at the same scale.	186
5.20	Cosine transform of the model pseudo-PDF in Eq. 5.42 fit separately to $\Re \mathfrak{M}(\nu, z^2)$ for distinct $z^2$ ; data correlations have been included in each fit. Starting from the upper left panel and traversing horizontally, $z/a$ increases from unity. The correlated figure of merit for each separate fit is also indicated.	188
5.21	The fitted value of $\alpha$ as a function of $z/a$ resulting from the cosine-transform of the model pseudo-PDF in Eq. 5.42 fit to $\Re \mathfrak{M}(\nu, z^2)$ . The decrease of $\alpha$ with $z/a$ is in agreement with expectations from the Altarelli-Parisi evolution of the pseudo-PDF. This dependence is however clearly linear.	189
5.22	Cosine transform of the two-parameter model PDF, with the same functional form as (5.42), fit separately to each $z^2$ of the matched ITD. The ITD was obtained using (5.44) for the evolution/matching step. Data correlations have been included in each fit. Starting from the upper left panel and traversing horizontally, $z/a$ increases from unity. The correlated figure of merit for each separate fit is also indicated.	190
5.23	The fitted values of $\alpha$ from the cosine-transform of the two-parameter PDF functional form (5.42) fit to each $z^2$ of the matched ITD. The latter was obtained using (5.44) for the evolution/matching step. The values of $\alpha$ are statistically constant for $4 \lesssim z/a \lesssim 11$ , with sharp deviations for small- $z/a$ .	192
5.24	Visualization of the discretization effects determined by the optimal Jacobi polynomial fits $\{n_{lt}, n_{az}, n_{t4}, n_{t6}\}_v = \{4, 1, 3, 2\}_v$ (left) and $\{n_{lt}, n_{az}, n_{t4}, n_{t6}\}_+ = \{3, 3, 1, 0\}_+$ (right) for $z/a \leq 7$ .	193
5.25	Juxtaposition of the raw $\Re \mathfrak{M}(\nu, z^2)$ and discretization corrected $\Re \mathfrak{M}'(\nu, z^2)$ distributions, represented by circles and wedges respectively. The $\Re \mathfrak{M}'(\nu, z^2)$ data is shifted horizontally for legibility.	194

5.26	(Left) The variation of $\alpha$ with $z/a$ resulting from the cosine-transform of the model pseudo-PDF in Eq. 5.42 fit to $\Re \mathcal{M}'(\nu, z^2)$ for each $z^2$ . The discretization effect captured by the optimal Jacobi polynomial expansion $\{n_{lt}, n_{az}, n_{t4}, n_{t6}\}_v = \{4, 1, 3, 2\}_v$ is subtracted from $\Re \mathcal{M}(\nu, z^2)$ prior to performing each fit. (Right) The variation of $\alpha$ with $z/a$ resulting from the cosine-transform of the two-parameter PDF form in Eq. 5.42 fit to the discretization corrected and matched ITD $\Re \mathcal{Q}'(\nu, z^2)$ for each $z^2$ . The discretization corrected ITD is considerably more independent of the interval $z^2$ . . . . .	195
6.1	The ratio $R_\Gamma(\vec{p}_f, \vec{p}_i; T, \tau)$ for the $\Gamma = \gamma_4$ insertion and $\vec{p}_f = \vec{0}$ and $\vec{p}_i = (0, 0, 1)$ . The top row is the real component of the ratio, and the bottom row the imaginary component. From left to right the Wilson line lengths increase monotonically in the set $z/a \in \{1, 3, 5, 8\}$ . . . . .	200
6.2	The ratio $R_\Gamma(\vec{p}_f, \vec{p}_i; T, \tau)$ for the $\Gamma = \gamma_x$ insertion and $\vec{p}_f = \vec{0}$ and $\vec{p}_i = (0, 0, 1)$ . The top row is the real component of the ratio, and the bottom row the imaginary component. From left to right the Wilson line lengths increase monotonically in the set $z/a \in \{1, 3, 5, 8\}$ . . . . .	200
6.3	Coverage of the unpolarized GPDs in $\xi$ vs. $t$ with source/sink nucleon interpolators with a component of momenta $ ap_j  \in \mathbb{Z}_7 \times 2\pi/L$ collinear to the Wilson line and nineteen distinct momentum transfers associated with the space-like quark bilinear. The unpolarized nucleon PDFs using the pseudo-distribution that were featured in Sec. 5.3 correspond to the $(\xi, t) = (0, 0)$ point. . . . .	201

# FORWARD & OFF-FORWARD PARTON DISTRIBUTIONS FROM LATTICE QCD



# CHAPTER 1

## Invitation

Astrophysical observations indicate the Cosmos is suffuse with so-called Dark Energy and Dark Matter. Recent measurements from the Planck Collaboration of the European Space Agency largely confirm previous measurements of the NASA/Wilkinson Microwave Anisotropy Probe (WMAP) [1], indicating the mass-energy content of the Universe is manifested nearly entirely ( $\sim 95.1\%$ ) within this dark sector [2]. The world with which we interact, observe and are most familiar is then relegated to the remaining  $\sim 4.9\%$ .

With the exception of Gravity, three of Nature's known fundamental forces, Electromagnetism and the Strong and Weak nuclear forces, have been successfully transcribed into the language of relativistic quantum field theory. The modern and unified particle framework for these three forces is the Standard Model of Particle Physics, or simply Standard Model for short. The Standard Model is constructed from three continuous groups

$$\mathrm{SU}(3)_C \otimes \mathrm{SU}(2)_L \otimes \mathrm{U}(1) \tag{1.1}$$

representing the local gauge symmetries each quantum field must respect. Within the confines of the Standard Model a paltry three generations of matter fields (fermions) and

their interactions mediated by exchange of vector bosons charged under the local gauge symmetries (1.1) conspire to give rise to nearly all phenomena from the femtoscale to the exascale. The Standard Model provides remarkably accurate predictions of the physical world, yet still only applies to the roughly 4.9% of the Universe encapsulated by ordinary baryonic matter. Thanks to the Weak nuclear force, or the  $SU(2)_L$  portion of the Standard Model, the majority of known particles in the Universe ultimately decay into a combination of electromagnetic radiation (photons) and the lightest matter fields, including the electron, the lightest quarks (up and down), and the nearly massless neutrinos. It is in this sense that nearly all the mass of the visible Universe is found in the familiar protons and neutrons, collectively nucleons, which are comprised of up and down quarks. In spite of the electromagnetic repulsion felt by pairs of protons and certain quark combinations, the Strong nuclear force is able to bind quarks into nucleons, and nucleons into the composite nuclei that are responsible for all complex structure in the Universe. The stellar fusion of nuclei that pervades the Cosmos to the stability of Life's molecular blueprint all depend on the fortuitous strength of the strong nuclear force.

Yet despite the ubiquity of the nucleon within the known Universe, many of its emergent properties crucial to this extant structure evade a theoretical understanding. Two principal examples include the mass and spin of the proton. The Quark Model describes the proton as three quarks, two up and one down, bound together by the exchange of gluons (the mediator of the strong nuclear force). The quark's respective masses sum to  $\sim 9$  MeV, while the proton itself has a mass of  $\sim 938$  MeV. This implies nearly all of the proton's mass arises dynamically from the strong interaction. In a similar vein, the proton's spin is known to receive only a small fraction from its constituent quarks. A quantitative understanding of these properties resides squarely within the low-energy or strong-coupling regime of the strong interaction, thus lacking a perturbative or approximate description.

Searches for physics Beyond the Standard Model (BSM) at the energy frontier are spearheaded by the ATLAS and CMS experiments within the Large Hadron Collider housed at the European Organization for Nuclear Research (CERN). The search for dark matter candidates, new fundamental particles beyond the Higgs boson and even extra dimensions, also depend intimately on a knowledge of the low-energy dynamics governing the internal structure of hadrons. Central to the interpretation of high-energy scattering cross-sections are the collinear parton distributions. These distributions not only aid in understanding and predicting these cross sections, but also provide a vehicle with which some of the proton's enigmatic features can be discerned.

This volume of work concerns the highly non-trivial strong nuclear force and the efforts to elucidate its non-perturbative regime through numerical calculation. You the reader are invited to join in this development.

# CHAPTER 2

## Quantum Chromodynamics

From the modern viewpoint, the principle of local gauge invariance is the central tenet from which Quantum Field Theories (QFTs) can be derived. Consider the free Dirac Lagrangian

$$\mathcal{L}_{Dirac} = \sum_f \bar{\psi}_f (i\not{D} - m_f) \psi_f, \quad (2.1)$$

where  $f$  denote distinct fermion flavors of mass  $m_f$ . Demanding the free theory be invariant under local U(1) phase rotations  $\psi(x) \rightarrow \exp(i\alpha(x))\psi(x)$  leads to the existence of a vector field, or connection,  $A_\mu(x)$ . Together with a kinetic term for  $A_\mu$ , the requirement of renormalizability, and the postulates of parity and time-reversal invariance, one is led uniquely<sup>1</sup> to Quantum Electrodynamics (QED)

$$\mathcal{L}_{QED} = \sum_f \bar{\psi}_f (i\not{D} - m_f) \psi_f - \frac{1}{4} F_{\mu\nu} F^{\mu\nu}, \quad (2.2)$$

---

<sup>1</sup>Were we to lessen the requirement of parity and time reversal invariance, an additional dimension-4 operator  $\epsilon^{\alpha\beta\mu\nu} F_{\alpha\beta} F_{\mu\nu}$  would appear. Operators of energy dimension greater than four can be constructed from the fermion fields  $\psi, \bar{\psi}$  and their covariant derivatives, and  $F_{\mu\nu}$  and its derivatives. However, any such term with dimension greater than four is nonrenormalizable.

where  $F_{\mu\nu} = \partial_\mu A_\nu - \partial_\nu A_\mu$  is the electromagnetic field strength tensor,  $D_\mu = \partial_\mu - ieA_\mu$  the gauge covariant derivative, with  $e$  the modulus of the electron charge - simply the QED coupling constant. The local phase rotations  $e^{i\alpha(x)}$  belong to the simple and compact, Abelian Lie group  $U(1)$ ; QED is then said to be a QFT imbued with an Abelian gauge symmetry, and happens to be the only Abelian constituent of the Standard Model.

The generalization of local gauge invariance under an Abelian group to generic Lie groups was first considered by Chen Ning Yang and Robert Mills [3] in 1954. Their efforts centered on the proton and neutron which, due to their small mass difference<sup>2</sup>, were experimentally inferred to be approximately related to each other through continuous rotations in  $SU(2)$  isospin, or isobaric, space. The observed (approximate) global conservation of isospin in nuclear physics processes led Yang and Mills to consider the physical consequences of demanding invariance of nuclear processes under local  $SU(2)$  isospin transformations

$$\psi(x) \rightarrow \tilde{\psi}(x) = \exp\left(i\alpha^c(x) \frac{\sigma^c}{2}\right) \psi(x), \quad (2.3)$$

where  $\alpha^c(x)$  is one of three spacetime dependent phases and  $\sigma^c$  are the usual Pauli sigma matrices. The modification of the free Dirac theory proceeds analogously to the development of QED, with the consequential difference that the gauge transformations instead belong to a non-Abelian Lie group. In the interest of brevity, the reader is referred to any standard QFT text for details of the derivation of the Nobel Prize winning Yang-Mills Lagrangian<sup>3</sup>

$$\mathcal{L}_{YM} = \sum_f \bar{\psi}_f^i (i\gamma^\mu D_\mu^{ij} - m_f \delta^{ij}) \psi_f^j - \frac{1}{4} F_{\mu\nu}^a F^{a\mu\nu}, \quad (2.4)$$

---

<sup>2</sup>Attributed today to the small mass difference between  $u$  and  $d$  quarks.

<sup>3</sup>It is important to note the distinction of  $\mathcal{L}_{YM}$  with a *pure* Yang-Mills Lagrangian, which describes the interaction of non-Abelian gauge fields in the absence of fermionic fields.

where the field strength tensor and covariant derivative are modified to  $F_{\mu\nu}^a = \partial_\mu A_\nu^a - \partial_\nu A_\mu^a - gf^{abc}A_\mu^b A_\nu^c$  and  $D_\mu^{ij} = \delta^{ij}\partial_\mu + igt_{ij}^c A_\mu^c$ , respectively, and Einstein summation convention is implied. Relative to QED, the Yang-Mills Lagrangian includes generators  $t^c$  of the non-Abelian, simple and compact Lie group, and indices  $\{i, j\}$  and  $\{a, b, c\}$  denoting the fundamental and adjoint representations of the group, respectively. The Lie group structure constants  $f^{abc}$  are defined via the commutator  $[t^a, t^b] = if^{abc}t^c$ . A dramatic consequence of a non-Abelian gauge symmetry, even in the absence of matter fields, is the emergence of an  $A_\mu^b A_\nu^c$  term in the field strength tensor. The kinetic term of a non-Abelian QFT evidently generates three and four particle vertices of the (self-interacting) gauge field.

Quantum Chromodynamics (QCD) is the accepted QFT describing the strong nuclear force, wherein fermionic fields called *quarks* interact through the exchange of mutually-interacting force carriers called *gluons*

$$\mathcal{L}_{QCD} = \sum_f \bar{\psi}_f^i \left( i\not{D}^{ij} - m_f \delta^{ij} \right) \psi_f^j - \frac{1}{4} G_{\mu\nu}^a G^{a\mu\nu}. \quad (2.5)$$

In certain contexts quarks and gluons in QCD are simply referred to as *partons*, where partons are most easily thought of as being the (asymptotically free) particles rather than the potentially collective QCD fields. QCD is a class of Yang-Mills theories imbued with an  $SU(3)_C$  symmetry, where  $C$  designates the local “color” or chromatic quantum number, with members of the group conventionally written as  $3 \times 3$  complex unitary matrices; the generators  $t^a$  of  $SU(3)$  are defined by the Gell-Mann matrices  $t^a = \lambda_a/2$  (see Appendix B). Found in six flavors  $f = u, d, c, s, t, b$ , the quarks transform under the fundamental or  $\mathbf{3}$  representation of  $SU(3)$ , with each quark forming a color-triplet; anti-quarks correspondingly transform under the conjugate or  $\bar{\mathbf{3}}$  representation of  $SU(3)$ . The strong force carrying gluons transform under the adjoint or  $\mathbf{8}$  representation of  $SU(3)$ ,

which places the gluons in a color-octet. Indeed there is no notion of *color* at the level of fields; rather the term arose as a description for an unseen quark degree of freedom.

The *Quark Model* [4, 5] proposed by Gell-Mann and Zweig provided order to the rapidly proliferating zoo of strongly-interacting particles discovered in the 1950s and 1960s. Positing the existence of three constituent particles deemed quarks with fractional electric charge and a *flavor* SU(3) symmetry, the Quark Model found phenomenological success by matching the strongly-interacting states with representations of SU(3). Many identified states however, such as the triply-strange  $\Omega^-$  or triply-up  $\Delta^{++}$ , were known to possess fully symmetric wavefunctions - the starkest of contradictions to the Spin-Statistics Theorem [6, 7], which states fermions must obey Fermi-Dirac statistics and thus be totally antisymmetric in their wavefunctions. *Color* SU(3) emerged as a gauge quantum number of quarks which, when assembled totally anti-symmetrically, restored the required anti-symmetry of the baryon wavefunctions.

QCD is characterized by ultraviolet divergences in perturbative calculations of processes beyond tree-level. These infinities arise from Feynman diagram loops involving integrals over unspecified momenta, and are managed by redefining a theory's bare parameters (e.g. coupling and field masses) with respect to a regulator. Ensuring a QFT then yields a finite result for a computed quantity involves introduction of counterterms, which likewise depend on the regulator, to counterbalance the infinite shifts between the theory's bare and physically measured parameters. This process, referred to as *renormalization*, has many profound consequences. One of particular significance, the physically measured parameters of any renormalizable QFT depend on the resolving energy the theory is probed at. This scale dependence, or running, equates to varied manifestations of a theory across energy regimes. Unlike the Electro-Weak sector of the Standard Model, the QCD coupling  $\alpha_s = g^2/4\pi$  runs to small values at high energy scales. Quarks and gluons within this regime may be treated as free entities of QCD, with perturbatively and sys-

tematically computable weak interactions. This aspect of QCD, and indeed a great many non-Abelian gauge theories, is referred to as *asymptotic freedom* - that is, the theory's fields become non-interacting in the limit of infinite probing energy [8, 9].

The low-energy regime of QCD, studied at experimental facilities for nearly the last century, is dramatically different. The asymptotic states of QCD observed in detectors are instead color-singlet objects or *hadrons*, of which the proton/neutron and pion triplet are examples. Such three quark hadrons, or *baryons*, are but a sliver of a plethora of color-singlet states in QCD. Other states include quark-antiquark pairs, or *mesons*, as well as the hypothetical tetra-/penta-quarks and particles of purely gluonic excitation (glueballs). This behavior of QCD is understood by the increase of  $\alpha_s$  as the resolving energy is reduced; at hadronic energy scales the strong coupling is of  $\mathcal{O}(1)$  and leads to the *confinement* of quarks/gluons into hadrons [10]. As perturbative methods are predicated on a small coupling constant, an order-by-order expansion of a low-energy QCD process must confront a proliferation of important Feynman diagrams. For low-enough energies this perturbative series fails to converge or is ill-defined entirely.

Although modeling can garner insight into the strong dynamics of QCD, the only known method to rigorously study the non-perturbative regime of QCD with systematically improvable results is through numerical solution of the theory itself. This paradigm is *Lattice QCD*, and its application to parton distributions is the focus of this dissertation. Before directing our attention to the formulation of Lattice QCD in Sec. 2.3, we introduce parton distributions as key measures of the non-perturbative dynamics responsible for hadronic structure.



## 2.1 Hadron Structure and Parton Distributions

The soft dynamics of a composite hadron  $h$  are generically encoded in parton correlations between initial and final hadronic states  $h$  via the parton correlation function

$$\mathcal{H}_{ij/h}^{[\Gamma;\lambda'\lambda]}(k, P, \Delta) = \int \frac{d^4z}{(2\pi)^4} e^{ik \cdot z} \langle h(P + \frac{\Delta}{2}, \lambda') | \bar{\psi}_i(\frac{z}{2}) \Gamma \Phi^{(f)}(\{\frac{z}{2}, -\frac{z}{2}\}) \psi_j(-\frac{z}{2}) | h(P - \frac{\Delta}{2}, \lambda) \rangle, \quad (2.6)$$

where the incoming and outgoing hadron momenta are denoted by  $P - \frac{\Delta}{2}$  and  $P + \frac{\Delta}{2}$ , the parton momenta is given by  $k$ , and helicity labels  $\{\lambda', \lambda\}$  are made explicit. The Dirac matrix  $\Gamma$  selects a particular polarization configuration for the flavor- $i/j$  parton fields. The gauge invariance of the parton bilinear is guaranteed by inclusion of a gauge link or Wilson line

$$\Phi^{(f)}\left(\left\{\frac{z}{2}, -\frac{z}{2}\right\}\right) = \mathcal{P} \exp\left(ig \int_{-z/2}^{z/2} d\eta^\nu A_\nu^c(\eta) t_c\right), \quad (2.7)$$

built from a path-ordered ( $\mathcal{P}$ ) collection of  $\mathfrak{su}(3)$  algebra valued gauge fields in the fundamental ( $f$ ) representation of  $SU(3)$ ,<sup>4</sup> weighted by the gauge coupling  $g$ . Although the Wilson line is shown here along a generic contour with differential line element  $d\eta^\nu$ , depending on the observable and choice of gauge the character of the Wilson line will change or reduce to unity entirely.

This generic correlation function, illustrated in Fig. 2.1, encapsulates all of the non-perturbative QCD dynamics of hadrons, even nuclei, and is the starting point with which the momentum and spatial distributions of partons and their mutual correlations can be quantified. Distinct parton flavors  $\{i, j\}$  may in general be considered, but for the entirety of this work we consider equal parton flavors and hence drop parton indices. These correlations are probed experimentally in collider or fixed-target experiments, for which

---

<sup>4</sup>As given, this Wilson line is relevant for quark correlations, with  $t_c$  denoting the generators of  $SU(3)$  in the fundamental representation. Were gluons considered, the generators and the Wilson line as a whole would then be in the adjoint representation of  $SU(3)$ .

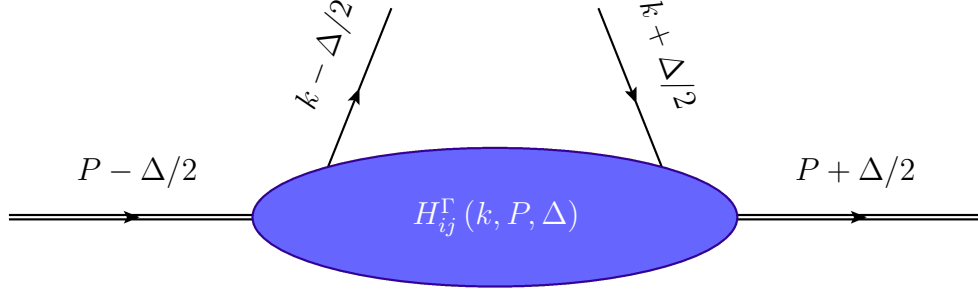


FIG. 2.1: A generic parton correlation function with momentum assignments.

the natural choice of coordinates are light-cone coordinates.<sup>5</sup> The hadron's momentum is then denoted  $P^\mu = \left(P^+, \frac{M_h^2}{2P^+}, \mathbf{0}_T\right)$ , while a parton carrying fraction  $x$  of its parent hadron's  $P^+$  momentum is denoted  $k^\mu = (xP^+, k^-, \mathbf{k}_T)$ . Physical observables depend on the momentum space correlation function (2.6) when integrated over different components of the parton's 4-momentum  $k^\mu$ , as well as what momenta  $\Delta$  is transferred to the hadron. We now consider some of these integrated parton distributions and pause to highlight the experimental processes sensitive to them; the developments closely follow those of Diehl [11]. By adopting this reductionist perspective we will arrive quite naturally to the forward and off-forward parton distributions that are this dissertation's namesake.

In a high-energy hadron-hadron or hadron-lepton scattering process, the target hadron's  $P^+$  momentum is large and its  $P^-$  component is highly suppressed. This leads to the natural consideration of the  $k^-$ -integrated correlator, for the parton  $k^-$  momentum is suppressed by  $\sim 1/P^+$ . Abbreviating the matrix element appearing in (2.6) as  $\mathcal{C}_{j/h}^{[\Gamma; \lambda' \lambda]}(P, \Delta, z)$  and carrying out the  $k^-$  integration

$$\begin{aligned} \mathcal{W}_{j/h}^{[\Gamma; \lambda' \lambda]} &\equiv \int dk^- \mathcal{H}_{j/h}^{[\Gamma; \lambda' \lambda]}(k, P, \Delta) = \int \frac{d^4 z}{(2\pi)^3} \int \frac{dk^-}{2\pi} e^{iz^+ k^-} e^{i(z^- k^+ - \mathbf{z}_T \cdot \mathbf{k}_T)} \mathcal{C}_{j/h}^{[\Gamma; \lambda' \lambda]}(P, \Delta, z) \\ &= \int \frac{d^4 z}{(2\pi)^3} \delta(z^+) e^{i(z^- k^+ - \mathbf{z}_T \cdot \mathbf{k}_T)} \mathcal{C}_{j/h}^{[\Gamma; \lambda' \lambda]}(P, \Delta, z) \Big|_{z^+=0} \end{aligned}$$

<sup>5</sup>Given some four-vector  $a^\mu$ , light-cone coordinates are defined by  $a^\pm = \frac{1}{\sqrt{2}}(a^0 \pm a^3)$  and  $\mathbf{a}_\perp = (a^1, a^2)$ .

$$= \int \frac{dz^- d^2 \mathbf{z}_T}{(2\pi)^3} e^{i(z^- k^+ - \mathbf{z}_T \cdot \mathbf{k}_T)} \mathcal{C}_{j/h}^{[\Gamma; \lambda' \lambda]}(P, \Delta, z) |_{z^+=0}, \quad (2.8)$$

one finds the effect of the  $k^-$ -integration is to restrict the parton fields at light-cone time  $z^+ = 0$ . An important consequence of this integration is partons lose any definite virtuality and hence no longer satisfy their respective on-mass-shell conditions. When broken down into its Lorentz structures, the  $k^-$ -integrated parton distribution (2.8) is parameterized by sixteen Generalized Transverse Momentum-dependent Distributions (GTMDs) at leading-twist [12]. Higher-twist distributions are suppressed by inverse powers of the hard scale  $P^+$  of the process<sup>6</sup>. These distributions can be accessed in certain exclusive Drell-Yan processes, such as  $\pi N \rightarrow \gamma_1^* \gamma_2^* N'$  [13]. There are however several theoretical issues pertaining to GTMDs, especially in the regularization of light-cone and rapidity divergences. All of these issues are far beyond the scope of this work. GTMDs are merely highlighted here as they serve as a waypoint in our reductionist development of the parton distributions we will consider.

Integrating the generic parton correlator (2.6) over both the  $k^-$  and transverse parton momenta  $\mathbf{k}_T$

$$\begin{aligned} \int d^2 \mathbf{k}_T \int dk^- \mathcal{H}_{j/h}^{[\Gamma; \lambda' \lambda]}(k, P, \Delta) &= \int d^2 \mathbf{k}_T \int \frac{dz^- d^2 \mathbf{z}_T}{(2\pi)^3} e^{iz^- k^+} e^{-i\mathbf{z}_T \cdot \mathbf{k}_T} \mathcal{C}_{j/h}^{[\Gamma; \lambda' \lambda]}(P, \Delta, z) |_{z^+=0} \\ &= \int \frac{dz^-}{(2\pi)} \int d^2 \mathbf{k}_T \int \frac{d^2 \mathbf{z}_T}{(2\pi)^2} e^{-i\mathbf{z}_T \cdot \mathbf{k}_T} e^{iz^- k^+} \mathcal{C}_{j/h}^{[\Gamma; \lambda' \lambda]}(P, \Delta, z) |_{z^+=0} \\ &= \int \frac{dz^-}{(2\pi)} \int d^2 \mathbf{k}_T \delta^2(\mathbf{k}_T) e^{iz^- k^+} \mathcal{C}_{j/h}^{[\Gamma; \lambda' \lambda]}(P, \Delta, z) |_{z^+=0, \mathbf{z}_T=\mathbf{0}} \\ \mathcal{G}_{j/h}^{[\Gamma; \lambda' \lambda]} &= \int \frac{dz^-}{(2\pi)} e^{iz^- k^+} \mathcal{C}_{j/h}^{[\Gamma; \lambda' \lambda]}(P, \Delta, z) |_{z^+=0, \mathbf{z}_T=\mathbf{0}}, \end{aligned} \quad (2.9)$$

one finds the parton fields are now restricted purely along the light-cone with  $z^- \neq 0$ .

---

<sup>6</sup>Twist, defined more rigorously in Sec. 2.2, is the difference between an operator's energy dimension and spin.

This particular integrated parton correlation function  $\mathcal{G}_{j/h}^{[\Gamma;\lambda'\lambda]}$  is parameterized by so-called *collinear* parton distributions, which are distributions appearing in physical observables that are insensitive to the transverse motion of partons. The only parton momentum dependence of a collinear distribution is then via  $k^+$ , which is collinear to the parent hadron's  $P^+$  momentum. The  $\mathbf{k}_T$ -integration above seems straightforward, however the  $\mathbf{z}_\perp$ -dependence of the correlator  $\mathcal{C}_{j/h}^{[\Gamma;\lambda'\lambda]}(P, \Delta, z)$  is especially subtle and leads to regions of large- $\mathbf{k}_T$  and parton virtuality (see e.g. [14]). These regions lead to ultraviolet (UV) divergences in (2.9) that must be regulated and renormalized - typically using the modified minimal subtraction or  $\overline{\text{MS}}$  prescription [15, 16]. Any renormalized collinear parton distribution hence acquires an explicit collinear scheme dependence on the UV renormalization scale  $\mu^2$ . The dependence on the scale  $\mu^2$  is described by the Renormalization Group (RG) equations.

### 2.1.1 Generalized Parton Distributions

Consider the  $k^-$ -,  $\mathbf{k}_T$ -integrated parton correlator  $\mathcal{G}_{j/h}^{[\gamma^+;\lambda'\lambda]}$  for a helicity-conserving flavor- $q$  quark. Lorentz invariance implies  $\mathcal{G}_{q/h}^{[\gamma^+]}$  can be parameterized, following Ji's conventions [17], according to

$$\mathcal{G}_{q/h}^{[\gamma^+]} = \frac{1}{2} \int \frac{dz^-}{2\pi} e^{ixP^+z^-} \langle h(p_f) | \bar{q}(-\frac{z}{2}) \gamma^+ \Phi_{z^-}^{(f)}(\{-\frac{z}{2}, \frac{z}{2}\}) q(\frac{z}{2}) | h(p_i) \rangle \Big|_{z^+=0, \mathbf{z}_T=0} \quad (2.10)$$

$$= \frac{1}{2P^+} \left[ H_{q/h}(x, \xi, t) \bar{u}(p_f) \gamma^+ u(p_i) + E_{q/h}(x, \xi, t) \bar{u}(p_f) \frac{i\sigma^{+\rho} \Delta_\rho}{2m_h} u(p_i) \right] \quad (2.11)$$

where  $P = \frac{p_f + p_i}{2}$  is the average hadron 4-momentum and  $\Delta = p_f - p_i$  the momentum transfer.<sup>7</sup> The Wilson line  $\Phi_{z^-}^{(f)}(\{-\frac{z}{2}, \frac{z}{2}\})$  manifests as a straight gauge connection along the  $z^-$ -direction. The parton correlator  $\mathcal{G}_{q/h}^{[\gamma^+]}$  is parameterized by the unpolarized *Generalized*

---

<sup>7</sup>As  $p_f \neq p_i$ ,  $\Delta \neq 0$  and the parton correlator defining  $\mathcal{G}_{q/h}^{[\gamma^+]}$  is often deemed an *off-forward* correlator.

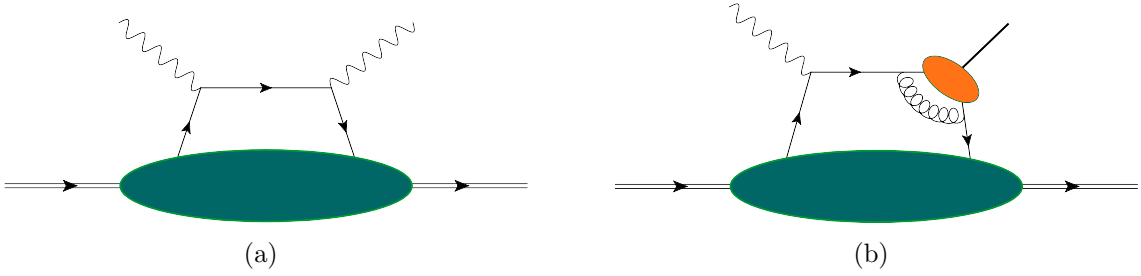


FIG. 2.2: (a) The leading contribution to the DVCS process. (b) A representative diagram contributing to the exclusive deeply virtual meson production channel. In each the blue/green blob denotes the non-perturbative off-forward parton bilinear encapsulated by GPDs, and the orange a meson distribution amplitude.

*Parton Distributions* (GPDs)  $H_{q/h}(x, \xi, t)$  and  $E_{q/h}(x, \xi, t)$  which depend on the Lorentz-invariants: the longitudinal momentum fraction  $x$ , skewness  $\xi \equiv \frac{p_i^+ - p_f^+}{p_i^+ + p_f^+}$  and momentum-transfer  $t = (p_f - p_i)^2$ . The Dirac structure  $\Gamma = \gamma^+ \gamma_5$  induces the quark helicity GPDs  $\tilde{H}_{q/h}, \tilde{E}_{q/h}$ . It is important to note these decompositions are merely in terms of the leading GPDs. Additional GPDs associated with operators of different energy dimension relevant to quarks, antiquarks and gluons can be found in Refs. [18, 12].

GPDs arise in the description of certain exclusive hard scattering processes. Examples include Deeply Virtual Compton Scattering (DVCS)  $\gamma^* p \rightarrow \gamma p$  and exclusive meson production  $\gamma^* p \rightarrow Mp$ , shown in Fig. 2.2(a) and Fig. 2.2(b), as well as the related time-like Compton scattering (TCS) process.<sup>8</sup> As GPDs depend both on the parton momentum fraction  $x$  and the momentum transfer  $t$ , GPDs unify the elastic form factors of local currents and the collinear Parton Distribution Functions discussed in the next subsection. The first  $x$ -Mellin moment of GPDs, or simply integrating the  $x$ -dependence,

$$\int_{-1}^1 dx \{H_{q/h}, E_{q/h}\}(x, \xi, t) = \{F_1^{q/h}, F_2^{q/h}\}(t) \quad (2.12)$$

<sup>8</sup>The TCS process is the inverse process to DVCS, when the incoming photon is real and the outgoing photon is virtual.

is equivalent to localizing the quark bilinear<sup>9</sup> in (2.10), which is parameterized by the Dirac and Pauli form factors when embedded within a spin-1/2 baryon. For completeness, we note the replacement of  $\gamma^+$  with  $\gamma^+\gamma_5$  in Eq. 2.10 and repeating the  $x$ -integration reduces  $\tilde{H}_{q/h}$  and  $\tilde{E}_{q/h}$  to the axial and induced pseudoscalar form factors.

Higher Mellin moments in  $x$  reduce GPDs to so-called generalized form factors of derivative-based operators featured in operator analyses of deep inelastic scattering (Ch. 4). The allure of this reduction captured the interest of the broader nuclear physics community [19] when Ji established that the low Mellin moments of the GPDs  $H_{a/h}(x, \xi, t)$  and  $E_{a/h}(x, \xi, t)$  directly quantify the total orbital angular momentum contribution of a partonic species to a hadron's spin [20]. Ji's sum rule reads

$$\frac{1}{2} \int_{-1}^1 dx x [H_{q/h}(x, \xi, t) + E_{q/h}(x, \xi, t)] \xrightarrow{t=0} J_{q/h} \quad (2.13)$$

$$\frac{1}{2} \int_0^1 dx [H_{g/h}(x, \xi, t) + E_{g/h}(x, \xi, t)] \xrightarrow{t=0} J_{g/h}, \quad (2.14)$$

where  $J_{a/h}$  is the total spin contribution of parton- $a$  to some hadron. The low Mellin moments of the unpolarized GPDs  $H_{a/h}(x, \xi, t)$  and  $E_{a/h}(x, \xi, t)$  thus offers a tantalizing path for resolution of the proton spin puzzle [21]. Further details on GPDs are reserved for Ch. 6.

### 2.1.2 Parton Distribution Functions

The off-forward integrated correlator (2.9) reduces in the forward-limit ( $\Delta = 0$ ) to

$$f_{q/h}^{[\Gamma]} = \frac{1}{2} \int \frac{dz^-}{2\pi} e^{ixP^+z^-} \langle h(p, \lambda') | \bar{q}(-\frac{z}{2}) \Gamma \Phi_{\hat{z}^-}^{(f)}(\{-\frac{z}{2}, \frac{z}{2}\}) q(\frac{z}{2}) | h(p, \lambda) \rangle, \quad (2.15)$$

---

<sup>9</sup>The relationship between Mellin moments in  $x$  of collinear distributions and local operators is established at the outset of Ch. 4

where the quark correlation is shown for specificity and the polarization dependence is made explicit. Parameterization of this correlator is the starting point for the familiar Parton Distribution Functions (PDFs). Specific choices of  $\Gamma$  define the unpolarized ( $\gamma^+$ ), helicity ( $\gamma^+\gamma_5$ ) and transversity ( $\gamma^+\gamma^i\gamma_5$ ) PDFs. The reduction of GPDs to PDFs in the forward limit is then obvious.

PDFs are generally introduced directly from (2.15) assuming the field operators have been properly renormalized in QCD. As noted above Sec. 2.1.1, when dealing with bare operators the collinear GPDs and PDFs require renormalization of the divergent  $\mathbf{k}_\perp$ -integral. Bare parton densities renormalize multiplicatively through convolution with a factor  $Z_{jj'}$  that mixes parton flavors

$$f_{j/h}(x) = \sum_{j'} \int_x^1 \frac{dz}{z} Z_{jj'}(z, g, \epsilon) f_{j'/h}^{(0)}(x/z). \quad (2.16)$$

Fortunately  $Z_{jj'}$ , which in  $\overline{\text{MS}}$  depends on the renormalized coupling  $g$  and spacetime dimension  $\epsilon$ , does not mix PDFs associated with different Dirac structures - namely, polarized and unpolarized PDFs do not mix under renormalization. The RG equations describing the scale dependence of the PDFs read

$$\frac{d}{d \ln(\mu^2)} f_{j/h}(x, \mu^2) = 2 \sum_{j'} \int \frac{dz}{z} P_{jj'}(z, \alpha_s(\mu^2)) f_{j'/h}\left(\frac{x}{z}, \mu^2\right). \quad (2.17)$$

These particular evolution equations are the famous Dokshitzer-Gribov-Lipatov-Altarelli-Parisi (DGLAP) [22, 23, 24], or simply Altarelli-Parisi, equations. The  $P_{jj'}(z, \alpha_s(\mu^2))$  are one of four all-orders Altarelli-Parisi kernels, or splitting functions, computable order-by-order in the strong coupling. Each kernel describes the emission of a flavor- $j$  parton from a flavor- $j'$  parton carrying momentum fraction  $z \leq 1$  of the momentum fraction  $x$  of the

flavor- $j'$  parton. For example, the scale dependence of a quark PDF at  $\mathcal{O}(\alpha_s)$  is given by

$$\frac{d}{d \ln(\mu^2)} f_{q/h}(x, \mu^2) = \frac{\alpha_s(\mu^2)}{\pi} \int_x^1 \frac{dz}{z} \left[ P_{qq}(z) f_{q/h}\left(\frac{x}{z}, \mu^2\right) + P_{qg}(z) f_{g/h}\left(\frac{x}{z}, \mu^2\right) \right] \quad (2.18)$$

where  $P_{qq}(z) = \frac{4}{3} \left( \frac{1+z^2}{(1-z)_+} + \frac{3}{2} \delta(1-z) \right)$  and  $P_{qg}(z) = \frac{1}{2} [z^2 + (1-z)^2]$ .<sup>10</sup> Evidently at  $\mathcal{O}(\alpha_s)$  a quark PDF's scale dependence is also driven by the gluonic PDF at the same scale, and vice-versa for a gluonic PDF.

Unlike QED, the DGLAP evolution equations cannot be used to explicitly compute PDFs, as the non-perturbative strong-coupling regime of QCD shrouds the initial conditions needed to integrate these differential equations. DGLAP remains a powerful asset however, as it relates physical observables dependent on PDFs across energy scales. Provided a measurement is made at some initial scale, DGLAP can be used to predict the same observable at a different scale. We now further develop these ideas by focusing on the chronologically first and quintessential hadronic scattering process sensitive to the collinear PDFs.

## 2.2 Deep Inelastic Scattering

The elastic scattering of leptons from a hadronic target is described by various elastic form factors, each quantifying the response of the target to varied external probes and momentum transfers. The Fourier conjugate to these responses expose the transfer profile of the target to be discerned and provide meaning to the size of a hadron. Form factor measurements were some of the first indicators for the extended size of hadrons, and continue to provide complementary information on the structure of hadrons.

---

<sup>10</sup>The notation  $1/(1-z)_+$  is an example of a *plus prescription* commonly encountered in calculations of structure functions. For some kernel, the plus prescription is defined with respect to an arbitrary smooth test function:  $\int_0^1 du G(u)_+ f(ux) \equiv \int_0^1 du G(u) [f(ux) - f(x)]$ .



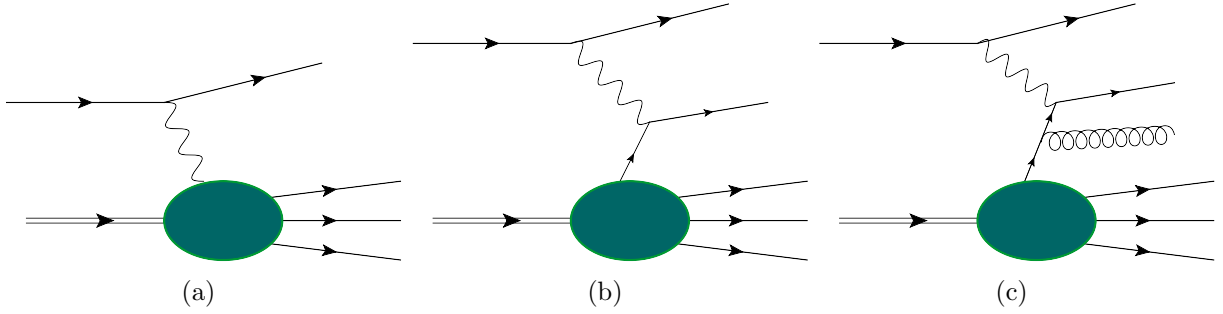


FIG. 2.3: (a) The DIS amplitude to lowest-order in electromagnetism. (b) The leading parton model approximation of DIS involves the highly virtual photon scattering from an individual quark within the hadron. (c) A higher-order correction to the parton model ultimately responsible for the scaling violations observed in the structure functions associated with the hadronic tensor.

Finer resolution of the internal partonic content of hadrons is provided by the Deep Inelastic Scattering (DIS) process  $\ell A \rightarrow \ell' X$ , where the target  $A$  is obliterated into a fully unresolved final state. The jargon *inclusive* scattering is assigned to such a process where all possible final states are included in measurements of the process. To be concrete, consider the scattering of a lepton of momentum  $\ell^\mu$  at tree-level in QED from a hadron  $h$  of momentum  $P^\mu$  via the exchange of an off-shell photon and where in the final state the lepton momentum is now  $\ell'^\mu$  and any remnant is unobserved:

$$\ell + h(P) \rightarrow \ell' + X. \quad (2.19)$$

To lowest-order in electromagnetism the DIS amplitude is illustrated in Fig. 2.3. A number of Lorentz invariants are useful in describing the process:

$$q^\mu = \ell^\mu - \ell'^\mu \quad Q^2 \equiv -q^2 \geq 0 \quad (2.20)$$

$$x_B = \frac{Q^2}{2P \cdot q} = \frac{Q^2}{2M\nu} \quad y = \frac{P \cdot q}{P \cdot \ell}, \quad (2.21)$$

with  $\nu = \frac{P \cdot q}{M}$  the energy transfer and where  $0 \leq y \leq 1$  represents the fractional energy

lost of the scattered lepton in the hadron's rest frame. Other common variables are the invariant mass of the hadronic system after the scattering event  $W^2 = (P + q)^2$ , the center-of-mass energy of the entire process  $s = (\ell + P)^2$  and the related  $\{t, u\}$  Mandelstam variables. The Bjorken variable  $x_B$ , or Bjorken- $x$ , is bounded by  $\frac{Q^2}{Q^2+s} \leq x_B \leq 1$ . The conditions for DIS are  $Q^2 \gg M_h^2$  and  $W^2 \gg M_h^2$ , where  $M_h$  is the target hadron mass. Neglecting the masses of the lepton  $m_\ell$  and hadron  $M_h$  relative to  $\sqrt{s}$ , as well as the lepton and target helicities, the Lorentz-invariant inclusive cross section differential in the outgoing lepton 4-momentum is given by [25]

$$E' \frac{d\sigma}{d^3\ell'} \simeq \frac{\pi e^4}{2s} \sum_X \delta^{(4)}(p_X - P - q) |q^{-2} \langle \ell' | \mathcal{J}_\rho | \ell \rangle \langle X, \text{out} | \mathcal{J}^\rho | P \rangle|^2 = \frac{2\alpha_{\text{QED}}^2}{sQ^4} L_{\mu\nu} W^{\mu\nu}, \quad (2.22)$$

where the Lorentz-invariant sum and integral over all hadronic final states is denoted by the sum over  $X$ . The various kinematic factors and momentum-conserving delta function follow from the Lorentz-invariant phase space factor relevant for an  $n$ -body decay<sup>11</sup>. The two matrix elements appearing in (2.22) are the leptonic and hadronic matrix elements of the probing current, which due to the modulus have been re-expressed in terms of the leptonic and hadronic tensors. The leptonic tensor is given by the relevant QED Feynman diagrams computed to an appropriate order in  $\alpha_{\text{QED}}$  - tree-level is sufficient at hadronic energy scales. The leptonic tensor for purely electromagnetic DIS takes the form

$$L_{\mu\nu} = \frac{1}{2} \text{Tr} \left[ \gamma_\mu \not{\ell} \gamma_\nu \not{\ell}' \right] = 2 (\ell_\mu \ell'_\nu + \ell'_\mu \ell_\nu - \ell \cdot \ell' g_{\mu\nu}). \quad (2.23)$$

For DIS involving a generic electroweak current,  $L_{\mu\nu}$  is modified to include the  $V - A$

---

<sup>11</sup>The Lorentz-invariant phase space factor for decay of an initial state with momentum  $P^\mu$  is given by  $d_n = \delta^4(P - \sum_{i=1}^n p_{f_i}) \prod_{i=1}^n \frac{d^3\vec{p}_{f_i}}{E_i}$ , with 4-momenta  $p_{f_i}^\mu$  of any final states.

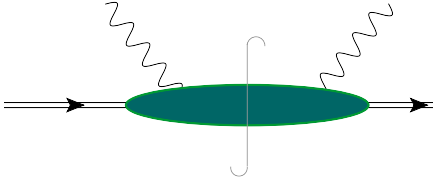


FIG. 2.4: Cut-diagram notation for the hadronic tensor in deep inelastic scattering. The cut through the hadronic blob denotes a sum and integral over final states.

structure of the charged/neutral weak currents [26]. The hadronic tensor is defined as

$$W^{\mu\nu}(q, P) \equiv 4\pi^3 \sum_X \delta^4(p_X - P - q) \sum_{\lambda', \lambda} \rho_{\lambda'\lambda} \langle P, \lambda' | \mathcal{J}^\mu(0) | X \rangle \langle X | \mathcal{J}^\nu(0) | P, \lambda \rangle \quad (2.24)$$

$$= \frac{1}{4\pi} \int d^4z e^{iq \cdot z} \langle P, S | \mathcal{J}^\mu(z) \mathcal{J}^\nu(0) | P, S \rangle, \quad (2.25)$$

with the most general polarization state of a target of momentum  $P$  given in terms of a spin density matrix  $\rho_{\lambda', \lambda}$  with helicity labels  $\lambda', \lambda$ . The final line makes the simplification of a pure unpolarized state of spin- $\frac{1}{2}$ , where  $\rho_{\lambda', \lambda} = \delta_{\lambda' \lambda} / (2S + 1)$  and  $S = \frac{1}{2}$ .<sup>12</sup> The form of the hadronic tensor is understood in terms of a *cut-diagram* exemplified for DIS in Fig. 2.4. The rightmost matrix element in (2.24) is the DIS amplitude represented by Feynman rules, with  $\langle P, \lambda' | \mathcal{J}^\mu(0) | X \rangle$  its conjugate. The vertical line in Fig. 2.4 is a final state cut denoting this sum over a complete set of hadronic states and integration over each respective phase space.

The hadronic tensor contains all information relevant to a hadron's structure involved in a DIS event. Whereas the leptonic tensor can be computed precisely because of the small electroweak coupling constants, the hadronic tensor resides in the non-perturbative regime of QCD and evades analytic calculation. To understand the information encoded in  $W^{\mu\nu}$  and how it is garnered from experiment, we consider the structure of  $W^{\mu\nu}$  more closely. The hadronic tensor depends on the momenta  $q$  and  $P$  and, if the target is polarized, also

<sup>12</sup>For a massive spin- $\frac{1}{2}$  target (standard in DIS) with definite momentum  $P$ , the spin vector  $S^\mu$  satisfies  $S \cdot P = 0$  and is normalized such that  $S^2 = -M^2$ .

on its spin four-vector  $S^\mu$ . When expressed in terms of the invariants  $x$  and  $Q^2$  several Lorentz-invariant functions, or *structure functions*, emerge.<sup>13</sup> In electroweak DIS on a polarized target this decomposition [25, 26, 27, 28, 29] reads

$$\begin{aligned}
W^{\mu\nu} = & \left( -g^{\mu\nu} + \frac{q^\mu q^\nu}{q^2} \right) F_1(x, Q^2) + \frac{\hat{P}^\mu \hat{P}^\nu}{P \cdot q} F_2(x, Q^2) \\
& + i\epsilon^{\mu\nu\alpha\beta} \frac{q_\alpha S_\beta}{P \cdot q} g_1(x, Q^2) + i\epsilon^{\mu\nu\alpha\beta} \frac{q_\alpha \left( S_\beta - P_\beta \frac{S \cdot q}{P \cdot q} \right)}{P \cdot q} g_2(x, Q^2) \\
& - i\epsilon^{\mu\nu\alpha\beta} \frac{q_\alpha P_\beta}{2P \cdot q} F_3(x, Q^2) + \frac{1}{P \cdot q} \left[ \frac{\hat{P}^\mu \hat{S}^\nu + \hat{S}^\mu \hat{P}^\nu}{2} - \frac{S \cdot q}{P \cdot q} \hat{P}^\mu \hat{P}^\nu \right] g_3(x, Q^2) \\
& + \hat{P}^\mu \hat{P}^\nu \frac{S \cdot q}{(P \cdot q)^2} g_4(x, Q^2) + \left( -g^{\mu\nu} + \frac{q^\mu q^\nu}{q^2} \right) \frac{S \cdot q}{P \cdot q} g_5(x, Q^2) \tag{2.26}
\end{aligned}$$

where the abbreviations

$$\hat{P}^\mu = P^\mu - \frac{P \cdot q}{q^2} q^\mu \quad \hat{S}^\mu = S^\mu - \frac{S \cdot q}{q^2} q^\mu \tag{2.27}$$

have been used, and the totally antisymmetric tensor  $\epsilon^{\mu\nu\alpha\beta}$  satisfies  $\epsilon^{0123} = -1$  and  $\epsilon_{0123} = 1$ . This exhaustive Lorentz decomposition encapsulates any (un)polarized electroweak DIS process, including charged-current ( $lN \rightarrow \bar{\nu}_l X$ ) and neutral-current ( $lN \rightarrow l'X$ ) processes, consistent with parity, the Ward identities implied by the conservation of electromagnetic currents  $\partial_\mu \mathcal{J}_{\text{EM}}^\mu = 0$ , and reflects the hermiticity (i.e.  $W^{\mu\nu} = (W^{\nu\mu})^*$ ) of the hadronic tensor. In the case of a strict electromagnetic probe, the DIS process is parity-conserving, and thus the parity-violating unpolarized structure function  $F_3(x, Q^2)$  and polarized structure functions  $g_3(x, Q^2), g_4(x, Q^2), g_5(x, Q^2)$  vanish. The parity-conserving polarized structure functions  $g_1(x, Q^2), g_2(x, Q^2)$  are then only relevant for the deep inelastic scattering of a photon off a polarized target.

---

<sup>13</sup>For brevity  $x_B \mapsto x$ .

### 2.2.1 The Parton Model

Consider the simplified case of deep inelastic scattering of a photon from an unpolarized target. The cross section for this process differential in  $\{x, y\}$  is given by

$$\frac{d^2\sigma}{dxdy} \simeq \frac{4\pi\alpha^2s}{Q^4} \left[ \frac{Q^4}{xs^2} F_1(x, Q^2) + \left( 1 - \frac{Q^2}{xs} - \frac{Q^2M^2}{s^2} \right) F_2(x, Q^2) \right]. \quad (2.28)$$

This form illustrates that by varying the kinematic arrangements the unpolarized structure functions  $F_1(x, Q^2)$  and  $F_2(x, Q^2)$  can be extracted from experimental data. At this stage however, it is not exactly clear how  $F_1, F_2$ , and  $g_i$  more generally, encode the partonic makeup of hadrons. Before the advent of QCD, Feynman developed a heuristic to make sense of the DIS data emerging from experiments in the late 1960s. His ideas are echoed here for a self-contained discussion.

The conjugacy that exists between coordinate and momentum space implies that the large DIS momentum transfers  $Q$  probe a hadron on a distance scale  $\mathcal{O}(1/Q)$ . Furthermore, on dimensional grounds it is reasonable to presume the constituents, or partons, of the target hadron interact with each other on a time scale  $\mathcal{O}(R_h/c)$  where  $R_h \sim 1$  fm is the typical size of a hadron. In boosting from the hadron rest frame to the center-of-momentum frame, the time scales over which parton interactions occur is greatly time-dilated. Not only does this dilation imply interactions between partons occur long before the virtual boson becomes relevant, but the lifetime of any particular configuration of partons becomes large. The boost of the target to large  $P^+$  likewise implies length contraction of the target in the center-of-mass frame. The lepton then sees a hadron in a single virtual state. For sufficiently large  $Q$ , the DIS process is then characterized to first approximation as the scattering of a virtual gauge boson from a single quasi-free parton carrying a definite fraction  $\xi$  of the hadron's momentum  $P^+$ .<sup>14</sup> This is the essence of the (naive) Parton

---

<sup>14</sup>Where the momentum fraction  $\xi$  in this context should not be confused with skewness defined for

Model (PM) initially put forward by Feynman [30, 31] and further formalized by Bjorken and Paschos [32] and Drell [33].

Under the above assumptions, at the moment of scattering the hadron with large- $P^+$  momentum is in a state of  $n$  partons whose fractional momenta sum to unity  $\sum_n \xi_n = 1$ . The PDFs enter in the parton model as number distributions of a parton flavor, and  $f_{a/h}(\xi) d\xi$  is the expected number of type- $a$  partons in hadron  $h$  to carry fractional momenta in the interval  $[\xi, \xi + d\xi]$ . The deep inelastic lepton-hadron scattering simplifies in the parton model into an incoherent sum of PDFs convolved with Born-level partonic cross sections

$$d\sigma_{\ell h} = \sum_a \int d\xi f_{a/h}(\xi) d\sigma_{\ell a}^{\text{Born}}(\xi). \quad (2.29)$$

We note there is no distinction between Bjorken- $x$  and the momentum fraction  $\xi$  in the parton model, and they are often used interchangeably in the literature.

The connection between the parity-conserving DIS structure functions and PDFs in the parton model is well-known [25]

$$F_1(x) = \frac{1}{2} \sum_a e_a^2 f_{a/h}(x) \quad F_2(x) = \sum_a e_a^2 x f_{a/h}(x) \quad (2.30)$$

$$g_1(x) = \frac{1}{2} \sum_a e_a^2 \Delta f_{a/h}(x) \quad g_2(x) = 0, \quad (2.31)$$

with each structure function a sum over partons with electromagnetic charge  $e_a$  and unpolarized (polarized) PDFs  $f_{a/h}$  ( $\Delta f_{a/h}$ ). The parton model makes the striking prediction that both the PDFs and the structure functions that depend on them are  $Q^2$ -independent in the deep inelastic, or Bjorken, limit  $Q^2, \nu \rightarrow \infty$  with  $x = \frac{Q^2}{2M\nu}$ . This prediction is deemed *Bjorken-scaling* [34]. The deep inelastic scattering from non-interacting partons at high- $Q^2$  and hence Bjorken-scaling in the parton model would seem to be at least par-

tially correct, given the asymptotic freedom of QCD. Strict scaling is clearly subject to violations, as  $\alpha_s$  is only asymptotically small at large- $Q^2$ .

## 2.2.2 PDFs from Structure Functions

The separation of scales assumed in the parton model are codified by the QCD factorization theorems [35], providing rigor and a proper field-theoretic construction. The QCD collinear factorization of the DIS hadronic tensor is given by

$$W^{\mu\nu}(q^\mu, P^\mu) = \sum_a \int_x^1 \frac{d\xi}{\xi} f_{a/h}(\xi, \mu^2) H_a^{\mu\nu}(q^\mu, \xi P^\mu, \mu^2, \alpha_s(\mu^2)) + \mathcal{O}\left(\frac{\Lambda_{\text{QCD}}^2}{Q^2}, \frac{M_h^2}{Q^2}\right). \quad (2.32)$$

The PDFs  $f_{a/h}$  retain their intuitive parton model interpretations, with the factorization scale  $\mu^2$  typically set by the momentum transfer  $Q^2$ .<sup>15</sup> This scale demarcates which parton fluctuations are to be included in the low-energy PDFs, and which are to be included in the hard scattering coefficient function  $H_a^{\mu\nu}$  computable in perturbation theory. Corrections to this factorized relationship are power-suppressed, and often called higher-twist corrections - the leading contribution  $f_{a/h}(\xi, \mu^2)$  is then deemed the leading-twist<sup>16</sup> PDF. Projecting onto the individual structure functions

$$F_i(x, Q^2) = \sum_{a=q, \bar{q}, g} \int_x^1 \frac{d\xi}{\xi} f_{a/h}(\xi, \mu^2) H_i^a\left(\frac{x}{\xi}, \frac{Q^2}{\mu^2}, \alpha_s(\mu^2)\right) + \mathcal{O}\left(\frac{\Lambda_{\text{QCD}}^2}{Q^2}, \frac{M_h^2}{Q^2}\right), \quad (2.33)$$

we see that measurements of the structure functions together with the hard coefficient functions enable the PDFs to be accessed.

---

<sup>15</sup>The scale of factorization can in general differ from the scale chosen to renormalize the field operators defining the PDF. In most cases, and in this work, these scales are taken to be equal.

<sup>16</sup>*Twist* originates from early attempts to understand  $W^{\mu\nu}$  at the operator level. The contribution of any particular operator with spin- $s$  to  $W^{\mu\nu}$  scales according to  $(Q^{-1})^{d-s-2}$ , with relative contribution  $d-s \equiv \text{twist}$  and  $d$  the operator dimension. The dominant (leading-twist) operators can be related to the PDFs, hence the notion of a leading-twist PDF. These points are further developed in Ch. 4.

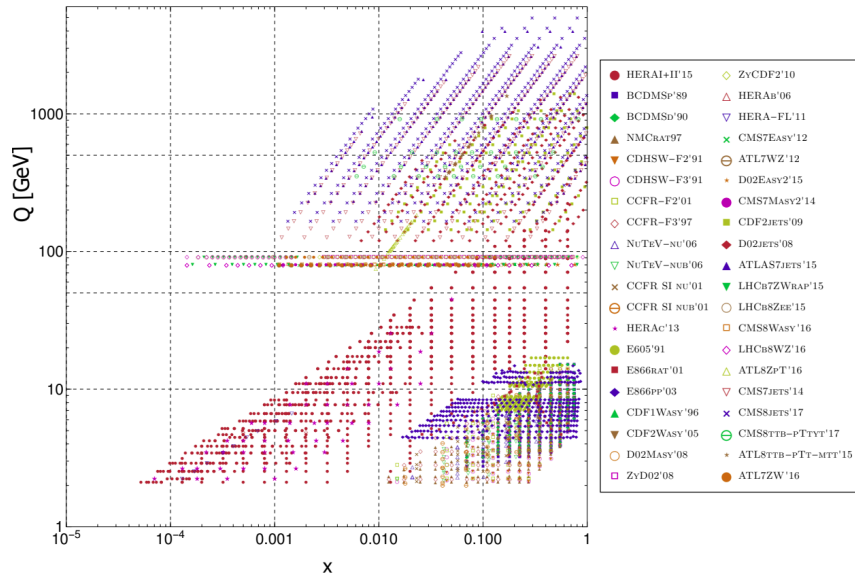


FIG. 2.5: The spread of experimental data used in a recent global analysis by the CT collaboration [36].

PDFs are extracted in large part by analysis of DIS scattering data, and to a lesser extent Drell-Yan scattering (e.g.  $h_A h_B \rightarrow \ell \ell' + X$ ) which involves a similar factorized relationship into PDFs. Measurements of the DIS structure functions are inherently discrete in Bjorken- $x$  and  $Q^2$ . A representative example from the CT collaboration's recent global analysis is shown in Fig. 2.5. However, the numerous collider and fixed-target experiments around the world provide coverage spanning several orders of magnitude in both variables. For instance, the canonical inclusive DIS process  $l^\pm p \rightarrow l^\pm X$  accesses the high- $x$  regime  $x \gtrsim 0.01$ , while photo-production of charm and bottom quark pairs (e.g.  $e^\pm p \rightarrow e^\pm \{c\bar{c}, b\bar{b}\} X$ ) helps to constrain the small- $x$  domain  $10^{-4} \lesssim x \lesssim 0.1$  [29].

As PDFs and other parton distributions are universal functions that are independent of the process in which they are probed, the most reliable determination of these quantities follows from global analyses of compatible experimental datasets. A number of collaborations, in the so-called global fitting community, have developed frameworks of considerable sophistication to extract these distributions. The precise details of each



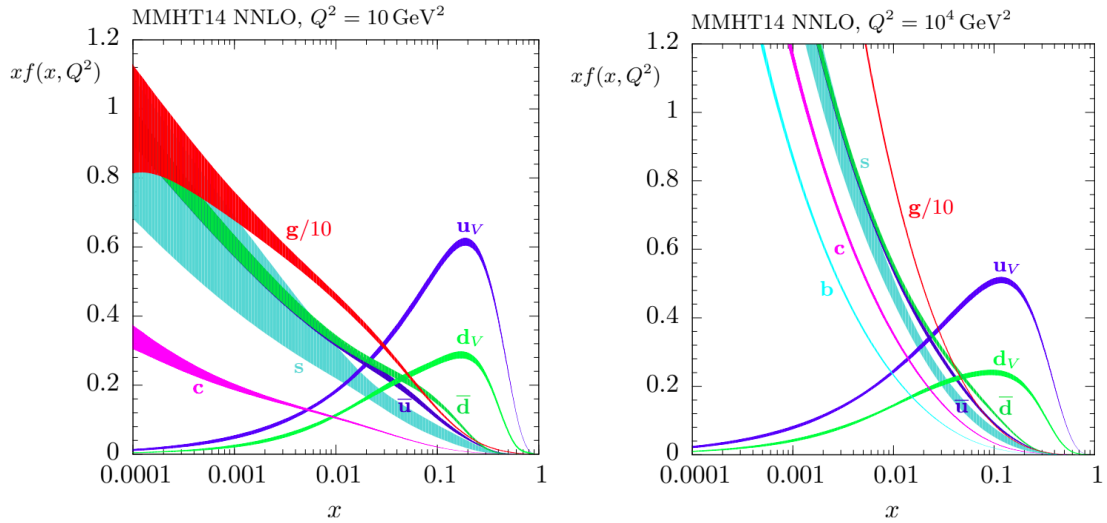


FIG. 2.6: Unpolarized proton PDFs determined by the MMHT collaboration via a global analysis of lepton-hadron and hadron-hadron data, where the perturbative hard coefficient functions and partonic cross sections are truncated at NNLO. The PDFs determined at  $Q^2 = 10 \text{ GeV}^2$  are shown at left, while those at  $Q^2 = 10^4 \text{ GeV}^2$  given at the right. Details of the extraction are contained in Ref. [37].

analysis are beyond the scope of this work. It is important to highlight, however, the standard formalism adopted by each. Equation 2.33 is applied by first specifying an order in perturbation theory at which the perturbative kernels  $H_i^a$  should be computed - namely, leading-order (LO), next-to-leading order (NLO), next-to-next-to-leading order (NNLO), etc. Despite the large numbers of measurements of the DIS structure functions, the factorization relationship (2.33) is ill-posed, as discrete  $F_i(x, Q^2)$  cannot fully constrain the functionally continuous PDFs. The prevailing mindset is to include additional information in the form of parametric PDFs that capture the  $x$ -dependence at an input scale  $Q_0^2$ . In the broadest terms, the convolution 2.33 is then numerically fit to experiment. Examples of PDFs extracted by the MMHT and NNPDF global fitting collaborations are presented respectively in Fig. 2.6 and Fig. 2.7. This paradigm will be expounded upon in Chapter 5.

The importance of PDFs in quantifying inclusive and semi-inclusive hadronic cross sections, especially in the search for BSM signals [39] and in processes involving challenging-

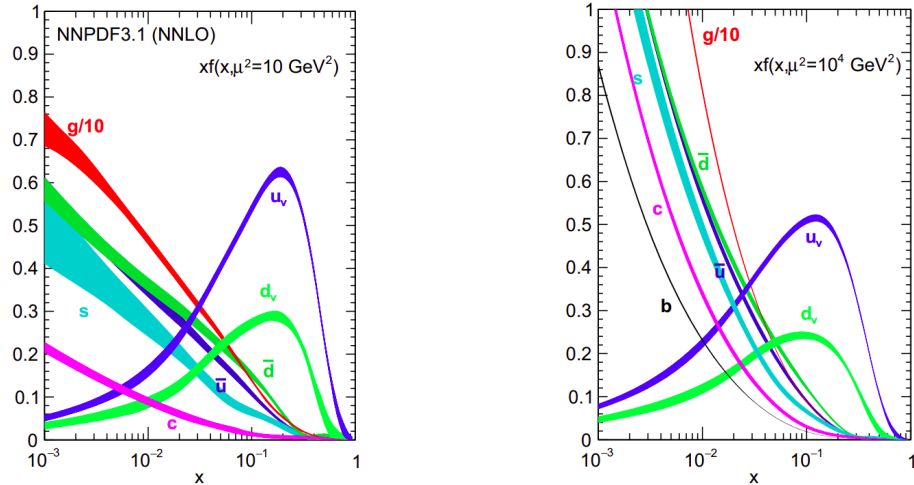


FIG. 2.7: Unpolarized proton PDFs determined by the NNPDF collaboration via a global analysis of lepton-hadron and hadron-hadron data, where the perturbative hard coefficient functions and partonic cross sections are truncated at NNLO. The PDFs determined at  $Q^2 = 10 \text{ GeV}^2$  are shown at left, while those at  $Q^2 = 10^4 \text{ GeV}^2$  given at the right. Details of the extraction are contained in Ref. [38].

to-access hadronic states (e.g. neutrons, kaons, etc.), makes their determination from first-principles a high priority.

## 2.3 Lattice QCD

Quantum mechanics and indeed canonical quantization in quantum field theory is formulated with respect to the Hamiltonian of the theory. Richard Feynman established an equivalent formulation in terms of a functional integral or *path integral* [40]. The principle of least action of classical fields, which states the trajectory between two times is the unique path in configuration space for which the classical action is minimized, is generalized by the path integral formulation to account for the infinitely many allowed trajectories of a quantum mechanical system. By summing, or functionally integrating, over these allowed trajectories the superposition principle is captured in a natural manner, while utilizing the action instead of the Hamiltonian explicitly preserves the symmetries

built into the Lagrangian  $\mathcal{L}$  of a theory. In this language the amplitude for a non-relativistic quantum to propagate between two points in one dimension is given by

$$\langle x_b | e^{-iHT} | x_a \rangle = c \int \mathcal{D}x(t) e^{iS[x(t)]} = c \int \mathcal{D}x(t) e^{i \int_0^T dt \mathcal{L}[x(t)]}, \quad (2.34)$$

where  $S$  is the action functionally dependent on all paths  $x(t)$ ,  $\int \mathcal{D}x(t)$  representing the sum over paths, and  $c \in \mathbb{C}$  a constant irrelevant at this stage.

The path integral formalism applied to quantum fields introduces the notion of a generating functional. For a generic collection of scalar field species, the generating functional reads

$$\mathbb{Z}[\{\mathcal{J}_i\}] = \int \mathcal{D}[\{\phi_i\}] \exp \left[ i \int d^4x \left[ \mathcal{L} + \sum_i \mathcal{J}_i(x) \phi_i(x) \right] \right], \quad (2.35)$$

where the path integral now captures all possible configurations of the field operators  $\mathcal{D}[\{\phi_i\}] = \prod_i \prod_x \phi_i(x)$ , with  $\mathcal{L}$  the Lagrangian of the theory and  $\mathcal{J}_i \phi_i$  the *sources*.<sup>17</sup> Functional methods allow the Green's functions, or correlation functions, of a theory to be computed directly from  $\mathbb{Z}[\{\mathcal{J}_i\}]$ , as well as expectations of field operators. A representative two-point Green's function and vacuum expectation of an operator in a theory with a single scalar field are given by

$$\begin{aligned} \langle \Omega | T \{ \phi(x_1) \phi(x_2) \} | \Omega \rangle &= \mathcal{Z}^{-1} \int \mathcal{D}[\phi] \phi(x_1) \phi(x_2) e^{iS[\phi]} \\ \langle \Omega | \hat{\mathcal{O}} | \Omega \rangle &= \mathcal{Z}^{-1} \int \mathcal{D}[\phi] \mathcal{O}[\phi] e^{iS[\phi]}, \end{aligned}$$

where the functional dependence of  $\mathcal{O}$  on  $\phi$  is manifest,  $\mathcal{Z} \equiv \mathbb{Z}[\{\mathcal{J}_i = 0\}]$ , and  $|\Omega\rangle$  represents the interacting vacuum.

---

<sup>17</sup>The term sources here refers to the fact that functional derivatives of  $\mathbb{Z}[\{\mathcal{J}_i\}]$  with respect to  $\mathcal{J}_i$  will produce factors of  $\phi_i$  in the path integral. This provides a convenient algorithm for isolating Green's functions of a theory by subsequently requiring  $\mathcal{J}_i = 0$ . The reader is directed to standard QFT texts (e.g. [41]) for further details.

*Lattice QCD* was first proposed in 1974 by Kenneth Wilson [10] as a first-principles scheme to numerically compute observables in QCD. The lattice regularization proposed by Wilson considers a finite hypercubic volume of spacetime points  $x$  defined by

$$\Lambda = \{x \in \mathbb{R}^d \mid x = (n_1, n_2, \dots, n_d) \times a, n_i \in \mathbb{Z}_{N_i}\}, \quad (2.36)$$

with  $a$  the *lattice spacing*,  $\mathbb{Z}_{N_i} = \{0, \dots, N_i - 1\}$  and  $N_i$  the number of spacetime points in each dimension. For a generic quantum field theory, the finite volume and non-zero lattice spacing impose strict infrared (IR) and ultraviolet (UV) cutoffs, respectively, thereby rendering finite any formally divergent expressions.

In the small coupling regime, this lattice regularization is a perfectly viable method to perturbatively compute quantities in QCD, and other QFTs more generally. Lattice regularization is, however, favored less than other schemes such as *Dimensional Regularization*, as lattice perturbation theory is often characterized by a cumbersome growth of trigonometric functions and slow convergence in perturbative calculations. Among established regularization schemes, the lattice regularization of Wilson is uniquely positioned to compute observables in strongly interacting theories by recognizing the path integral in a finite discretized volume reduces to a countable, albeit large, sum over the finite possible field configurations. In contemporary LQCD calculations it is not uncommon for this finite path integral to exceed dimension of  $\mathcal{O}(10^8)$ .

### 2.3.1 Euclidean Lattice Field Theory

The finiteness of the lattice path integral immediately suggests a numerical approach for its evaluation. To develop this idea, we abandon toy scalar QFTs and turn our attention

to QCD. The generating functional of QCD in Minkowski space

$$\mathcal{Z} = \int \mathcal{D} [\psi_i, \bar{\psi}_i, A_\mu] e^{iS_{\text{QCD}}[\psi_i, \bar{\psi}_i, A_\mu]} \quad (2.37)$$

involves functional integration over all quark ( $\psi_i$ ) and anti-quark ( $\bar{\psi}_i$ ) flavors and  $\mathfrak{su}(3)$  algebra valued fields  $A_\mu$ . The oscillatory phase containing the QCD action  $S_{\text{QCD}}$  does not lend itself well to numerical computation, as differing regions of the configuration space tend to cancel. This colloquially embodies a so-called *Sign Problem* that is regulated by performing a Wick rotation to imaginary time  $t \mapsto -it_E$ . Before determining the effect of this mapping, we pause to consider how 4-vectors and the Dirac matrices are modified.

This rotation of time into the complex plane amounts to mapping quantities in Minkowski space into Euclidean space, as seen by transformation of a Minkowski invariant interval:

$$x^2 = t^2 - |\vec{x}|^2 \mapsto -t_E^2 - |\vec{x}|^2 \equiv -|x_E|^2 = -x_E^\mu x_E^\nu \delta_{\mu\nu} \quad (2.38)$$

In addition to modifying the temporal component of any 4-vector, the Dirac matrices must also reflect the identity metric of Euclidean space. As the  $4 \times 4$  Dirac matrices in Minkowski space generate a matrix representation of the Clifford algebra  $\text{Cl}_{1,3}(\mathbb{R})$  defined by the anticommutator  $\{\gamma^\mu, \gamma^\nu\} = 2g^{\mu\nu}$ , a matrix representation of the Euclidean Clifford algebra  $\text{Cl}_4(\mathbb{R})$  generated by  $\{\gamma_\mu, \gamma_\nu\} = 2\delta_{\mu\nu}$  follows from

$$\gamma_1 = -i\gamma_1^M \quad \gamma_2 = -i\gamma_2^M \quad \gamma_3 = -i\gamma_3 \quad \gamma_4 = \gamma_0^M. \quad (2.39)$$

Returning to the QCD generating functional, consider the free Dirac action in Minkowski space  $S_M^0 = \int d^4x \mathcal{L}_0 = \int d^4x \bar{\psi} (i\cancel{\partial} - m) \psi$ . Performing the Wick rotation to imaginary

time, observe

$$\begin{aligned}
S_M^0 &= \int dx^0 d^3x \bar{\psi} (i g_{\mu\nu} \gamma^\mu \partial^\nu - m) \psi \\
&= \int dx^0 d^3x \bar{\psi} \left( i \gamma_0 \frac{\partial}{\partial x_0} + i \gamma^j \nabla_j - m \right) \psi \\
&\mapsto \int d(-it_E) d^3x_E \bar{\psi} \left( i \gamma_E^4 \cdot i \frac{\partial}{\partial t_E} + i \cdot i \gamma_E^j \nabla_j^E - m \right) \psi \\
S_E^0 &= -i \int d^4x_E \bar{\psi} (-\gamma_E^4 \partial_E^4 - \gamma_E^j \partial_E^j - m) \psi \\
&= i \int d^4x \bar{\psi} (\gamma_\mu^E \partial_\mu^E + m) \psi.
\end{aligned}$$

Therefore the free Dirac action in Euclidean space<sup>18</sup> is given by  $S_E^0 = \int d^4x \bar{\psi} (\gamma_\mu^E \partial_\mu^E + m) \psi$ , and the Euclidean generating functional is

$$\mathcal{Z}_E = \int \mathcal{D} [\psi_i, \bar{\psi}_i, A_\mu] e^{-S_E[\psi_i, \bar{\psi}_i, A_\mu]}. \quad (2.40)$$

Instead of an oscillatory exponential factor, the Wick rotation has led to an exponential factor that exactly corresponds to the Boltzmann weight of a statistical ensemble. This guarantees not only a numerical implementation, but a strict probabilistic interpretation of the Euclidean path integral.

The connection of lattice field theory with statistical mechanics and the numerical arsenal that is brought to bear will be touched on in Sec. 2.3.5. We first continue with Wilson's construction of Lattice QCD by introducing fermion and gluon fields onto the discrete lattice  $\Lambda$ , and establish correct discretized actions for each. We note the coupling of a QFT is most conveniently introduced into a numerical lattice field theory calculation

---

<sup>18</sup>The distinction between contravariant and covariant indices is irrelevant since the Euclidean metric is simply the identity.

by rescaling the gauge fields  $A_\mu(x) \mapsto \frac{1}{g}A_\mu(x)$ . In the case of QCD this maps

$$\begin{aligned} D_\mu &\mapsto \partial_\mu + iA_\mu^a t^a \\ G_{\mu\nu}^a &\mapsto g^{-1} (\partial_\mu A_\nu^a - \partial_\nu A_\mu^a - f_{abc}A_\mu^b A_\nu^c) \\ \mathcal{L}_{QCD} &\mapsto \sum_f \bar{\psi}_f^i \left( i\mathcal{D}^{ij} - m_f \delta^{ij} \right) \psi_f^j - \frac{1}{4g^2} G_{\mu\nu}^a G^{\mu\nu a}. \end{aligned} \quad (2.41)$$

The reason for this choice will be elaborated on in Sec. 2.3.5.

### 2.3.2 Fermions on the Lattice

In Wilson's original formulation, Dirac spinors  $\psi(x)$  and  $\bar{\psi}(x)$  are assigned to each lattice site  $x \in \Lambda$ . This assignment of these 12-component objects, four Dirac and three color, represents all possible configurations of the quark and antiquark fields in a finite and discretized volume. The free Euclidean lattice fermion action follows from discretization of the continuum counterpart. The integral over an infinitesimal Euclidean spacetime element simplifies to a discrete sum over lattice sites  $\int d^4x \rightarrow a^4 \sum_{n \in \Lambda}$ , while the symmetric difference approximates the kinetic term:

$$\partial_\mu \psi \rightarrow \frac{\psi(x + \hat{\mu}) - \psi(x - \hat{\mu})}{2a}. \quad (2.42)$$

This direct discretization of the continuum Euclidean action

$$S_F^0 = a^4 \sum_{n \in \Lambda} \bar{\psi}(x) \left\{ \sum_{\mu=1}^4 \gamma_\mu \frac{\psi(x + \hat{\mu}) - \psi(x - \hat{\mu})}{2a} + m\psi(x) \right\} \quad (2.43)$$

is however not gauge invariant. Analogous to the introduction of Lie algebra valued gauge fields in the continuum, appropriate inclusion of gauge group valued elements  $\Omega(x) \in \text{SU}(3) \forall x \in \Lambda$  will allow a gauge invariant action to be constructed.

The lattice fermionic fields are modified under a gauge transformation according to

$$\begin{aligned}\psi(x) &\mapsto \psi'(x) = \Omega(x) \psi(x) \\ \bar{\psi}(x) &\mapsto \bar{\psi}'(x) = \bar{\psi}(x) \Omega^\dagger(x).\end{aligned}$$

It is easy to see these transformation properties, adopted from local gauge transformations in the continuum, are not sufficient to maintain gauge invariance in the discretized action (2.43). The trouble arises from the discretized kinetic term, which following a gauge transformation involves terms like  $\bar{\psi}(x) \Omega^\dagger(x) \Omega(x + \hat{\mu}) \psi(x + \hat{\mu})$ . Provided a new  $\hat{\mu}$ -oriented field  $U_\mu(x) \in \text{SU}(3)$  that transforms as

$$U_\mu(x) \mapsto U'_\mu(x) = \Omega(x) U_\mu(x) \Omega^\dagger(x + a\hat{\mu}) \quad (2.44)$$

is introduced between neighboring lattice sites, the discretized kinetic term involving terms  $\bar{\psi}(x) U_\mu(x) \psi(x + a\hat{\mu})$  can be made gauge-invariant. These *link variables* or *gauge links* are thus attached between lattice sites. How the group-valued gauge links and algebra-valued gauge fields  $A_\mu$  of the continuum are related is seen by recalling the continuum *gauge transporter* or *Wilson line*

$$U([A], \mathcal{C}; x, y) = \mathcal{P} \left\{ \exp \left( i \int_0^1 ds \frac{dy^\mu(s)}{ds} A_\mu(y(s)) \right) \right\}, \quad (2.45)$$

defined as a path-ordered  $\mathcal{P}\{\}$  exponential along a contour  $\mathcal{C}$ , transforms under a gauge transformation as  $U([A], \mathcal{C}; x, y)' = \Omega(x) U([A'], \mathcal{C}; x, y) \Omega^\dagger(y)$ . Comparing this transformation law with (2.44), we conclude the gauge links may be viewed as straight Wilson lines between  $x$  and  $x + a\hat{\mu}$ :  $U_\mu(x) \equiv e^{iaA_\mu}$ .



The gauge links facilitate a naive gauge-invariant fermion action

$$\begin{aligned}
S_F^0 &= a^4 \sum_{x \in \Lambda} \bar{\psi}(x) \left\{ \sum_{\mu=1}^4 \gamma_\mu \frac{U_\mu(x) \psi(x + a\hat{\mu}) - U_{-\mu}(x) \psi(x - a\hat{\mu})}{2a} + m\psi(x) \right\} \\
&\equiv a^4 \sum_{x, y \in \Lambda} \bar{\psi}(x) D_{xy}^N \psi(y), \tag{2.46}
\end{aligned}$$

with the naive Dirac operator  $D_{xy}^N = m\delta_{xy} + \frac{1}{2a} \sum_{\mu=1}^4 \gamma_\mu \{U_\mu(x) \delta_{x+a\hat{\mu}, y} - U_{-\mu}(x) \delta_{x-a\hat{\mu}, y}\}$ .

Important for the following discussion are the notion of quark *propagators*, which are the Green's functions satisfying the system of equations

$$a^4 \sum_x D(y, x) G(x, z) = \delta^{(4)}(y - x). \tag{2.47}$$

In coordinate space, a propagator  $G(x, z)$  describes the propagation of each quark color/spin component between two spacetime points, pictorially represented in Fig. 2.8. Returning to  $S_F^0$  above, this action is deemed naive as the chiral (i.e.  $m = 0$ ) propagator in momentum space features spurious unphysical poles.

To isolate these unphysical poles, consider the discrete Fourier transform of  $D_{xy}^N$

$$\begin{aligned}
\tilde{D}_{pq}^N &= \frac{1}{N_L^3 N_T} \sum_{x, y \in \Lambda} e^{-i(ap) \cdot x} D_{xy}^N e^{i(aq) \cdot y} \\
&= \frac{1}{N_L^3 N_T} \sum_{x, y \in \Lambda} e^{-i(p-q) \cdot xa} \left( \sum_{\mu=1}^4 \gamma_\mu \frac{e^{iaq_\mu} - e^{-iaq_\mu}}{2a} + m\mathbb{1} \right) \\
&= \delta(p - q) \left( m\mathbb{1} + \frac{i}{a} \sum_{\mu=1}^4 \gamma_\mu \sin(p_\mu a) \right).
\end{aligned}$$

In the chiral limit, the free quark propagator reads

$$\tilde{D}_{pq}^N \equiv G(p) = \frac{-ia^{-1} \sum_\mu \gamma_\mu \sin(p_\mu a)}{a^{-2} \sum_\mu \sin(p_\mu a)^2} \implies \lim_{a \rightarrow 0} G(p) = -\frac{i\not{p}}{p^2} \tag{2.48}$$

As expected, the naive lattice fermion action correctly reproduces the  $p^2 = 0$  pole in the continuum massless fermion propagator - up to an overall sign due to the difference in metric. Evidently for non-zero lattice spacings, additional poles appear in  $G(p) \forall p_\mu$  with non-trivial components equal to  $\pi/a$ . These fifteen additional poles are deemed *fermion doublers*. As the spectrum of a theory is dictated by the locations of poles in its two-point Green's functions, these additional poles lead to a total of 16 “flavors” of a single quark, 15 of which are entirely unphysical.

Wilson's solution to the doubler problem [10] is to include an additional term in the momentum space representation of the free lattice propagator:

$$\mathbb{1} \frac{1}{a} \sum_{\mu=1}^4 (1 - \cos(p_\mu a)). \quad (2.49)$$

This so called *Wilson term* has no effect for  $p_\mu = 0$ , but increases the doubler mass in a  $d$ -dimensional Euclidean spacetime to  $m_d = m + \frac{2(2^d-1)}{a}$ . It is then evident the doubler effectively decouples from the theory as the lattice spacing is reduced. The coordinate space representation of the Wilson term (2.49)

$$- a \sum_{\mu=1}^4 \frac{U_\mu(x) \delta_{x+a\hat{\mu},y} - 2\delta_{x,y} + U_{-\mu}(x) \delta_{x-a\hat{\mu},y}}{2a^2}, \quad (2.50)$$

follows from an inverse Fourier transform, and corresponds to the discretized Laplacian  $\nabla^2$ .

At this stage we summarize with Wilson's gauge-invariant lattice fermion action

$$S_W = a^2 \sum_x \bar{\psi}(x) \left\{ \sum_{\mu} (1 - \gamma_\mu) \frac{U_\mu(x) \psi(x + a\hat{\mu}) - U_{-\mu}(x) \psi(x - a\hat{\mu})}{2a} \right\} + \left( m + \frac{4}{a} \right) \bar{\psi}(x) \psi(x). \quad (2.51)$$

Although Wilson's fermion action is gauge-invariant and may be used to systematically and correctly compute QCD observables, the Wilson term has introduced  $\mathcal{O}(a)$  discretization errors. For a continuum extrapolation of a computed quantity to then be reliable, calculations with Wilson's action must be performed on fine lattices, which are both computationally expensive to generate and operate on. Improving the continuum extrapolation of quantities computed on coarse lattice spacings mandates removal of these  $\mathcal{O}(a)$  artifacts. A scheme to remove these effects, and thereby improve Wilson's action to  $\mathcal{O}(a^2)$ , is formalized by the Symanzik improvement program [42, 43] and will be our focus in subsection 2.3.4.

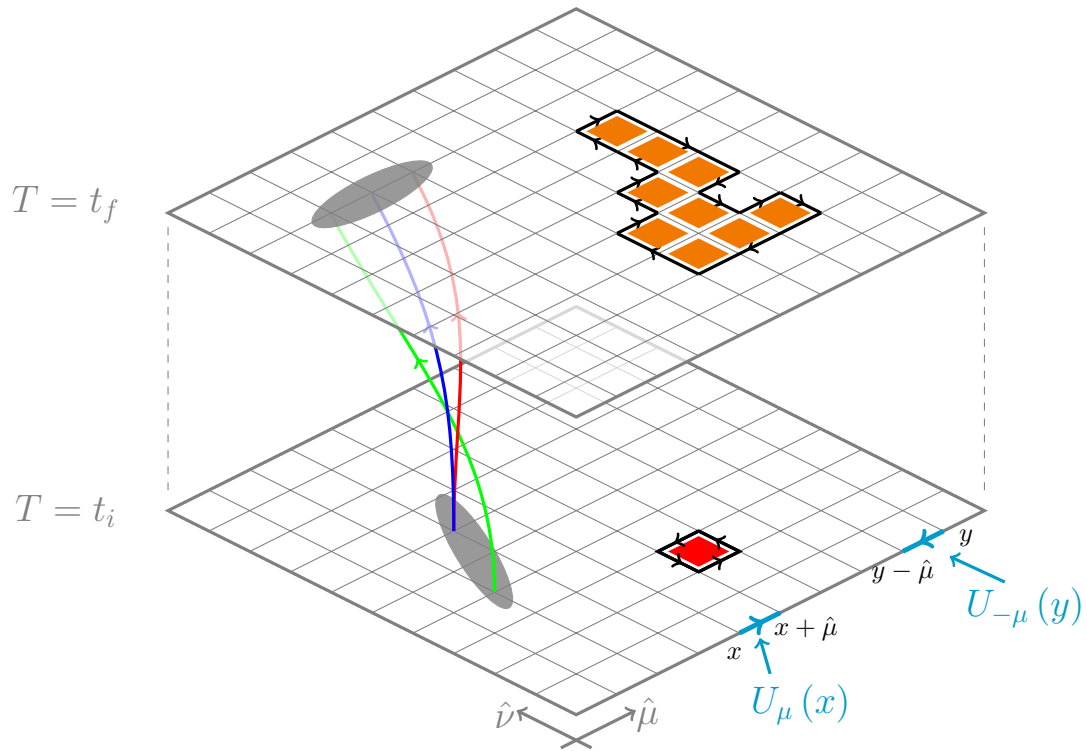


FIG. 2.8: Two dimensional time slices of a hypercubic Euclidean lattice. The coordinate space propagation of a three quark interpolator is shown with the red/green/blue directional lines, a plaquette with filled red, and a generic gauge invariant loop in orange. Directional gauge links are also shown in cyan.

### 2.3.3 Gluons & Wilson's Gauge Action

An obvious requirement of a discretized gauge action is its invariance under gauge transformations. The gauge links, introduced to maintain gauge invariance in the symmetrized derivative (2.43), are the only source of the continuum algebra-valued gauge fields, and are thus the starting point for a gauge action.

Based on the gauge transformation properties of the gauge links (2.44), it is clear a continuous path of gauge links

$$P[U] \equiv \prod_{(x,\mu) \in P} U_\mu(x) \quad (2.52)$$

transforms as  $P'[U] = \Omega(x_0) P[U] \Omega^\dagger(x_f)$ . This path of link variables then becomes invariant under gauge transformations by either attaching fermionic fields  $\{\psi, \bar{\psi}\}$  to the origin/terminus of  $P[U]$ , or by constructing  $P[U]$  to form a closed *Wilson loop*  $L[U]$  (c.f. Fig. 2.8). A gauge transformation of the latter represents a similarity transformation within the group space - an overall trace enforces the invariance of  $L[U]$ . Gauge actions found in the literature are distinguished by different loop constructions comprising the lattice gauge action; each are equally valid, provided the continuum action is correctly recovered in the  $a \rightarrow 0$  limit.

The simplest such Wilson loop one may consider is the *plaquette*

$$P_{\mu\nu}(x) \equiv U_\mu(x) U_\nu(x + a\hat{\mu}) U_\mu^\dagger(x + a\hat{\nu}) U_\nu^\dagger(x). \quad (2.53)$$

This smallest Wilson loop is the basis of the Wilson gauge action [10] - the reader is directed to Fig. 2.8 for an illustration. Expanding the gauge links in terms of the algebra-valued

fields to  $\mathcal{O}(a^3)$ , we have

$$\begin{aligned}
P_{\mu\nu}(x) &= e^{iaA_\mu(x)} e^{iaA_\nu(x+a\hat{\mu})} e^{-iaA_\mu(x+a\hat{\nu})} e^{-iaA_\nu(x)} \\
&\simeq \exp \left[ iaA_\mu(x) + iaA_\nu(x+a\hat{\mu}) - iaA_\mu(x+a\hat{\nu}) - iaA_\nu(x) \right. \\
&\quad - \frac{a^2}{2} [A_\mu(x), A_\nu(x+a\hat{\mu})] + \frac{a^2}{2} [A_\mu(x), A_\mu(x+a\hat{\nu})] \\
&\quad + \frac{a^2}{2} [A_\mu(x), A_\nu(x)] + \frac{a^2}{2} [A_\nu(x+a\hat{\mu}), A_\mu(x+a\hat{\nu})] \\
&\quad \left. + \frac{a^2}{2} [A_\nu(x+a\hat{\mu}), A_\nu(x)] - \frac{a^2}{2} [A_\mu(x+a\hat{\nu}), A_\nu(x)] + \mathcal{O}(a^3) \right],
\end{aligned}$$

where the Baker-Campbell-Hausdorff relation<sup>19</sup> has been applied. Approximating each shifted field via a Taylor series to  $\mathcal{O}(a)$ , that is  $A_\nu(x+a\hat{\mu}) \simeq A_\nu(x) + a\partial_\mu A_\nu(x)$ , one finds many of the commutators above cancel or may be grouped into the neglected  $\mathcal{O}(a^3)$  corrections. Substituting these truncated Taylor series and omitting the ensuing algebra for brevity, we find the plaquette in the small- $a$  limit reduces to

$$P_{\mu\nu} \simeq \exp \left\{ ia^2 \underbrace{(\partial_\mu A_\nu(x) - \partial_\nu A_\mu(x) + i[A_\mu(x), A_\nu(x)])}_{G_{\mu\nu}(x)} + \mathcal{O}(a^3) \right\}.$$

The series of expansions above lead to Wilson's gauge action [10]

$$S_G[U] = \frac{2}{g^2} \sum_{x \in \Lambda} \sum_{\mu < \nu} \Re \text{Tr} \{ \mathbb{1} - P_{\mu\nu}(x) \}, \quad (2.54)$$

where all plaquettes are summed over, and the ordering  $\mu < \nu$  ensures each plaquette is counted once. A common abbreviation found in the literature is the *inverse coupling*  $\beta = \frac{6}{g^2}$ , for which the prefactor of Wilson's gauge action is  $\frac{2}{g^2} \rightarrow \frac{\beta}{3}$ . In the approach to

---

<sup>19</sup>Given noncommutative members  $X$  and  $Y$  in the Lie algebra of some Lie group, the Baker-Campbell-Hausdorff formula provides the solution  $Z$  to the equation  $e^X e^Y = e^Z$ . The solution  $Z$  is a series in  $X$ ,  $Y$ , and iterated commutators of  $X$  and  $Y$ .

the continuum

$$S_G [U] \rightarrow \frac{a^4}{4g^2} \sum_{x \in \Lambda} \sum_{\mu, \nu} G_{\mu\nu}^a G_{\mu\nu}^a + \mathcal{O}(a^2), \quad (2.55)$$

the  $\mathcal{O}(a^2)$  corrections vanish and the discrete sum  $a^4 \sum_{x \in \Lambda}$  becomes a continuous space-time integral, thereby agreeing with the continuum gauge action in Eq. 2.41. Alternative lattice gauge actions naturally have the same continuum limit, but differ from Wilson's gauge action in the order at which finite lattice spacing errors arise.

Improved gauge actions generically include a larger class of Wilson loops in the action; by carefully tuning these additional contributions, the gauge action can be improved to  $\mathcal{O}(a^4)$ . Such an action includes the Lüscher-Weisz gauge action [44, 45]

$$S_{LW} = \frac{2}{g^2} \sum_{i=0}^2 c_i \sum_{L_i} \Re \text{Tr} [\mathbb{1} - L_i [U]] \quad (2.56)$$

which includes Wilson loops  $L_i$  of Wilson's gauge action (plaquettes),  $1 \times 2$  rectangular planar loops and non-planar analogs, with respective weights  $c_i$ . Results presented in this dissertation feature the tadpole improved Symanzik gauge action [46], which is the Lüscher-Weisz gauge action  $S_{LW}$  with weights  $\{c_0 = \frac{5}{3}, c_1 = -\frac{1}{12}, c_2 = 0\}$  [44]. We note another common choice includes the Iwasaki gauge action [47]. Even without improvement different group representations of the plaquette yield distinct lattice gauge actions, such as the fundamental plus adjoint gauge action [48].

### 2.3.4 Symanzik Improvement

As was seen in subsection 2.3.2, Wilson's fermion action features  $\mathcal{O}(a)$  discretization effects that may skew the approach to the continuum if not properly controlled. Near the continuum limit, K. Symanzik envisioned the lattice theory being described by an effective continuum theory with the lattice spacing  $a$  serving as an expansion parameter [49]. The

action of such an effective theory is then

$$S_{\text{eff}} = S_{(0)} + aS_{(1)} + a^2S_{(2)} + \mathcal{O}(a^3), \quad (2.57)$$

where  $S_{(0)}$  is the continuum action and  $S_{(j)} \forall j > 1$  are higher-dimensional operator insertions. The Lagrangians  $\mathcal{L}_{(j)}$  of each correction to the action  $S_{(j)} = \int d^4x \mathcal{L}_{(j)}(x)$  are built from the local fields of the lattice theory, and have energy dimension  $[L_{(j)}] = [E]^{4+j}$ . Naturally each correction must be invariant under gauge and flavor rotations, and respect the discrete symmetries of the lattice theory. Symanzik improvement and removal of  $\mathcal{O}(a)$  errors is then achieved by adding a suitable  $\mathcal{O}(a)$  counterterm to Wilson's fermion action (Eq. 2.51), such that  $\mathcal{L}_{(1)}$  is canceled. We now summarize this process.

With the considerations above, the QCD lattice action admits five dimension-5 corrections

$$\begin{aligned} \mathcal{O}_1 &= \bar{\psi} \sigma_{\mu\nu} G_{\mu\nu} \psi \\ \mathcal{O}_2 &= \bar{\psi} \vec{D}_\mu \vec{D}_\mu \psi + \bar{\psi} \overleftarrow{D}_\mu \overleftarrow{D}_\mu \psi \\ \mathcal{O}_3 &= m \text{Tr} [G_{\mu\nu} G_{\mu\nu}] \\ \mathcal{O}_4 &= m \left( \bar{\psi} \vec{D} \psi - \bar{\psi} \overleftarrow{D} \psi \right) \\ \mathcal{O}_5 &= m^2 \bar{\psi} \psi, \end{aligned} \quad (2.58)$$

where the  $\mathcal{L}_{(1)}(x)$  effective Lagrangian is a linear combination of these local operators.<sup>20</sup> The equations of motion (e.g.  $(\not{D} + m)\psi = 0$ ) for each quark flavor allow  $\mathcal{O}_2, \mathcal{O}_4$  to be removed in place of  $\mathcal{O}_{1,3,5}$  [50]. As operators  $\mathcal{O}_{3,5}$  already exist in  $S_0$ , their role amounts to a renormalization of the bare coupling  $g_0$  and masses  $m_{i,0}$ . The remaining operator  $\mathcal{O}_1$

---

<sup>20</sup> $\sigma_{\mu\nu} = \frac{1}{2i} [\gamma_\mu, \gamma_\nu]$

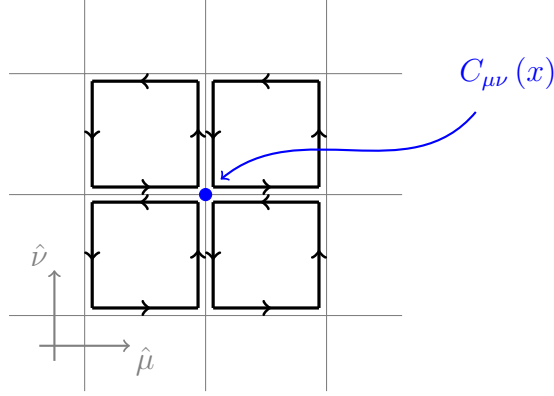


FIG. 2.9: Illustration of the plaquette sum appearing in the discretization of the field strength tensor  $\hat{G}_{\mu\nu}$ .

then yields the  $\mathcal{O}(a)$ -improved Wilson fermion action<sup>21</sup>

$$S_{impr} [U, \bar{\psi}, \psi] = S_W [U, \bar{\psi}, \psi] + a^5 c_{sw} \sum_{x \in \Lambda} \bar{\psi}(x) \sigma_{\mu\nu} \hat{G}_{\mu\nu}(x) \psi(x), \quad (2.59)$$

where  $\hat{G}_{\mu\nu}$  is a standard discretization of the field strength tensor [50]

$$\hat{G}_{\mu\nu}(x) \simeq -\frac{i}{8a^2} [C_{\mu\nu}(x) - C_{\nu\mu}(x)], \quad (2.60)$$

with  $C_{\mu\nu}(x) = \sum_{\hat{\nu}=\pm\nu}^{\hat{\mu}=\pm\mu} \{ \delta_{\text{sgn}(\hat{\mu}), \text{sgn}(\hat{\nu})} P_{\hat{\mu}\hat{\nu}}(x) + \delta_{\text{sgn}(-\hat{\mu}), \text{sgn}(\hat{\nu})} P_{\hat{\nu}\hat{\mu}}(x) \}$ . As the shape of the plaquette sum  $C_{\mu\nu}(x)$ , illustrated in Fig. 2.9, resembles a clover, the  $\mathcal{O}(a)$  correction to Wilson's fermion action is deemed the *clover term*; the improved action is also frequently referred to as the *Wilson clover* or *clover improved* action. The coefficient  $c_{sw}$  appearing in the clover term is the *Sheikholeslami-Wohlert* coefficient, named for the authors who first wrote the counterterm that improves Wilson's fermion action [51]. Determination of  $c_{sw}$  may be done perturbatively [52] or non-perturbatively, typically by requiring the partially conserved axial current (PCAC) relation hold [53]; the latter will ensure the  $\mathcal{O}(a)$

<sup>21</sup>The literature often features the oriented sum  $\frac{1}{2} \sum_{\mu < \nu}$  in place of the implied contraction of each Dirac index.



discretization errors cancel exactly when recomputed on new lattice ensembles, while the former will lessen these effects and may be reused on different ensembles.

The Symanzik improvement program may likewise be applied to operators appearing in the Euclidean correlation functions computed in a Lattice Field Theory calculation [54]. Without this further step of improvement, a lattice calculation will not be fully  $\mathcal{O}(a)$ -improved. Some observables are inextricably linked with  $\mathcal{O}(a)$  errors (see e.g. [55]), however for the observables featured in this dissertation the Wilson clover action and unimproved operators are sufficient.

### 2.3.5 Lattice Observables & the Equivalence with Statistical Mechanics

To complete our discussion of this section, we return to the Wick rotated QCD generating functional (2.40). In this form, the Euclidean generating functional is structurally identical to the partition function of a thermal system

$$Z = \sum_{\{c\}} e^{-\beta_{\text{thermal}} H[c]}, \quad (2.61)$$

given as a sum over configurations weighted by a Gibbs probability measure  $\beta_{\text{thermal}} H[c]$  with inverse temperature  $\beta_{\text{thermal}} = 1/k_B T$ . Considering just the SU(3) lattice gauge sector  $S_G[U] = \frac{a^4}{4g^2} \sum_{x \in \Lambda} \sum_{\mu, \nu} G_{\mu\nu}^a G^{a\mu\nu}$  given in Eq. 2.55, one can further push the similarity between Lattice Field Theory and statistical mechanics by making the association

$$1/4g^2 \longleftrightarrow \beta_{\text{thermal}} = 1/k_B T. \quad (2.62)$$

A low-temperature or large- $\beta_{\text{thermal}}$  expansion of a statistical system then corresponds to a small-coupling expansion of QCD, or a numerical study in a regime where perturbative

methods are viable. Conversely, the small- $\beta_{\text{thermal}}$  or  $T \rightarrow \infty$  expansion is then associated with the confining or strong-coupling regime of QCD.

By regularizing QCD in a finite and discretized Euclidean spacetime volume, an observable, such as a time-ordered product of operators, is obtained in a lattice QCD calculation by evaluating the finite path integral

$$\left\langle T \left\{ \prod_i \mathcal{O}_i \right\} \right\rangle = \frac{1}{\mathcal{Z}_E} \int \prod_j \mathcal{D} [\psi_j, \bar{\psi}_j] \mathcal{D} [U] \prod_i \mathcal{O}_i [\psi_j, \bar{\psi}_j, U] e^{-S_F[\psi_j, \bar{\psi}_j, U] - S_G[U]}, \quad (2.63)$$

where the measures over all fermion/gluon configurations are given by

$$\mathcal{D} [\psi_j, \bar{\psi}_j] = \prod_{x \in \Lambda} \prod_{\mu, c} d\psi_j(x)_\mu d\bar{\psi}_j(x)_\mu \quad \mathcal{D} [U] = \prod_{x \in \Lambda} \prod_{\mu=1}^4 dU_\mu(x), \quad (2.64)$$

with  $\mu$  and  $c$  denoting the relevant Dirac and color components of each field. In this manner, the quantum fields of QCD have been replaced in lattice QCD by a finite and countable number of classical variables.

The appearance of the anticommuting degrees of freedom, namely the fermions in QCD, prevent a naive application of Monte Carlo methods directly to the path integral (2.63) we have arrived at. It will be convenient to separate the gauge and fermion path integrals accordingly:

$$\left\langle T \left\{ \prod_i \mathcal{O}_i \right\} \right\rangle = \frac{1}{\mathcal{Z}_E} \int \mathcal{D} [U] e^{-S_G[U]} \int \prod_j \mathcal{D} [\psi_j, \bar{\psi}_j] \prod_i \mathcal{O}_i [\psi_j, \bar{\psi}_j, U] e^{-S_F[\psi_j, \bar{\psi}_j, U]},$$

where  $\mathcal{Z}_E = \int \mathcal{D} [U] e^{-S_G[U]} \int \prod_j \mathcal{D} [\psi_j, \bar{\psi}_j] e^{-S_F[\psi_j, \bar{\psi}_j, U]}$ . The task at hand is to integrate out the fermionic fields from the path integral, leaving the path integral purely in terms of the bosonic gauge fields. Appendix C recapitulates these steps. The first key result is the Matthews-Salam relation (C.14) which replaces the partition function for a flavor- $j$

fermion by the determinant of its Dirac operator  $D_j$ :

$$Z_F [U]_j = \int \mathcal{D} [\psi_j, \bar{\psi}_j] e^{-S_F[\psi_j, \bar{\psi}_j, U]} = \det (D_j [U]). \quad (2.65)$$

The term *fermion determinant* is an often used alias for the fermionic path integral. A generalized version of this relation (C.18) makes a convenient connection with Wick's Theorem which facilitates the reduction of Eq. 2.63 into

$$\left\langle T \left\{ \prod_i \mathcal{O}_i \right\} \right\rangle = \int \mathcal{D} [U] e^{-S_G[U]} \mathcal{Z}_G^{-1} \prod_j \det [D_j [U]] \langle \prod_i \mathcal{O}_i \rangle_F \equiv \int \mathcal{D} [U] \langle \prod_i \mathcal{O}_i \rangle_F P [U], \quad (2.66)$$

where  $\mathcal{Z}_G = \int \mathcal{D} [U] e^{-S_G[U]} \prod_j \det [D_j [U]]$  and  $P [U] = \mathcal{Z}_G^{-1} \prod_j \det [D_j [U]] e^{-S_G[U]}$  is the probability distribution that must be sampled. The final step is to evaluate the Wick contractions appearing in the fermionic expectation of the operators  $\langle \prod_i \mathcal{O}_i \rangle_F$  per sampled configuration. This will depend on the specific operator constructions, but in general will be given by the Dirac trace over members  $\Gamma$  of the Dirac algebra and additional fermion propagators  $D_j^{-1} [U]$ .

The final form (2.66) is now amenable to evaluation by a computer. Given that the Dirac operator  $D_j [U]$  for each fermion flavor- $j$  in modern lattice QCD calculations has dimensionality in excess of  $\mathcal{O} (10^7)$ , brute force evaluation of the various determinants and inverses is infeasible. Monte Carlo methods and importance sampling are thus routinely brought to bear on this bosonic path integral. An ensemble of gauge fields of cardinality  $N$  is sampled according to the distribution  $P [U]$ . By computing the observable  $\langle \prod_i \mathcal{O}_i \rangle$  on each configuration, a statistical estimate

$$\left\langle T \left\{ \prod_i \mathcal{O}_i \right\} \right\rangle \approx \frac{1}{N} \sum_{k=1}^N \prod_i \mathcal{O}_i [U_k] \quad (2.67)$$

is obtained that is systematically improvable.

## 2.4 Numerical Techniques of Lattice QCD

Due to the confinement of partons within hadrons, the precise wavefunction of any hadronic state is not known. Operators in any lattice calculation are thus constructed in a manner that best reflects the properties of the targeted hadron, such as its parity and spin/orbital angular momenta. Such operators, or rather *interpolators*, are functionals of the lattice fields. Together with limited knowledge of a hadron's wavefunction, the reduced rotational symmetry of a cubic lattice ensures any interpolator  $\hat{\mathcal{O}}$  in LQCD will couple to an infinite tower of states of the same quantum numbers.

A central demand of any lattice calculation thus is to optimize the interpolation of a state from the QCD vacuum, while minimizing overlap onto unwanted neighboring states. This section establishes several unavoidable theoretical challenges in LQCD that make such an operational paradigm essential. To begin, we review the basic numerical LQCD observables from which physical information may be garnered. A number of numerical techniques are subsequently developed whose broad objectives are to optimize the construction of LQCD interpolators.

Quantitative information pertaining to hadronic spectra and structure are obtained by studying the correlations of quark-gluon operators, with quantum numbers of a particular hadron, across Euclidean time. The fundamental components in any lattice calculation are the correlations of operators  $\{\mathcal{O}_i\}$  across spacetime. Those needed for the calculations in this body of work are *two-point* and *three-point* correlation functions of the form

$$C_2(\vec{y}, t_f; \vec{x}, t_i) = \langle \mathcal{O}(\vec{y}, t_f) \mathcal{O}^\dagger(\vec{x}, t_i) \rangle \quad (2.68)$$

$$C_3(\vec{y}, t_f; \vec{z}, \tau; \vec{x}, t_i) = \langle T\{\mathcal{O}(\vec{y}, t_f) \mathcal{J}(\vec{z}, \tau) \mathcal{O}^\dagger(\vec{x}, t_i)\} \rangle, \quad (2.69)$$

where  $\{\mathcal{O}\}$  and  $\mathcal{J}$  are generic hadron interpolators and external currents, respectively.

### Spatial Smearing

Lattice QCD calculations of the spectrum and properties of hadrons are afflicted by exponentially worsening signal-to-noise ratios as the Euclidean time extent between operators grows. The argument, originally attributed to Lepage, centers on the leading time dependence of the ratio of a two-point correlation function and its variance:

$$R_{S/N}(T) = \frac{C_H(T)}{\sqrt{\text{var}\{C_H(T)\}}} \sim \frac{|Z_H|^2 e^{-E_H(\vec{p})T}}{(|Z_M|^2 e^{-m_M T})^{n_q/2}} \propto e^{-(E_H(\vec{p}) - \frac{n_q}{2} m_M)T} \quad (2.70)$$

where  $Z_j(\vec{p}) = \langle 0 | \hat{\mathcal{O}}_j(\vec{p}) | h(\vec{p}) \rangle$  are operator-state overlap factors,  $\vec{p}$  is the hadron's 3-momentum, and  $m_M$  is the lightest meson mass produceable with the lightest  $n_q$  quark flavors in the hadron interpolator. The case of a pure light-quark baryon (e.g. nucleon with degenerate  $u/d$  quarks) is depicted in Fig. 2.10, where  $n_q = 3$  leads to three  $u/d$  mesons (e.g. pions) in the variance of the baryon correlation function; a nucleon's signal-to-noise ratio evidently scales as  $R_{S/N}^{\text{nucleon}}(T) \propto e^{-(E_N(\vec{p}) - \frac{3}{2} m_\pi)T}$ . The same exercise for meson interpolators, assuming charge conjugation symmetry, reveals  $R_{S/N}^M(T) \propto e^{-(E_M(\vec{p}) - m_M)T}$ .

$$C_B(T) = \langle \mathcal{O}_B(T) \mathcal{O}_B^\dagger(0) \rangle \quad \sigma_{C_B(T)}^2 \sim \langle \mathcal{O}_B(T) \mathcal{O}_B^\dagger(0) \mathcal{O}_B(0) \mathcal{O}_B^\dagger(T) \rangle$$



FIG. 2.10: Wick contractions to realize a light-quark baryon two-point function (left) and the square of its variance (right). The correlation function variance induces Wick contractions that may be ordered into three light-quark mesons. Additional contraction permutations omitted for brevity.

The lightest pseudoscalar mesons at rest then do not suffer from an exponential increase in noise as the Euclidean time  $T$  is increased.

A key demand of lattice calculations then is for the hadron of interest to saturate a correlation function at as short a Euclidean time separation as possible. As a correlation function receives contributions from an infinite tower of states of the same quantum numbers (excited-states), satisfying this saturation relies on the identification of an operator whose overlap with the hadron of interest is maximized relative to those with other states:  $\langle 0 | \hat{\mathcal{O}}(\vec{p}) | h(\vec{p}) \rangle \gg \langle 0 | \hat{\mathcal{O}}(\vec{p}) | h'(\vec{p}) \rangle$ .

Interpolating operators constructed of point-like quark and gluonic fields couple to hadronic states at all energy scales, and thus do not single out the hadronic energy scales of QCD most desired in Lattice calculations. This is most easily noted by recalling the uncertainty relationship between coordinate and momentum space. Spatial *smearing* algorithms are employed ubiquitously in LQCD computations to increase the overlap of interpolators onto the low-lying spectrum (i.e. confinement scale physics). Any such spatial smearing procedure of quark fields  $\psi(\vec{x}, t)$  proceeds generically according to

$$\tilde{\psi}(\vec{x}, t) = \sum_{\vec{y}} S[U](\vec{x}, \vec{y}) \psi(\vec{y}, t), \quad (2.71)$$

where  $S[U]$  is a surjective, gauge-covariant mapping that is functionally dependent upon equal-time gauge fields  $U$ . A realization frequently utilized in lattice calculations is that of the Jacobi smearing kernel  $J_{\sigma, n_\sigma}(t) = (1 + \sigma \nabla^2(t))^{n_\sigma}$  [56], with  $\sigma$  a tunable parameter,  $n_\sigma$  the number of successive applications, and  $\nabla^2$  the three-dimensional discretized gauge-covariant Laplacian. With a single application of the Jacobi smearing kernel, quark fields

$\psi(\vec{y})$  are then modified according to

$$\tilde{\psi}_a(\vec{x}, t) = \psi_a(\vec{x}, t) (1 + 6\sigma) - \sigma \sum_{j=1}^3 \left[ \tilde{U}_j(\vec{x}, t)_{ab} \psi_b(\vec{x} + \hat{j}, t) + \tilde{U}_j^\dagger(\vec{x} - \hat{j}, t)_{ab} \psi_b(\vec{x} - \hat{j}, t) \right], \quad (2.72)$$

with color indices made explicit, and  $\hat{j}$  a displacement of unity in the  $\hat{j}$  direction. In the large- $n_\sigma$  limit, the kernel approaches a Gaussian profile of width  $\rho = \sigma/n_\sigma$ , ideally commensurate with the size of the desired hadronic state. Although simple to realize numerically, the number of Jacobi smearing iterations must increase as the lattice spacing is reduced in order to maintain the same physical width. This divergent behavior is characteristic of all such iterative smearing schemes, and motivates more sophisticated non-iterative approaches - especially as the continuum limit must be taken for all computed quantities.

## Optimizing State Interpolations

The non-perturbative dynamics of QCD at hadronic energy scales precludes an exact solution for a hadron's wavefunction. Although interpolating operators in lattice QCD are constructed with definite quantum numbers, each is only a well-informed best guess and necessarily overlaps onto other hadronic states of the same quantum numbers - notably, excited and multi-particle states. The breaking of continuum rotational symmetry by the hypercubic lattice compounds this difficulty, as continuum operators residing in distinct irreducible representations (irreps) of the Lorentz group can mix under subduction to the same lattice irrep. The net effect is an infinite number of continuum states contribute to the signal of a correlator within some lattice irrep.

One way to improve the isolation of a particular energy eigenstate contribution to a

correlation function is to consider a matrix of correlation functions

$$C_{ij}(T) = \langle 0 | \mathcal{O}_i(T) \mathcal{O}_j^\dagger(0) | 0 \rangle \quad (2.73)$$

where each operator  $\mathcal{O}_{i,j}$  belongs to a basis of interpolators of the same lattice irrep. The optimal combination of operators to interpolate an energy eigenstate  $|\mathbf{n}\rangle$  can be formulated with respect to a variational principle [57]. The variational method corresponds to the solution of a generalized eigenvalue problem (GEVP) of the form

$$C(T) v_{\mathbf{n}}(T, T_0) = \lambda_{\mathbf{n}}(T, T_0) C(T_0) v_{\mathbf{n}}(T, T_0). \quad (2.74)$$

Optimal operators, in a variational sense, for energy eigenstates  $|\mathbf{n}\rangle$  are defined by  $\sum_i v_{\mathbf{n}}^i \mathcal{O}_i^\dagger$ . Associated with each eigenvector is a *principal correlator*  $\lambda_{\mathbf{n}}(T, T_0)$ . The energy of each state  $|\mathbf{n}\rangle$  is obtained by fitting its principal correlator according to

$$\lambda_{\mathbf{n}}(T, T_0) = (1 - A_{\mathbf{n}}) e^{-E_{\mathbf{n}}(T-T_0)} + A_{\mathbf{n}} e^{-E'_{\mathbf{n}}(T-T_0)}. \quad (2.75)$$

The inclusion of a second exponential serves to quantify the extent to which a single state dominates the principal correlator; any deviation is encapsulated by the amplitude  $A_{\mathbf{n}}$  and “excited” energy  $E'_{\mathbf{n}}$ .

The variational analysis of a matrix of correlation functions, or GEVP for short, is especially advantageous as it leads to a more rapid relaxation of a correlator in Euclidean time. As a result, spectral information can be reliably isolated at earlier Euclidean times where the signal is exponentially more precise. This fact is demonstrated explicitly in Sec. 3.1.3.



## Distillation

The low-mode filter that is the Jacobi smearing kernel, and in general other smearing kernels, can be enforced more rigorously by forming an alternative smearing kernel comprised of only the leading eigenmodes of the smearing operator. Such an explicit low-rank approximation is formulated by isolating eigenvectors of the discretized three-dimensional gauge-covariant Laplacian

$$-\nabla^2(T)\xi^{(k)}(T) = \lambda^{(k)}(T)\xi^{(k)}(T). \quad (2.76)$$

The outer product of equal-time eigenvectors  $\xi^{(k)}(T)$ , ordered monotonically according to decreasing<sup>22</sup> eigenvalue magnitudes  $\lambda^{(k)}(T)$ , defines the *Distillation* [58] smearing kernel

$$\square(\vec{x}, \vec{y}; T)_{ab} = \sum_{k=1}^{R_{\mathcal{D}}} \xi_a^{(k)}(\vec{x}, T) \xi_b^{(k)\dagger}(\vec{y}, T), \quad (2.77)$$

where  $R_{\mathcal{D}}$  is the chosen rank of the distillation space with color indices  $\{a, b\}$ . The maximal rank of the distillation kernel thus cannot exceed the dimension of the vector space  $\mathcal{V}$  of scalar fields, or time-local lattice sites, charged under  $SU(3)$ . When  $R_{\mathcal{D}} = \text{rk}(\mathcal{V})$  the distillation kernel reduces trivially to the identity map, while a spatial broadening of quark fields is induced for  $R_{\mathcal{D}} < \text{rk}(\mathcal{V})$ .

Beyond projecting out the dominant contribution to a correlation function signal, distillation possess several convenient, yet powerful, side-effects. Consider a meson two-point correlation function with quark fields smeared with distillation,

$$C_2^M(\vec{p}; T_f, T_0) = \left\langle \bar{d}(T_f)_a^w \square(T_f)_{ab}^{wz} \Gamma^B(T_f)_{\alpha\beta}^{zy} \square(T_f)_{cd}^{yx} u(T_f)_\beta^x \right\rangle_d$$

---

<sup>22</sup>The Jacobi smearing kernel  $\exp(\alpha\nabla^2)$  that distillation approximates leads to an exponential suppression of high eigenmodes of the discretized Laplacian. The low eigenmodes correspond to the low-energy contributions and have the largest eigenvalues.

$$\times \bar{u}(T_0)_{\beta' d'}^{x'} \square(T_0)_{d' c'}^{x' y'} \Gamma^A(T_0)_{\beta' \alpha'}^{y' z'} \square(T_0)_{z' w'}^{z' w'} d(T_0)_{\alpha' a'}^{w'} \Big\rangle_F \quad (2.78)$$

where indices are made explicit, potentially distinct meson  $M$  constructions in coordinate, spin, and color space are encoded with  $\Gamma^{A[B]}$ , and  $\langle \dots \rangle_F$  denotes a fermionic expectation.

Proceeding to carry out the relevant Wick contractions we have

$$\begin{aligned} C_2^M(\vec{p}; T_f, T_0) &= \square(T_f)_{ab}^{wz} \square(T_f)_{cd}^{yx} \square(T_0)_{d' c'}^{x' y'} \square(T_0)_{b' a'}^{z' w'} \Gamma^B(T_f)_{\alpha\beta}^{zy} \Gamma^A(T_0)_{\beta' \alpha'}^{y' z'} \\ &\quad \times \overbrace{d(T_f)_{\alpha}^w u(T_f)_{\beta}^x \bar{u}(T_0)_{\beta'}^{x'} d(T_0)_{\alpha'}^{w'}} \\ &= -\square(T_f)_{ab}^{wz} \square(T_f)_{cd}^{yx} \square(T_0)_{d' c'}^{x' y'} \square(T_0)_{b' a'}^{z' w'} \Gamma^B(T_f)_{\alpha\beta}^{zy} \Gamma^A(T_0)_{\beta' \alpha'}^{y' z'} \\ &\quad \times D_d^{-1}(T_f | T_0)_{\alpha' \alpha}^{w' w} D_u^{-1}(T_f | T_0)_{\beta\beta'}^{xx'} \\ &= -\text{Tr} [\square(T_f) \Gamma^B(T_f) \square(T_f) D_u^{-1}(T_f | T_0) \square(T_0) \Gamma^A(T_0) \square(T_0) D_d^{-1}(T_f | T_0)] \\ &= -\text{Tr} [\xi^\dagger(T_f) \Gamma^B(T_f) \xi(T_f) \xi^\dagger(T_f) D_u^{-1}(T_f | T_0) \xi(T_0) \xi^\dagger(T_0) \Gamma^A(T_0) \\ &\quad \times \xi(T_0) \xi^\dagger(T_0) D_d^{-1}(T_f | T_0) \xi(T_f)] \\ &= -\text{Tr} [\Phi^B(T_f) \tau(T_f, T_0) \Phi^A(T_0) \tau(T_0, T_f)], \end{aligned} \quad (2.79)$$

where in the final two lines the distillation kernels have been expressed in terms of contributing eigenvectors, revealing that the meson two-point correlator can be obtained by evaluating the trace of distinct objects within the distillation space. These objects

$$\begin{aligned} \text{Elementals} : \Phi_{\alpha\beta}^{(i,j)}(T) &= \xi^{(i)\dagger}(T) [\Gamma(T)]_{\alpha\beta} \xi^{(j)}(T) \equiv \xi^{(i)\dagger}(T) \mathcal{D}(T) \xi^{(j)}(T) S_{\alpha\beta} \\ \text{Perambulators} : \tau_{\alpha\beta}^{(i,j)}(T', T) &= \xi^{(i)\dagger}(T') D_{\alpha\beta}^{-1}(T', T) \xi^{(j)}(T), \end{aligned} \quad (2.80)$$

respectively capture the source/sink interpolator constructions and quark propagation within the distillation space. An analogous exercise performed for baryons, reveals a

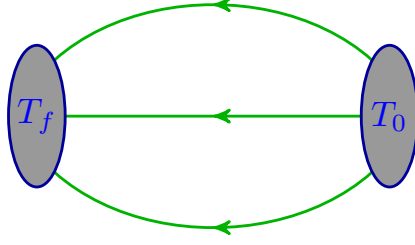


FIG. 2.11: Pictorial representation of the factorization of a baryon two-point correlation function. Perambulators are shown in green and elementals as gray ovals.

baryon two-point function factorizes into the same perambulators as for mesons, while the elementals are modified according to

$$\Phi_{\alpha\beta\gamma}^{(i,j,k)}(T) = \epsilon^{abc} (\mathcal{D}_1 \xi^{(i)})^a (\mathcal{D}_2 \xi^{(j)})^b (\mathcal{D}_3 \xi^{(k)})^c (T) S_{\alpha\beta\gamma}. \quad (2.81)$$

The factorization of a baryon two-point function with distillation is visualized in Fig. 2.11. In the constructions above,  $S_{\alpha\beta\{\gamma\}}$  encode the Dirac structure of the elemental, while  $\mathcal{D}_i$  are covariant derivatives enabling states of spin- $J$  exceeding those possible with two or three quark fields to be accessed. Each perambulator is built from a quark propagator, or the inverse of the Dirac operator  $D^{-1}(T', T)$  with the eigenvectors treated as sources.

### Momentum Smearing

Coordinate-space correlation functions computed in LQCD (cf. Eqns. (2.68) & (2.69)) possess completely unspecified momenta, and are thus only reconcilable with experimental data, often measured with respect to energy and momentum dependence, following a Fourier transform to momentum space. Projection to definite momentum involves a discrete sum over the spatial sites of the lattice, and would naively appear to be free of theoretical issues. However as pointed out by Bali et al. [59], the momentum projection of a correlation function whose quark fields are Gaussian-smearred is in fact detrimental

$\forall \vec{p} \neq \vec{0}$ . This is seen by noting the Fourier transform of a Gaussian centered at the origin in coordinate space is likewise a Gaussian centered at the origin in momentum space (i.e.  $\vec{p} = \vec{0}$ ). Consequently, conventional spatial smearing will lead to a suppression of momentum space overlaps  $Z_j(\vec{p})$  for  $\vec{p} \neq \vec{0}$ , and will make extraction of observables in boosted frames exponentially more challenging as the hadron momentum is increased.

The remedy proposed by Bali et al., known now as *momentum smearing*, shifts a quark's momentum space distribution to some non-zero value by introducing appropriately tuned phases onto a set of gauge links:  $\tilde{U}_\mu(x) = e^{iK_\mu d_\mu(x)} U_\mu(x)$ . In this scenario, a shift in momentum space is induced along the directional vector  $d_\mu(x)$  by the phase factor  $K_\mu$ . As the phase  $e^{iK_\mu d_\mu(x)}$  does not operate on the  $U_\mu(x)$  color indices, we are assured  $\tilde{U}_\mu(x) \in \text{SU}(3)$ . Furthermore, the phase factor need not be restricted to allowed lattice momenta  $\frac{2\pi}{L_s} \vec{n}$ , with  $L_s$  the spatial lattice extent and  $n_i \in \mathbb{Z}$ .

Momentum smearing is implemented in practice by substituting the phase modified gauge links into the iterative mapping (2.72). The choice of a smearing direction indeed breaks the octahedral group  $O_h$ , or its double-cover  $O_h^D$  in the case of fermions, potentially complicating state identification. However, the phase  $K_\mu$  is applied collinear to the momentum  $\vec{p}$  to be optimized for, thereby ensuring the smearing operation resides in the  $A_1$  irrep of the  $O_h$  little group associated with  $\vec{p}$ . This guarantees that momentum smearing will leave the irrep construction of any interpolator unaffected.

The choice of a momentum smearing parameter will depend on whether a single momentum or a range of momenta are targeted, and the additional computational cost incurred. In the absence of gluons, one would naively expect two- and three-quark interpolators with momentum  $\vec{p}$  to have their quark fields momentum smeared with  $\vec{K} = \vec{p}/2$  and  $\vec{K} = \vec{p}/3$ , respectively. How the ideal smearing parameters in the presence of gluons

deviate from these naive choices can be determined by deriving the effective energy

$$E_{\text{eff}}(\vec{p}, T + \delta t/2) = \frac{1}{\delta t} \log \left( \frac{C_2(\vec{p}, T)}{C_2(\vec{p}, T + \delta t)} \right) \quad (2.82)$$

of momentum-smearred two-point correlator. The ideal smearing values will yield minimal statistical errors for the fitted energies of the correlator, and earlier plateaux relative to alternate values.

The unavoidable degradation of signal-to-noise ratios (2.70) of boosted interpolators in practice limits the usefulness of momentum smearing to momenta  $\lesssim 3$  GeV. In order to garner useful physics from such high momentum correlators, analysis of the correlation function at earlier Euclidean times becomes a necessity. However, it is the early timeslices of a correlator that are most susceptible to excited-state contamination. Hence any further improvements of a momentum-smearred correlation function signal must then come with refined control of excited-states.

# CHAPTER 3

## Nucleon Matrix Elements & Excited-State Effects

As developed in Section 2.1, the structure of hadrons is studied experimentally via the scattering of point-like leptons, and often other hadrons, from a hadronic target in both collider and fixed-target configurations. As the proton is the only state of QCD stable from decay within the Standard Model, its structure is readily probed with lepton-proton DIS or Drell-Yan scattering. Free hadron targets of any other species, such as neutrons or pions, do not exist and thus complicate the feasibility of directly quantifying the structural properties of these hadrons from experiment. Scattering is instead performed on nuclear targets, which require secondary processes and sophisticated models of nuclear structure to reconstruct structural images of hadrons. A common example encountered for mesonic structure is the Sullivan process [60], whereby the colliding particle interacts with a cloud of mesons enveloping the target. Regardless of the experimental apparatus or theoretical model, structural insight is formulated in terms of hadronic matrix elements of an external current.

Lattice QCD is uniquely positioned to directly study challenging to access hadronic states, such as pions and kaons, as their partonic content can be excited from the QCD vacuum and remain stable in the absence of the weak interaction. Crucial to the fidelity of a quantity computed in lattice QCD is the degree to which systematic effects have been mitigated or eliminated entirely. Apart from errors induced by the discretized spacetime and unphysical quark masses often used to reduce the numerical cost of a calculation, some of the largest sources of uncertainty in lattice calculations are excited-state contamination and statistical precision. This chapter dives deeper into the role excited states play in determining hadronic matrix elements accurately from lattice QCD. Whereas iterative spatial smearing kernels are ubiquitous algorithms for excited-state reduction, only a few matrix element calculations using distillation [61, 62, 63] exist in the literature. Motivated by the success of distillation in identifying a plethora of excited and exotic hadronic spectra [64, 65, 66, 67, 68, 69], the first structure calculations with distillation are reported herein. We will find distillation affords a powerful and computationally efficient method of taming excited-state contributions to hadronic matrix elements, especially when complemented by a variational analysis of an extended operator basis which it cheaply facilitates. The additional time-slice sampling provided by distillation furthermore leads to demonstrably improved statistical precision of data relative to conventional smearing kernels. These same conclusions are reached following an adjustment of distillation to high momentum observables, thus building a strong case for the use of distillation in future, more elaborate, structure calculations.

### 3.1 Excited-State Contributions to Nucleon Isovector Charges

Certain experimentally measured quantities have long been considered “standard candles” in lattice QCD. The axial charge of the nucleon is a quintessential example given its high experimental precision  $g_A^{u-d} = 1.2756(13)$  [29], and broad phenomenological impact, including quantifying the difference between  $u$  and  $d$  quark contributions to the proton spin, and the neutron decay rate through the process  $n \rightarrow pe^- \bar{\nu}_e$ . The nucleon matrix element of the isovector axial current  $A_\mu^{u-d} = \bar{\psi} \gamma_\mu \gamma_5 \frac{\tau^3}{2} \psi$  expressed in terms of its Lorentz-invariant form factors reads

$$\langle N | A_\mu | N \rangle = \bar{u}_N(p_f) \left[ \gamma_\mu \gamma_5 G_A^{u-d}(q^2) + \frac{q_\mu}{2M_N} \gamma_5 G_P(q^2) \right] u_N(p_i), \quad (3.1)$$

with  $M_N$  the nucleon mass and  $q^2 = (p_f - p_i)^2$ . That  $g_A^{u-d}$  is taken as a standard candle in lattice QCD is seen by noting the induced pseudoscalar form factor  $G_P^{u-d}$  does not contribute in the forward limit ( $q_\mu = 0$ ), leaving  $g_A^{u-d} \equiv G_A^{u-d}(0)$  as a local axial current between nucleon states. Despite the simplicity, the bulk of lattice calculations have systematically underdetermined  $g_A^{u-d}$  by  $\sim 10 - 15\%$  - only recently have lattice results fallen to within  $\sim 1\%$  [70, 71, 72]. This apparent tension with experiment is often largely attributed to excited-state effects. To attain sub-percent accuracy, a delicate control of discretization, finite volume and quark mass effects is likewise required.

The ability to postdict from lattice QCD certain highly precise experimental measurements is one method used to quantify and claim control of excited states. We will follow, in part, this philosophy by computing  $g_A^{u-d}$ , but will extend our study of excited-state effects with distillation to the nucleon’s scalar  $g_S^{u-d}$  and tensor  $g_T^{u-d}$  charges, which are less



known experimentally and impact BSM searches at the TeV scale<sup>1</sup> and dark matter direct detection searches. The need for distillation will be illustrated by contrasting the same charges computed using the standard Jacobi smearing kernel.

### 3.1.1 Computational Methodology

The proton and neutron are each  $J^P = \frac{1}{2}^+$  baryons with leading Fock states  $|p\rangle = |uud\rangle$  and  $|n\rangle = |ddu\rangle$ , respectively. The SU(2) isospin symmetry introduced in the opening remarks of Ch. 2 treat  $u$  and  $d$  quarks as the same entity, *light quarks*  $\ell$  for our purposes, each transmutable into the other via SU(2) transformations. Nature does not respect isospin symmetry given the difference in the neutron and proton masses  $m_n - m_p \simeq 1.2933$  MeV [29]. This broken symmetry at  $\mathcal{O}(0.1\%)$  is so small in fact that the proton and neutron are often treated as isospin projections  $I_z = \pm\frac{1}{2}$  of an  $I(J^P) = \frac{1}{2}(\frac{1}{2}^+)$  state called the *nucleon*. Isovector charges of the nucleon  $g_\Gamma^{u-d}$  are then measured experimentally through neutron to proton transitions  $\langle p(k, s') | \bar{u}\Gamma d | n(k, s) \rangle$  or proton/neutron charge differences weighted by the light quark charges.

It is likewise commonplace in lattice QCD, and this calculation, to treat QCD as having two flavors of mass degenerate light quarks (i.e. isospin symmetric). Isovector quantities then only involve fully connected quark lines, a numerically cheaper arena than the isoscalar sector which include expensive disconnected quantities. The isovector charges of the nucleon are defined according to

$$\langle N(p, s) | \mathcal{O}_\Gamma^{u-d} | N(p, s) \rangle = g_\Gamma^{u-d} \bar{u}_s(p) \Gamma u_s(p), \quad (3.2)$$

with  $\mathcal{O}_\Gamma^{u-d} = \bar{u}\Gamma u - \bar{d}\Gamma d$  and where  $\sum_s u_s(p) \bar{u}_s(p) = -i\not{p}_E + m_N$  is our prescribed nor-

---

<sup>1</sup>When combined with measurements of the neutron decay distribution,  $g_S^{u-d}$  and  $g_T^{u-d}$  can help constrain novel scalar and tensor interactions at the TeV scale that are not present in the Standard Model. The interested reader is directed to Refs. [73, 74].

malization for the Euclidean nucleon spinors.

The ground-state nucleon charges  $g_S^{u-d}$ ,  $g_A^{u-d}$ ,  $g_T^{u-d}$  are computed using four different types of interpolating operators, three utilizing distillation and the other a common nucleon interpolator found in the literature smeared with the Jacobi kernel. We explore the efficacy of each to reduce excited-state contributions to the requisite matrix elements. As our conclusions are unaffected by multiplicative renormalization constants, we present bare (unrenormalized) charges  $\hat{g}_S^{u-d}$ ,  $\hat{g}_A^{u-d}$ ,  $\hat{g}_T^{u-d}$ .

A 350 configuration ensemble of  $32^3 \times 64$  isotropic lattices with  $2 \oplus 1$  dynamical flavors (two degenerate light quarks and one heavier strange quark) of stout-smeared (one-hit) Wilson clover fermions and a tree-level tadpole-improved Symanzik gauge action [44, 46] (c.f. Sec. 2.3.3) is utilized for this study. A consequence of this stout-smearing is the tree-level tadpole-improved  $c_{\text{sw}}$  coefficient is near its non-perturbative value [75]. The ensemble is characterized by an inverse coupling  $\beta = 6.3$ , with a lattice spacing of  $a = 0.094(1)$  fm determined by the Wilson-flow scale  $w_0$  [76] and a resultant pion mass of  $m_\pi = 358(3)$  MeV [75]. The nucleon charges  $\hat{g}_S^{u-d}$ ,  $\hat{g}_A^{u-d}$ ,  $\hat{g}_T^{u-d}$  are computed in the nucleon's rest frame, as this frame in lattice QCD is subject to smaller systematic effects, including excited-state and unwanted mixings with other symmetry channels that arise for in-flight calculations.

### 3.1.2 Interpolator Constructions

As a benchmark with which to compare to distillation, we begin with the simplest nucleon interpolator consistent with the  $J^{PC}$  quantum numbers of the nucleon

$$\mathfrak{N}_\alpha(x) = \epsilon^{abc} \left[ u^{a\top}(x) C \frac{(1 \pm \gamma_4)}{2} \gamma_5 d^b(x) \right] u_\alpha^c(x) \quad (3.3)$$

where  $u, d$  are the two flavors of (degenerate) light quarks,  $\{a, b, c\}$  color indices,  $C = \gamma_2 \gamma_4$  the charge conjugation matrix, and  $\alpha$  an open Dirac index. The projector  $(1 + \gamma_4)/2$  is included to select the non-relativistic forward propagating state, although in some calculations the backward propagating non-relativistic projector  $(1 - \gamma_4)/2$  is likewise considered. In the interest of comparison with earlier works on this same ensemble [77, 78],  $\mathfrak{N}_\alpha$  is smeared with 60 applications of the Jacobi kernel with width  $\sigma = 5.0$ . The smeared interpolator  $\mathfrak{N}_\alpha$  is then referred to as *Jacobi-SS* to reflect smeared creation/annihilation interpolators.

The distilled nucleon interpolators we consider are expressed generically as

$$\mathcal{O}_i(t) = \epsilon^{abc} (\mathcal{D}_1 \square u)_a^\alpha (\mathcal{D}_2 \square d)_b^\beta (\mathcal{D}_3 \square u)_c^\gamma (t) S_i^{\alpha\beta\gamma}, \quad (3.4)$$

where  $\mathcal{D}_i$  in general contain a Dirac structure and covariant derivatives, introduced to probe the radial/angular structure of the nucleon, and  $S^{\alpha\beta\gamma}$  encode the subduction of the interpolator into  $O_h^D$  irreps. A comprehensive construction of the interpolators we introduce below is given in [69] - essential details for a contained discussion are presented as follows. When expressed in a form exposing the permutational symmetry of the flavor ( $\mathcal{F}$ ), spatial ( $\mathcal{D}$ ) and Dirac ( $\mathcal{S}$ ) structures, distilled baryon interpolators take the form

$$\mathcal{O}_B = (\mathcal{F}_{\mathcal{P}(\mathcal{F})} \otimes \mathcal{S}_{\mathcal{P}(\mathcal{S})} \otimes \mathcal{D}_{\mathcal{P}(\mathcal{D})}) \{q_1 q_2 q_3\} \quad (3.5)$$

where the symmetric (S), mixed-symmetric (M) and antisymmetric (A) character of each structure is expressed by the permutation symbol  $\mathcal{P}(\dots)$ . Explicitly the distilled interpolators employed are

1.  $(N_M \otimes (\frac{1}{2}^+)_M^1 \otimes D_{L=0,S}^{[0]})^{J^P=\frac{1}{2}^+} \equiv N^2 S_S \frac{1}{2}^+$
2.  $(N_M \otimes (\frac{1}{2}^+)_M^1 \otimes D_{L=0,M}^{[2]})^{J^P=\frac{1}{2}^+} \equiv N^2 S_M \frac{1}{2}^+$

3.  $(N_M \otimes (\frac{1}{2}^+)_M^1 \otimes D_{L=0,S}^{[2]})^{J^P=\frac{1}{2}^+} \equiv N^2 S'_S \frac{1}{2}^+$
4.  $(N_M \otimes (\frac{1}{2}^+)_M^1 \otimes D_{L=1,A}^{[2]})^{J^P=\frac{1}{2}^+} \equiv N^2 P_A \frac{1}{2}^+$
5.  $(N_M \otimes (\frac{1}{2}^+)_M^1 \otimes D_{L=1,M}^{[2]})^{J^P=\frac{1}{2}^+} \equiv N^2 P_M \frac{1}{2}^+$
6.  $(N_M \otimes (\frac{3}{2}^+)_S^1 \otimes D_{L=1,M}^{[2]})^{J^P=\frac{1}{2}^+} \equiv N^4 P_M \frac{1}{2}^+$
7.  $(N_M \otimes (\frac{3}{2}^+)_S^1 \otimes D_{L=2,M}^{[2]})^{J^P=\frac{1}{2}^+} \equiv N^4 D_M \frac{1}{2}^+.$

This selection was based on a study [79] which found these seven, especially  $N^2 S_S \frac{1}{2}^+$  and the hybrid  $N^2 P_M \frac{1}{2}^+$  and  $N^4 P_M \frac{1}{2}^+$ , had predominant overlap onto the ground-state nucleon. These operators are projections onto the lattice irreps of discretized continuum-like operators, which are classified according to the spectroscopic notation  $N^{(2S+1)} L_{\mathcal{P}} J^P$ , where  $S$  represents the Dirac spin,  $L$  the angular momentum introduced via derivatives,  $\mathcal{P}$  the permutational symmetry of such derivatives, and  $J^P$  the total angular momentum and parity of the nucleon-flavored interpolator  $N$ .

The construction of the nucleon operators follows the procedure developed in Refs. [69, 79]. Each interpolator is built from three quark fields and covariant derivatives, each respectively combined into objects of definite half-integer and integer spin using SU(2) and SO(3) Clebsch-Gordan coefficients. When combined into an overall  $J^P = \frac{1}{2}^+$  operator consistent with the ground-state nucleon, these interpolators subduce trivially into the  $G_{1g}$  irrep of  $O_h^D$ . Recall from Sec. 2.4, the act of distillation applied to quark fields facilitates the factorization of a correlation function into perambulators and elementals. The spectroscopic notations above are in practice expressed in terms of the baryon elementals introduced in Eq. 2.81.

The first distilled interpolator we consider is  $N^2 S_S \frac{1}{2}^+$ , which is the closest non-relativistic analogue of (3.3). The two additional distilled interpolators follow from a

variational analysis of a matrix of two-point correlation functions constructed from interpolators in the operator bases

$$\mathcal{B}_{\vec{p}=\vec{0}}^{[3]} = \left\{ N^2 S_{S\frac{1}{2}^+}, N^2 P_{M\frac{1}{2}^+}, N^4 P_{M\frac{1}{2}^+} \right\} \quad (3.6)$$

$$\mathcal{B}_{\vec{p}=\vec{0}}^{[7]} = \left\{ N^2 S_{S\frac{1}{2}^+}, N^2 S_{M\frac{1}{2}^+}, N^2 S'_{S\frac{1}{2}^+}, N^2 P_{A\frac{1}{2}^+}, N^2 P_{M\frac{1}{2}^+}, N^4 P_{M\frac{1}{2}^+}, N^4 D_{M\frac{1}{2}^+} \right\}. \quad (3.7)$$

These bases admit flexible descriptions of the radial/orbital structures of the nucleon that are resolved by the QCD dynamics and variational analyses. The variationally optimized operators originating from  $\mathcal{B}_{\vec{p}=\vec{0}}^{[3]}$  and  $\mathcal{B}_{\vec{p}=\vec{0}}^{[7]}$  are denoted  $\hat{\mathcal{P}}_3$  and  $\hat{\mathcal{P}}_7$ .

### 3.1.3 Correlator Behavior & Matrix Elements

The structure content of the nucleon, and indeed any hadronic state, is clarified by two-point and three-point correlation functions. With generic momentum assignments, these correlation functions for the nucleon read

$$C_{\alpha\beta}^{2\text{pt}}(T_f, \vec{p}_f; T_i, \vec{p}_i) = \sum_{\vec{x}, \vec{y}} e^{i\vec{p}_f \cdot \vec{x}} e^{-i\vec{p}_i \cdot \vec{y}} \langle \Omega | \mathcal{N}_\alpha(\vec{x}, T_f) \bar{\mathcal{N}}_\beta(\vec{y}, T_i) | \Omega \rangle \quad (3.8)$$

$$C_{\alpha\beta}^{3\text{pt}}(T_f, \vec{p}_f; \tau, \vec{q}; \vec{p}_i, T_i) = \sum_{\vec{x}, \vec{y}, \vec{z}} e^{i\vec{p}_f \cdot \vec{x}} e^{-i\vec{q} \cdot \vec{y}} e^{-i\vec{p}_i \cdot \vec{z}} \langle \Omega | \mathcal{N}_\alpha(\vec{x}, T_f) \mathcal{J}(\vec{y}, \tau) \bar{\mathcal{N}}_\beta(\vec{z}, T_i) | \Omega \rangle, \quad (3.9)$$

where  $\mathcal{J}(\vec{y}, \tau)$  is an external current introduced between the source and sink interpolator for the time-ordering  $T_i \leq \tau \leq T_f$ . Although expressed as generic correlation functions, momentum conservation restricts the momentum combinations for which (3.8) and (3.9) are non-vanishing (i.e.  $C_{\alpha\beta}^{2\text{pt}} \neq 0$  for  $\vec{p}_f = \vec{p}_i$ ). In addition to elementals and perambulators,

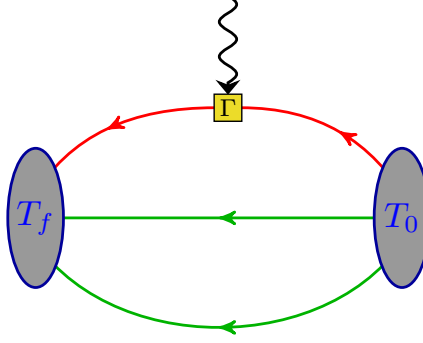


FIG. 3.1: Pictorial representation of the factorization of a baryon three-point correlation function with a local current insertion of Dirac structure  $\Gamma$ . Perambulators are shown in green, elementals as gray ovals, and a generalized perambulator in red.

distillation breaks a connected three-point function into so-called *generalized perambulators*

$$\Xi_{\alpha\beta}^{(i,j)}(T_f, T_i; \tau, \vec{q}) = \sum_{\vec{z}} e^{i\vec{q}\cdot\vec{z}} \xi^{(i)\dagger}(T_f) D_{\alpha\mu}^{-1}(T_f; \vec{z}, \tau) \Gamma_{\mu\nu}(\tau) D_{\nu\beta}^{-1}(\vec{z}, \tau; T_i) \xi^{(j)}(T_i). \quad (3.10)$$

The generalized perambulators, or genprops for short, are analogs of perambulators, encoding quark propagation within the distillation space with the inclusion of a momentum projected current. The factorization of a three-point function via the application of distillation is illustrated in Fig. 3.1.

The correlators (3.8) and (3.9) are arbitrary in their current form, as information on the nucleon spinors is absent. Projecting out a desired parity and polarization require the additional operators  $\{\Gamma^{2\text{pt}}, \Gamma^{3\text{pt}}\}$ , engendering a form amenable to numerical computation. In writing (3.8) and (3.9) it is assumed distillation is implemented, whereby the source interpolator possesses a spatial dependence; enforcing overall 3-momentum conservation will lead to a spatial volume prefactor  $V_3$ . Conventionally this factor is absorbed into the interpolator normalizations. This factor is absent however for standard point-smeared interpolators.

A spectral representation of the two- and three-point correlation functions projected

onto specific Dirac components exposes the competing effects from excited-states and any kinematic contributions. The two-point spectral representation follows from the completeness relation for finite-volume energy eigenstates (A.8) and the Euclidean time-evolution operator:

$$\begin{aligned}
C_{2\text{pt}}(T, \vec{p}_f, \vec{p}_i) &= \sum_{\vec{x}, \vec{y}} e^{i\vec{p}_f \cdot \vec{x}} e^{-i\vec{p}_i \cdot \vec{y}} \sum_{B, k, s} \Gamma_{\beta\alpha}^{2\text{pt}} \langle \Omega | \mathcal{N}_\alpha(\vec{x}, T) \frac{|B, k, s\rangle \langle B, k, s|}{2E_B(k) V_3} \overline{\mathcal{N}}_\beta(\vec{x}, 0) | \Omega \rangle \\
&= \sum_{\vec{x}, \vec{y}} \sum_{B, k, s} \frac{e^{i\vec{p}_f \cdot \vec{x}} e^{-i\vec{p}_i \cdot \vec{y}}}{2E_B(k) V_3} \Gamma_{\beta\alpha}^{2\text{pt}} \langle \Omega | e^{\hat{H}T - i\vec{p} \cdot \vec{x}} \mathcal{N}_\alpha e^{i\vec{p} \cdot \vec{x} - \hat{H}T} |B, k, s\rangle \langle B, k, s| e^{-i\vec{p} \cdot \vec{y}} \overline{\mathcal{N}}_\beta e^{i\vec{p} \cdot \vec{y}} | \Omega \rangle \\
&= \sum_{B, k, s} \frac{\Gamma_{\beta\alpha}^{2\text{pt}}}{2E_B(k) V_3} e^{-E_B(k)T} \sum_{\vec{x}, \vec{y}} e^{i(\vec{p}_f + \vec{k}) \cdot \vec{x}} e^{-i(\vec{p}_i + \vec{k}) \cdot \vec{y}} \langle \Omega | \mathcal{N}_\alpha |B, k, s\rangle \langle B, k, s| \overline{\mathcal{N}}_\beta | \Omega \rangle \\
&= \sum_{B, s} \frac{\Gamma_{\beta\alpha}^{2\text{pt}}}{2E_B(p_i)} e^{-E_B(p_i)T} \sum_{\vec{x}} e^{i(\vec{p}_f + \vec{p}_i) \cdot \vec{x}} \langle \Omega | \mathcal{N}_\alpha |B, p_i, s\rangle \langle B, p_i, s| \overline{\mathcal{N}}_\beta | \Omega \rangle \\
&= V_3 \sum_{B, s} \frac{\Gamma_{\beta\alpha}^{2\text{pt}}}{2E_B(p_f)} e^{-E_B(p_f)T} \langle \Omega | \mathcal{N}_\alpha |B, p_f, s\rangle \langle B, p_f, s| \overline{\mathcal{N}}_\beta | \Omega \rangle \\
&= V_3 \sum_s \frac{|\mathcal{Z}_0(p)|^2}{2E_0(p)} \Gamma_{\beta\alpha}^{2\text{pt}} u_\alpha(p, s) \bar{u}_\beta(p, s) e^{-E_0(p)T} + \mathcal{O}(e^{-E_1(p)T}) \\
C_{2\text{pt}}(T, \vec{p}) &= V_3 \frac{|\mathcal{Z}_0(p)|^2}{2E_0(p)} \text{Tr} \left[ \Gamma^{2\text{pt}} \left( -i\not{p}_E + m \right) \right] e^{-E_0(p)T} + \mathcal{O}(e^{-E_1(p)T}) \tag{3.11}
\end{aligned}$$

where the final spatial sum has enforced a momentum conserving delta function. As the interpolators we employ are non-relativistic, the trace appearing in the two-point function can be further reduced by applying the unpolarized, forward-propagating positive parity projector  $\Gamma^{2\text{pt}} = \frac{1}{2}(1 + \gamma_4)$  in the Dirac-Pauli representation (c.f. Appendix A.1):

$$\begin{aligned}
C_{2\text{pt}}(T, \vec{p}) &= V_3 \frac{|\mathcal{Z}_0(p)|^2}{2E_0(p)} \text{Tr} \left[ \frac{1}{2} (1 + \gamma_4) \left( -i\not{p}_E + m \right) \right] e^{-E_0(p)T} + \mathcal{O}(e^{-E_1(p)T}) \\
&= V_3 \frac{|\mathcal{Z}_0(p)|^2}{2E_0(p)} \frac{1}{2} \text{Tr} \left[ -ip_\mu^E \gamma_\mu + m - ip_\mu^E \gamma_4 \gamma_\mu + m\gamma_4 \right] e^{-E_0(p)T} + \mathcal{O}(e^{-E_1(p)T}) \\
&= V_3 \frac{|\mathcal{Z}_0(p)|^2}{E_0(p)} [E_0(p) + m] e^{-E_0(p)T} + \mathcal{O}(e^{-E_1(p)T}). \tag{3.12}
\end{aligned}$$

The three-point spectral representation proceeds in the same manner:

$$\begin{aligned}
C_{3\text{pt}}(T, \vec{p}_f; \tau, \vec{q}; \vec{p}_i) &= \sum_{\vec{x}, \vec{y}, \vec{z}} \sum_{B, k, s} \sum_{B', k', s'} e^{i\vec{p}_f \cdot \vec{x}} e^{-i\vec{q} \cdot \vec{y}} e^{-i\vec{p}_i \cdot \vec{z}} \Gamma_{\beta\alpha}^{3\text{pt}} \langle \Omega | \mathcal{N}_\alpha(\vec{x}, T) \frac{|B, k, s\rangle \langle B, k, s|}{2E_B(k) V_3} \\
&\quad \times \mathcal{J}(\vec{y}, \tau) \frac{|B', k', s'\rangle \langle B', k', s'|}{2E_{B'}(k') V_3} \overline{\mathcal{N}}_\beta(\vec{z}, 0) | \Omega \rangle \\
&= \sum_{\vec{x}, \vec{y}, \vec{z}} \sum_{B, k, s} \sum_{B', k', s'} \frac{e^{i\vec{p}_f \cdot \vec{x}} e^{-i\vec{q} \cdot \vec{y}} e^{-i\vec{p}_i \cdot \vec{z}}}{4E_B(k) E_{B'}(k') V_3^2} \Gamma_{\beta\alpha}^{3\text{pt}} \langle \Omega | e^{\hat{H}T - i\hat{p} \cdot \vec{x}} \mathcal{N}_\alpha e^{i\hat{p} \cdot \vec{x} - \hat{H}T} |B, k, s\rangle \\
&\quad \times \langle B, k, s | e^{\hat{H}\tau - i\hat{p} \cdot \vec{y}} \mathcal{J} e^{i\hat{p} \cdot \vec{y} - \hat{H}\tau} |B', k', s'\rangle \langle B', k', s' | e^{-i\hat{p} \cdot \vec{z}} \overline{\mathcal{N}}_\beta(0) e^{i\hat{p} \cdot \vec{z}} | \Omega \rangle \\
&= \sum_{B, k, s} \sum_{B', k', s'} \frac{\Gamma_{\beta\alpha}^{3\text{pt}}}{4E_B(k) E_{B'}(k') V_3^2} \sum_{\vec{x}, \vec{y}, \vec{z}} e^{i(\vec{p}_f + \vec{k}) \cdot \vec{x}} e^{-i(\vec{q} + \vec{k} - \vec{k}') \cdot \vec{y}} e^{-i(\vec{p}_i + \vec{k}') \cdot \vec{z}} e^{-E_B(k)(T-\tau)} e^{-E_{B'}(k')\tau} \\
&\quad \times \langle \Omega | \mathcal{N}_\alpha |B, k, s\rangle \langle B, k, s | \mathcal{J} |B', k', s'\rangle \langle B', k', s' | \overline{\mathcal{N}}_\beta | \Omega \rangle \\
&= \sum_{B, k, s} \sum_{B', s'} \frac{\Gamma_{\beta\alpha}^{3\text{pt}}}{4E_B(k) E_{B'}(p_i) V_3} \sum_{\vec{x}, \vec{y}} e^{i(\vec{p}_f + \vec{k}) \cdot \vec{x}} e^{-i(\vec{q} + \vec{k} - \vec{p}_i) \cdot \vec{y}} e^{-E_B(k)(T-\tau)} e^{-E_{B'}(p_i)\tau} \\
&\quad \times \langle \Omega | \mathcal{N}_\alpha |B, k, s\rangle \langle B, k, s | \mathcal{J} |B', p_i, s'\rangle \langle B', p_i, s' | \overline{\mathcal{N}}_\beta | \Omega \rangle \\
&= \sum_{B, s} \sum_{B', s'} \frac{\Gamma_{\beta\alpha}^{3\text{pt}}}{4E_B(p_f) E_{B'}(p_i)} \sum_{\vec{y}} e^{-i(\vec{q} + \vec{p}_f - \vec{p}_i) \cdot \vec{y}} e^{-E_B(p_f)(T-\tau)} e^{-E_{B'}(p_i)\tau} \\
&\quad \times \langle \Omega | \mathcal{N}_\alpha |B, p_f, s\rangle \langle B, p_f, s | \mathcal{J} |B', p_i, s'\rangle \langle B', p_i, s' | \overline{\mathcal{N}}_\beta | \Omega \rangle \\
&= V_3 \sum_{B, s} \sum_{B', s'} \frac{e^{-E_B(p_f)(T-\tau)} e^{-E_{B'}(p_i)\tau}}{4E_B(p_f) E_{B'}(p_i)} \mathcal{Z}_B(p_f) \mathcal{Z}_{B'}^\dagger(p_i) \Gamma_{\beta\alpha}^{3\text{pt}} u_\alpha^B(p_f, s) \bar{u}_\beta^{B'}(p_i, s') \\
&\quad \times \langle B, p_f, s | \mathcal{J} |B', p_i, s'\rangle \\
&= V_3 \sum_{B, B'} \frac{e^{-E_B(p_f)(T-\tau)} e^{-E_{B'}(p_i)\tau}}{4E_B(p_f) E_{B'}(p_i)} \mathcal{Z}_B(p_f) \mathcal{Z}_{B'}^\dagger(p_i) \\
&\quad \times \sum_{s, s'} \Gamma_{\beta\alpha}^{3\text{pt}} u_\alpha^B(p_f, s) \bar{u}_\mu^B(p_f, s) \mathcal{J}_{\mu\nu} u_\nu^{B'}(p_i, s') \bar{u}_\beta^{B'}(p_i, s') \\
&= V_3 \frac{\mathcal{Z}_0(p_f) \mathcal{Z}_0^\dagger(p_i)}{4E_0(p_f) E_0(p_i)} \text{Tr} \left[ \Gamma^{3\text{pt}} \left( -i\not{p}_f^E + m_0 \right) \mathcal{J} \left( -i\not{p}_i^E + m_0 \right) \right] e^{-E_0(p_f)(T-\tau)} e^{-E_0(p_i)\tau} \\
&\quad + V_3 \frac{\mathcal{Z}_0(p_f) \mathcal{Z}_1^\dagger(p_i)}{4E_0(p_f) E_1(p_i)} \text{Tr} \left[ \Gamma^{3\text{pt}} \left( -i\not{p}_f^E + m_0 \right) \mathcal{J} \left( -i\not{p}_i^E + m_1 \right) \right] e^{-E_0(p_f)(T-\tau)} e^{-E_1(p_i)\tau}
\end{aligned}$$



$$+ (|0\rangle \mapsto |1\rangle) + \mathcal{O}\left(e^{-(E_2(p_i)-E_0(p_f))\tau}\right), \quad (3.13)$$

where the final line expands the spectral representation up to corrections from the second excited-state. Charges of the nucleon are in general accessed by selecting a particular spin component from a Dirac spinor using the Euclidean space spin projector  $(1 \pm i\gamma_5\not{k})$ . The combined action of the non-relativistic (positive parity) and spin projectors yields the three-point projector  $\Gamma^{3\text{pt}} = \frac{1}{2}(1 \pm \gamma_4)(1 \pm i\gamma_5\not{k})$  we implement. For instance, to project out a forward-propagating positive parity state with spin oriented in the  $\pm k$ -direction  $\Gamma^{3\text{pt}} = \frac{1}{2}(1 + \gamma_4)(1 \pm i\gamma_5\not{k})$ .

As the charges associated with a Dirac structure are defined as the  $q^2 = 0$  limit of their parent form factors, the traces appearing in (3.13) are reduced by applying  $\Gamma^{3\text{pt}}$  and imposing momentum conservation:  $\vec{p}_f = \vec{p}_i \equiv \vec{p}$ . We restrict our attention to the leading time dependence of (3.13), whose trace contains the ground-state matrix element we seek to extract. In the vector channel the trace reduces accordingly,

$$\begin{aligned} \text{Tr} [\Gamma^{3\text{pt}} (-i\not{p} + m) g_V \gamma_\mu (-i\not{p} + m)] &= \frac{g_V}{2} \text{Tr} [(1 + i\gamma_5\not{p}_3 + \gamma_4 + i\gamma_4\not{p}_5\not{p}_3) \\ &\quad \times (-\not{p}\gamma_\mu\not{p} - im\not{p}\gamma_\mu - im\gamma_\mu\not{p} + m^2\gamma_\mu)] \\ &= \frac{g_V}{2} \text{Tr} [-imp_\alpha\gamma_\alpha\gamma_\mu - imp_\alpha\gamma_\mu\gamma_\alpha + ip_\alpha p_\beta \gamma_1\gamma_2\gamma_4\gamma_\alpha\gamma_\mu\gamma_\beta - im^2\gamma_1\gamma_2\gamma_4\gamma_\mu \\ &\quad - p_\alpha p_\beta \gamma_4\gamma_\alpha\gamma_\mu\gamma_\beta + m^2\gamma_4\gamma_\mu - m\gamma_1\gamma_2\gamma_\nu\gamma_\mu p_\nu - mp_\alpha\gamma_1\gamma_2\gamma_\mu\gamma_\alpha] \\ &= \frac{g_V}{2} [-8imp_\mu + ip_\alpha p_\beta \text{Tr} (\gamma_1\gamma_2\gamma_4\gamma_\alpha\gamma_\mu\gamma_\beta) - 4p_\alpha p_\beta (\delta_{4\alpha}\delta_{\mu\beta} - \delta_{4\mu}\delta_{\alpha\beta} + \delta_{4\beta}\delta_{\alpha\mu}) \\ &\quad + 4m^2\delta_{4\mu} - 4mp_\nu (-\delta_{1\nu}\delta_{2\mu} + \delta_{1\mu}\delta_{2\nu}) - 4mp_\alpha (-\delta_{1\mu}\delta_{2\alpha} + \delta_{1\alpha}\delta_{2\mu})] \\ &= \frac{g_V}{2} [-8imp_\mu + ip_\alpha p_\beta \text{Tr} (\gamma_1\gamma_2\gamma_4\gamma_\alpha\gamma_\mu\gamma_\beta) - 4p_4 p_\mu + 4p^2\delta_{4\mu} - 4p_\mu p_4 + 4m^2\delta_{4\mu}] \\ &= \frac{g_V}{2} [-8imp_\mu + ip_\alpha p_\beta \text{Tr} (\gamma_1\gamma_2\gamma_4\gamma_\alpha\gamma_\mu\gamma_\beta) - 8p_4 p_\mu]. \end{aligned} \quad (3.14)$$

$\text{Tr} [\dots]^{[\Gamma]}$	$\vec{p} \neq \vec{0}$	$\vec{p} = \vec{0}$
$\mathbb{1}$	$4g_S m (E(\vec{p}) + m)$	$8m^2 g_S$
$\gamma_j$	$-4ig_V^{[\gamma_j]} p_j (E(\vec{p}) + m)$	0
$\gamma_4$	$4g_V^{[\gamma_4]} E(\vec{p}) (E(\vec{p}) + m)$	$8m^2 g_V^{[\gamma_4]}$
$\gamma_4 \gamma_5$	$-4g_A^{[\gamma_4 \gamma_5]} p_3 (E(\vec{p}) + m)$	0
$\gamma_j \gamma_5$	$4ig_A^{[\gamma_j \gamma_5]} p_3 p_j$	0
$\gamma_3 \gamma_5$	$4ig_A^{[\gamma_3 \gamma_5]} [mE(\vec{p}) + m^2 + p_3^2]$	$8im^2 g_A^{[\gamma_3 \gamma_5]}$
$\gamma_j \gamma_4$	$(-1)^j 4g_T^{[\gamma_j \gamma_4]} p_{3-j} (E(\vec{p}) + m)$	0
$\gamma_3 \gamma_4$	0	0
$\gamma_4 \gamma_j$	$(-1)^{j+1} 4g_T^{[\gamma_4 \gamma_j]} p_{3-j} [E(\vec{p}) + m]$	0
$\gamma_4 \gamma_3$	0	0
$\gamma_1 \gamma_2$	$4ig_T^{[\gamma_1 \gamma_2]} (m^2 + mE(\vec{p}) + \vec{p}_\perp^2)$	$8im^2 g_T^{[\gamma_1 \gamma_2]}$
$\gamma_j \gamma_3$	$(-1)^{j-1} 4ig_T^{[\gamma_j \gamma_3]} p_{3-j} p_3$	0

TABLE 3.1: Kinematic factors arising from the traces appearing in the spectral representation of the three-point function (3.13) in the forward-limit. Each factor is the result of applying  $\Gamma_{\alpha\beta}^{3\text{pt}}$  as described in the text for each possible Dirac structure of the external current.

For the time-like vector current, one finds

$$\begin{aligned}
\text{Tr} [\dots]^{[\gamma_4]} &= \frac{g_V^{[\gamma_4]}}{2} [-8imp_4 + 2ip_\alpha p_\beta \delta_{\alpha 4} \text{Tr} (\gamma_1 \gamma_2 \gamma_4 \gamma_\beta) - ip_\alpha p_\beta \text{Tr} (\gamma_1 \gamma_2 \gamma_\alpha \gamma_\beta) - 8p_4^2] \\
&= \frac{g_V^{[\gamma_4]}}{2} [-8imp_4 - 4ip_\alpha p_\beta (\delta_{1\beta} \delta_{2\alpha} - \delta_{1\alpha} \delta_{2\beta}) - 8p_4^2] \\
&= 4g_V^{[\gamma_4]} E(\vec{p}) [E(\vec{p}) + m].
\end{aligned} \tag{3.15}$$

The same tedious exercise when repeated for the remaining 15 Dirac structures yield kinematic factors that are summarized in Tab. 3.1. It is then clear  $\mathring{g}_S^{u-d}, \mathring{g}_V^{u-d}, \mathring{g}_A^{u-d}, \mathring{g}_T^{u-d}$  are accessible at rest only with the Dirac structures  $\mathbb{1}, \gamma_4, \gamma_3 \gamma_5, \gamma_1 \gamma_2$ , respectively.

In order to study the asymptotic  $0 \ll \tau \ll T$  behavior, we parameterize our two- and

three-point correlation functions according to the two-state forms:

$$C_{\text{fit}}^{2\text{pt}}(T, \vec{p}) = e^{-E_0 T} (a + b e^{-\Delta E T}) \quad (3.16)$$

$$C_{\text{fit}}^{3\text{pt}}(T, \tau; \vec{p}) = e^{-E_0 T} \left( \mathcal{A} + \mathcal{B} e^{-\Delta E T} + \mathcal{C} e^{-\Delta E \frac{T}{2}} \cosh \left[ \Delta E \left( \tau - \frac{T}{2} \right) \right] \right), \quad (3.17)$$

where  $\Delta E$  is the ground-/excited-state energy gap,  $\mathcal{B}$  and  $\mathcal{C}$ , respectively, contain the first-excited and transition matrix elements and  $\mathcal{A}$  contains the desired ground-state matrix element. Constraints ensure the positivity of the overlap parameters  $\{a, b\}$  in the two-point fit. Unless stated otherwise, all correlator fits (3.16) and (3.17) considering in this dissertation will fit data only for  $T/a \geq 2$  to avoid contact terms induced by the Wilson-clover action. The two- and three-point correlators are simultaneously fit with (3.16) and (3.17), accounting for data correlation, to extract the unknown masses, overlap factors and matrix elements. Since the two-point spectral representation (3.12) at rest reduces to  $2V_3 |\mathcal{Z}_0|^2 e^{-m_0 T} + \mathcal{O}(e^{-m_1 T})$ , it follows the desired ground-state matrix element is given by  $g_{00}^\Gamma = \mathcal{A}/a$  in the large- $T$  limit [80].

### 3.1.4 Results

The two-point functions for each interpolator are computed for  $T^{2\text{pt}}/a \in [0, 20]$  and subsequently averaged over three temporal origins. The three-point functions are computed with these same origins for  $T^{3\text{pt}}/a \in \{8, 12, 16\}$  and the currents inserted  $\forall \tau/a \in [0, T^{3\text{pt}} - 1]$ . The quality of each interpolator is judged first by considering the effective energy (mass) (2.82) shown in Fig. 3.2. The importance of a sufficient number of distillation eigenvectors is evident in the higher statistical quality of the distilled data with  $\mathcal{R}_D = 64$  in Fig. 3.2(b) relative to  $\mathcal{R}_D = 32$  in Fig. 3.2(a). For this reason we make the following observations based on the  $\mathcal{R}_D = 64$  results in Fig. 3.2(b). The lack of a

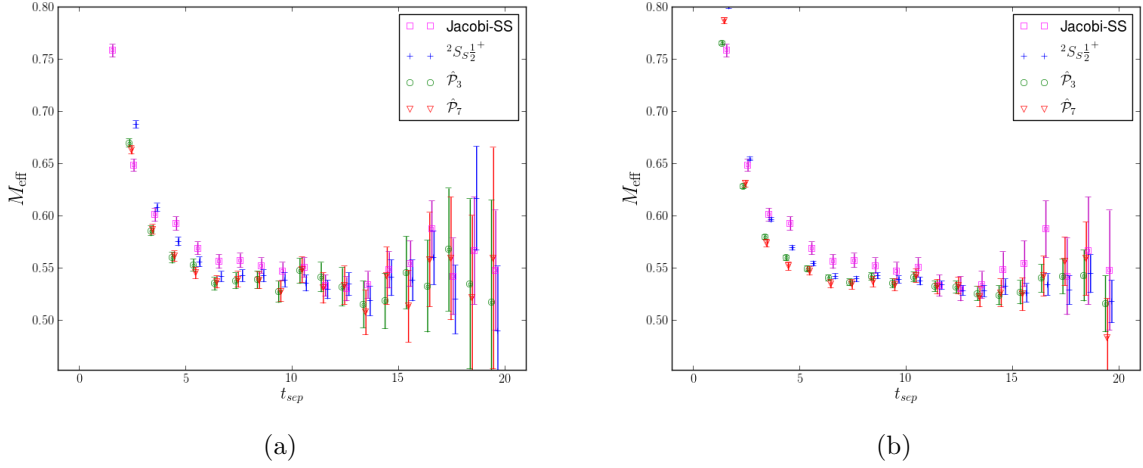


FIG. 3.2: Nucleon effective mass when using Jacobi-SS (purple) and distilled interpolators constructed from 32 (left) and 64 (right) eigenvectors. The distilled interpolators  ${}^2S_S^{1+}$  (blue),  $\hat{\mathcal{P}}_3$  (green), and  $\hat{\mathcal{P}}_7$  (red) demonstrate a plateau in the effective mass as early as  $t_{\text{sep}} = 6$ , but the statistical uncertainty is comparable to that of the Jacobi-SS when 32 eigenvectors are used. Considerable improvement in statistics is seen for the case of 64 eigenvectors.

plateau in the effective mass of the Jacobi-SS interpolator until  $T^{2\text{pt}}/a \sim 10$  is indicative of excited-state contamination for source-sink separations of  $\lesssim 1$  fm. Use of the  $N^2S_S^{1+}$  distilled interpolator leads to an earlier onset of a plateau in the effective mass, with statistical uncertainty that is at least 50% smaller than that of the Jacobi-SS interpolator. This plateau is seen to begin for  $T^{2\text{pt}}/a \sim 6$ , or  $\sim 0.6$  fm. The exponentially increasing noise in the nucleon effective mass is also substantially suppressed at larger source-sink separations when distillation is used in place of Jacobi smearing. The variationally improved interpolators  $\hat{\mathcal{P}}_3$  and  $\hat{\mathcal{P}}_7$  lead to a more rapid relaxation of the two-point correlator to the ground-state at early Euclidean times. The  $\hat{\mathcal{P}}_3$  and  $N^2S_S^{1+}$  effective masses exhibit plateaus of commensurate statistical precision, yet the  $\hat{\mathcal{P}}_3$  excited-states are seen to decay more rapidly for  $T^{2\text{pt}}/a < 5$ . Consistent with an expanded operator basis capturing and removing higher excited-states [57],  $\hat{\mathcal{P}}_7$  leads to a sharper relaxation to the ground-state for  $T^{2\text{pt}}/a < 5$ . The  $\hat{\mathcal{P}}_7$  effective mass plateau likewise begins around  $T^{2\text{pt}}/a = 6$ , but is slightly lower than those of  $N^2S_S^{1+}$  and  $\hat{\mathcal{P}}_3$ .

In general, the statistical precision of all distilled interpolators appears to be comparable, except for large Euclidean times where the variationally improved interpolators become increasingly unconstrained. This behavior is unsurprising and does not affect the two-point fits, as elements of the correlator matrices (2.73), especially the multi-derivative containing operators, are themselves dominated by noise at large- $T/a$ .

The statements above are rigorously anchored by one- and two-state fits (3.16) applied to the two-point correlation functions induced by each interpolator. The reader is directed to [80] for the results of these fits. The most striking conclusion are the mass gaps, or energy differences between the ground-state and first contributing excited-state, determined via the two-state fits:

$$\left. \begin{array}{ll} \text{Jacobi-SS,} & 0.497(80) \simeq \\ N^2S_{S\frac{1}{2}^+}, & 0.714(30) \simeq \end{array} \right\} a\Delta m = a(M_1 - M_0) \left\{ \begin{array}{ll} \simeq 0.730(51), & \hat{\mathcal{P}}_3 \\ \simeq 0.895(80), & \hat{\mathcal{P}}_7 \end{array} \right.$$

Since energy eigenstate contributions to a two-point correlator are of  $\mathcal{O}(e^{-E_n T})$ , a larger mass gap translates into saturation of the correlation function by the ground-state at earlier Euclidean times. Evidently distillation and the variational method lead to greater elimination of excited-state contributions to the two-point correlators, where the mass gap is  $\sim 44\%$ ,  $\sim 58\%$ , and  $\sim 80\%$  larger for  ${}^2S_{S\frac{1}{2}^+}$ ,  $\hat{\mathcal{P}}_3$ , and  $\hat{\mathcal{P}}_7$ , respectively, relative to the Jacobi-SS interpolator. Although increasing the smearing radius of the Jacobi-SS interpolator certainly would have increased its mass gap, any potential gains would still be less than distillation, as distillation explicitly and cheaply projects out the lowest-lying contributions to a correlator signal. Moreover, a variational analysis of Jacobi-SS interpolators of different radii would require repeated calculation of quark propagators, a considerable increase in numerical cost that is avoided by distillation.

## Unrenormalized Charges - Results

The unrenormalized charges are determined with simultaneous two- and three-point fits in the temporal windows  $T_{\text{fit}}^{2\text{pt}}/a \in [2, 16]$  and  $\tau_{\text{fit}}/a \in [2, T^{3\text{pt}} - 2]$ . To illustrate the extracted isovector charges and to quantify the degree of excited-state contamination, we plot an effective unrenormalized charge

$$\mathring{g}_{\Gamma}^{\text{eff}}(T, \tau) = C_{\Gamma}^{3\text{pt}}(T, \tau) / C_{\text{fit}}^{2\text{pt}}(T) \quad (3.18)$$

defined as the ratio of a computed three-point function and the corresponding best fit applied to the two-point function of the same interpolators and source-sink separation. Errors are purely statistical, and estimated via a simultaneous jackknife resampling of the correlators. Atop the effective unrenormalized charge data are the ratios of (3.17) to (3.16) for each  $T^{3\text{pt}}/a \in \{8, 12, 16\}$ , which plateau to the respective charge (gray bands).

The effective and extracted  $\mathring{g}_A^{u-d}$  determined with each interpolator are shown in Fig. 3.3 and the simultaneous fit results are given in Tab. 3.2. The Jacobi-SS interpolator is seen to be plagued by poor statistics - near 10% error per datum. Although  $\mathring{g}_A^{\text{eff}}(T, \tau)$  for  $T^{3\text{pt}}/a = 8, 12$  is symmetric about the midpoint  $\tau - T/2$ , indicative of equal excited-state effects on source/sink sides, at this level of statistics the Jacobi smearing of the standard nucleon interpolator (3.3) is simply insufficient to be of practical use. With the same number of measurements,  $N^2S_{S_2}^{1+}$  leads to a dramatic reduction in statistical uncertainty of  $\mathring{g}_A^{\text{eff}}(T, \tau)$ . Furthermore, the extracted value of  $\mathring{g}_A^{u-d}$  increases by  $\sim 7\%$ . The broader plateaux for each  $T/a$  imply the ground-excited state transition matrix element ( $\mathcal{C}$  of (3.17)) has been mitigated. This is confirmed in Tab. 3.2 where the ratio  $|\mathcal{C}|/|\mathcal{A}|$  is more than 50% less with the  $N^2S_{S_2}^{1+}$  interpolator. The results following from  $\hat{\mathcal{P}}_3$  and  $\hat{\mathcal{P}}_7$  offer a statistically consistent description of  $\mathring{g}_A^{\text{eff}}$ , yet the improvement over  $N^2S_{S_2}^{1+}$  is not as pronounced.

The unrenormalized tensor charge is observed in Fig. 3.4 to be consistently determined

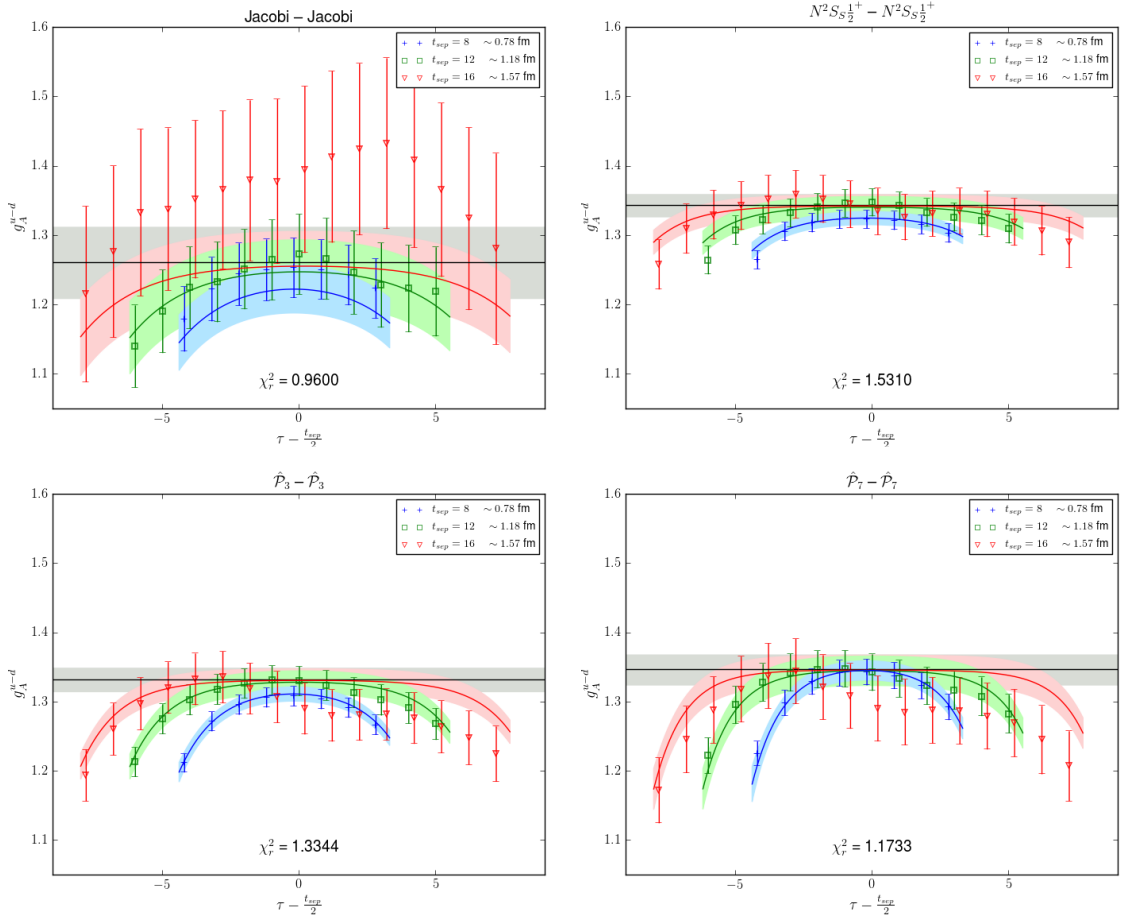


FIG. 3.3: Effective  $\hat{g}_A^{u-d}$  using the Jacobi-SS (upper-left),  $N^2 S_{S_2}^{1+}$  (upper-right),  $\hat{\mathcal{P}}_3$  (lower-left), and  $\hat{\mathcal{P}}_7$  (lower-right) distilled interpolators with  $\mathcal{R}_{\mathcal{D}} = 64$ . The bands are the ratio of the simultaneous fits (3.17) & (3.16) with  $T_{\text{fit}}^{2\text{pt}}/a \in [2, 16]$  and  $\tau_{\text{fit}}/a \in [2, T^{3\text{pt}} - 2]$ , and error estimated via jackknife resampling. The figure of merit for each simultaneous fit is also shown.

by each interpolator. However, as with the axial determination, the statistical quality of the Jacobi-SS results would conventionally warrant more measurements on an expanded gauge ensemble. Each distilled interpolator again reflects the additional volume average for distilled correlators via the considerable reduction in statistical uncertainty. Each of  $N^2 S_{S_2}^{1+}$ ,  $\hat{\mathcal{P}}_3$ ,  $\hat{\mathcal{P}}_7$  share a plateau in  $\hat{g}_T^{\text{eff}}$  for  $T/a = 12, 16$ . This suggests the excited-state matrix element ( $\mathcal{B}$  of (3.17)) is either small or its associated time-dependence is negligible for these temporal separations. As documented in Tab. 3.3, the increased resolving power of distillation has measured a non-zero excited-state matrix element, while the Jacobi-SS

$\hat{\mathcal{O}}$	$\mathcal{A}$	$\mathcal{B}$	$\mathcal{C}$	$M_0$	$M_1$	$a$	$b$	$\hat{g}_A^{u-d}$
Jacobi-SS	5.00(33)e-08	3.23(7.15)e-08	-7.66(2.12)e-09	0.540(6)	1.010(67)	3.96(23)e-08	3.81(21)e-08	1.261(51)
$N^2S_S \frac{1}{2}^+$	1.96(03)e-02	-3.03(5.78)e-02	-1.33(0.23)e-03	0.536(1)	1.244(28)	1.46(02)e-02	1.68(05)e-02	1.343(16)
$\hat{\mathcal{P}}_3$	1.41(3)e+00	-1.86(5.26)e+00	-2.28(0.22)e-01	0.535(1)	1.263(43)	1.06(1)e+00	9.22(48)e-01	1.332(17)
$\hat{\mathcal{P}}_7$	1.35(3)e+00	11.5(26.9)e+00	-2.87(0.38)e-01	0.535(2)	1.442(72)	9.99(12)e-01	1.10(12)e+00	1.347(22)

TABLE 3.2: Results of simultaneous fits to the two-point and three-point correlators with  $\gamma_3\gamma_5$  insertion. The distilled interpolators were constructed from 64 eigenvectors.

$\hat{\mathcal{O}}$	$\mathcal{A}$	$\mathcal{B}$	$\mathcal{C}$	$M_0$	$M_1$	$a$	$b$	$\hat{g}_T^{u-d}$
Jacobi-SS	4.49(32)e-08	3.36(7.57)e-08	1.21(0.19)e-08	0.542(6)	1.043(73)	4.07(23)e-08	3.78(23)e-08	1.101(42)
$N^2S_S \frac{1}{2}^+$	1.66(03)e-02	5.08(3.88)e-02	5.51(0.22)e-03	0.535(1)	1.225(26)	1.45(02)e-02	1.64(05)e-02	1.147(13)
$\hat{\mathcal{P}}_3$	1.19(2)e+00	4.48(3.28)e+00	2.22(0.16)e-01	0.535(1)	1.232(40)	1.053(13)e+00	8.86(40)e-01	1.133(14)
$\hat{\mathcal{P}}_7$	1.13(3)e+00	24.2(17.6)e+00	1.55(0.23)e-01	0.534(2)	1.387(70)	9.94(13)e-01	1.01(10)e+00	1.133(17)

TABLE 3.3: Results of simultaneous fits to the two-point and three-point correlators with  $\gamma_1\gamma_2$  insertion. The distilled interpolators were constructed from 64 eigenvectors.

fit would indicate an excited-state matrix element consistent with zero. The consistent plateaux for  $T/a = 12, 16$  with each distilled interpolator reiterates the ability of distillation to increase the ground-excited state energy gap. In expanding from  $N^2S_S \frac{1}{2}^+$  to  $\mathcal{B}_{\vec{p}=\vec{0}}^{[3]}$  and  $\mathcal{B}_{\vec{p}=\vec{0}}^{[7]}$ , the variational method serves to remove the excited-to-ground transition matrix element. This is seen visually in Fig 3.4 where each  $T/a$  plateau becomes broader as the operator basis is increased; the effect is seen numerically by considering the ratio  $\mathcal{C}/\mathcal{A}$  for each distilled interpolator. We are left with the remarkable conclusion that a variational analysis of an expanded basis of distilled interpolators yields  $\hat{g}_T^{\text{eff}}$  that resembles the vector charge - a matrix element that is constant in  $\tau/a$  within minor statistical fluctuations.

A complete accounting of each unrenormalized charge determined from this analysis and the sensitivity of the results on the rank of the distillation space can be found in [80]. Distillation clearly affords a considerable improvement in the statistical quality of the data when compared to standard Jacobi smearing. The explicit low-rank projection of the Jacobi kernel that forms the scaffolding of distillation is seen to reduce the impact of excited-states in both two- and three-point functions. We turn now to an investigation of distillation in boosted frames.



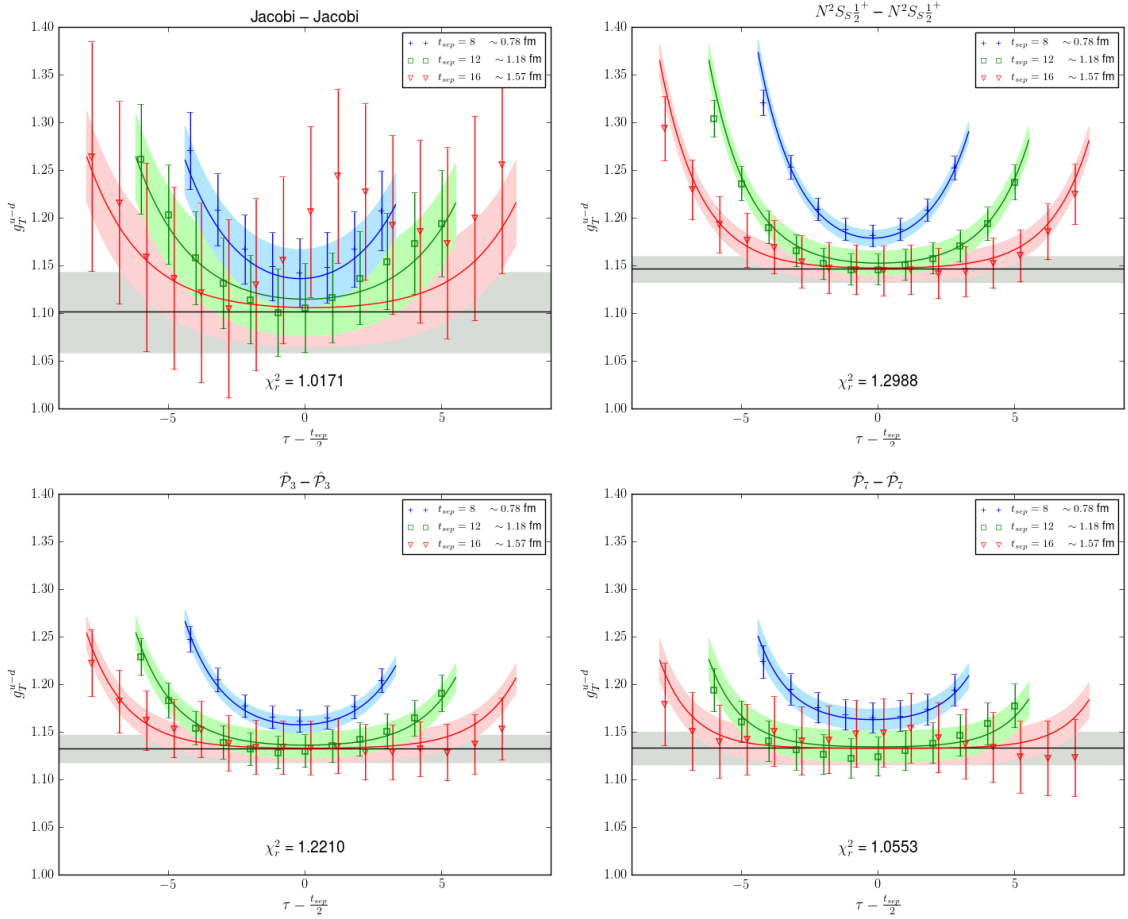


FIG. 3.4: Effective  $\hat{g}_T^{u-d}$  using the Jacobi-SS (upper-left),  $N^2 S_{S_2}^{1+}$  (upper-right),  $\hat{P}_3$  (lower-left), and  $\hat{P}_7$  (lower-right) distilled interpolators with  $\mathcal{R}_{\mathcal{D}} = 64$ . The bands are the ratio of the simultaneous fits (3.17) & (3.16) with  $T_{\text{fit}}^{2\text{pt}}/a \in [2, 16]$  and  $\tau_{\text{fit}}/a \in [2, T^{3\text{pt}} - 2]$ , and error estimated via jackknife resampling. The figure of merit for each simultaneous fit is also shown.

## 3.2 High-Momentum Matrix Elements with Distillation

Conventional spatial smearing schemes and momentum smearing work in concert to enhance the overlap of interpolating operators onto low-lying boosted hadronic states. The momentum smearing paradigm does not, however, address the increased overlap of momentum-smearred interpolators onto neighboring single- and multi-particle excited

states. This overlap onto unwanted neighboring energy eigenstates is exacerbated as the discrete particle spectrum becomes dense for increasing spatial momenta. Moreover, the reduced lattice symmetry of correlators at some non-zero spatial momentum further increase the density of unwanted states. Distillation introduced in Sec. 2.4, when employed with the extended basis of interpolators it facilitates, provides a powerful means of addressing these issues.

In the previous section it was established that distillation facilitates improved volume sampling and control of excited-state contributions relative to conventional smearing paradigms. Nucleon charges extracted in the lab rest-frame are some of the simplest measures of nucleon structure, collectively representing the  $Q^2 = 0$  limit of the respective form factors. This raises the prospect of distillation providing a similar benefit in more sophisticated structure calculations, especially PDF and GPD calculations which demand matrix elements across large kinematic windows.

Contemporary spectroscopic calculations employing distillation (e.g. [81, 82]), the largest benefactor of distillation at the time of this writing, generically consider hadron momenta  $\vec{p}$  in the rather limited shell  $|a_s \vec{p}|^2 \lesssim 4(2\pi/L_s)^2$ , with  $a_s$  and  $L_s$  the spatial lattice spacing and extent respectively. Single and multi-particle distilled interpolators with these momenta have adequate momentum-space overlaps to not warrant modifications to the distillation framework. The demand for a dramatic increase in interpolator momenta will become apparent in Ch. 4. For now, our goal in this section is to construct a version of momentum smearing within the distillation paradigm. Following simple theoretical arguments and the modifications to distillation, we perform proof of principle calculations by mapping the nucleon's dispersion relation and subsequently isolate form factors (charges) in highly boosted frames using the modified distillation space.

### 3.2.1 A Modified Distillation Space

The original momentum smearing idea of Bali et. al. [59], shifts interpolator-state overlaps in momentum-space by re-weighting gauge fields  $U_\mu(x)$  prior to source creation in a direction  $z_\mu$  with weight  $\zeta = \frac{2\pi}{L}\mathbf{r}$  according to

$$\tilde{U}_\mu(x) = e^{i\frac{2\pi}{L}\mathbf{r}z_\mu}U_\mu(x). \quad (3.19)$$

The phase factors  $\mathbf{r} \in \mathbb{R}$  are not restricted to allowed lattice momenta, as an explicit momentum projection is the only instance when translation invariance must be satisfied. Bali et al. state the same arbitrary smearing can be applied to a gauge configuration prior to computing distillation eigenvectors.

From a practical viewpoint, distillation is costly initially in both computational storage and construction of its components. Important for the construction of correlation functions with distillation are the number of distinct Wick contractions that must be evaluated. Mesons and baryons comprised purely of isospin symmetric light quarks require Wick contractions that scale as  $R_{\mathcal{D}}^3$  and  $R_{\mathcal{D}}^4$ , respectively (cf. Fig. 3.5). These scalings result from counting the matrix multiplications in the distillation space needed to evaluate a correlation function. For instance, it was found in Eq. 2.79 that a meson two-point function smeared with distillation involves three distinct multiplications of perambulators and meson elementals; as each are constructed from  $R_{\mathcal{D}}$  eigenvectors, the net scaling is  $R_{\mathcal{D}}^3$ . It has furthermore been established that in order to maintain the same statistical quality, or resolution, in correlation functions computed on different gauge ensembles,  $R_{\mathcal{D}}$  should scale with the lattice spatial volume [58]. Implementing momentum smearing within the distillation framework is then only computationally practical by minimizing the number of additional eigenvector bases constructed. Rather than compute a distinct eigenvector basis for each unique three-momentum desired, we set out to modify an already com-

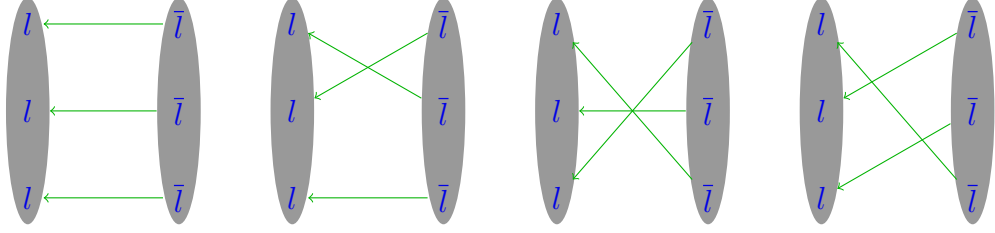


FIG. 3.5: Distinct Wick contraction topologies required to evaluate a light-quark baryon two-point correlation function.

puted eigenvector basis. Any modifications will be minimal in number to reflect the above considerations.

A series of potential modifications to a pre-computed eigenvector basis includes:

1. *Single Phase*

$$\tilde{\xi}_a^{(k)}(\vec{z}, t) = e^{i\vec{\zeta} \cdot \vec{z}} \xi_a^{(k)}(\vec{z}, t) \quad (3.20)$$

2. *Opposing Phases*

$$\tilde{\xi}_a^{(k)}(\vec{z}, t) = 2 \cos(\vec{\zeta} \cdot \vec{z}) \xi_a^{(k)}(\vec{z}, t) \quad (3.21)$$

3. *Identity and Opposing Phases*

$$\tilde{\xi}_a^{(k)}(\vec{z}, t) = \left[ 1 + 2 \cos(\vec{\zeta} \cdot \vec{z}) \right] \xi_a^{(k)}(\vec{z}, t) \quad (3.22)$$

4. *Multiple Phases*

$$\tilde{\xi}_a^{(k)}(\vec{z}, t) = \left[ e^{i\vec{\zeta}_1 \cdot \vec{z}} + e^{i\vec{\zeta}_2 \cdot \vec{z}} \right]_{\vec{\zeta}_1 \neq \vec{\zeta}_2} \xi_a^{(k)}(\vec{z}, t), \quad (3.23)$$

where  $\vec{\zeta}_j$  are the hadron momenta for which a momentum-projected elemental constructed from the modified eigenvectors should maximally overlap with in a free-field calculation. Since the eigenvectors entering either of these potential modifications already reflect the spatial periodic boundary conditions of the lattice, the phase factors are restricted to allowed lattice momenta contrary to the original momentum smearing formulation of Bali

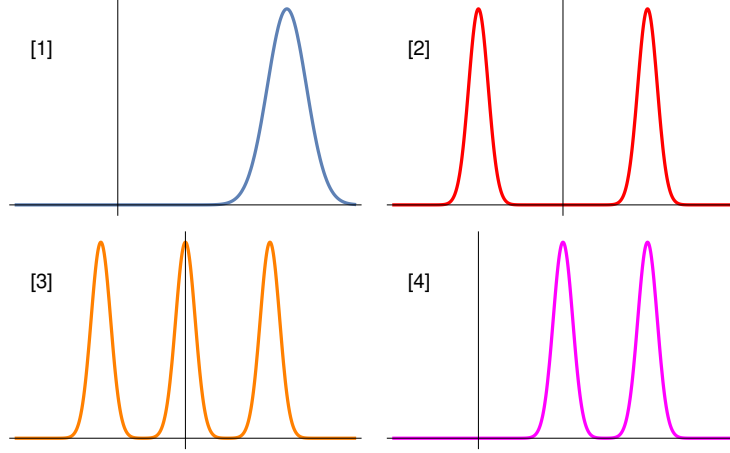


FIG. 3.6: Qualitative momentum space overlaps following modification of a computed eigenvector basis. Translation invariance is expressly violated for all but Panel 1, nullifying computational gains with Panels 2-4 were translation symmetry preserved.

et al. [59]. These modifications, qualitatively shown in Fig. 3.6, suggest naively several, potentially opposing, hadron momenta could be improved simultaneously. Essential for definite momentum projection of operators appearing in a lattice correlation function is the translational invariance (on an ensemble average) of all components of said Green's function. By performing a spatial translation  $\vec{x} \rightarrow \vec{x} + \vec{d}$  of a Type-1 perambulator

$$\begin{aligned}\tilde{\tau}_{\mu\nu}^{ij}(t', t) &= \xi^{(i)\dagger}(\vec{x}, t') e^{-i\vec{\zeta} \cdot (\vec{x} + \vec{d})} M_{\mu\nu}^{-1}(\vec{x}, t'; \vec{y}, t) e^{i\vec{\zeta} \cdot (\vec{y} + \vec{d})} \xi^{(j)}(\vec{y}, t) \\ &= \xi^{(i)\dagger}(\vec{x}, t') e^{-i\vec{\zeta} \cdot \vec{x}} M_{\mu\nu}^{-1}(\vec{x}, t'; \vec{y}, t) e^{i\vec{\zeta} \cdot \vec{y}} \xi^{(j)}(\vec{y}, t),\end{aligned}$$

we see translation symmetry is respected when a single phase is applied to the distillation eigenvectors. Repeating this exercise for the Type-4 modification

$$\begin{aligned}\tilde{\tau}_{\mu\nu}^{ij}(t', t) &= \xi^{(i)\dagger}(\vec{x}, t') \{e^{-i\vec{\zeta}_2 \cdot (\vec{x} + \vec{d})} + e^{-i\vec{\zeta}_1 \cdot (\vec{x} + \vec{d})}\} M_{\mu\nu}^{-1}(\vec{x}, t'; \vec{y}, t) \\ &\quad \times \{e^{i\vec{\zeta}_1 \cdot (\vec{y} + \vec{d})} + e^{i\vec{\zeta}_2 \cdot (\vec{y} + \vec{d})}\} \xi^{(j)}(\vec{y}, t) \\ &= \xi^{(i)\dagger}(\vec{x}, t') e^{-i\vec{\zeta}_2 \cdot \vec{x}} e^{i(\vec{\zeta}_1 - \vec{\zeta}_2) \cdot \vec{d}} M_{\mu\nu}^{-1}(\vec{x}, t'; \vec{y}, t) e^{i\vec{\zeta}_1 \cdot \vec{y}} \xi^{(j)}(\vec{y}, t) + \{\vec{\zeta}_1 \leftrightarrow \vec{\zeta}_2\} + \mathcal{T.I.},\end{aligned}$$

the result includes a combination of translationally invariant ( $\mathcal{T.I.}$ ) and variant pieces for  $\vec{\zeta}_1 \neq \vec{\zeta}_2$ . The same conclusion is reached for the proposed Type-2 and Type-3 modifications. We are forced to conclude that momentum-space shifts introduced into a distillation space are allowed only for multiples of allowed lattice momenta and in a single direction. For the remainder of this dissertation when momentum smeared distillation is referenced, Type-1 is utilized and the modified (*phased*) bases considered are given by

$$\vec{\zeta}_1 = \frac{2\pi}{L}\hat{z} \qquad \vec{\zeta}_2 = 2 \times \frac{2\pi}{L}\hat{z}. \qquad (3.24)$$

### 3.2.2 Demonstration of Efficacy

Having established that Type-1 phased distillation will preserve the translational symmetry required for definite momentum projections on a spatial lattice, we turn our attention to simple calculations to demonstrate that phased distillation indeed improves energy and matrix element extractions in boosted frames. We will find ground-state nucleon energies can be extracted reliably for  $|\vec{p}| \lesssim 3$  GeV and matrix elements featuring a large momentum dependence can be resolved. It is important to keep in mind that each object within the distillation space will need to be recomputed for every new eigenvector basis.

#### Nucleon Spectrum and Dispersion Relation

The excited and exotic spectra of mesonic [64, 65, 66, 67] and baryonic [68, 69] systems has been thoroughly mapped via the use of distillation. Indeed phased distillation will provide little novel insight for these systems at rest. Knowledge of a hadron's spectrum is important in non-stationary frames, especially in lattice QCD, as access to matrix elements sensitive to the structural properties of a hadron depend on high fidelity energy extractions. Whereas form factor studies at low- $Q^2$  illuminate the radial charge distributions in a single

state and in state transitions (e.g. [61]), high- $Q^2$  calculations of practical numerical cost necessitate phased distillation.

With this backdrop in mind, the utility and efficacy of phased distillation is demonstrated by mapping the ground-state nucleon's dispersion relation on an ensemble of  $32^3 \times 64$  lattices with  $2 \oplus 1$  dynamical Wilson-clover fermions. This ensemble, denoted *a094m358*, is the same one on which the nucleon isovector charges were computed at rest in Sec. 3.1. The reader is referred to the previous section or Refs. [77, 78] for specifics, however details of *a094m358* relevant to this calculation are summarized in Tab. 3.4. A relatively small number of measurements - four distinct (randomized) temporal source origins on 100 configurations of *a094m358*, was sufficient to demonstrate the benefits of phased distillation. We begin by highlighting the construction of our interpolators and the analysis techniques used to extract the nucleon dispersion relation.

To best capture the non-relativistic<sup>2</sup> ground-state  $J^P = \frac{1}{2}^+$  nucleon at rest we recycle the basis of interpolators  $\mathcal{B}_{\vec{p}=\vec{0}}^{[7]}$  defined in Eq. 3.7. Projection of the lattice interpolating fields to non-zero spatial momenta ( $\vec{p} \neq \vec{0}$ ) breaks the discrete parity symmetry, allowing positive and negative parity states, even in the continuum, to mix. The boost  $\vec{p}$  furthermore breaks the  $O_h^D$  symmetry group to little groups dependent on the  $^*(\vec{p})$  [83] - the group of rotations for which a momentum vector  $\vec{p}$  is left invariant. The union of these broken symmetries entails that additional states contribute to a correlator signal, a compounding factor to a spectrum that becomes dense as the hadron momentum is increased.

To simplify the analysis of boosted (un)phased correlators, focus is given to Lorentz boosts along a spatial axis. In this case, the lattice little group is the order-16 dicyclic group or  $\text{Dic}_4$  and interpolators are now classified according to their patterns of helicity subduction. Based on a rest-frame study of the  $J^P = \frac{1}{2}^\pm, \frac{3}{2}^\pm, \frac{5}{2}^\pm, \frac{7}{2}^\pm$  nucleon spectrum [79],

---

<sup>2</sup>Non-relativistic in this context refers to the operator construction. Each quark field comprising the interpolator is restricted to its upper two Dirac components.

ID	$a$ [fm]	$m_\pi$ [MeV]	$L^3 \times N_t$	$N_{\text{cfg}}$	$N_{\text{srcs}}$	$R_{\mathcal{D}}$
$a094m358$	0.094(1)	358(3)	$32^3 \times 64$	100	4	64
$a094m278$	0.094(1)	278(4)	$32^3 \times 64$	259	4	64

TABLE 3.4: Lattice ensembles utilized in the phased distillation proof of principle calculations. The rank of the distillation space  $R_{\mathcal{D}}$  and distinct source positions  $N_{\text{srcs}}$  per configuration are also indicated. The choice of  $R_{\mathcal{D}} = 64$  in both cases is justified in the Appendix of [85].

we extend our interpolator basis to<sup>3</sup>

$$\begin{aligned}
\mathcal{B}_{\vec{p} \neq \vec{0}}^{[16]} = \{ & N^2 S_{S\frac{1}{2}^+}, N^2 S_{M\frac{1}{2}^+}, N^2 P_{A\frac{1}{2}^+}, N^2 P_{M\frac{1}{2}^+}, N^4 P_{M\frac{1}{2}^+}, N^4 D_{M\frac{1}{2}^+}, \\
& N^4 S_{M\frac{3}{2}^+}, N^2 D_{S\frac{5}{2}^+}, N^2 P_{M\frac{1}{2}^-}, N^4 P_{M\frac{1}{2}^-}, N^2 P_{M\frac{3}{2}^-}, \\
& N^4 P_{M\frac{3}{2}^-}, N^4 P_{M\frac{5}{2}^-}, N^2 D_{S\frac{3}{2}^+}, N^4 D_{M\frac{3}{2}^+}, N^2 D_{M\frac{3}{2}^+} \}. \quad (3.25)
\end{aligned}$$

These interpolators were found to have appreciable overlaps onto low-lying nucleon spectra within each  $J^P$  channel [79]. Although the spectroscopic notation for these interpolators is maintained, each interpolator is assembled as a continuum operator of definite helicity that is then subduced into the requisite little group. This process of helicity operator constructions in lattice QCD was first developed for mesons in flight [84].

The standard implementation of distillation, without phasing, is used first to compute the ground-state nucleon energies for  $\hat{z}$ -boosted momenta  $ap_z \leq 4(2\pi/L)$ . In particular, the spatially-local, non-relativistic interpolator  $N^2 S_{S\frac{1}{2}^+}$  is used to benchmark variational improvement, phasing, and their amalgam. Two-state fits (3.16) and the derived effective energies are shown in Fig. 3.7(a), along with energies predicted from the continuum dispersion relation with the rest mass obtained in Sec. 3.1 and assuming a speed of light of unity. The data for  $ap_z \leq 2(2\pi/L)$  exhibit a clear signal over the entire  $T/a$  range, being

<sup>3</sup>Note  $N^2 S'_{S\frac{1}{2}^+}$  of the  $\mathcal{B}_{\vec{p}=\vec{0}}^{[7]}$  basis has been removed.



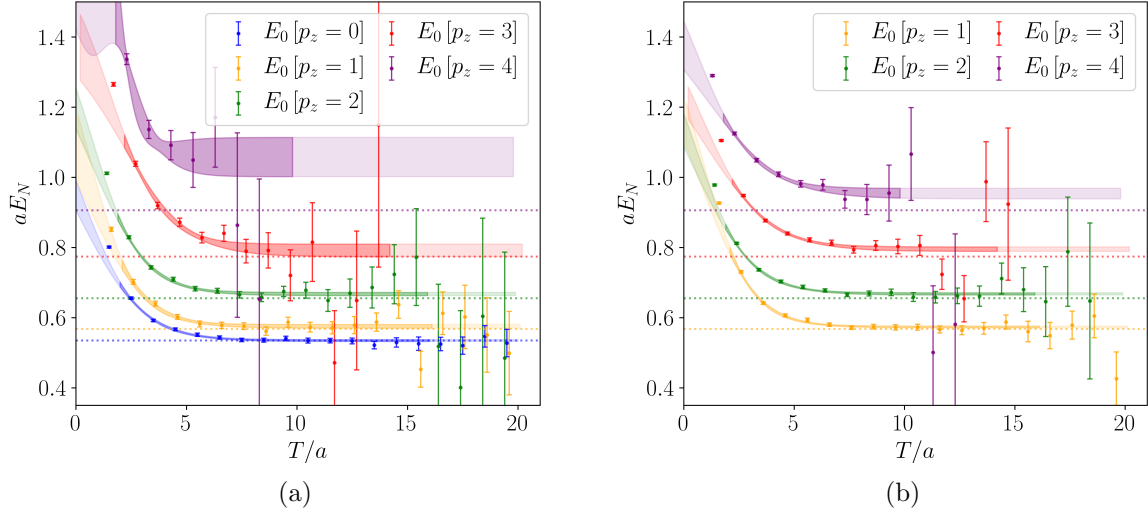


FIG. 3.7: The left-hand (a) and right-hand (b) plots show the effective energies for the nucleon obtained on the  $a094m358$  ensemble, using the spatially-local, non-relativistic interpolator  $N^2S_S^{\frac{1}{2}^+}$  subduced into the  $G_{1g}$  and  $E_1$  irreps of  $O_h^D$  and  $Dic_4$ , respectively. Panel (a) results from standard eigenvectors and panel (b) from  $\vec{\zeta}_1$ -phased eigenvectors. Data are shown for points where the signal-noise ratios are  $\geq 1.35$  (a) and  $\geq 2$  (b), and are shifted horizontally for legibility. The bands show the two-state fits to the correlators, where the dark regions indicate data included in the fits. The dashed lines are energies expected from the continuum dispersion relation.

well described by a two-state fit and in agreement with the continuum dispersion. The predictable onset of signal degradation is seen for  $ap_z = \{3, 4\} \times (2\pi/L)$ , and the data at early Euclidean times  $T/a \lesssim 5$  are increasingly at odds with a simple two-state fit. Switching to  $\vec{\zeta}_1$ -phased eigenvectors (3.24) in Fig. 3.7(b), the  $ap_z = \{3, 4\} \times (2\pi/L)$  signals are now readily resolved and exhibit a plateau indicative of single-state dominance. The slight deviations from continuum predictions suggest an incomplete determination of the ground-state contribution that is best addressed with a variational analysis.

To assess the degree excited-states may have affected the preceding  $N^2S_S^{\frac{1}{2}^+}$  extractions, variational analyses were applied to correlator matrices formed by interpolators in the bases  $\mathcal{B}_{\vec{p}=\vec{0}}^{[7]}$  (3.7) and  $\mathcal{B}_{\vec{p}\neq\vec{0}}^{[16]}$  (3.25) both for unphased and  $\vec{\zeta}_1$ -phased eigenvectors. The  $\vec{\zeta}_1$ -phased variational analysis was completed for momenta  $1 \leq (2\pi/L)^{-1}ap_z \leq 4$ . The

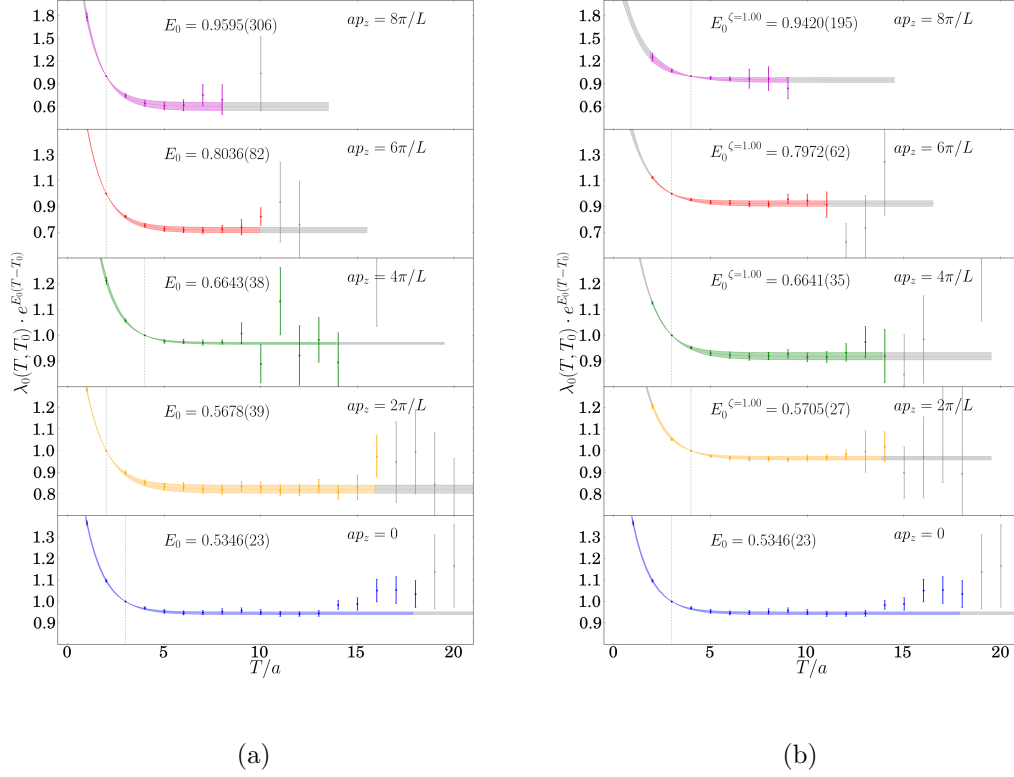


FIG. 3.8: The ground-state nucleon principal correlators rescaled as  $\lambda_0 e^{E_0(T-T_0)}$  for the  $a094m358$  ensemble using projected interpolators within each momentum channel obtained from  $\mathcal{B}_{\vec{p}=0}^{[7]}$  and  $\mathcal{B}_{\vec{p}\neq\vec{0}}^{[16]}$ . The left-hand and right-hand panels are obtained from the unphased and  $\vec{\zeta}_1$ -phased eigenvectors, respectively. The ground-state principal correlator from the unphased  $\mathcal{B}_{\vec{p}=0}$  basis is shown for reference (blue). In each case, data are shown for signal-to-noise ratios  $\geq 2$ . The bands show the two-exponential fits of Eq. 2.75, with data excluded from the fits in gray.

principal correlators and applied two-state fits (2.75) stemming from these analyses are shown in the left- and right-hand panels of Fig. 3.8. The principal correlators in each case demonstrate a rather uniform plateau near unity, indicating that unwanted eigenstates have decayed away. The  $\vec{\zeta}_1$ -phased principal correlators, however, are better determined than the unphased equivalent - up to  $\sim 35\%$  more precise ground-state energy determination in the  $ap_z = 4(2\pi/L)$  channel. A further variational analysis is completed in the  $4 \leq (2\pi/L)^{-1}ap_z \leq 8$  channels for operators  $\mathcal{O}_i \in \mathcal{B}_{\vec{p}\neq\vec{0}}^{[16]}$  built from  $\vec{\zeta}_2$ -phased eigen-

vectors (3.24). The  $\vec{\zeta}_2$  principal correlators have been omitted, as statistical fluctuations prevail in the unphased principal correlators at such high momenta; the reader is directed to [85] for further detail.

The results for the variational analyses of the unphased and phased bases for all momenta considered are aggregated in Fig. 3.9, juxtaposed with the unphased  $N^2S_S^{\frac{1}{2}+}$  results and the continuum and lattice dispersion relations for a free fermion particle. Energies from the  $\vec{\zeta}_1$ -phasing were found to be consistent with those determined from the variational analysis of the unphased  $\mathcal{B}_{\vec{p}\neq\vec{0}}^{[16]}$ , but of higher statistical quality. Despite the use of an extended operator basis and the improved isolation of eigenstates that it entails, distillation without phasing is unable to cleanly resolve the ground-state nucleon energy for  $ap_z = 4(2\pi/L)$  - whether  $N^2S_S^{\frac{1}{2}+}$  or an optimized operator is used, the signal is noise-dominated. Most encouraging, the  $\vec{\zeta}_2$  eigenvectors, even with limited statistics, have enabled accurate energy determinations to at least  $ap_z = 6(2\pi/L)$  and perhaps as high as  $p_z \simeq 3$  GeV where  $\mathcal{O}(ap)$  discretization errors accrue. One final variational analysis of a set of purely-local and mostly relativistic interpolators (red in Fig. 3.9) yielded consistent results. This sanity check confirms the interpolator group theory, especially in the derivative constructions, is not spoiled by the addition of momentum phase factors. In regards to the agreement between the extracted nucleon energies and the continuum dispersion relation, the reader is reminded the lattice dispersion relation shown in Fig. 3.9 applies for a naively discretized point particle. The faithful mapping of the ground-state nucleon's continuum dispersion relation up to  $\sim 3$  GeV by the lattice data is indicative of the considerable overlap our lattice interpolators have with the continuum nucleon. In particular, the chosen operator bases have effectively captured the extended structures of the nucleon, and the use of a phased eigenvector basis has enabled a continued description of the nucleon up to  $\sim 3$  GeV. These observations are supported by the disagreement between the continuum dispersion relation and the  $N^2S_S^{\frac{1}{2}+}$  energies without phasing for

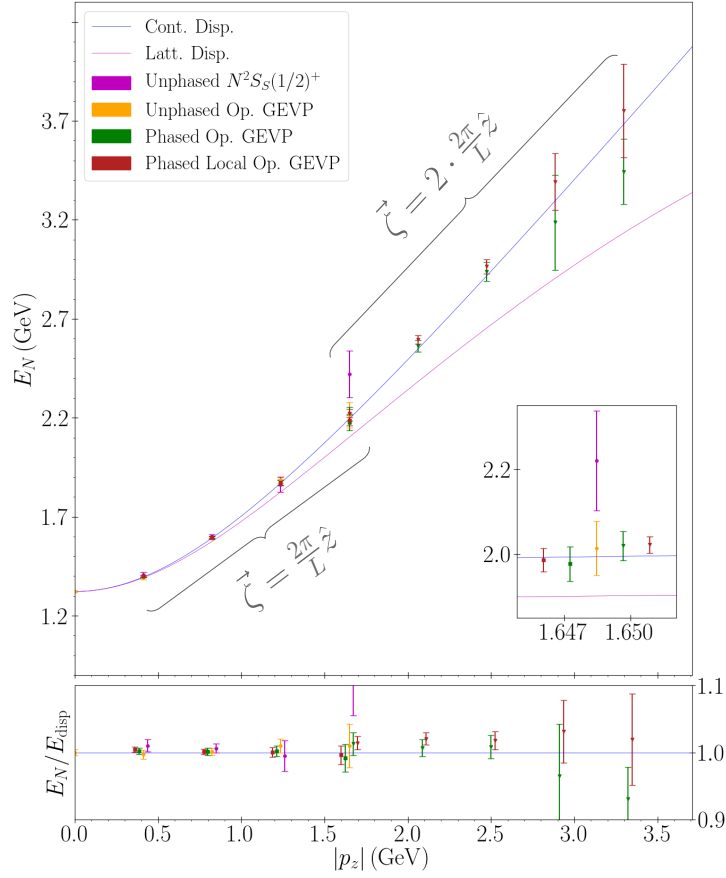


FIG. 3.9: The ground-state nucleon dispersion relation for the  $a094m358$  ensemble, together with expectations from the continuum (blue) and free lattice scalar (purple) dispersion relations. Energies without the use of phasing are shown in magenta for the  $N^2S_S \frac{1}{2}^+$  operator, and orange for the variational analyses using the bases  $\mathcal{B}_{\vec{p}=\vec{0}}^{[7]}$ ,  $\mathcal{B}_{\vec{p}\neq\vec{0}}^{[16]}$ . The squares and triangles are results from the variational analyses of  $\vec{\zeta}_1$  and  $\vec{\zeta}_2$  phased eigenvectors. A subsequent GEVP of a purely local basis (red), demonstrates the phase factors do not invalidate the group theory used to construct our operators. The energies for  $ap_z = 4(2\pi/L)$ , where each phase and unphased eigenvectors were used, are shown in the inset plot. The lower panel emphasizes the differences between each method by normalizing each with respect to the continuum dispersion relation.

$p_z \geq 4(2\pi/aL)$  ( $\sim 1.65$  GeV). Of course, for high enough momenta the continuum dispersion relation should be violated, and this appears to be the case around the highest momenta ( $\sim 3$  GeV) we access in this proof of principle calculation.

These results emphasize that broad momentum space overlaps are possible in distillation with a minimal set of eigenvectors, thereby obviating the need for precisely tuned eigenvector phases for each momentum. The resolution of the ground-state nucleon to

at least  $ap_z = 6(2\pi/L)$  marks a considerable improvement in the distillation/GEVP infrastructure. Before leveraging this new paradigm to its fullest extent in Ch. 4, similar benefits should be demonstrated in matrix elements at high-momenta.

### 3.2.3 Towards Matrix Elements at High Momentum

The investigation of phased distillation is extended here to the nucleon's isovector charges, in the forward direction, both for the nucleon at rest and in moving frames of increasing  $\hat{z}$ -oriented momenta. Our aim is to demonstrate consistency between charges computed in different forward frames, and likewise gauge whether currents that vanish by symmetry at rest can provide a complementary channel in motion to access a given charge; this will exercise distillation's ability to minimize pollution from unwanted form factors and excited-states. This is an especially nuanced venture even with the explicit three-momentum transfer  $\vec{q} = \vec{0}$ , as numerous form factors become relevant to a matrix element as the momentum frame is varied from zero. In this sense, some reported charges are instead a blend of form factors. We note these situations as they arise.

A second  $32^3 \times 64$  isotropic ensemble of  $2 \oplus 1$  dynamical flavors of Wilson-clover fermions is exploited for this study. The inverse coupling is once more  $\beta = 6.3$  and is otherwise identical to *a094m358*, but the pion mass has been reduced to 278 MeV. Table 3.4 summarizes this ensemble, abbreviated *a094m278*. The renormalization constants for each isovector current were previously computed in [78], allowing direct comparison with any continuum results. Three nucleon boosts of  $ap_z = \{0, 1, 4\} \times (2\pi/L)$  were considered. At the lower values of momentum [ $ap_z = \{0, 1\} \times (2\pi/L)$ ] we use distillation without phasing, while for  $ap_z = 4(2\pi/L)$  results both without and with  $\vec{\zeta}_2$ -phasing (3.24) are compared as a consistency check of the phased distillation method. These choices are motivated by calculation of the ground-state nucleon effective energies for  $0 \leq ap_z \leq 4(2\pi/L)$  using

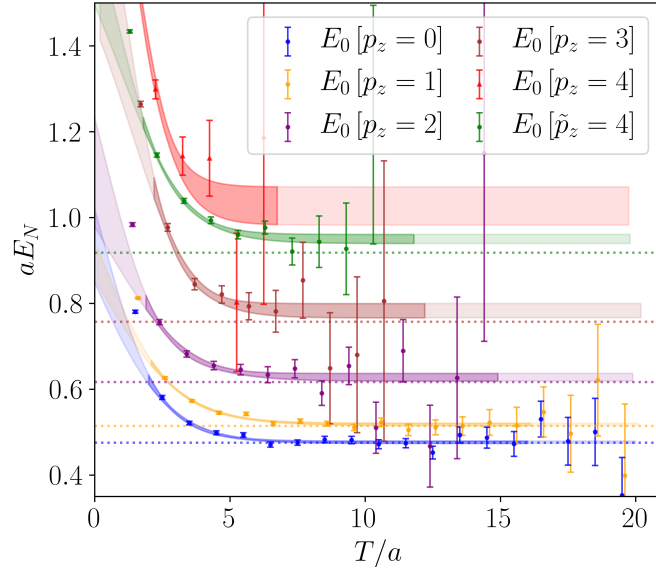


FIG. 3.10: Nucleon effective energies for the  $a094m278$  ensemble using a projected interpolator obtained from the  $\mathcal{B}_{\vec{p}=\vec{0}}^{[7]}$  and  $\mathcal{B}_{\vec{p}\neq\vec{0}}^{[16]}$  bases subduced into the relevant little group, together with continuum expectations (dashed), and 2-state fits (bands), where in each case the darker region denotes the time series included in the fit. No phasing was used to extract the ground-state nucleon energy for lattice momenta  $ap_z \in \mathbb{Z}_5$ , while  $ap_z = 4 (2\pi/L)$  was also determined with  $\zeta_2$ -phasing (3.24). In the case of  $ap_z = 4 (2\pi/L)$ , the results with and without phased eigenvectors are shown as the green and red points respectively, clearly demonstrating the need for phasing. Data shifted for legibility, and shown for signal-to-noise ratios greater than 1.35.

a variationally optimized interpolator from the  $\mathcal{B}_{\vec{p}=\vec{0}}^{[7]}$  (3.7) and  $\mathcal{B}_{\vec{p}\neq\vec{0}}^{[16]}$  (3.25) bases. From the effective energies and applied 2-state fits illustrated in Fig. 3.10, it is clear the variational method without phasing is insufficient to extract the ground-state nucleon energy for  $ap_z \geq 3 (2\pi/L)$ . The highest momentum  $ap_z = 4 (2\pi/L)$  was then chosen to compare with unphased distillation to underscore the compulsory use of phasing in order to obtain meaningful physics results in such highly-boosted frames.

The needed forward isovector matrix elements are again accessed by constructing two- and three-point correlation functions given by Eqns. 3.8 & 3.9. These correlation functions were computed on each of 259 configurations in the  $a094m278$  ensemble and averaged over four temporal origins. In anticipation of poorer statistics at this pion mass,

the three-point functions are computed for source-sink separations  $T/a \in \{6, 8, 10, 12, 14\}$  and currents inserted  $\forall \tau/a \in [0, T - 1]$ . The projector  $\Gamma^{\text{3pt}} = \frac{1}{2}(1 + \gamma_4)(1 + i\gamma_5\gamma_3)$  is used to select the forward-propagating, positive parity nucleon with spin aligned in the  $\hat{z}$ -direction. As was noted in Sec. 3.1.3 the isovector charges  $g_S^{u-d}$ ,  $g_V^{u-d}$ ,  $g_A^{u-d}$ ,  $g_T^{u-d}$  are only accessible at rest with the Dirac structures  $\mathbb{1}, \gamma_4, \gamma_3\gamma_5, \gamma_1\gamma_2$ . For the  $\Gamma^{\text{3pt}}$  projected nucleon in motion, a rich structure of Dirac channels opens, as codified in Tab. 3.1. The vector structure of the nucleon is now accessible with any component of the vector current  $\bar{\psi}\gamma_\mu\psi$ . The axial structure is probed with the time-like axial current  $\bar{\psi}\gamma_4\gamma_5\psi$  and  $\bar{\psi}\gamma_3\gamma_5\psi$ . The tensor structure of the nucleon remains accessible only with  $\bar{\psi}i\sigma_{12}\psi$ , which has important consequences for computing  $g_T^{u-d}$  in our moving frames.

Correlated simultaneous fits of the two- (3.16) and three-point (3.17) data are used once more to extract the matrix elements. The time series fit to are  $\tau_{\text{fit}}/a \in [2, T - 2]$  and  $T_{\text{fit}}/a \in [2, T_{\text{fit}}^{\text{max}}]$ . The maximal temporal range for which the principal correlator associated with each momenta has signal-to-noise ratios exceeding unity sets  $T_{\text{fit}}^{\text{max}}$ . The effective charge (3.18) was used in Sec. 3.1.4 to quantify the degree of excited-state contamination in each matrix element extraction. This quantity has the advantage of plateauing to the ground-state matrix element in the temporal regimes  $0 \ll \tau/a \ll T/a$ , but is only useful in so far as the two-point fit is well determined. As the high-momentum two-point data encountered on *a094m278* are generally not well-determined, especially without phasing, we instead illustrate the quality of our matrix element extractions by forming a direct ratio of the computed correlators:

$$R_\Gamma(T, \tau) = C_\Gamma^{\text{3pt}}(T, \tau) / C_\Gamma^{\text{2pt}}(T). \quad (3.26)$$

The following figures show  $R_\Gamma(T, \tau)$  together with the ratio of the fitted three- and two-point functions. Data excluded from fits are in gray, and each isolated  $g_\Gamma^{u-d}$  is present as

a black line with a gray error band. Lastly, errors are purely statistical and estimated via a simultaneous jackknife resampling.

## Results – Renormalized Scalar Matrix Elements

A Lorentz decomposition of the nucleon isovector scalar matrix element

$$\langle N | \bar{\psi} \frac{\tau^3}{2} \psi | N \rangle = (2M_N)^{-1} \bar{u}_N(p_f) G_S^{u-d}(q^2) u_N(p_i) \quad (3.27)$$

produces a single isovector scalar form factor  $G_S^{u-d}$ . Absent lattice systematics, the zero virtuality limit of  $G_S^{u-d}(0) \equiv g_S^{u-d}$  should be accessible and equivalent in each forward frame we consider. Figure 3.11 indicates this supposition is realized within statistical precision for the frames  $ap_z = \{0, 1\} \times (2\pi/L)$ . Both extractions are heavily weighted by the precise data for  $T/a \leq 10$ , consistent with the effective energies of Fig. 3.10. We highlight that  $g_S^{u-d} \simeq 0.953(22)$ , determined herein at rest, is nearly 75% more precise than a recent high statistics study on the same ensemble [78].

Without surprise, the role of excited-states is more pronounced for the case  $ap_z = 2\pi/L$ , as evidenced by the increased curvature of  $R_S(T, \tau)$  of a given  $T/a$  and the vertical spacing between each  $R_S(T, \tau)$ . These effects are described by  $\mathcal{B}$  and  $\mathcal{C}$  of Eq. 3.17, which the reader is reminded contain the excited  $\langle N' | S | N' \rangle$  and transition  $\langle N' | S | N \rangle$  matrix elements, respectively. Despite the increased contamination from excited-states, the consistent determinations of  $g_S^{u-d}$  in these frames is encouraging for the distillation/GEVP infrastructure.

Isolation of  $g_S^{u-d}$  in the unphased  $ap_z = 4(2\pi/L)$  frame is meaningless, but makes manifest the dramatic gains afforded by phased distillation (lower panel of Fig. 3.11). The dubiously low value of  $g_S^{u-d}$  in the  $ap_z = 4(2\pi/L)$  frame with  $\vec{\zeta}_2$ -phased eigenvectors may find an explanation in the mixing of the scalar current with  $D_\mu \{ \bar{\psi} \gamma_\mu \psi(x) e^{-iq \cdot x} \}$ .



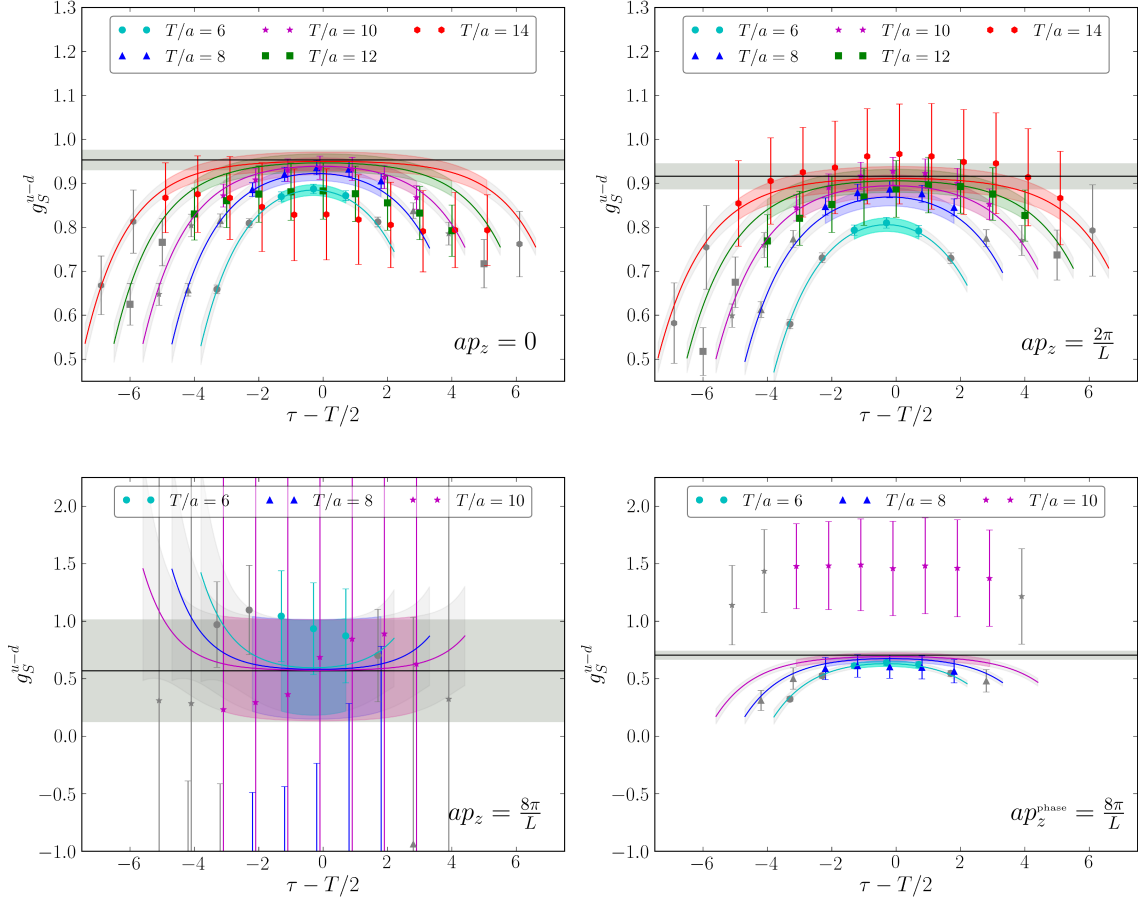


FIG. 3.11: Renormalized  $R_S(T, \tau)$  and  $g_S^{u-d}$  for momenta  $ap_z = 0$  (upper-left),  $ap_z = (2\pi/L)$  (upper-right),  $ap_z = 4 \times (2\pi/L)$  without phasing (lower-left), and  $ap_z = 4 \times (2\pi/L)$  with  $\zeta_2$ -phasing (lower-right). Variationally improved operators were used within each momentum channel, with  $T_{\text{fit}}^{\text{max}} = 16, 16, 7, 12$  respectively.

The derivative mixing receives contributions from two terms, one proportional to  $q_\mu$  and another to the four-divergence of the vector current. The explicit  $\vec{q} = 0$  projection here implies the former can contribute only for excited-to-ground transitions, which should be picked up by the three-point fit. The latter is a worrying possibility, as the vector current conservation is violated at  $\mathcal{O}(a)$  by the lattice regularization. Pending a follow-up study on a finer lattice ensemble, the apparent discrepancy of the phased  $g_S^{u-d}$  determination can conceivably be due to limited statistics and fluctuations of  $R_S(T, \tau)$  [85]. The possibility

of strong correlated fluctuations in the phased  $ap_z = 4(2\pi/L)$  frame can be seen in the lower-right panel of Fig. 3.11, where the  $R_S(T = 10, \tau)$  data deviate considerably from the data for smaller separations. The scalar charge computed in each frame and the correlated figure of merit is summarized in Tab. 3.5.

## Results – Renormalized Vector Matrix Elements

The conservation of the vector current in the continuum is a symmetry of the QCD action, and implies the time-like component between nucleon states simply yields the baryon number of the nucleon and its excitations. Our use of a local vector current, however, violates this conservation. A useful sanity check then for phased distillation is whether the renormalized  $g_{V_4}^{u-d}$  is unity and temporally invariant for all frames considered. As illustrated in Fig. 3.12(a) and the right column of Fig. 3.13, the conservation  $Z_V g_{V_4, \text{bare}}^{u-d} = 1 + \mathcal{O}(a^2)$  is observed for each nucleon boost, with the crucial exception of the  $ap_z = 4(2\pi/L)$  frame when standard distillation is used. Remarkably when  $\vec{\zeta}_2$ -phased eigenvectors are put to use  $g_{V_4}^{u-d}$  in the  $ap_z = 4(2\pi/L)$  frame is once more unity.

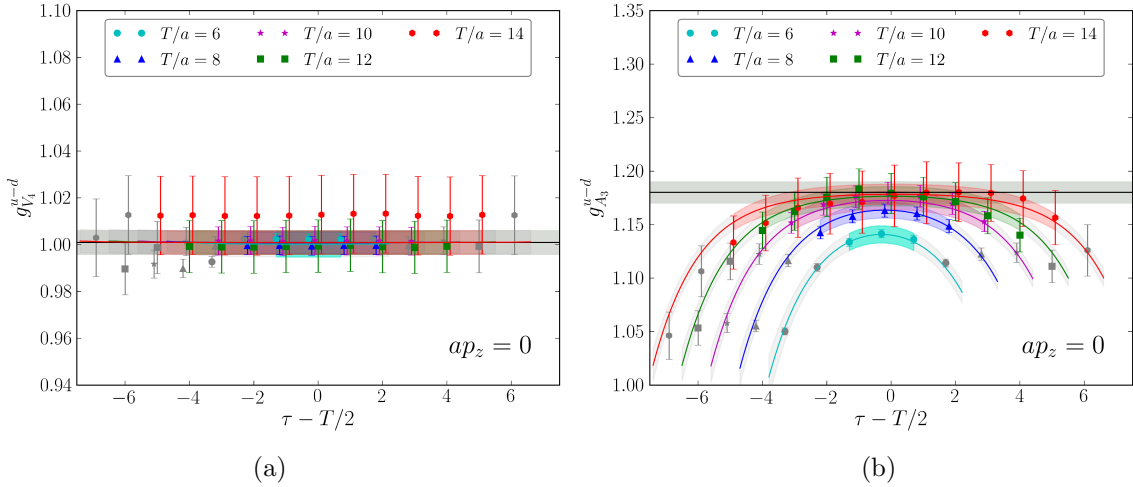


FIG. 3.12: Rest-frame renormalized  $R_{V_4}(T, \tau)$  and  $g_{V_4}^{u-d}$  (left), and  $R_{\gamma_3\gamma_5}(T, \tau)$  and  $g_{A_3}^{u-d}$  (right). A variationally improved operator was used in these determinations.

The spectral representation of a  $\Gamma^{3pt}$  projected nucleon boosted to non-zero  $\hat{z}$ -momenta stipulates  $\bar{\psi}\gamma_j\psi$  can likewise expose the nucleon's vector content. Even with  $\vec{q} = \vec{0}$  in this calculation, the spatial vector current between the ground-state nucleon and an excited  $J^P = \frac{1}{2}^+$  partner receives contributions from the Dirac and Pauli form factors according to

$$\langle N' | \bar{\psi}\gamma_j\psi | N \rangle = \bar{u}_{N'}(p_f) \left[ F_1^{u-d}(q^2) \left( \gamma_j - \frac{q_j}{q^2} \not{q} \right) + \frac{\sigma_{j\nu} q_\nu}{M_{N'} + M_N} F_2^{u-d}(q^2) \right] u_N(p_i).$$

In the ideal scenario that excited states are completely removed, the energy transfer  $q_4$  will vanish and the Dirac form factor can be accessed without impact from the Pauli form factor  $F_2^{u-d}$ . The upper-left of Fig. 3.13 clearly indicates the presence of excited-states. Thus without a dedicated study and removal of the Pauli contamination, discussion of the  $\bar{\psi}\gamma_j\psi$  results herein would be merely qualitative. For completeness  $R_{V_3}^{u-d}$  and the extracted ‘‘charge’’ are shown in the left column of Fig. 3.13. As before the unphased  $ap_z = 4(2\pi/L)$  is useless, while the  $\vec{\zeta}_2$ -phased equivalent returns a picture similar to the unphased  $ap_z = 2\pi/L$  frame up to an overall concavity flip. Repeat calculations are needed to assess the statistical stability of this behavior.

## Results – Renormalized Axial Matrix Elements

The renormalized  $R_{\gamma_3\gamma_5}(T, \tau)$  and  $g_{A_3}^{u-d}$  isolated at rest are shown in Fig. 3.12(b). Apart from  $T/a = 6, 8$ , broad consistency is observed in the renormalized ratios indicative of minimal impact from the first-excited state matrix element at these times. Even though the distillation/GEVP paradigm boasts control of excited-state effects, our value of  $g_{A_3}^{u-d} \simeq 1.18(1)$  differs from experiment by nearly 7%. Expansion of the axial current matrix

element into form factors

$$\langle N | A_\mu | N \rangle = \bar{u}_N(p_f) \left[ \gamma_\mu \gamma_5 G_A^{u-d}(q^2) - i \frac{q_\mu}{2M_N} \gamma_5 \tilde{G}_P^{u-d}(q^2) \right] u_N(p_i) \quad (3.28)$$

confirms for  $\vec{q} = \vec{0}$ , the induced pseudoscalar form factor cannot explain this tension with experiment. It has been shown that closely spaced excited states in the  $\gamma_3\gamma_5$  channel at rest, when incorrectly identified, can lead to effective excited states that violate the PCAC relation and thus skew  $g_{A_3}^{u-d}$  [86]. Although the ensemble *a094m278* is rather coarse and has unphysically heavy dynamical light quarks, numerous calculations (see introduction of e.g. [80]) exhibit weak dependence on the lattice spacing and pion mass. This alone warrants a detailed follow-up study; not to obtain exact agreement with experiment, but to elucidate what mechanism in the lattice regularization causes even distillation to experience this discrepancy.

The  $R_{\gamma_3\gamma_5}(T, \tau)$  data for  $ap_z = 2\pi/L$  shown in the upper-left panel of Fig. 3.14 do not exhibit consistent plateaux until  $T/a \simeq 12$  (1.13 fm). Even then it is difficult to claim a plateau has been reached, as the ratios appear to be rising at this level of statistics. Together with the decrease of  $g_{A_3}^{u-d}$  in the  $ap_z = 2\pi/L$  frame relative to the rest case (see Tab. 3.5) suggests excited-states are not under control.

In passing, we note the  $\vec{\zeta}_2$ -phased determination of  $g_{A_3}^{u-d}$  in the lower-left of Fig. 3.14 is inconsistent with the prior determinations, but agrees with experiment. The most logical explanation is this determination is largely unconstrained, as  $R_{\gamma_3\gamma_5}^{u-d}$  is well-determined for only two source-sink separations. An alternative viewpoint is the nucleon is Lorentz contracted at this momenta  $\sim 1.65$  GeV causing the lattice volume to appear larger. This perspective is supported by some of the few lattice studies which have isolated  $g_{A_3}^{u-d}$  to within  $\sim 1\%$  of experiment [71, 72] using lattices up to eight times the cubic volume as *a094m278*.

Discussion of the  $\gamma_4\gamma_5$  channel is reserved for [85], as the  $R_{\gamma_4\gamma_5}^{u-d}$  ratios in the  $ap_z = 2\pi/L$  frame are considerably less than their space-like counterparts. Since the induced pseudoscalar form factor of the nucleon is known to be large for small virtualities, even mild excited-to-ground transitions will skew  $\langle N|A_4|N\rangle$  from  $\langle N|A_3|N\rangle$  (see (3.28)). Hence a reported  $g_{A_4}^{u-d}$  “charge” in this context is instead a detailed interplay between the  $G_A^{u-d}$  and  $\tilde{G}_P^{u-d}$  form factors.

### Results – Renormalized Tensor Matrix Elements

The tensor current between nucleon states induces the following expansion in form factors

$$\langle N|T_{\mu\nu}|N\rangle = \bar{u}_N(p_f) \left[ i\sigma_{\mu\nu}A_{10}^{u-d}(q^2) + \frac{[\gamma_\mu, q_\nu]}{2M_N}B_{10}^{u-d}(q^2) + \frac{[P_\mu, q_\nu]}{2M_N^2}\tilde{A}_{10}^{u-d}(q^2) \right] u_N(p_i), \quad (3.29)$$

where  $P = p_f + p_i$  and  $T_{\mu\nu} = i\bar{\psi}\sigma_{\mu\nu}\frac{\tau^3}{2}\psi$ . At the outset of this subsection it was noted that the spectral representation of the  $\hat{z}$ -boosted and  $\Gamma^{3\text{pt}}$  projected nucleon three-point correlator is non-vanishing only for  $T_{12}$ . The Lorentz decomposition (3.29) shows  $A_{10}^{u-d}(q^2)$  is the only form factor that contributes in this channel, so long as  $\vec{q} = \vec{0}$ . As  $g_{T_{12}}^{u-d} \equiv A_{10}^{u-d}(0)$ , the tensor matrix element is perhaps the litmus test for a consistent charge determination with and without phasing.

It is indeed found in Fig. 3.15 that  $g_{T_{12}}^{u-d}$  is statistically consistent across the rest and boosted frames we have considered. The sub-percent error of our determination in the frames  $ap_z = \{0, 1\} \times (2\pi/L)$  marks a considerable reduction relative to a recent high-statistics estimate of  $g_{T_{12}}^{u-d} \simeq 0.973(36)$  on the same ensemble [78]. Unlike the other Dirac structures considered, even the unphased  $ap_z = 4(2\pi/L)$  determination is consistent. This is certainly attributable to the single relevant form factor  $A_{10}^{u-d}(q^2)$  for this channel. On the question of whether the  $\vec{\zeta}_2$ -phased effort was worth the computational cost, we highlight the

use of phasing has led to a  $\sim 12\%$  reduction in uncertainty of  $g_{T_{12}}^{u-d}$  in the  $ap_z = 4(2\pi/L)$  frame. The excellent mutual agreement of these determinations is presented in Tab. 3.5.

### 3.2.4 Closing Remarks

In this chapter we have seen that distillation, especially when coupled with the variational method (GEVP), leads to better determined hadronic energies and matrix elements, relative to conventional smearing kernels. Other than more faithfully representing the radial/orbital structures of a desired hadronic state, an extended basis of  $N$  operators enables principal correlators  $\lambda_{\mathbf{n}}(T, T_0)$  (Eq. 2.75) to be isolated from a correlator signal with leading excited-state contamination of  $\mathcal{O}(e^{-\Delta E'_{\mathbf{n}}T})$ , where  $\Delta E'_{\mathbf{n}} = E_{N+1} - E_{\mathbf{n}}$  and  $E_{N+1}$  the lowest energy not spanned by the operator basis [57].

$g_{\Gamma}$	$ap_z = 0$	$ap_z = 2\pi/L$	$ap_z = 8\pi/L$	$ap_z^{\text{phase}} = 8\pi/L$
$g_S^{u-d}$	0.953(22)	0.916(28)	0.57(44)	0.705(35)
$\chi_r^2$	0.920	1.010	12.482	2.037
$g_{V_4}^{u-d}$	1.001(5)	1.003(4)	0.84(9)	0.982(18)
$\chi_r^2$	0.901	1.767	12.317	1.902
$g_{V_3}^{u-d}$	–	0.915(15)	0.63(8)	0.995(23)
$\chi_r^2$	–	1.216	12.544	2.150
$g_{A_3}^{u-d}$	1.18(1)	1.145(9)	0.8(1)	1.275(29)
$\chi_r^2$	1.255	1.421	12.301	2.761
$g_{A_4}^{u-d}$	–	0.970(14)	0.71(9)	1.302(24)
$\chi_r^2$	–	1.148	12.353	1.990
$g_{T_{12}}^{u-d}$	1.049(7)	1.048(8)	0.99(14)	1.06(3)
$\chi_r^2$	1.267	1.064	12.603	1.999

TABLE 3.5: Renormalized isovector charges determined at rest and in boosted frames. The comparatively large correlated  $\chi^2/\text{d.o.f}$  for each  $g_{\Gamma}^{u-d}$  in the  $ap_z = 8\pi/L$  frame can be traced to the large fluctuations of the corresponding two-point correlator (cf. Fig. 3.10), which suffers from few measurements to constrain the needed energies and overlaps.

The benefits of distillation and the GEVP deteriorate as the hadron momentum is increased. We proposed and demonstrated the efficacy of a momentum-smeared version of distillation. With this approach coined *phased distillation*, the nucleon’s dispersion relation was correctly mapped in excess of 3 GeV and with high precision. A scan across nucleon boosts and repeat charge calculations in each was taken as the final proof-of-principle study of phased distillation. Emphasis was placed on charges being consistently determined across the considered boosts. For certain channels, namely  $\gamma_4$  and  $\gamma_1\gamma_2$ , this was realized beautifully even in a highly-boosted frame, so long as phased eigenvectors were utilized. The scalar and axial channels indeed quell any notion of a “free lunch” with distillation.

The phased distillation proof of principle study, and to a lesser extent the comparison of standard distillation with Jacobi smearing in Sec. 3.1, relied on a variational analysis of a matrix of two-point correlators. The same suppression of excited-states in two-point functions via a GEVP likewise applies to three-point functions. The charges computed within this chapter, however, were computed using the projected operator associated with each principal correlator determined from the relevant two-point function. This decision was based on reducing the overall cost of the three-point functions herein; were a GEVP applied, the Wick contraction costs would expand by a factor of  $N^2$ . It is important to note that our use of projected operators in the three-point functions is not incorrect, but rather suboptimal perhaps, as excited-states altered by the external current may be missed.

A useful follow-up study to consider would be to apply the GEVP to a matrix of three-point functions constructed from operators in a small basis and compare the matrix element extractions with those using the corresponding two-point projected operator - for instance, the  $\mathcal{B}_{\vec{p}=\vec{0}}^{[3]}$  basis and  $\hat{\mathcal{P}}_3$  projected operator. Such a future work would open the possibility to further explore the impact of excited-states by exploiting the so-called *summed* GEVP [87] method for matrix element extractions. In this case, a matrix of

three-point functions is again computed, but the insertion time slice is summed over. This leads to an even greater suppression of excited-states that scales as  $\mathcal{O}(Te^{-\Delta E_n T})$ . Such sophisticated strategies, although not explored in this body of work, remain essential tools to quantify and fit away stubborn excited states. Nevertheless these studies epitomize the potential benefits phased distillation can provide in high-impact calculations of the nucleon's collinear structures given in Chapters 4 and 6.



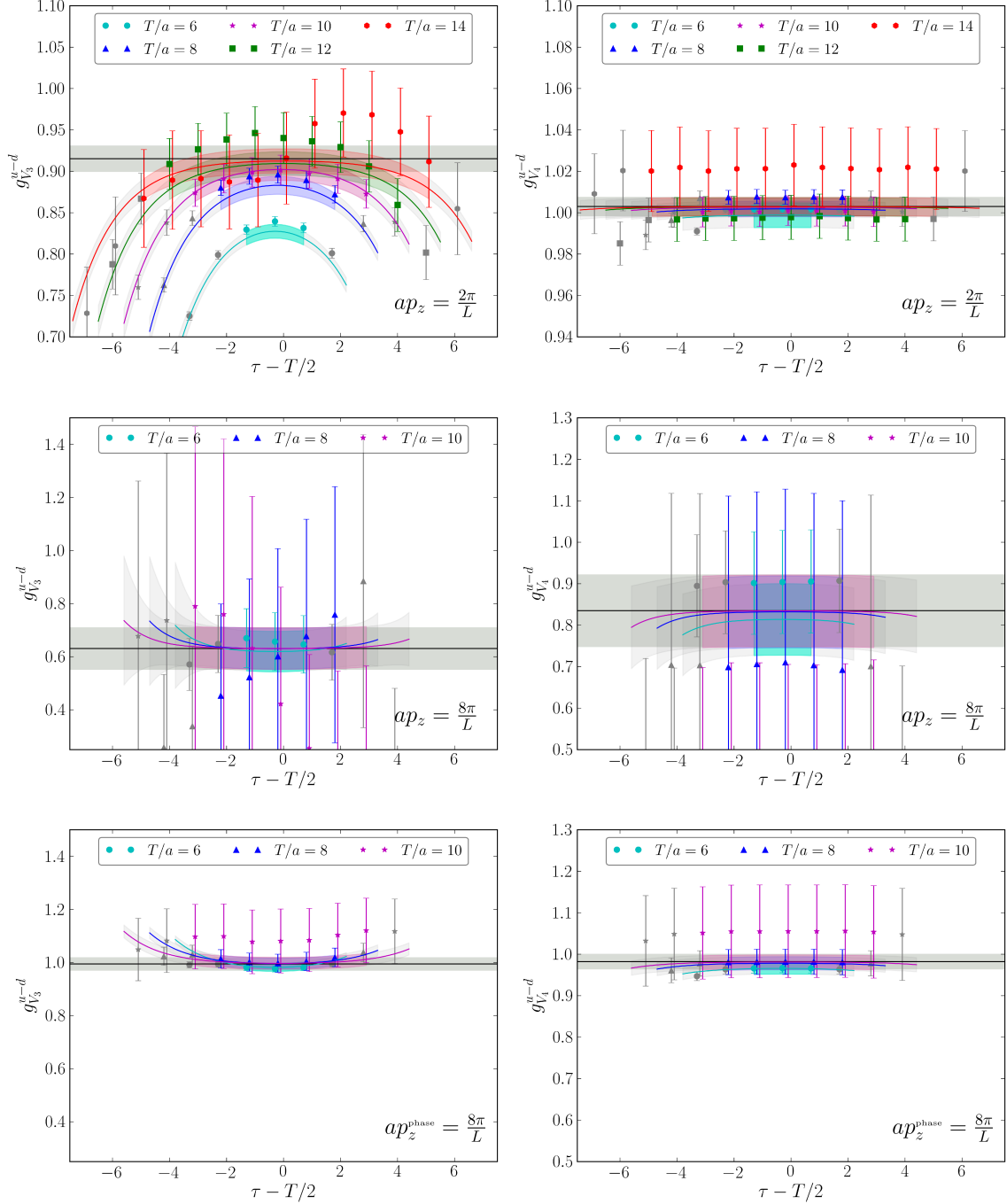


FIG. 3.13: Renormalized  $R_{V_\mu}(T, \tau)$  and  $g_{V_\mu}^{u-d}$  determined from  $\gamma_3$  (left panel) and  $\gamma_4$  (right panel) insertions. External nucleon momentum according to  $ap_z = (2\pi/L)$  (upper),  $ap_z = 4(2\pi/L)$  without phasing (middle),  $ap_z = 4(2\pi/L)$  with  $\vec{\zeta}_2$ -phasing (lower). Variationally improved operators were used within each momentum channel.

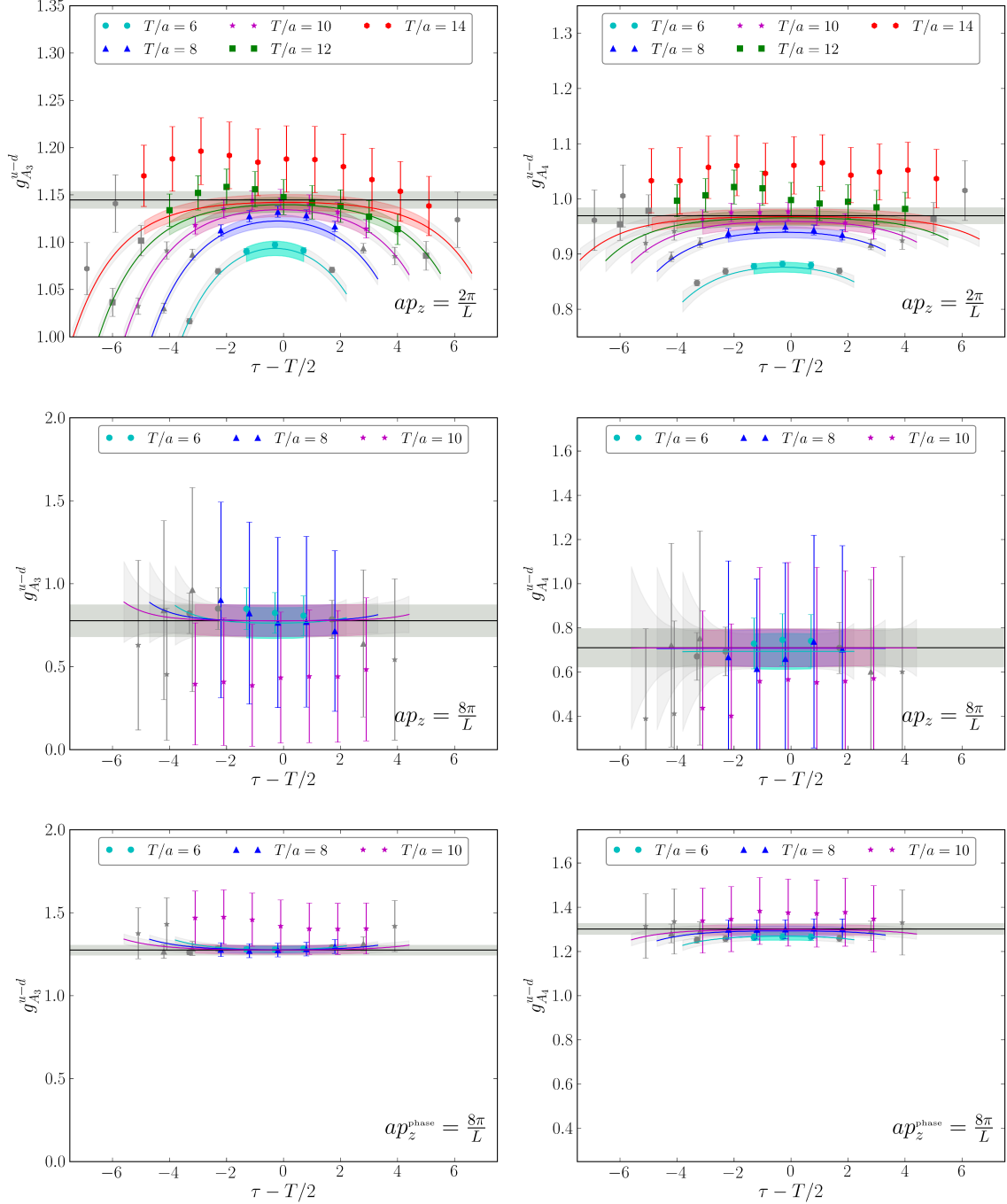


FIG. 3.14: Renormalized  $R_{A_\mu}(T, \tau)$  and  $g_{A_\mu}^{u-d}$  determined from  $\gamma_3\gamma_5$  (left panel) and  $\gamma_4\gamma_5$  (right panel) insertions. External nucleon momentum according to  $ap_z = (2\pi/L)$  (upper),  $ap_z = 4(2\pi/L)$  without phasing (middle),  $ap_z = 4(2\pi/L)$  with  $\zeta_2$ -phasing (lower). Variationally improved operators were used within each momentum channel.

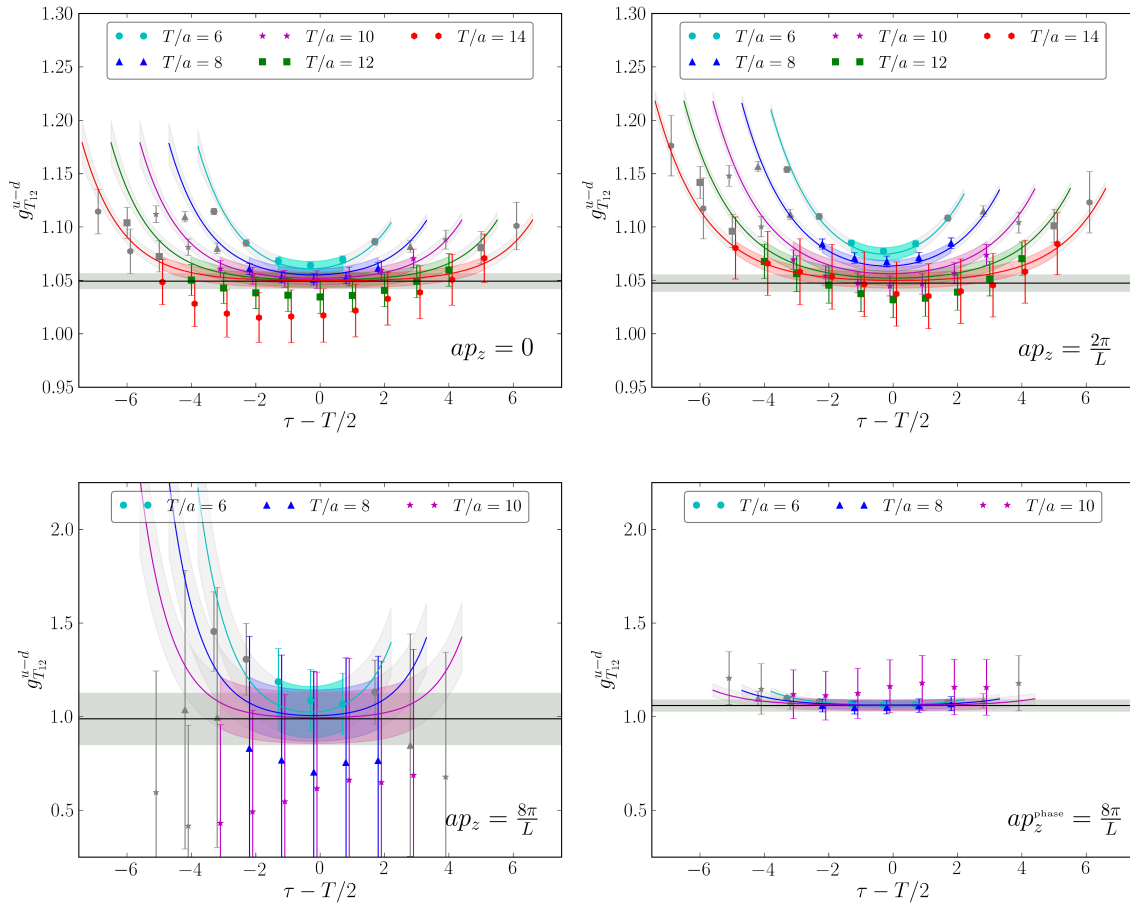


FIG. 3.15: Renormalized  $R_{T_{12}}(T, \tau)$  and  $g_{T_{12}}^{u-d}$  for momenta  $ap_z = 0$  (upper-left),  $ap_z = (2\pi/L)$  (upper-right),  $ap_z = 4(2\pi/L)$  without phasing (lower-left), and  $ap_z = 4(2\pi/L)$  with  $\vec{\zeta}_2$ -phasing (lower-right). Variationally improved operators were used within each momentum channel.

# CHAPTER 4

## Coordinate-Space Factorizable Matrix Elements

Parton Distribution Functions (PDFs), introduced in Sec. 2.1, are indispensable objects to describe the non-perturbative dynamics of hadrons. Recall that the operator definition of a flavor- $a$  PDF in some hadron  $h$  is given by the Fourier transform of a hadronic matrix element of a non-local parton bilinear along the  $z^-$  light-like direction

$$f_{a/h}^{[\Gamma]}(x, \mu^2) = \int \frac{dz^-}{4\pi} e^{-ixp^+ z^-} \langle h(p) | \bar{\psi}_a(z^-) \Gamma^+ \Phi_{\hat{z}^-}^{(f)}(\{z^-, 0\}) \psi_a(0) | h(p) \rangle_{\overline{\text{MS}}}, \quad (4.1)$$

where the polarization dependence has been omitted and the PDF is assumed to be renormalized at a scale  $\mu^2$  in  $\overline{\text{MS}}$ . The use of a Euclidean spacetime provides for the numerical solution to a number of key quantities in QCD. However this metric signature precludes a direct calculation of PDFs, and indeed of any operator constructed on the light-cone. There is no point in a Euclidean spacetime that is displaced from the origin and has a null invariant interval  $z^2 = 0$ . In effect, the natural arena in which to describe much of a hadron's structure collapses onto the proverbial "light-point".

Any lattice effort to access PDFs would appear fruitless. Consider nonetheless the following  $x$ -moments, or Mellin moments, of the PDFs

$$\begin{aligned} m_a^{(j)}(\mu^2) &= \frac{1}{s_a} \int_{-1}^1 \frac{dx}{x} x^j f_{a/h}^{[\Gamma]}(x, \mu^2) = \int_0^1 \frac{dx}{x} x^j \left[ f_{a/h}^{[\Gamma]}(x, \mu^2) + (-1)^j f_{\bar{a}/h}^{[\Gamma]}(x, \mu^2) \right] \\ &= \frac{1}{s_a} \int_{-\infty}^{\infty} dx x^{j-1} f_{a/h}^{[\Gamma]}(x, \mu^2), \end{aligned} \quad (4.2)$$

with a symmetry factor  $s_a = 1, 2$  for  $a = q, g$ . We note the symmetry factor  $s_g = 2$  corresponds to the identification of the anti-gluon with the gluon. The last line follows from PDFs being non-vanishing on the interval  $x \in [-1, 1]$ , and by CP-symmetry which relates parton/anti-parton PDFs according to  $f_{a/h}(-x) = -f_{\bar{a}/h}(x)$ . As the parton struck in an inclusive process is ejected along the  $z^-$ -direction, we have  $x = \frac{k^+}{p^+} = \frac{-i\partial^+}{p^+} = \frac{-i}{p^+} \frac{\partial}{\partial z^-}$ .

Substituting (4.1) into (4.2), we have

$$\begin{aligned} m_a^{(j)}(\mu^2) &= s_a^{-1} \int \frac{dz^-}{4\pi} \int_{-\infty}^{\infty} dx x^{j-1} e^{-ixp^+z^-} \langle h(p) | \bar{\psi}_a(z^-) \Gamma^+ \Phi_{\hat{z}^-}^{(f)}(\{z^-, 0\}) \psi_a(0) | h(p) \rangle \\ &= s_a^{-1} \int \frac{dz^-}{4\pi} \int_{-\infty}^{\infty} dx \left( \frac{-i}{p^+} \frac{\partial}{\partial z^-} \right)^{j-1} e^{-ixp^+z^-} \langle h(p) | \bar{\psi}_a(z^-) \Gamma^+ \Phi_{\hat{z}^-}^{(f)}(\{z^-, 0\}) \psi_a(0) | h(p) \rangle \\ &= s_a^{-1} \frac{(-i)^{j-1}}{2(p^+)^j} \int dz^- \delta(z^-) \left( \frac{\partial}{\partial z^-} \right)^{j-1} \langle h(p) | \bar{\psi}_a(z^-) \Gamma^+ \Phi_{\hat{z}^-}^{(f)}(\{z^-, 0\}) \psi_a(0) | h(p) \rangle. \end{aligned}$$

The  $z^-$  differential applies to the quark fields and the Wilson line, where the latter will bring down factors of  $igA_c^+ t_c$ :

$$\begin{aligned} m_a^{(j)}(\mu^2) &= \frac{s_a^{-1} (-i)^{j-1}}{2(p^+)^j} \langle h(p) | \bar{\psi}_a(0) \Gamma^+ [-\partial_- + igA_c^+ t_c]^{j-1} \psi_a(0) | h(p) \rangle \\ &= \frac{s_a^{-1}}{2(p^+)^j} \langle h(p) | \bar{\psi}_a(0) \Gamma^+ (iD^+)^{j-1} \psi_a(0) | h(p) \rangle \end{aligned} \quad (4.3)$$

$$2(p^+)^j m_a^{(j)}(\mu^2) = s_a^{-1} \langle h(p) | \bar{\psi}_a \Gamma^+ iD^+ \dots iD^+ \psi_a | h(p) \rangle. \quad (4.4)$$

This result shows that the Mellin moments of the PDFs are proportional to matrix elements of local operators. More generally, the local operators  $\mathcal{O}_a^{\mu_1 \dots \mu_j} = \bar{\psi}_a \Gamma^{\mu_1} iD^{\mu_2} \dots iD^{\mu_j} \psi_a$  with  $j$  Lorentz indices is reducible under the Lorentz group, and hence can be expressed as a sum of objects that transform irreducibly. As we will now find, each irreducible component is associated with a distinct energy dependence and hence rescaling law under renormalization.

Let us digress for a moment and consider application of the Operator Product Expansion (OPE) [88] to the two-current matrix element (2.25) defining the DIS hadronic tensor in Sec. 2.1:

$$\mathcal{J}^\mu(z) \mathcal{J}^\nu(0) = \sum_a \sum_j C_a(z^2, \mu^2) z_{\mu_1} \dots z_{\mu_j} \mathcal{O}_a^{\mu\nu\mu_1 \dots \mu_j}(\mu^2). \quad (4.5)$$

The OPE expresses this non-local operator product at a renormalization scale  $\mu^2$  as an infinite sum of local operators  $\mathcal{O}_a^{\mu\nu\mu_1 \dots \mu_j}(\mu^2)$  and perturbatively calculable Wilson coefficients  $C_a(z^2, \mu^2)$ . For large virtualities of the incoming virtual gauge boson, the relative contribution of each operator  $\mathcal{O}_a^{\mu\nu\mu_1 \dots \mu_j}(\mu^2)$  to the DIS amplitude scales as  $(Q^{-2})^{d-s}$ , where  $d$  and  $s$  are respectively the energy dimension and spin of the operator; this defines (geometric) twist  $t \equiv d - s$ , and the different irreps of the Lorentz group are labeled by the operator spin. The leading contributions are then given by generic twist-2 operators of the form

$$\mathcal{O}_a^{\mu_1 \dots \mu_j} = \bar{\psi}_a \Gamma^{\{\mu_1} iD^{\mu_2} \dots iD^{\mu_j\}} \psi_a - \text{traces}, \quad (4.6)$$

where braces denote index symmetrization and pairwise traces are removed; the trace terms involve factors of the metric tensor  $g^{\mu_i \mu_j}$  and higher dimension operators with fewer Dirac indices (i.e. higher-twist). Note, when substituted into (4.5) the higher-twist terms are proportional to  $z^2$  and vanish for the light-like separations defining the PDF.

The OPE establishes that PDFs can be alternatively defined as distributions whose Mellin moments are matrix elements of the local twist-2 operators (4.6). This connection is ideally suited for calculation in lattice QCD, and indeed has historically been the method PDFs and even GPDs have been studied from lattice QCD. The breaking of the continuum Euclidean space-time  $O(4)$  to the discrete hypercubic group  $H(4) \leq O(4)$  induces mixing between twist-2 and higher-twist operators. This mixing diverges with the lattice spacing - consequently the continuum limit is not well-defined. Furthermore, operators of increasing twist are sensitive to increased gauge noise. The net effect is an insufficient number of local operators (Mellin moments) to reliably reconstruct a PDF [89].

## 4.1 Quasi-Distributions

Attempts to circumvent the preclusion of light-like quantities by the Euclidean space-time of lattice QCD date to early efforts to compute the hadronic tensor [90, 91], forward Compton amplitude [89], and distribution amplitudes (e.g. [92]) from suitably constructed Euclidean correlation functions. Although the parton model can readily interpret the hadronic tensor and forward Compton amplitude in terms of PDFs, the ability to resolve PDFs from lattice QCD was revolutionized with Xiangdong Ji's introduction of the quasi-PDF [93].

Supposing a hadron is moving with momentum  $p^\mu = (p^0, \mathbf{0}_\perp, p^3)$ , Ji's reasoning begins with the realization that (4.1) is boost invariant along the  $\hat{z}$ -direction. Furthermore, from Eq. 4.4 it follows that hadronic matrix elements of a generic local twist-2 operator (4.6) are given by

$$\langle h(p) | \mathcal{O}_a^{\mu_1 \dots \mu_j}(\mu^2) | h(p) \rangle = 2m_a^{(j)}(\mu^2) (p^{\mu_1} \dots p^{\mu_j} - \text{traces}), \quad (4.7)$$

with  $m_a^{(j)}(\mu^2)$  the scale-dependent reduced matrix elements. Selecting the components  $\mathcal{O}_a^{+\cdots+}$ , which corresponds to the  $z^-$  separated parton fields, the traces vanish due to their nominal proportionality to  $g^{++}$ , recovering the time-dependent correlation defining the PDF (4.4). Removing the time-dependence from (4.7), and thus creating a setup amenable to lattice QCD, Ji considers different components of the local twist-2 operator:

$$\mathcal{O}_a^{\mu_1 3 \cdots 3} = \bar{\psi}_a \Gamma^{\{\mu_1 i D^3 \cdots i D^3\}} \psi_a - \text{traces}. \quad (4.8)$$

Hadronic matrix elements of  $\mathcal{O}_a^{\mu_1 3 \cdots 3}$  are

$$\begin{aligned} \langle h(p) | \mathcal{O}_a^{\mu_1 3 \cdots 3}(\mu^2) | h(p) \rangle &= 2m_a^{(j)}(\mu^2) p^{\mu_1} (p^3)^{j-1} - \langle h(p) | \text{traces} | h(p) \rangle \\ &= 2m_a^{(j)}(\mu^2) p^{\mu_1} (p^3)^{j-1} + g^{\mu_1 3} \mathcal{O}([p^3]^{j-2}) + g^{33} \mathcal{O}([p^3]^{j-2}) \\ &= 2m_a^{(j)}(\mu^2) p^{\mu_1} (p^3)^{j-1} + \mathcal{O}\left(\frac{\Lambda_{\text{QCD}}^2}{p_3^2}, \frac{M_h^2}{p_3^2}\right), \end{aligned}$$

where Lorentz invariance demands the matrix elements of the trace terms appearing in  $\mathcal{O}_a^{\mu_1 3 \cdots 3}$  scale at most as  $(p^3)^{j-2}$  with metric tensor components  $\{g^{\mu_1 3}, g^{33}\}$ . This result implies a finite-momentum hadronic matrix element of a space-like separated parton bilinear

$$\langle h(p^3) | \underbrace{\bar{\psi}_a(z_3) \gamma^3 \Phi_{z_3}^{(f)}(\{z_3, 0\}) \psi_a(0)}_{\mathcal{O}_{\text{WL}}^{[\gamma^3]}(z_3)} | h(p^3) \rangle, \quad (4.9)$$

yields the light-cone PDF up to power-suppressed corrections in the inverse square of the hadron momentum. The corrections  $\mathcal{O}(\Lambda_{\text{QCD}}^2/p_3^2)$  are genuine higher-twist corrections, while the  $\mathcal{O}(M_h^2/p_3^2)$  corrections are so-called target mass effects.

The Fourier transform of the finite-boosted space-like matrix element (4.9), now cast



in Euclidean space, defines the unpolarized quasi-PDF<sup>1</sup>

$$\tilde{f}_{a/h}(\tilde{x}, p_3, \tilde{\mu}^2) = \int \frac{dz_3}{4\pi} e^{-i\tilde{x}p_3z_3} \langle h(p_3) | \bar{\psi}_a(z_3) \gamma_3 \Phi_{z_3}^{(f)}(\{z_3, 0\}) \psi_a(0) | h(p_3) \rangle. \quad (4.10)$$

Ji notes in Ref. [95] that the differences between the light-cone PDF and the quasi-PDF vanish for infinite boost, namely  $p_3 \rightarrow \infty$ . Furthermore, the approach to large- $p_3$  only modifies the UV structure of the quasi-PDF, and its IR structure is the same as the PDF. The Large Momentum Effective Theory (LaMET) [95] formalizes these observations by computing and subsequently removing these differences in perturbation theory:<sup>2</sup>

$$\tilde{f}_{a/h}(\tilde{x}, p_3, \tilde{\mu}^2) = \int_{-1}^1 \frac{dx}{|x|} Z\left(\frac{\tilde{x}}{x}, \frac{\mu}{p_3}, \frac{\Lambda}{p_3}\right) f_{a/h}(x, \mu^2) + \mathcal{O}\left(\frac{\Lambda_{\text{QCD}}^2}{p_3^2}, \frac{M_h^2}{p_3^2}\right), \quad (4.11)$$

where  $Z\left(\frac{\tilde{x}}{x}, \frac{\mu}{p_3}, \frac{\Lambda}{p_3}\right)$  is a perturbative coefficient function that matches the renormalized quasi-PDF to the light-cone PDF, and  $\Lambda$  is an ultraviolet cutoff such as the inverse lattice spacing  $a^{-1}$ . The matrix element (4.9) is gauge invariant and space-like, both of which are amenable to lattice QCD and guarantee the same result when computed in Euclidean and Minkowski spacetimes [96]. A complicating factor is the integration over the length of the Wilson line; this leaves the Fourier conjugate  $\tilde{x}p_z$  as the hard scale of the quasi-PDF. Quasi-PDFs in this sense describe the distribution of a parton's  $z_3$ -component of the parent hadron's longitudinal momentum  $p_z$ :  $\tilde{x} = k_3/p_3$ , contrary to the familiar light-cone PDFs. It is clear quasi-PDFs are not boost-invariant, freeing the “quasi momentum fraction” to assume any value  $\tilde{x} = k_3/p_3 \in (-\infty, \infty)$  and hence violate the conservation of total parton momentum. A series of recent quasi-PDF results are shown in Fig. 4.1 which illustrate the

---

<sup>1</sup>Contemporary quasi-distribution calculations now make use of the temporal vector current  $\gamma_4$ . It has been shown in lattice perturbation theory that the vector current with index collinear with the Wilson line will mix with the scalar current, a twist-3 operator, under renormalization [94].

<sup>2</sup>LaMET is actually not an effective field theory in the strictest sense, as sub-leading powers of the hadron momentum are neglected in the large momentum expansion.

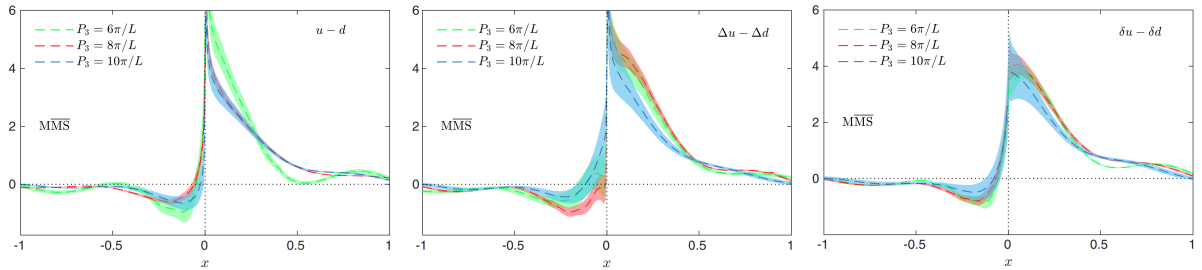


FIG. 4.1: Recent isovector unpolarized (left), helicity (center), and transversity (right) PDFs obtained by the ETM collaboration using the quasi-distribution formalism [97]. The momentum fraction  $x$ -dependence is obtained from the LaMET procedure. A strong dependence on the hadron's momentum is evident.

strong momentum dependence of quasi-PDFs.

A considerable challenge of using the Wilson line operator  $\hat{\mathcal{O}}_{\text{WL}}^{[\gamma^\mu]}(z_3)$  is the appearance of additional ultraviolet (UV) divergences for space-like separations [98]. These divergences manifest as power divergences in perturbation theory, and renormalize to all orders with the factor  $Z_{\text{link}}(z_3, a) \simeq e^{-A|z_3|/a}$ , with  $a$  a UV regulator. These unwanted UV divergences are also known to be independent of the invariant  $p \cdot z = p_z z_3$  [99]. Prior to taking the continuum limit of  $\hat{\mathcal{O}}_{\text{WL}}^{[\gamma^\mu]}(z_3)$ , these divergences must be regularized and removed. Recently, and to great benefit in Sec. 4.2.2,  $\mathcal{O}_{\text{WL}}^{[\gamma^\mu]}(z_3)$  was shown to renormalize multiplicatively [100, 101, 102].

## 4.2 Lattice Cross Sections

A comprehensive and generic framework for the extraction of PDFs from Lattice QCD involves the construction of hadronic matrix elements of time-local and space-like separated operators. These matrix elements are generically written as the time-ordered product of a collection of partonic field operators featuring a purely space-like extent within some hadronic state:

$$M_n(p \cdot z, z^2) = \langle h(p) | \hat{\mathcal{T}}\{\mathcal{O}_n(z)\} | h(p) \rangle, \quad (4.12)$$

where  $n$  classifies distinct operator constructions,  $\hat{T}$  a time-ordered product, and the renormalization scale  $\mu^2$  has been suppressed. A broad class of operators fall into this framework, and under certain situations factorize into the convolution of perturbative coefficient functions and PDFs up to power-suppressed corrections. This paradigm is inspired by the QCD factorization of (semi-)inclusive cross sections to extract PDFs and other distributions. These matrix elements have hence been deemed *Lattice Cross Sections* [103, 104] (LCSs), as they too may be analyzed in a global framework to provide a best estimate of the universal PDFs from lattice QCD.

The astute reader will note (4.12) was precluded by demanding time-locality. The time-ordering operator in (4.12) is included to ensure all relevant field orderings are considered for the composite operator  $\mathcal{O}_n$ , after which the temporal separation is taken to zero. Time-locality is an essential ingredient of any *good* LCS, as a matrix element computed in Euclidean space will then equal its Minkowski counterpart [96]. To have any physical relevance, any good LCS must also possess a well-defined continuum limit and share the same factorizable logarithmic collinear divergences as PDFs.

One choice for the non-local operator  $\mathcal{O}_n(z)$  is the Wilson line operator  $\mathcal{O}_{\text{WL}}^{\circ[\gamma^\mu]}(z_3)$  used to define the quasi-PDF. Its utility as an operator sensitive to the light-cone structure of hadrons in a manner distinct from quasi-distributions will be further developed in the context of pseudo-distributions in Sec. 4.2.2.

### 4.2.1 Two-Current Correlations

A broader class of operators with factorizable matrix elements (4.12) are pairs of local gauge-invariant currents  $\{\mathcal{J}_1, \mathcal{J}_2\}$  with a space-like separation  $z$ :

$$\mathcal{O}_{\mathcal{J}_1, \mathcal{J}_2}^{\{\mu\nu\}}(z) = z^{d_{\mathcal{J}_1} + d_{\mathcal{J}_2} - 2} Z_{\mathcal{J}_1} Z_{\mathcal{J}_2} \mathcal{J}_1(z) \mathcal{J}_2(0), \quad (4.13)$$

with  $Z_{\mathcal{J}_k}$  and  $d_{\mathcal{J}_k}$  respectively the renormalization constant and energy dimension associated with the currents  $\mathcal{J}_k$ . The simplest choice of operators are those with no Dirac indices or that are fully contracted, including

$$\mathcal{O}_S(z) = z^4 Z_S^2 \{\bar{\psi}\psi\}(z) \{\bar{\psi}\psi\}(0) \quad (4.14)$$

$$\mathcal{O}_V(z) = z^2 Z_V^2 \{\bar{\psi}\not{z}\psi\}(z) \{\bar{\psi}\not{z}\psi\}(0), \quad \mathcal{O}_{V'}(z) = z^2 Z_{V'}^2 \{\bar{\psi}\not{z}\Psi\}(z) \{\bar{\Psi}\not{z}\psi\}(0) \quad (4.15)$$

$$\mathcal{O}_{\tilde{V}}(z) = -\frac{z^4}{2} Z_V^2 \{\bar{\psi}\gamma_\mu\psi\}(z) \{\bar{\psi}\gamma^\mu\psi\}(0) \quad (4.16)$$

$$\mathcal{O}_{\tilde{V}\tilde{A}}(z) = -\frac{z^4}{2} Z_V Z_A \{\bar{\psi}\gamma_\mu\psi\}(z) \{\bar{\psi}\gamma^\mu\gamma^5\psi\}(0) \quad (4.17)$$

$$\mathcal{O}_{VA}(z) = z^4 Z_V Z_A \{\bar{\psi}\gamma^\mu\psi\}(z) \{\bar{\psi}\gamma^\nu\gamma^5\psi\}(0). \quad (4.18)$$

The choice of currents is quite general, even allowing for flavor-changing currents such as  $\mathcal{O}_{V'}(z)$  above. More generic operators featuring one or several open Dirac indices are also possible. For such Lorentz covariant operators, it is the invariant amplitudes, or pseudo-structure functions,  $T_i(\nu, z^2)$  dependent on the space-like interval  $z^2$  and Ioffe-time  $\nu = p \cdot z$  [105, 106]<sup>3</sup> that factorize into the PDFs. The proof of this factorization is essential for a large remainder of this body of work. The logical steps of the proof [103, 104] are closely followed here.

Consider the matrix element of a non-local scalar operator (4.12). Analogous to the factorization of an inclusive DIS cross section, take the current separation  $z$  to define the hard scale and suppose  $z^2$  is small but non-vanishing. In this short-distance regime, apply the operator product expansion (OPE) to  $\mathcal{O}_n(z)$ :

$$M_n(\nu, z^2) = \sum_{j=0} \sum_a C_n^{(j,a)}(z^2 \mu^2, \alpha_s) z^{\mu_1} \dots z^{\mu_j} \langle p | \mathcal{O}_{\mu_1 \dots \mu_j}^{(j,a)}(\mu^2) | p \rangle \quad (4.19)$$

---

<sup>3</sup>The Ioffe-time may be thought of as the amount of time, in units of the inverse hadron mass, a DIS probe interacts with a target hadron.

where  $C_n^{(j,a)}(z^2\mu^2, \alpha_s)$  are Wilson coefficients dependent on the renormalization scale and invariant interval between the currents. The operators  $\mathcal{O}_{\mu_1 \dots \mu_j}^{(j,a)}(\mu^2)$  are traceless, local, and symmetric operators of spin- $j$ , with  $a$  delineating operators of the same  $j$  value. The matrix element of  $\mathcal{O}_{\mu_1 \dots \mu_j}^{(j,a)}(\mu^2)$  has the Lorentz decomposition

$$\langle p | \mathcal{O}_{\mu_1 \dots \mu_j}^{(j,a)}(\mu^2) | p \rangle = 2\tilde{m}_a^{(j)}(\mu^2) (p_{\mu_1} \dots p_{\mu_j} - \text{traces}) \equiv 2\tilde{m}_a^{(j)}(\mu^2) \Pi_{\mu_1 \dots \mu_j}, \quad (4.20)$$

where the reduced matrix element  $\tilde{m}_a^{(j)}(\mu^2)$  absorbs the scale dependence and  $\forall j$  is otherwise a Lorentz scalar with a  $j$ -dependent mass dimension. The traces denote terms proportional to at least one factor of the metric tensor  $g_{\mu_i \mu_j}$ . Note  $\Pi_{\mu_1 \dots \mu_j}$  is the unique traceless and symmetric rank- $j$  tensor that can be constructed from the hadron four-momentum [107]. Substituting (4.20) into (4.19)

$$\begin{aligned} M_n(\nu, z^2) &= 2 \sum_{j=0} \sum_a C_n^{(j,a)}(z^2\mu^2, \alpha_s) z^{\mu_1} \dots z^{\mu_j} \tilde{m}_a^{(j)}(\mu^2) (p_{\mu_1} \dots p_{\mu_j} - \text{traces}) \\ &= 2 \sum_{j=0} \sum_a C_n^{(j,a)}(z^2\mu^2, \alpha_s) \tilde{m}_a^{(j)}(\mu^2) \sum_{k=0}^{\lfloor j/2 \rfloor} \binom{j-k}{j} \left(-\frac{z^2 p^2}{4}\right)^k \nu^{j-2k}, \end{aligned} \quad (4.21)$$

where the  $\mathcal{O}(z^2 p^2)$  terms are induced by contractions of the four-vectors  $z^{\mu_k}$  with the trace terms. The leading contribution to  $M_n(\nu, z^2)$  comes from the reduced matrix element  $\tilde{m}_a^{(j)}(\mu^2)$  with the smallest mass dimension. These are precisely the local twist-2 operators which we found in Eq. 4.4 are given in terms of the Mellin moments of the PDF. The higher-dimensional contributions then scale as  $\mathcal{O}(z^2 \Lambda_{\text{QCD}}^2)$ . With our prescription of small  $z^2$  these higher-dimensional terms are power-suppressed and can be neglected to leading

approximation. We are then left with

$$M_n(\nu, z^2) = \sum_a \int_{-1}^1 \frac{dx}{x} f_{a/h}(x, \mu^2) \sum_{j=1} \frac{2}{s_a} C_a^{(j,a)}(z^2 \mu^2, \alpha_s) x^j \sum_{k=0}^{\lfloor j/2 \rfloor} \binom{j-k}{j} \left( -\frac{z^2 p^2}{4} \right)^k \nu^{j-2k}. \quad (4.22)$$

Note the spin sum has shifted to start at  $j = 1$ , as no twist-2 scalar operator can be constructed with QCD fields - the scalar operator in QCD is of twist-3, and is thus a sub-leading effect to the twist-2 component. This factorization establishes a connection between the Ioffe-time dependence of a lattice cross section and the Mellin moments of the PDF via the matching kernel

$$K_n^a = \sum_{j=1} \frac{2}{s_a} C_n^{(j,a)}(z^2 \mu^2, \alpha_s) (x\nu)^j. \quad (4.23)$$

As the OPE is valid only in the regime wherein all components of  $z^{\mu k}$  uniformly go to zero but with all other variables fixed, the Taylor series in (4.22) then implies this factorization is valid only for  $|z^2 p^2| \ll 1$  and  $|\nu| \ll 1$ .

The factorization (4.22) shows that the LCS Ioffe-time behavior is inextricably linked with the parton momentum fraction. To be of any practical use, the validity of this factorization must exist for finite  $\nu$  as well. The OPE ensures  $M_n(\nu, z^2)$  is analytic in a small neighborhood about  $\nu = 0$ , represented by the Taylor expansion (4.22). This same expansion shows analyticity in  $z^2 p^2$ . By fixing the operator separation  $z$  to be small, the Ioffe-time is increased by boosting the hadronic state to higher momenta  $p$ . No additional perturbative divergences, except for the point at infinity, can be produced, establishing the factorization defined in (4.22) remains valid  $\forall \{\nu, z^2 p^2\}$  that are finite. The final LCS factorization relationship is then

$$M_n(\nu, z^2) = \sum_a \int_{-1}^1 \frac{dx}{x} f_{a/h}(x, \mu^2) K_n^a(x\nu, z^2 \mu^2, x^2 p^2) + \mathcal{O}(z^2 \Lambda_{\text{QCD}}^2, z^2 p^2), \quad (4.24)$$

where  $a$  runs over all parton flavors.

Unlike the hard momentum scale that enables factorization of an inclusive cross section, a large hadron momentum in an LCS calculation does not guarantee the validity of the OPE of Eq. 4.12. Any contributions from large separations  $z$  will invalidate the factorized relationship regardless of whether two currents or the quasi-/pseudo-distribution operator  $\mathcal{O}_{\text{WL}}^{[\gamma^\mu]}(z_3)$  are used. The hard scale analog in an LCS calculation is the invariant interval  $z^2$ , which is a valid parameter to expand in perturbatively so long as the separation is much smaller than the inverse square of the typical hadronic scale, namely  $z^2 \Lambda_{\text{QCD}}^2 \ll 1$ .

Theoretically the coordinate space factorization has several advantages over similar matching schemes formulated in momentum space. To understand these advantages, consider the momentum space representation of  $M_n(\nu, z^2)$

$$\widetilde{M}_n(\tilde{\nu}, q^2) = \int d^4z z^{-4} e^{iq \cdot z} M_n(\nu, z^2), \quad (4.25)$$

with  $\tilde{\nu} \equiv \frac{2p \cdot q}{-q^2} = 1/x_B$  and  $x_B$  the Bjorken variable from DIS (Eq. 2.21). The first, and perhaps most obvious, realization is that although  $q$  is related to  $z$  via the Fourier transform, it is not a one-to-one mapping. Regions of  $\widetilde{M}_n(\tilde{\nu}, q^2)$  with small and large values of  $q$  receive contributions from its Fourier conjugate  $z$  both when it is large and small. It is these contributions from large separations that spoils the coordinate space factorization we have demonstrated. The analytic behavior of  $M_n(\nu, z^2)$  is likewise altered, and in a highly non-trivial manner, by the Fourier transform. This is seen by recognizing  $\widetilde{M}_n(\tilde{\nu}, q^2)$  is much the same as the Compton amplitude, which through the optical theorem is related to the hadronic tensor. For sufficiently deep inelastic scattering, real propagating final state particles of arbitrary momentum are created. This in turn leads to a non-analytic cut in the  $\widetilde{M}_n(\tilde{\nu}, q^2)$  amplitude. The origin of this cut was explored in Ref. [104] and found to be produced by the large- $z$  integration regime of (4.25). In other words, the kinematic

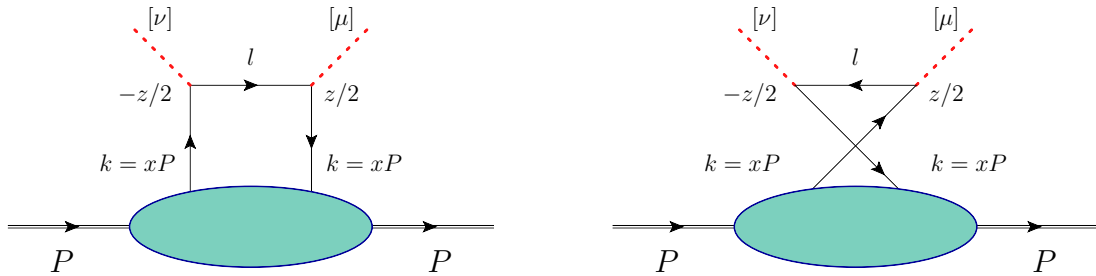


FIG. 4.2: Lowest order Feynman diagrams contributing to the quark partonic matching coefficient. Each current is spatially separated by  $z$ . The current insertions are denoted as red dashed lines with a potential open Dirac index indicated.

demand  $|q^2| \gg \Lambda_{\text{QCD}}^2$  employed in the factorization of experimental inclusive cross sections is insufficient to exclude large- $z$  contributions to  $\widetilde{M}_n(\widetilde{\nu}, q^2)$  for  $\widetilde{\nu}^2 > 1$ . This separation of  $z^2$  scales should be compared with the quasi-distribution formalism, which mixes different invariant scales.

### Tree-Level Perturbative Matching Kernel

The perturbative coefficient functions  $K_n^a(x\nu, z^2\mu^2, x^2p^2)$  are determined by projecting the factorized relationship (4.24) onto an asymptotic parton with momentum  $k$  and on-shell condition  $k^2 = 0$ . This strategy clarifies the matching coefficients are process-dependent, but are independent of the hadronic state. Each side is then expanded as a power series in the strong coupling  $\alpha_s$ . At tree-level  $\mathcal{O}(\alpha_s^0)$  we have two diagrams shown in Fig. 4.2 to consider. Supposing one is interested in measuring a quark PDF, the factorization relationship projected onto an asymptotic quark reads

$$M_n^{q(0)}(\nu, z^2) = \sum_{a=q, \bar{q}, g} \int_0^1 \frac{dx}{x} f_{a/h}^{q(0)}(x, \mu^2) K_n^a(x\nu, z^2\mu^2, x^2p^2) + \mathcal{O}(z^2\Lambda_{\text{QCD}}^2, z^2p^2). \quad (4.26)$$



As the quark distribution of an on-shell quark at tree-level is simply a delta function with no scale dependence  $f_{a/h}^{q(0)}(x, \mu^2) = \delta(1-x)\delta^{qa}$ , it trivially follows

$$M_n^{q(0)}(\nu, z^2) = K_n^{q(0)}(\nu, z^2). \quad (4.27)$$

The leading order matching coefficient therefore follows from  $M_n^{q(0)}$ , namely the Feynman diagrams of Fig. 4.2, expressed in coordinate space.

Consider the generic tensor operator embedded between an arbitrary hadronic state

$$M_{ij}^{\mu\nu}(p, z) = \langle h(p) | \mathcal{J}_i^\mu(z/2) \mathcal{J}_j^\nu(-z/2) | h(p) \rangle. \quad (4.28)$$

For generality this matrix element is given with two open Dirac indices, but the precise character of the currents will be left unspecified allowing for a generic leading-order result. Projecting (4.28) onto an asymptotic quark and averaging over the quark spin, the left diagram gives

$$\begin{aligned} M_{ij}^{(a)} &= \frac{1}{2} \sum_s \langle 0 | \bar{u}_s(k) e^{ik \cdot z/2} \Gamma_i^\mu \psi(z/2) \bar{\psi}(-z/2) \Gamma_j^\nu e^{ik \cdot z/2} u_s(k) | 0 \rangle \\ &= \frac{1}{2} \sum_s e^{ik \cdot z} \bar{u}_s(k) \Gamma_i^\mu \langle 0 | \overline{\psi(z/2) \bar{\psi}(-z/2)} | 0 \rangle \Gamma_j^\nu u_s(k) \\ &= \frac{1}{2} e^{ik \cdot z} \text{Tr} \left[ \not{k} \Gamma_i^\mu \int \frac{d^4 l}{(2\pi)^4} \frac{i \not{l}}{l^2 + i\epsilon} e^{-il \cdot z} \Gamma_j^\nu \right], \\ &= \frac{1}{2} e^{ik \cdot z} k_\alpha \text{Tr} [\gamma^\alpha \Gamma_i^\mu \gamma^\beta \Gamma_j^\nu] \int \frac{d^4 l}{(2\pi)^4} \frac{i l_\beta}{l^2 + i\epsilon} e^{-il \cdot z} \\ &= \frac{1}{2} e^{ik \cdot z} k_\alpha \text{Tr} [\gamma^\alpha \Gamma_i^\mu \gamma^\beta \Gamma_j^\nu] i \frac{\partial}{\partial z^\beta} \left( \frac{i}{4\pi^2} \frac{1}{z^2 - i\epsilon} \right) \\ &= \frac{i}{4\pi^2} \frac{k_\alpha z_\beta}{z^4} e^{ik \cdot z} \text{Tr} [\gamma^\alpha \Gamma_i^\mu \gamma^\beta \Gamma_j^\nu], \end{aligned} \quad (4.29)$$

where the massless momentum-space quark propagator has been cast in coordinate space

via a Fourier transform. The second tree-level Wick contraction yields

$$\begin{aligned}
M_{ji}^{(b)} &= \frac{1}{2} \sum_s \langle 0 | \bar{u}_s(k) e^{-ik \cdot z/2} \Gamma_j^\nu \overbrace{\psi(-z/2) \bar{\psi}(z/2)} \Gamma_i^\mu e^{-ik \cdot z/2} u_s(k) | 0 \rangle \\
&= \frac{1}{2} e^{-ik \cdot z} k_\alpha \text{Tr} [\gamma^\alpha \Gamma_j^\nu \gamma^\beta \Gamma_i^\mu] \int \frac{d^4 l}{(2\pi)^4} \frac{-il_\beta}{l^2 + i\epsilon} e^{-il \cdot z} \\
&= -\frac{i}{4\pi^2} \frac{k_\alpha z_\beta}{z^4} e^{-ik \cdot z} \text{Tr} [\gamma^\alpha \Gamma_j^\nu \gamma^\beta \Gamma_i^\mu]. \tag{4.30}
\end{aligned}$$

Combining (4.29) and (4.30) and noting the struck parton momentum  $k_\mu = xp_\mu$ , the general leading-order quark matrix element in coordinate space is

$$M_{ij}^{\mu\nu(0)}(p, z; \nu) = \frac{i}{4\pi^2} \frac{xp_\alpha z_\beta}{z^4} [e^{ixp \cdot z} \text{Tr} (\gamma^\alpha \Gamma_i^\mu \gamma^\beta \Gamma_j^\nu) - e^{-ixp \cdot z} \text{Tr} (\gamma^\alpha \Gamma_j^\nu \gamma^\beta \Gamma_i^\mu)]. \tag{4.31}$$

Since the trace of an odd number of Dirac matrices vanishes, it follows that the leading-order matching kernel for a scalar (S) current paired with either a pseudoscalar (P), vector (V), or axial-vector (A) current vanishes:  $M_{SP}(p, z) = M_{SV}^\mu(p, z) = M_{SA}^\mu(p, z) = 0$ . It is also easily shown that  $\mathcal{O}_{\tilde{V}\tilde{A}}(z)$  (Eq. 4.17) is in fact vanishing at leading-order. The leading-order perturbative kernels for the representative scalar current combinations in Eq. 4.14 - 4.18 are presented in Tab. 4.1.

The flavor structure of the probing currents naturally probes the same flavor PDF of the target hadron. Since the factorization connecting an LCS to a PDF involves parton momentum fractions in the interval  $x \in [-1, 1]$ , it is worth considering at leading order what CP-even/-odd PDF combinations each matching kernel accesses. Consider the leading-order matching kernel for the operator  $\mathcal{O}_S(z)$ :

$$\begin{aligned}
\int_{-1}^1 \frac{dx}{x} f_{q/h}(x) K_S^{q(0)}(x\nu) &= -\frac{2\nu}{\pi^2} \left\{ \int_0^1 dx f_{q/h}(x) \sin(x\nu) + \int_{-1}^0 dx f_{q/h}(x) \sin(x\nu) \right\} \\
&= -\frac{2\nu}{\pi^2} \left\{ \int_0^1 dx f_{q/h}(x) \sin(x\nu) + \int_0^1 dx f_{q/h}(-x) \sin(-x\nu) \right\}
\end{aligned}$$

$\mathcal{O}_n$	Prefactor	$\Gamma_i$	$\Gamma_j$	$M_{ij}^{\mu\nu}(p, z; \nu)$
$\mathcal{O}_S(z)$	$z^4$	$\mathbb{1}$	$\mathbb{1}$	$\frac{i}{\pi^2} x\nu (e^{ix\nu} - e^{-ix\nu})$
$\mathcal{O}_V(z)$	$z^2$	$z_\mu \gamma^\mu$	$z_\nu \gamma^\nu$	$\frac{i}{\pi^2} x\nu (e^{ix\nu} - e^{-ix\nu})$
$\mathcal{O}_{\tilde{V}}(z)$	$-z^4/2$	$g_{\nu\mu} \gamma^\mu$	$\gamma^\nu$	$\frac{i}{\pi^2} x\nu (e^{ix\nu} - e^{-ix\nu})$
$\mathcal{O}_{V'}(z)$	$z^2$	$z_\mu \gamma^\mu$	$z_\nu \gamma^\nu$	$\frac{i}{\pi^2} x\nu e^{ix\nu}$
$\mathcal{O}_{\tilde{V}\tilde{A}}(z)$	$-z^4/2$	$g_{\nu\mu} \gamma^\mu$	$\gamma^\nu \gamma^5$	0
$\mathcal{O}_{VA}(z)$	$z^4$	$\gamma^\mu$	$\gamma^\nu \gamma^5$	$\frac{1}{\pi^2} \epsilon^{\mu\nu\alpha\beta} x p_\alpha z_\beta (e^{ix\nu} + e^{-ix\nu})$

TABLE 4.1: Leading-order coordinate space matrix elements resulting from the scalar operators presented in Eq. 4.14 - 4.18. The Dirac structure of each current, and the prefactor of each current-current pair are indicated. Powers of the invariant interval  $z^2$  are included to ensure each leading-order kernel has the same Ioffe-time dependence where possible.

$$\begin{aligned}
&= -\frac{2\nu}{\pi^2} \left\{ \int_0^1 dx f_{q/h}(x) \sin(x\nu) + \int_0^1 dx f_{\bar{q}/h}(x) \sin(x\nu) \right\} \\
&= -\frac{2\nu}{\pi^2} \int_0^1 dx \{f_{q_v/h}(x) + 2f_{\bar{q}/h}(x)\} \sin(x\nu),
\end{aligned}$$

where CP-symmetry relates the quark and anti-quark PDFs according to  $f_{q/h}(x, \mu^2) = -f_{\bar{q}/h}(-x, \mu^2)$ , and  $f_{q_v/h}(x)$  is the *valence* PDF defined as  $f_{q_v/h}(x) \equiv f_{q/h}(x) - f_{\bar{q}/h}(x)$ . Thus at leading-order the current-current operators  $\{\mathcal{O}_S(z), \mathcal{O}_V(z), \mathcal{O}_{\tilde{V}}(z)\}$  all access the CP-odd combination  $f_{q_v/h}(x) + 2f_{\bar{q}/h}(x) \equiv f_{q_+/h}(x)$ , deemed the *plus* quark PDF. The leading-order Wick contractions (Fig. 4.2) imply generally that any symmetric current combination will only probe the CP-odd PDF combination  $f_{q_+/h}(x)$ . The same exercise performed for the remaining operators listed in Tab. 4.1 demonstrates that  $\mathcal{O}_{VA}(z)$  probes the CP-even PDF combination, while the flavor changing operator  $\mathcal{O}_{V'}(z)$  simultaneously accesses the valence and plus quark content. Evidently more intricate operator constructions are required to exclusively sample the valence content of a hadron.

Theoretically the valence PDFs of a hadron are important, due to quark number

conservation in QCD. As a result

$$\int_0^1 dx [f_{q/h}(x) - f_{\bar{q}/h}(x)] = \int_0^1 dx f_{q_v/h}(x) = N_{q/h}, \quad (4.32)$$

where  $N_{q/h} \in \mathbb{N}$  is the number of flavor- $q$  quarks in a hadron. In the moderate to large- $x$  region, the valence quark PDFs are then the dominant collinear momentum distributions of a hadron. The sea and gluonic distributions, in say the nucleon, are then highly suppressed for these same momentum fractions. From a practical standpoint, the flavor isovector currents we utilize in Sec. 4.3 lead to cancellation of any disconnected quark lines. In this sense, extraction of  $f_{q_+/h}(x)$  provides only a partial snapshot of the the sea quark PDFs. The rather limited current-current Lorentz structures considered above will be expanded in Sec. 4.3 to allow unambiguous access of the valence quark PDF of the pion.

### Next-to-Leading Order (NLO) Perturbative Matching Kernel

To perturbatively calculate the matching coefficient  $K_n(x\nu, z^2\mu^2)$  valid to NLO of an on-shell struck parton satisfying  $k^2 = x^2p^2 = 0$ , the coordinate space calculations become challenging analytically and often result in complicated admixtures of modified Bessel functions (e.g. Appendix of [108]). An alternate strategy is to Fourier transform the coordinate space factorization into a momentum space representation in  $D = 4 - 2\epsilon$  dimensions

$$\widetilde{M}_n(\tilde{\nu}, q^2) = \int \frac{d^D z}{z^4} e^{iqz} M_n(\nu, z^2) = \int_{-1}^1 \frac{dx}{x} \widetilde{K}(x\tilde{\nu}, q^2\mu^2) f_{q/h}(x, \mu^2) + \mathcal{O}(\Lambda_{\text{QCD}}^2/q^2), \quad (4.33)$$

with  $\tilde{\nu} = \frac{1}{x_B + i0^+} = \frac{2p \cdot q}{-q^2 - i0^+}$ . As in the tree-level case, to calculate  $\widetilde{K}(x\tilde{\nu}, q^2\mu^2)$  for, say the valence quark PDF, Eq. 4.33 is projected onto an asymptotic quark and each side is

expanded in powers of  $\alpha_s$ . The tree-level and NLO expansions are given by

$$\widetilde{M}_n^{q(0)}(\tilde{\nu}, q^2) = \int_0^1 dx \widetilde{K}^{(0)}(x\tilde{\nu}, q^2\mu^2) f_{q_v/q}^{(0)}(x, \mu^2) \quad (4.34)$$

$$\widetilde{M}_n^{q(1)}(\tilde{\nu}, q^2) = \int_0^1 dx \widetilde{K}^{(1)}(x\tilde{\nu}, q^2\mu^2) f_{q_v/q}^{(0)}(x, \mu^2) + \int_0^1 dx \widetilde{K}^{(0)}(x\tilde{\nu}, q^2\mu^2) f_{q_v/q}^{(1)}(x, \mu^2). \quad (4.35)$$

The choice of renormalization scheme for the above ‘‘quark-in-quark’’ PDFs means the matching prescription will be scheme dependent. A standard choice are the perturbative  $\overline{\text{MS}}$  PDFs

$$f_{q_v/q}^{(0)}(x, \mu^2) = \delta(1-x) \quad (4.36)$$

$$f_{q_v/q}^{(1)}(x, \mu^2) = -\frac{1}{\epsilon} \frac{(4\pi)^\epsilon}{\Gamma(1-\epsilon)} \frac{\alpha_s C_F}{2\pi} \left( \frac{1+x^2}{1-x} \right)_+, \quad (4.37)$$

with the plus-prescription denoted  $\int_0^1 d\alpha G(\alpha)_+ h(\alpha x) = \int_0^1 d\alpha G(\alpha) [h(\alpha x) - h(x)]$ .

The coordinate space matching kernel valid up to NLO is then obtained by applying an inverse Fourier transform to the momentum space kernel obtained from (4.34) and (4.35)

$$K(x\nu, z^2\mu^2) = z^4 \int \frac{d^D q}{(2\pi)^D} e^{-iq \cdot z} \widetilde{K}(x\tilde{\nu}, q^2\mu^2). \quad (4.38)$$

A specific matching relationship valid to NLO will be given in Sec. 4.3 wherein numerical implementation and the first results using the two-current LCS formalism are reported by the HadStruc Collaboration.

## 4.2.2 Wilson Line Operator

Consider the non-local quark bilinear  $\bar{\psi}(z) \gamma^\alpha \Phi_{\hat{z}}^{(f)}(\{z, 0\}) \psi(0)$  connected with a straight  $z$ -separated Wilson line  $\Phi_{\hat{z}}^{(f)}(\{z, 0\})$  in the fundamental representation of  $\text{SU}(3)$ . Lorentz

invariance dictates that the forward helicity-averaged matrix element of this operator decompose according to

$$M^\alpha(p, z) = \langle h(p) | \bar{\psi}(z) \gamma^\alpha \Phi_z^{(f)}(\{z, 0\}) \psi(0) | h(p) \rangle = 2p^\alpha \mathcal{M}(\nu, z^2) + 2z^\alpha \mathcal{N}(\nu, z^2). \quad (4.39)$$

For a fast-moving hadron, the usual unpolarized PDFs are defined with light-cone coordinates where  $\alpha = +$ ,  $p^\alpha = \left(p^+, \frac{m_h^2}{2p^+}, \mathbf{0}_\perp\right)$  and  $z^\alpha = (0, z^-, \mathbf{0}_\perp)$ . In this scenario  $M^+(p, z)$  only receives contributions from  $\mathcal{M}(p^+z^-, 0)$ . Provided the logarithmic singularity that arises for  $z^2 = 0$  (generated by the DGLAP evolution of the PDF) is regularized (typically in  $\overline{\text{MS}}$ ),  $\mathcal{M}(p^+z^-, 0)$  defines the Ioffe-time distribution (ITD) [106]:

$$\mathcal{M}(p^+z^-, 0)_{\mu^2} \equiv \mathcal{Q}(\nu, \mu^2) = \int_{-1}^1 dx e^{i\nu x} f_{q/h}(x, \mu^2). \quad (4.40)$$

The finding that the  $\nu$ -dependence of the ITD dictates the  $x$ -dependence of the conventional twist-2 PDFs is unsurprising given the proof of factorization of the coordinate space LCSs given in Sec. 4.2.1.

Lorentz invariance implies the  $\nu$ -dependence of  $\mathcal{M}(p^+z^-, 0)_{\mu^2}$  can be computed in any frame, and with any choice of  $\{z, \alpha\}$  that may be convenient. A particular choice amenable to calculation with lattice QCD is  $\alpha = 0$ ,  $p^\alpha = (E, \mathbf{0}_\perp, p_z)$  and  $z^\alpha = (0, \mathbf{0}_\perp, z_3)$ , which excludes the contamination from the pure higher-twist term  $\mathcal{N}(\nu, z^2)$ . The remaining term  $\mathcal{M}(\nu, z^2 \neq 0)$  is deemed the *Ioffe-time Pseudo-distribution* [109] or pseudo-ITD. It is important to note that in addition to the twist-2 contributions, the pseudo-ITD also contains higher-twist contributions  $\mathcal{O}(z^2 \Lambda_{\text{QCD}}^2)$  that vanish only in the light-cone limit. For all relevant Feynman diagrams, the Fourier transform of the pseudo-ITD with respect to  $\nu$  has been shown [110] to carry support only in the canonical parton momentum fraction

interval  $x \in [-1, 1]$ :

$$\mathcal{M}(\nu, z^2) = \int_{-1}^1 dx e^{i\nu x} \mathcal{P}(x, z^2) \quad (4.41)$$

$$\mathcal{P}(x, z^2) = \frac{1}{2\pi} \int_{-\infty}^{\infty} d\nu e^{-i\nu x} \mathcal{M}(\nu, z^2). \quad (4.42)$$

The so-called *pseudo-PDF* [109]  $\mathcal{P}(x, z^2)$  therefore provides a Lorentz covariant notion of parton  $x$  and a generalization of light-cone PDFs onto space-like intervals.

The separation of (4.39) into its invariant amplitudes and subsequent analysis with respect to Ioffe-time casts an important distinction between pseudo- and quasi-distributions. Pseudo-PDFs and quasi-PDFs each share the matrix element in Eq. 4.39 as the basic numerical object to compute. The Fourier transform over the length of the Wilson line defining the quasi-PDF corresponds to

$$\begin{aligned} \tilde{f}_{q/h}(\tilde{x}, p_z, \tilde{\mu}^2) &\propto \int dz_3 e^{-i\tilde{x}p_z z_3} \langle h(p_z) | \bar{\psi}(z) \gamma_0 \Phi_{z_3}^{(f)}(\{z_3, 0\}) \psi(0) | h(p_z) \rangle \\ &\propto \int dz_3 e^{-i\tilde{x}p_z z_3} \mathcal{M}(\nu, z_3^2) = \int dz_3 e^{-i\tilde{x}p_z z_3} \mathcal{M}(p_z z_3, z_3^2). \end{aligned}$$

In other words quasi-PDFs, and quasi-distributions more generally, are the result of complicated dependencies on both invariants  $\nu$  and  $z_3^2$ , most notably large- $z_3^2$ . The  $z^2$ -dependence of the pseudo-ITD was shown in [110] to correspond to the  $\mathbf{k}_\perp$ -dependence of the primordial straight-link transverse momentum dependent parton distributions. The mixing of invariant scales by the quasi-PDF explains the considerable dependence on the hadron momentum  $p_z$  seen in Fig. 4.1 and the slow approach to the light-cone PDF. The pseudo-PDF (4.42) however avoids the mixing of different  $z_3^2$  scales by integrating only the  $\nu$ -dependence of  $\mathcal{M}(\nu, z_3^2)$  for fixed  $z_3$ .

Since the Wilson line operator  $\mathring{O}_{\text{WL}}^{[\gamma^\mu]}(z)$  is multiplicatively renormalizable and Ioffe-

time independent, instead of the pseudo-ITD we consider the *reduced* pseudo-ITD [109]

$$\mathfrak{M}(\nu, z^2) = \frac{\mathcal{M}(\nu, z^2)}{\mathcal{M}(0, z^2)}. \quad (4.43)$$

Since the rest-frame pseudo-ITD  $\mathcal{M}(0, z^2)$  has the same gauge-link associated power divergence, the reduced pseudo-ITD cancels this divergent factor, thereby ensuring a finite continuum limit. For the reduced pseudo-ITD to be more than an algebraic trick, the normalizing quantity should be a finite constant in the  $z^2 \rightarrow 0$  limit. This aspect will guarantee that when the OPE is applied to the pseudo-ITD and its reduced counterpart, the resulting Mellin moments and thus factorization into PDFs are identical. The choice to construct the reduced pseudo-ITD with  $\mathcal{M}(0, z^2)$  is especially straightforward, as  $\mathcal{M}(0, z^2)$  is simply the bare vector charge  $Z_V^{-1}$  in the light-cone limit. Motivation for the reduced pseudo-ITD also extends to the mitigation of soft higher-twist  $\mathcal{O}(z^2 \Lambda_{\text{QCD}}^2)$  effects. Such large- $z^2$  effects correspond to the soft  $\mathbf{k}_\perp^2$ -dependence of the associated Transverse Momentum Dependent PDF (TMD), which is commonly assumed to factorize from its  $x$ -dependence [111]. The first calculation of pseudo-distributions in the nucleon indeed found  $\mathfrak{M}(\nu, z^2)$  is subject to polynomial- $z^2$  corrections of lesser magnitude than  $\mathcal{M}(\nu, z^2)$  at large- $z^2$  [112]. This is understood in terms of at least a partial factorization of the  $\nu$  and  $z^2$  dependencies of the pseudo-ITD, or again the  $x$  and  $\mathbf{k}_\perp^2$  dependencies of the TMD. Alternatives have recently been proposed that make use of a vacuum matrix element of  $\mathcal{O}_{\text{WL}}^{[\gamma^\mu]}(z)$  [113] or a pseudo-ITD in a boosted frame [114]. These are not considered here.

Following removal of the UV singularities produced by the space-like Wilson line, the remaining UV divergences in (4.43) stem from  $\ln z_3^2$  contributions in QCD. These divergences generate the perturbative evolution of the collinear PDFs and complicate the naive  $z_3^2 \rightarrow 0$  limit at which  $\mathcal{P}(x, 0) = f_{a/h}(x)$ . Fortunately  $\mathfrak{M}(\nu, z^2)$  is a good LCS and the factorization in Sec. 4.2.1 applies. The reduced pseudo-ITD  $\mathfrak{M}(\nu, z^2)$  therefore factorizes in



the perturbative short-distance regime into PDFs with perturbatively calculable hard coefficients. The factorization relationship has been computed to NLO in  $\overline{\text{MS}}$  [115, 116, 117] and matches the  $\overline{\text{MS}}$  ITD  $\mathcal{Q}(\nu, \mu^2)$  to the reduced pseudo-ITD  $\mathfrak{M}(\nu, z^2)$ :

$$\mathfrak{M}(\nu, z^2) = \int_0^1 du \left\{ \delta(1-u) - \frac{\alpha_s C_F}{2\pi} \left[ \ln \left( \frac{e^{2\gamma_E+1} z^2 \mu^2}{4} \right) B(u) + L(u) \right] \right\} \mathcal{Q}(u\nu, \mu^2) + \sum_{k=1}^{\infty} \mathcal{B}_k(\nu) (z^2)^k. \quad (4.44)$$

The matching involves a scale-independent kernel  $L(u) = \left[ 4 \frac{\ln(1-u)}{1-u} - 2(1-u) \right]_+$  due to the  $\overline{\text{MS}}$  matching, and a scale-dependent kernel that relates the  $z^2$  and  $\mu^2$  scales through the flavor non-singlet DGLAP evolution kernel  $B(u) = \left[ \frac{1+u^2}{1-u} \right]_+$  [22, 23, 24]. The factorization is valid in so far as the polynomial corrections  $\mathcal{B}_k(\nu) (z^2)^k$  can be mitigated.

### 4.3 Pion Ioffe-time Pseudo-Structure Functions

The first community results of a PDF obtained using the two-current LCS matrix elements are that of the pion valence quark PDF  $f_{q_v/\pi}(x)$ . The pion is chosen as the numerical arena in which to study this formalism, as fewer Wick contractions are needed to fully calculate a correlation function and it is naively less susceptible to signal-to-noise degradation relative to baryons. We note in practice that high-momentum pion correlation functions are considerably more noisy than baryon correlation functions of the same lattice momenta (see e.g. [118]). Whereas in mesonic systems it will prove to be relatively straightforward to measure the two-current LCS matrix elements, selecting the current separation in baryons presents the greatest roadblock to baryonic LCS measurements, and is left for a future study.

Pionic LCS matrix elements are computed on four separate isotropic gauge ensem-

bles with  $2 \oplus 1$  dynamical flavors of Wilson-clover fermions [75] and a tree-level tadpole improved Symanzik gauge action. Characteristics of each ensemble as well as the number of configurations employed are gathered in Tab. 4.2. These ensembles were chosen to illuminate potential variability in LCS matrix elements as the pion mass, volume and lattice spacings are changed. Although extrapolation in any one variable is generally performed on data from three different ensembles with all other parameters fixed, we will find a flexible global analysis of these data to be instructive.

As in previous chapters, the sought-after pion matrix elements require overlap and spectroscopic information garnered from pion two-point correlation functions (2.68). A combination of Jacobi smearing and standard momentum-smearing [59] (Sec. 2.4) is implemented to ameliorate the effects of excited-states and improve the overlap of our interpolating fields onto boosted pions. The resulting momentum-projected pion annihilation interpolator we use is given by

$$\Pi_{\vec{p}}(T) = \sum_x e^{i\vec{p}\cdot\vec{x}} \bar{q}(\vec{x}, T) \gamma^5 \tilde{q}(\vec{x}, T), \quad (4.45)$$

where  $\tilde{q}$  is a light quark field modified by the combined action of momentum and Jacobi smearing. The spatial smearing parameters are kept fixed on a given ensemble, while the momentum smearing parameter is tuned for all lattice momenta  $p_z^{\text{latt}}$  such that  $2 \leq |p_z^{\text{latt}}| \leq$

ID	$a$ (fm)	$m_\pi$ (MeV)	$L^3 \times N_T$	$N_{\text{cfg}}$
<i>a127m413</i>	0.127(2)	413(4)	$24^3 \times 64$	2124
<i>a127m413L</i>	0.127(2)	413(5)	$32^3 \times 96$	490
<i>a94m358</i>	0.094(1)	358(3)	$32^3 \times 64$	417
<i>a94m278</i>	0.094(1)	278(4)	$32^3 \times 64$	503

TABLE 4.2: Parameters for each gauge ensemble used in this work: lattice spacing, pion mass, spatial and temporal sizes, and number of configurations used.

6. A representative sample of these parameters can be found in [119, 120]. Indeed with a single local pion interpolator, and especially without the combined benefit of distillation and the variational method, increased excited-state contamination should be expected. The use of a single interpolator is rooted in numerical cost and is discussed below.

The relevant four-point function is given by

$$C_{4\text{pt}}(\vec{p}, z; T, \tau) = \langle \Pi(-\vec{p}, T) \mathcal{J}_\Gamma^\dagger(\vec{z} + \vec{z}_0, \tau) \mathcal{J}_{\Gamma'}(\vec{z}_0, \tau) \bar{\Pi}(\vec{p}, 0) \rangle, \quad (4.46)$$

with the spatially separated currents inserted at time  $\tau$ . If the currents were composed entirely of mass degenerate light quarks  $\mathcal{J}_\Gamma = \bar{\ell}\Gamma\ell$ , the set of Wick contractions to be evaluated numerically would be large. The topology of each contraction in the case of flavor-conserving currents is illustrated in Fig. 4.3. Notable is the appearance of several diagrams involving disconnected quark loops, which would require expensive all-to-all propagators. On the basis of power-suppressed diagrams in DIS, such as the *cat's ears* diagram, one might expect several of these diagrams to be suppressed as well in coordinate space. Each of the above concerns is addressed by introduction of currents that couple light and auxiliary heavy quarks  $\mathcal{J}_\Gamma = \bar{\ell}\Gamma Q$ . Such heavy-light flavor changing currents render Figs. 4.3(a) & 4.3(d) as the only possible contraction topologies. An overall flavor isovector combination (i.e. the two currents transform with isospin-1) then cancels the Fig. 4.3(d) diagram. A similar scheme was used in [89] to exclude higher-twist pollution in moments calculations of PDFs and distribution amplitudes. Since the auxiliary quark field is quenched by construction and any disconnected diagrams are excluded by the flavor construction of our currents, we are guaranteed that the auxiliary PDFs vanish and do not mix with the valence PDF we target. Moreover, the phase space between the two currents, where the equal-time heavy quark propagator resides, is more thoroughly saturated with a quark  $m_Q > m_\ell$ . We set the auxiliary quark mass equal to the strange quark mass on

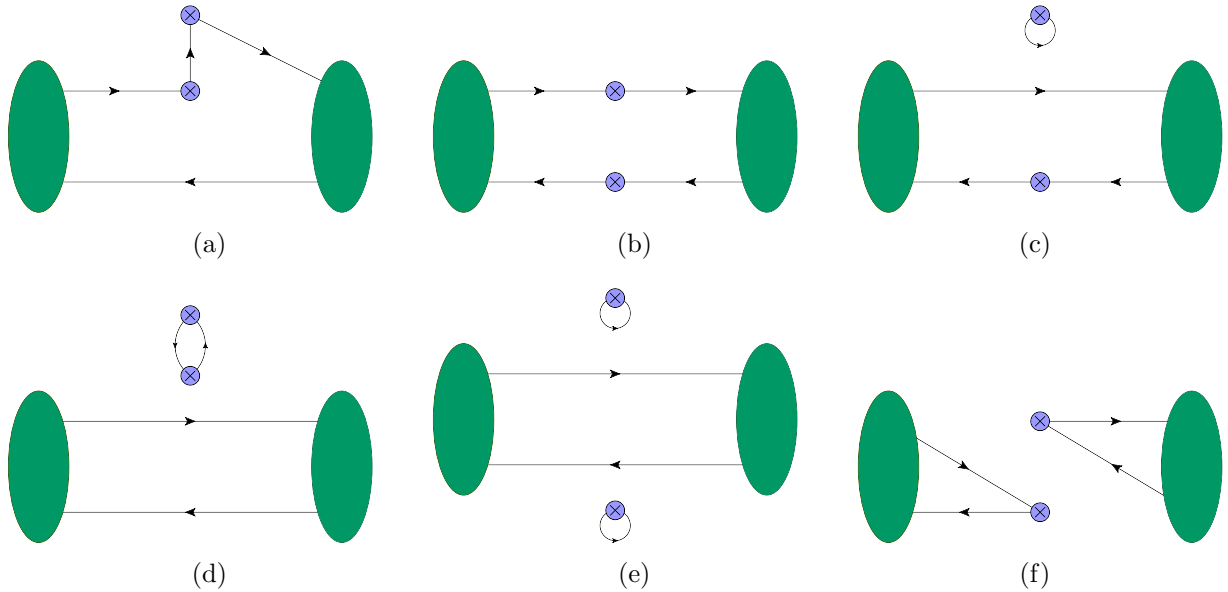


FIG. 4.3: Wick contraction topologies resulting from two current correlators with each current conserving flavor. The use of flavor changing currents cancels all but contractions (a) and (d), while the latter is canceled by an isovector construction.

the ensembles we consider. Higher yet masses may lead to further reduced statistical noise from the equal-time propagator, but discretization errors  $\mathcal{O}(am_Q)$  will begin to accrue.

The factorization of the composite operator LCS matrix elements is again valid only for short-distances  $|z| \ll \Lambda_{\text{QCD}}^{-1}$ . Any momentum projection at either current, although to zero three-momentum in this calculation, would sum over the spatial lattice sites thereby mixing small and large  $z^2$  scales. Each current must therefore be introduced on a time slice at precisely one lattice site. The sequential source method common in matrix element calculations consequently is not a viable numerical tool here, because of the need for many point-to-point propagators. Fortunately for mesonic systems a modified sequential operator method can be implemented to calculate the Wick contraction in Fig. 4.3(a). The modified sequential source is constructed through sequential inversions of the light quark Dirac operator, reusing already computed propagators. The algorithm we implement for the modified sequential source is as follows: first a light quark propagator from a point-

source at one of the currents to the source interpolator is computed. This object is then used as the source for a subsequent inversion to the sink interpolator. This resulting larger sequential operator is lastly used as the source for an inversion from the sink to the second current. Mathematically this algorithm proceeds by solving the sequential systems of equations for  $\{G_q, H_q^p, I_q^p\}$ :

$$\begin{aligned} \sum_{z',t'} D_q(z,t; z',t') G_q(z',t'; z_0, \tau) &= \delta(z - z_0) \delta(t - \tau) \\ \sum_{z',t'} D_q(z,t; z',t') H_q^p(z',t'; z_0, \tau) &= e^{-iz \cdot p} \sum_{y',y''} S[z; y'] \gamma^5 S[y'; y''] G_q(y'', t; z_0, \tau) \delta(t) \\ \sum_{z',t'} D_q(z,t; z',t') I_q^p(z',t'; z_0, \tau) &= e^{iz \cdot p} \sum_{y',y''} S[z; y'] \gamma^5 S[y'; y''] H_q(y'', t; z_0, \tau) \delta(t - T), \end{aligned}$$

where  $D_q$  is the light quark Dirac matrix,  $S[*; *]$  is the combined smearing procedure, and color and Dirac indices have been suppressed for clarity. The phase factors in the second and third inversions project the interpolators to definite momenta, while the duplicate smearing operators  $S[*; *]$  handle the distinct smearing for each quark field. We note the momentum smearing phases are opposite in sign for the quark/anti-quark fields, and the currents are left unsmeared. This algorithm, illustrated in Fig. 4.4, is clearly inversion dominated. It is however advantageous, as it allows currents of arbitrary Lorentz structure and separation to be correlated after the inversions have been performed. Any modification to the source/sink interpolators, including the temporal separation, will then require repeating the final two inversions. Expanding to a basis of pion-like interpolators is thus impractical and avoided in this calculation due to the proliferation of inversions.

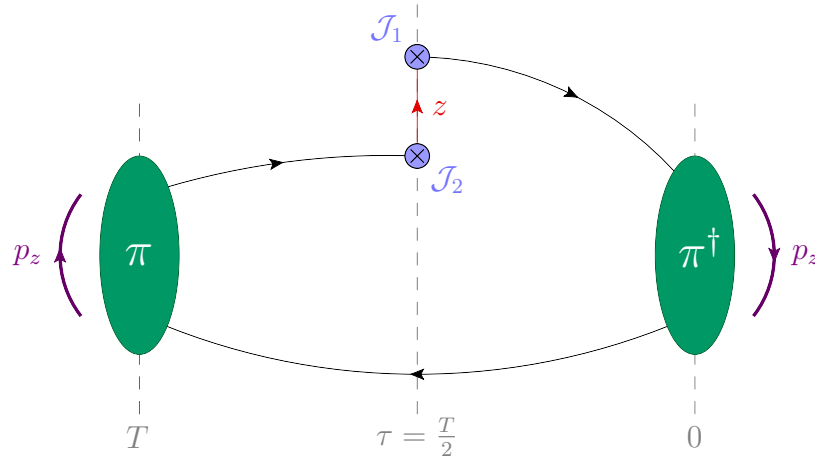


FIG. 4.4: Diagrammatic construction of the pion four-point function built from a modified sequential source (black) and a time-local auxiliary heavy quark propagator (red). This setup admits correlation of currents with arbitrary Lorentz structure and separation independent of the costly Dirac inversions.

### 4.3.1 Vector-Axial Currents and $f_{q_v/\pi}(x)$

To access the CP-even pion valence quark PDF  $f_{q_v/\pi}(x)$ , a set of currents different from most considered in Sec. 4.2.1 need to be constructed. The precise form of any current-current combination is restricted by the invariance of QCD under parity ( $\hat{\mathcal{P}}$ ) and time-reversal ( $\hat{\mathcal{T}}$ ) transformations. Specifically scalar/pseudoscalar two-current matrix elements must obey

$$\langle p | \mathcal{O}_{ij}^{\mu\nu}(z) | p \rangle = \langle p | (\hat{\mathcal{P}}\hat{\mathcal{T}})\mathcal{O}_{ij}^{\mu\nu}(z)^\dagger (\hat{\mathcal{P}}\hat{\mathcal{T}})^{-1} | p \rangle.$$

Consider a vector  $\mathcal{J}_V^\mu = \bar{\psi}\gamma^\mu\psi$  and axial-vector  $\mathcal{J}_A^\nu = \bar{\psi}\gamma^\nu\gamma^5\psi$  current, whose transformation properties are  $(\hat{\mathcal{P}}\hat{\mathcal{T}})\mathcal{J}_V^\mu(z)(\hat{\mathcal{P}}\hat{\mathcal{T}})^{-1} = \mathcal{J}_V^\mu(-z)$  and  $(\hat{\mathcal{P}}\hat{\mathcal{T}})\mathcal{J}_A^\mu(z)(\hat{\mathcal{P}}\hat{\mathcal{T}})^{-1} = -\mathcal{J}_A^\mu(-z)$ . The linear combination  $M_{VA}^{\mu\nu}(p, z) + M_{AV}^{\mu\nu}(p, z) \equiv \langle \pi(p) | [\mathcal{O}_{VA}^{\mu\nu}(z) + \mathcal{O}_{AV}^{\mu\nu}(z)] | \pi(p) \rangle$  is then antisymmetric in Lorentz indices. The only Lorentz decomposition antisymmetric in the

Lorentz structures  $\{p^\mu, z^\mu\}$  is

$$\sigma_{VA}^{\mu\nu} \equiv \frac{z^4}{2} [M_{VA}^{\mu\nu}(p, z) + M_{AV}^{\mu\nu}(p, z)] = \frac{\epsilon^{\mu\nu\alpha\beta} p_\alpha z_\beta}{\nu} T_1(\nu, z^2) + \frac{(p^\mu z^\nu - z^\mu p^\nu)}{\nu} T_2(\nu, z^2). \quad (4.47)$$

Appropriate tensor contractions can isolate each pseudo-structure function:

$$T_1(\nu, z^2) = \frac{\nu}{2(\nu^2 - p^2 z^2)} \epsilon_{\mu\nu\alpha\beta} p^\alpha z^\beta \sigma_{VA}^{\mu\nu}, \quad T_2(\nu, z^2) = \frac{\nu}{2(\nu^2 - p^2 z^2)} (z_\mu p_\nu - p_\mu z_\nu) \sigma_{VA}^{\mu\nu}.$$

In light of the sequential inversions above, computation of all elements of  $\sigma_{VA}^{\mu\nu}$  followed by the appropriate projections for  $T_1(\nu, z^2)$  and  $T_2(\nu, z^2)$  is wholly impractical numerically. Each  $T_i(\nu, z^2)$  can be accessed with a judicious choice of Dirac indices, momenta, and current separations. With pion momenta  $p_\mu = (p_0, \mathbf{0}_\perp, p_3)$  and current separation  $z_\mu = (0, \mathbf{0}_\perp, z_3)$ , each  $T_i(\nu, z^2)$  is accessed by selecting particular components of  $\sigma_{VA}^{\mu\nu}$

$$T_1(\nu, z^2) = \frac{\nu}{p_0 z_3} \sigma_{VA}^{12}, \quad T_2(\nu, z^2) = \frac{\nu}{p_0 z_3} \sigma_{VA}^{03}. \quad (4.48)$$

Applying the general leading-order on-shell quark matrix element result in coordinate space (4.31) to the vector-axial combination first, we have

$$\begin{aligned} M_{VA}^{\mu\nu(0)}(p, z; \nu) &= \frac{i}{4\pi^2} \frac{x p_\alpha z_\beta}{z^4} [e^{ix\nu} \text{Tr}(\gamma^\alpha \gamma^\mu \gamma^\beta \gamma^\nu \gamma^5) - e^{-ix\nu} \text{Tr}(\gamma^\alpha \gamma^\nu \gamma^5 \gamma^\beta \gamma^\mu)] \\ &= \frac{i}{4\pi^2} \frac{x p_\alpha z_\beta}{z^4} [-4i\epsilon^{\alpha\mu\beta\nu} e^{ix\nu} + 4i\epsilon^{\alpha\nu\beta\mu} e^{-ix\nu}] \\ &= \frac{2}{\pi^2 z^4} \epsilon^{\mu\nu\alpha\beta} x p_\alpha z_\beta \cos(x\nu) \end{aligned}$$

using the identity  $\text{Tr}(\gamma^\mu \gamma^\nu \gamma^\rho \gamma^\sigma \gamma^5) = -4i\epsilon^{\mu\nu\rho\sigma}$  subject to the convention  $\epsilon^{0123} = 1$ . Repeating the traces for the axial-vector combination, the same result is obtained. Therefore

at leading-order in coordinate space we have

$$\sigma_{VA}^{\mu\nu(0)} \equiv \frac{z^4}{2} \left[ M_{VA}^{\mu\nu(0)}(p, z) + M_{AV}^{\mu\nu(0)}(p, z) \right] = \frac{2}{\pi^2} \epsilon^{\mu\nu\alpha\beta} x p_\alpha z_\beta \cos(x\nu). \quad (4.49)$$

To derive the leading-order perturbative coefficients, Eq. 4.49 is substituted into the relations of Eq. 4.48 relevant to the kinematics we have identified. It follows

$$T_1^{q(0)}(\nu, z^2) = \frac{2\nu x}{\pi^2} \cos(x\nu) \quad T_2^{q(0)}(\nu, z^2) = 0. \quad (4.50)$$

As the leading-order "quark-in-quark" PDF is simply  $f_a^{q(0)}(x, \mu^2) = \delta(1-x) \delta^{qa}$ , the LCS factorization (4.26) of a quark state at LO implies

$$K_1^{q(0)}(x\nu, z^2) = T_1^{q(0)}(x\nu, z^2) = \frac{2\nu x}{\pi^2} \cos(x\nu) \quad (4.51)$$

$$K_2^{q(0)}(x\nu, z^2) = T_2^{q(0)}(x\nu, z^2) = 0. \quad (4.52)$$

Since  $K_1^{q(0)}(x\nu, z^2)$  is proportional to the parity-even  $\cos(x\nu)$ , it easily shown

$$\begin{aligned} \int_{-1}^1 \frac{dx}{x} K_1^{(0)}(x\nu) &= \frac{2\nu}{\pi^2} \left\{ \int_0^1 dx f_{q/h}(x) \cos(x\nu) + \int_0^1 dx f_{q/h}(-x) \cos(-x\nu) \right\} \\ &= \frac{2\nu}{\pi^2} \int_0^1 dx \{ f_{q/h}(x) - f_{\bar{q}/h}(x) \}. \end{aligned}$$

This demonstrates that pion matrix elements of an antisymmetric vector-axial two-current operator factorize in a short-distance regime at LO into the valence quark PDF of the pion  $f_{q_v/\pi}(x)$ .



## NLO Matching

Determination of the next-to-leading order (NLO) matching kernel for the same anti-symmetric vector-axial current combination adopts the strategy outlined in Sec. 4.2.1. The NLO kernel that matches the valence PDF to the vector-axial LCS is presented in [120] and stated here for completeness:

$$K_{\text{NLO}} = \frac{1}{\pi^2} \frac{\epsilon^{12\alpha\beta} p_\alpha z_\beta}{2\nu} \left[ K^{(0)}(\nu) + \frac{\alpha_s C_F}{2\pi} \left\{ K^{(1,0)}(\nu) + K^{(1,1)}(\nu) \ln \left[ -z^2 \mu^2 \frac{e^{2\gamma_E}}{4} \right] \right\} \right], \quad (4.53)$$

where  $K^{(0)}(\nu) = \nu \cos(\nu)$  is the tree-level result, while  $K^{(1,0)}(\nu)$  and  $K^{(1,1)}(\nu)$  are the NLO kernels given respectively by

$$K^{(1,0)}(\nu) = \nu \int_0^1 du \cos(u\nu) \left[ \frac{1}{2} \delta(1-u) - \left( \frac{2 \ln(1-u)}{1-u} - \frac{u^2 - 3u + 1}{1-u} \right)_+ \right] \quad (4.54)$$

$$K^{(1,1)}(\nu) = -\nu \int_0^1 du \cos(u\nu) \left( \frac{1+u^2}{1-u} \right)_+, \quad (4.55)$$

where in Euclidean space it is understood the interval  $z^2 < 0$ . As was the case for the pseudo-distributions, the full NLO kernel involves a scale-independent contribution  $K^{(1,0)}(\nu)$  responsible for matching the lattice and  $\overline{\text{MS}}$  schemes, as well as a kernel  $K^{(1,1)}(\nu)$  describing the scale-dependence of the data; the latter containing the familiar flavor non-singlet DGLAP kernel [22, 23, 24]. The plus-prescription designation in  $K^{(1,0)}(\nu)$  and  $K^{(1,1)}(\nu)$  reflect the perturbative cancellation of infrared (IR) divergences between real and virtual diagrams in momentum space (i.e. before the  $D$ -dimensional Fourier transformation to coordinate space). Near the point of IR cancellation, however, it is not uncommon for diagrams to receive large logarithmic corrections [121] from soft and collinear gluons. In applying standard QCD factorization in momentum space to hadronic cross sections, these potentially large corrections must be re-summed before making contact with experimental

data. The short-distance matching of the LCS coordinate space matrix elements to the PDFs is then less sensitive to these corrections [120], a further benefit of this paradigm. The stability and effect of the  $K^{(1,0)}(\nu)$  and  $K^{(1,1)}(\nu)$  kernels is explicitly demonstrated in Sec. 5.2.3.

### 4.3.2 Numerical Implementation

The modified sequential source recasts the four-point function (4.46) as

$$\begin{aligned}
C_{4\text{pt}}(p, z; T, \tau) &= \langle \Pi_{\vec{p}}(\vec{x}, T) \mathcal{J}_{\Gamma}^{\dagger}(\vec{z} + \vec{z}_0; \tau) \mathcal{J}_{\Gamma'}(\vec{z}_0, \tau) \bar{\Pi}_{\vec{p}}(\vec{y}, 0) \rangle \\
&= \sum_{\vec{x}, \vec{y}} e^{i(\vec{x} - \vec{y}) \cdot \vec{p}} \left\langle \bar{d} \gamma^5 \tilde{u}(\vec{x}, T) [\bar{Q} \Gamma u + \bar{u} \Gamma Q](\vec{z} + \vec{z}_0; \tau) \times [\bar{u} \Gamma' Q + \bar{Q} \Gamma' u](\vec{z}_0; \tau) \tilde{u} \gamma^5 \tilde{d}(\vec{y}; 0) \right\rangle \\
&= \text{Tr} \left[ I_q^p(\vec{z} + \vec{z}_0, \tau; \vec{z}_0, \tau) \Gamma \gamma^5 G_Q(\vec{z} + \vec{z}_0, \tau; \vec{z}_0, \tau)^{\dagger} \gamma^5 \Gamma' \right] + (\Gamma \mapsto \Gamma'),
\end{aligned}$$

where  $G_Q(\vec{z} + \vec{z}_0, \tau; \vec{z}_0, \tau)$  is the equal-time auxiliary quark propagator that ties together the modified sequential source  $I_q^p$ . The source point  $(\vec{z}_0, \tau)$  is randomly determined per configuration and is fixed midway between the source and sink interpolators (i.e.  $\tau = T/2$ ). This choice eliminates the ability to resolve the excited-state dependence in the two-current matrix elements for  $\tau/a \in [0, T]$ , at the benefit of avoiding an additional  $4 \times T$  Dirac inversions. By requiring  $\tau/a = T/2$  and constructing the source and sink interpolators in identical manners, we are assured excited-state contamination is equal in the intervals  $\tau/a \in [0, T/2), [T/2, T]$ . The desired pion ground-state matrix element is then accessed by successively increasing the source-sink separations, repeating the series of inversions, and studying the large- $T$  behavior. Due to the decreasing signal to noise ratio, the higher momentum states require more source points per configuration and shorter source-sink separations  $T$ . The two-current matrix element is extracted following a correlated simul-

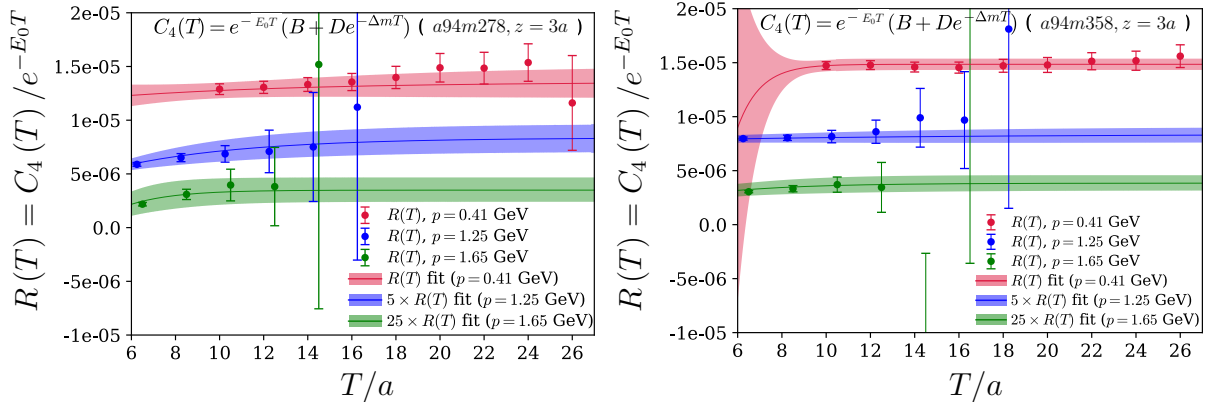


FIG. 4.5: Representative matrix element extractions for  $z = 3a$  and increasing pion boosts on the ensembles  $a94m278$  (left) and  $a94m358$  (right). The leading time dependence has been removed to expose the asymptotic plateau in the data. The  $p = 1.25, 1.65$  GeV data have been rescaled by factors of 5 and 25, respectively, to illustrate the rapid deterioration of the matrix element signals as the pion momentum is increased.

taneous fit to the pion two- and four-point correlators:

$$C_{2\text{pt}}^\pi(T) = \mathcal{A}e^{-E_0T} \quad (4.56)$$

$$C_{4\text{pt}}^\pi(T) = e^{-E_0T} (\mathcal{B} + \mathcal{D}e^{-\Delta m T}). \quad (4.57)$$

The ground-state energy and its gap relative to excited-states are respectively given by  $E_0$  and  $\Delta m$ , while the matrix element is the asymptotic plateau of  $\mathcal{B}/\mathcal{A}$ .

Selected fit results on the ensembles  $a94m278$  and  $a94m358$  are shown in Fig. 4.5 for a current separation of  $z = 3a$  and momenta in the range  $p_z \in \{0.41 - 1.65\}$  GeV. The numerical challenges manifest in this formalism are reflected in the signal-to-noise ratio of the largest momentum  $p_z = 1.65$  GeV relative to that of the smallest  $p_z = 0.41$  GeV - the former is nearly three times smaller. Despite this, these data can be fit for source-sink separations up to  $T/a \simeq 14$  ( $\sim 1.32$  fm), even for the highest momentum  $p_z = 1.65$  GeV on the lightest pion mass  $m_\pi = 278$  MeV ensemble. The fitted time series for each momentum and two-current separation is tuned to only include data with signal-to-noise ratios of at least unity. All matrix elements with  $z/a = 1$  are excluded from our analysis on the basis

of contact terms arising from the Wilson clover fermion action.

Although the representative  $z = 3a$  matrix element extractions shown in Fig. 4.5 do exhibit signal for source/sink pion separations in excess of 1 fm, the loss of signal is considerable as the lattice momenta is increased from  $p_z^{\text{latt}} = 1$  to  $p_z^{\text{latt}} = 3, 4$ . These reductions in the signal-to-noise ratios are consistent with expectations following momentum projections at the source and sink pions. However, the lack of a volume average (i.e. momentum projection) on the current-current time slice translates into  $\mathcal{O}(10^4)$  fewer measurements of the two current operator on the ensembles we consider. The remarkable loss of signal relative to conventional matrix element calculations is then most certainly due to the single measurement of the two current operator per time slice. By considering smaller pion interpolator separations and current-current separations for larger momenta, we attempt to limit this observed noise growth. To provide a specific example, on the  $a127m413L$  ensemble the largest source-sink separation is limited to  $T \leq 16a$  for  $p_z \simeq 1.525$  GeV. For the corresponding highest lattice momenta we consider on the  $a94m278$  and  $a94m358$  ensembles (green in Fig. 4.5), the source-sink separations are also restricted to  $T \leq 16a$  but a meager  $\mathcal{O}(4)$  measurements of  $R(T)$  are used to constrain the ground-state matrix element. Due to the currents being equidistant between the source and sink pions in our calculation, we cannot populate  $R(T)$  further by repeating the series of sequential inversions for odd values of  $T/a$  (i.e.  $T/a \in \mathbb{Z} \setminus 2\mathbb{Z}$ ). The only remaining value of  $T = 4a$  was not considered, as  $R(T = 4a)$  was found to be quite precise and skewed the high momentum fits.

The aggregate determination of the  $T_1^\pi(\nu, z^2)$  Ioffe-time pseudo-structure function (4.48) from all four ensembles is presented in Fig. 4.6. The data exhibit the expected monotonic decrease as  $\nu$  is increased, however much of these data are characterized by large uncertainty, especially at the largest values of Ioffe-time we consider. The poor precision again originates from the vanishingly small window of reasonable statistical signal for  $R(T)$ ,

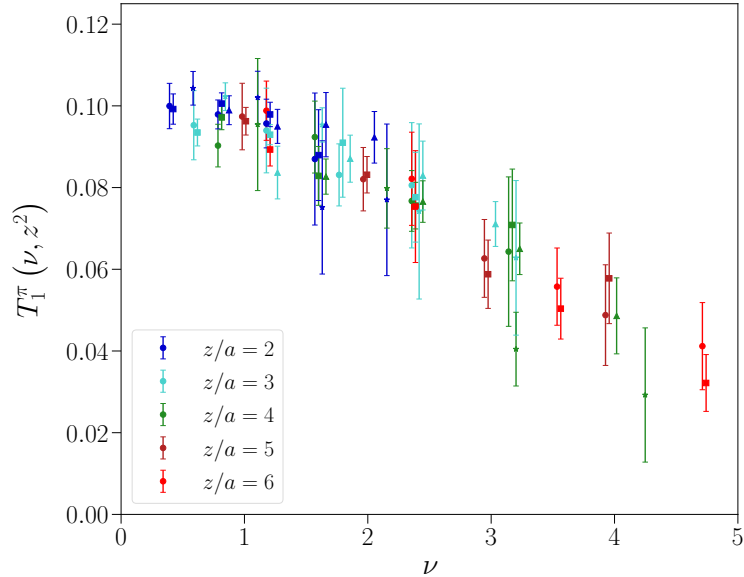


FIG. 4.6: The Ioffe-time pseudo-structure function  $T_1^\pi(\nu, z^2)$  computed on the  $a94m278$  ( $\circ$ ),  $a94m358$  ( $\square$ ),  $a127m413$  ( $\star$ ), and  $a127m413L$  ( $\triangle$ ) ensembles. In the small- $z$  regime  $T_1^\pi(\nu, z^2)$  factorizes into the valence quark PDF of the pion  $f_{q_v/\pi}(x)$ .

especially at the highest momenta on each ensemble. This is indeed a symptom of the manner in which we have implemented the two-current LCS formalism. This is discussed further in Sec. 5.2.4. The final step to obtain  $f_{q_v/\pi}(x)$  will be developed in Ch. 5.

## 4.4 Unpolarized Nucleon Ioffe-time

### Pseudo-Distributions with Distillation

The pseudo-distribution formalism has been leveraged in several lattice calculations of partonic structure of hadrons, including the valence quark content of the pion [122], and the unpolarized valence quark [123, 124, 118, 112] and recently gluon [125] contents of the nucleon. Even though each calculation makes use of standard spatial and momentum smearing techniques, considerable statistical fluctuations are manifest for Ioffe-times in excess of  $\nu \gtrsim 5$  (and at even smaller values for gluonic matrix elements).

Motivated by the demonstrable success of the distillation and momentum smearing amalgam in Ch. 3, we apply for the first time the distillation spatial smearing program to the extraction of PDFs from lattice QCD. The isovector unpolarized valence and plus quark PDFs of the nucleon are obtained on a 349 configuration subset of the  $a94m358$  ensemble listed in Tab. 3.4. This same ensemble, but with a different number of configurations, was used in Sec. 3.1 to compute the nucleon's isovector charges at rest, validate phased distillation in Sec. 3.2.2, and in part compute pion two-current LCS matrix elements in Sec. 4.3. The designation  $a94m358$  is retained for convenience.

To isolate the unpolarized quark PDFs of the nucleon from Ioffe-time pseudo-distributions, we compute the matrix element (4.39) using a purely  $\hat{z}_3$ -boosted nucleon with  $p^\alpha = (E, \mathbf{0}_\perp, p_z)$ , a space-like Wilson line with  $z^\alpha = (0, \mathbf{0}_\perp, z_3)$  and  $\gamma^\alpha = \gamma^4$ . In this setup, the pseudo-ITD is directly related to the space-like matrix element we compute:

$$M_4(p, z_3) = \langle h(p) | \bar{\psi}(z_3) \gamma_4 \Phi_{\hat{z}_3}^{(f)}(\{z_3, 0\}) \frac{\tau^3}{2} \psi(0) | h(p) \rangle = 2EM(\nu, z_3^2), \quad (4.58)$$

where  $\tau^3$  is a Pauli spin matrix and  $\tau^3/2$  projects onto the isovector combination. Accessing this matrix element requires computation of standard two-point

$$C_2(p_z, T) = \langle \mathcal{N}(-p_z, T) \bar{\mathcal{N}}(p_z, 0) \rangle = \sum_n |\mathcal{A}_n|^2 e^{-E_n T} \quad (4.59)$$

and three-point functions featuring the unrenormalized Wilson line operator  $\mathring{\mathcal{O}}_{\text{WL}}^{[\gamma_4]}(z_3, \tau)$ :

$$\begin{aligned} C_3(p_z, T, \tau; z_3) &= V_3 \langle \mathcal{N}(-p_z, T) \mathring{\mathcal{O}}_{\text{WL}}^{[\gamma_4]}(z_3, \tau) \bar{\mathcal{N}}(p_z, 0) \rangle \\ &= V_3 \sum_{n, n'} \langle \mathcal{N}|n'\rangle \langle n|\bar{\mathcal{N}}\rangle \langle n'|\mathring{\mathcal{O}}_{\text{WL}}^{[\gamma_4]}(z_3, \tau)|n\rangle e^{-E_{n'}(T-\tau)} e^{-E_n T}, \end{aligned} \quad (4.60)$$

where the nucleon interpolating fields  $\mathcal{N}$  are smeared with distillation and are separated

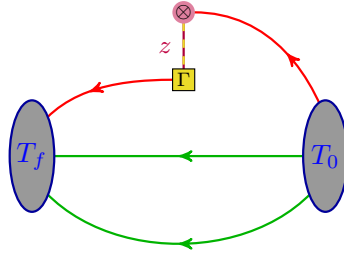


FIG. 4.7: The factorization of a baryonic three-point with the non-local space-like operator  $\mathcal{O}_{\text{WL}}^{[\gamma^4]}(z, \tau)$ . Distillation splits this correlation function into reusable elements (blue), perambulators (green) and generalized perambulators (red) of the form in Eq. 4.61.

by a Euclidean time  $T$ . An explicit momentum projection is performed using the initial points of the Wilson line, thereby leading to an overall spatial volume factor  $V_3$  in the forward case. The Wilson line operator is inserted for  $0 < \tau < T$ . We elect to use the single spatially-local, non-relativistic nucleon interpolating operator  $N^2S_S^{\frac{1}{2}+}$  constructed according to Refs. [69, 79, 84] and summarized in Sections 3.1 and 3.2.2. The reader is reminded distillation factorizes a correlation function into distinct reusable components. The generalized perambulators produced in this case are of the form

$$\begin{aligned} \Xi_{\alpha\beta}^{(l,k)}(T_f, T_0; \tau, z_3) = & \sum_{\vec{y}} \xi^{(l)\dagger}(T_f) D_{\alpha\sigma}^{-1}(T_f, \tau; \vec{y} + z_3 \hat{z}) [\gamma^4]_{\sigma\rho} \\ & \times \Phi_{\hat{z}}^{(f)}(\{\vec{y} + z_3 \hat{z}, \vec{y}\}) D_{\rho\beta}^{-1}(\tau, T_0; \vec{y}) \xi^{(k)}(T_0), \end{aligned} \quad (4.61)$$

where the sum over the initial spatial coordinates of the Wilson line  $\vec{y}$  ensures a zero 3-momentum projection. The genprops are illustrated in Fig. 4.7; the two-point factorization is visualized in Fig. 2.11.

To ensure the matrix elements (4.58) are in the perturbative small- $z$  regime while also maximizing coverage in Ioffe-time, we adopt three eigenvector bases. A precomputed unphased eigenvector basis, and two oppositely phased bases to enhance the boosted nucleon signal in the  $\pm\hat{z}$ -directions. More specifically, the unphased basis is used for the nucleon at

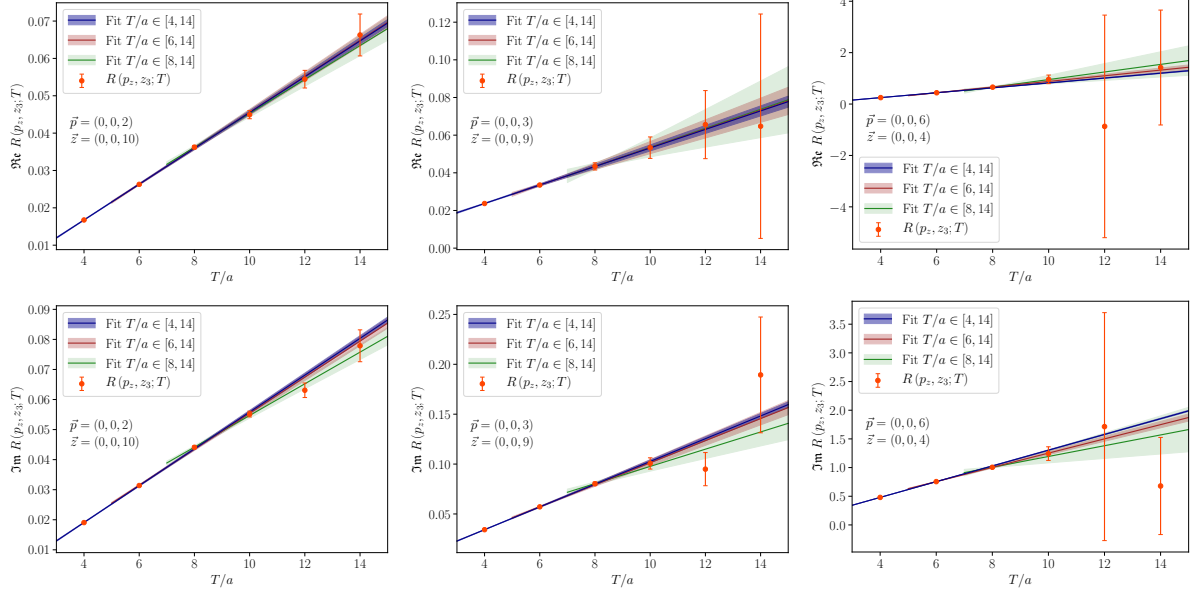


FIG. 4.8: Real (above) and imaginary (below) summation data  $R(p_3, z_3; T)$  for  $\{p_3, z_3/a\} = (0.82 \text{ GeV}, 10), (1.24 \text{ GeV}, 9), (2.47 \text{ GeV}, 4)$  from left to right, together with the linear fit (4.63) applied for different time series. The slope of each linear fit yields the bare matrix element, which is seen to be consistently determined for varied fitting windows. Slight tension in the  $(2.47 \text{ GeV}, 4)$  extracted matrix element is observed as the fitting window is altered. Although minor, this stems from the poorly determined  $T/a = 12, 14$  data.

rest and with small  $\hat{z}$  momenta  $|ap_z| \leq 3[2\pi/L]$ . The phased bases are formed according to Eq. 3.20, where  $\vec{\zeta}_{\pm} = \pm 2 \cdot \frac{2\pi}{L} \hat{z}$  is chosen to respectively resolve the ground-state nucleon in  $\hat{z}$ -boosted frames  $|ap_z| \geq 4[2\pi/L]$ . We employ  $R_{\mathcal{D}} = 64$  eigenvectors within each basis.

The spectral contributions to (4.59) and (4.60) show that the desired ground-state matrix element follows from ratios of the three-point to two-point correlation functions, which plateau asymptotically for  $0 \ll \tau \ll T$ . This was the strategy to extract the nucleon's isovector charges in Ch. 3. The contamination from excited-states is reduced further in this calculation by extracting the matrix elements using the *Summation method* [126, 127], whereby the time slice  $\tau$  on which  $\hat{\mathcal{O}}_{\text{WL}}^{\circ[\gamma_4]}(z_3)$  is introduced is summed over

$$R(p_z, z_3; T) = \sum_{\tau=1}^{T-1} \frac{C_3(p_z, T, \tau; z_3)}{C_2(p_z, T)}. \quad (4.62)$$



Note any contact terms are explicitly excluded. Excited-states in (4.62) scale as  $\exp[-\Delta ET]$ , while in plateau and multi-state fits these effects scale as  $\exp[-\Delta ET/2]$  (cf. Eq. 3.17). As the ground-excited state gap  $\Delta E$  is generally large at low-momenta, the gains afforded by the summation method over plateau/multi-state fits are modest. However, at high-momenta  $\Delta E$  becomes small and the summation method offers considerable suppression of excited-states relative to plateau and multi-state fits. The geometric series resulting from (4.62) depends linearly on the targeted matrix element  $M_4(p_z, z_3)$ , for which we implement the fitting functional

$$R_{\text{fit}}(p_z, z_3; T) = \mathcal{A} + M_4(p_z, z_3)T + \mathcal{O}(e^{-\Delta ET}). \quad (4.63)$$

We note in practice, the excited-state term  $\mathcal{O}(e^{-\Delta ET})$  is found to have no impact on the summation fits performed and is hence omitted from our results.

The two- and three-point functions are computed on four temporal source origins per configuration with  $T/a \in \{4, 6, 8, 10, 12, 14\} \sim 0.38 - 1.32$  fm. This number of source-sink separations is chosen to filter out any excited-states that are not captured by the combined effect of distillation and the summation method, and to ensure our linear fits (4.63) do not over fit our data as signal-to-noise problems become unavoidable. We consider nucleon momenta up to  $|p_z| = 6 \times [2\pi/aL] \sim 2.47$  GeV and Wilson line lengths up to  $z_3/a = 16$ , although only  $z_3/a \leq 12$  will be subsequently used in our analysis. A representative set of  $R(p_3, z_3; T)$  and applied linear fits are shown in Fig. 4.8.

Recall that formation of the reduced pseudo-ITD (4.43) cancels the multiplicative UV divergences produced by the space-like Wilson line and is an important step in our analysis. Normalizing the pseudo-ITD  $\mathcal{M}(\nu, z_3^2)$  by its rest-frame amplitude  $\mathcal{M}(0, z_3^2)$  amounts to dividing  $\mathcal{M}(\nu, z_3^2)$  by the local vector current matrix element. Strictly speaking, the local vector current  $\bar{\psi}\gamma_4\psi$  in lattice QCD is not conserved and contains  $\mathcal{O}(ap)$  effects. To create

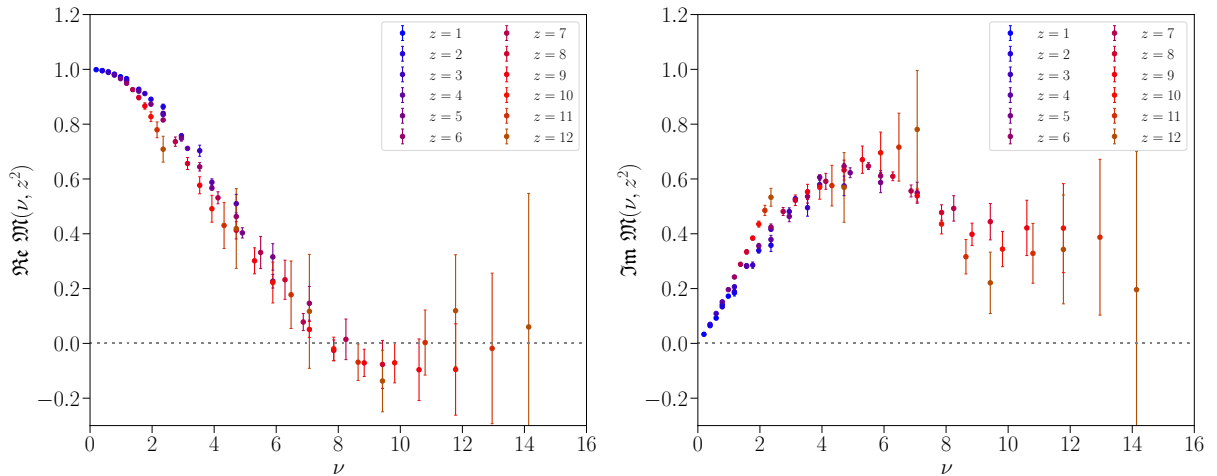


FIG. 4.9: The real (left) and imaginary (right) component of the unpolarized reduced pseudo-ITD on the  $a94m358$  ensemble with Wilson like extents  $z/a < 13$ .

an absolute normalization for  $\mathfrak{M}(\nu, z_3^2)$  originating from each momentum we consider, this  $\mathcal{O}(ap)$  dependence must be removed. An effective prescription [112] to do this involves introduction of a renormalization constant  $Z_V^{eff}$  for each nucleon momentum to ensure  $\lim_{z_3 \rightarrow 0} Z_V^{eff} \mathcal{M}(p_z \cdot z_3, z_3^2) = 1$ . The  $Z_V^{eff}$  factor is simply the bare vector charge  $\hat{g}_V^{u-d}$  in the  $p_z$ -frame. The reduced pseudo-ITD we construct is then obtained by the double ratio

$$\mathfrak{M}(\nu, z_3^2) = \frac{\mathcal{M}(\nu, z_3^2) / [\mathcal{M}(\nu, z_3^2) |_{z_3=0}]}{\mathcal{M}(0, z_3^2) / [\mathcal{M}(0, z_3^2) |_{z_3=0}]} \quad (4.64)$$

This modified ratio is now guaranteed to be unity in the light-cone limit  $z^2 \rightarrow 0$ , leaving its factorization into PDFs from the OPE unaltered. Repeating the matrix element extraction for all momenta and displacements, the real/imaginary components of the unpolarized reduced pseudo-ITD are given in Fig. 4.9.

## 4.5 Closing Remarks

A broad class of matrix elements computable in lattice QCD factorize into PDFs with perturbatively-calculable matching coefficient functions. These so-called Lattice Cross Sections (LCSs) include two-current correlators and Wilson line parton bilinears each of a space-like extent. Although quasi-PDFs catalyzed the resurgence of interest in the light-cone structure of hadrons from lattice QCD, the two-current and pseudo-distribution LCSs offer distinct theoretical advantages. The formalisms of each were developed, and calculations were respectively performed in the pion and nucleon. In the following chapter we will move to discuss how PDFs can reliably be obtained from the Ioffe-time dependent amplitudes computed in this chapter.

# CHAPTER 5

## Extraction of Parton Distributions from LQCD

The two Lattice Cross Sections (LCSs) studied in this dissertation, the two-current correlators and pseudo-distributions, establish coordinate-space factorization schemes between certain lattice calculable matrix elements and the light-cone distributions of hadrons. Untangling the convolutional relationship connecting these data with a desired continuum light-cone distribution represents an inverse problem that is grossly ill-posed - the coordinate-space factorizations of Eq. 4.24 and Eq. 4.44 match discrete lattice data to the continuous PDFs. Even as state-of-the-art computational capabilities have facilitated these studies, contemporary LCS calculations are limited in practice to  $\mathcal{O}(50)$  measurements of the Ioffe-time dependent distributions. The approaching Exascale frontier will most certainly push this number higher, but the central ill-posed inverse problem will remain.

Naively inverting each matching relationship against a discrete dataset produces an infinite set of viable solutions, each having little predictive or postdictive credibility. The

futility of direct inversions has been demonstrated in a few LCS calculations [124, 118], wherein each inversion yielded unstable PDFs with spurious oscillations. The limited range of Ioffe-time accessible to present LCS calculations only compounds the need for refined extraction methods.

This inversion problem is shared with other lattice formalisms that rely on QCD factorization, and indeed the global analysis of inclusive/semi-inclusive processes (see Ch. 2). Although different in character, this problem pervades the quantitative sciences and even impacts the image reconstruction of black holes [128]. Arguably the most serious systematic that must then be confronted in LCS studies is how to reliably extract a targeted distribution, while minimizing numerical artifacts and bias. Numerous sophisticated methods, such as the Backus-Gilbert, maximum entropy, and Bayesian reconstruction methods have been explored as tools to aid in PDF extractions [129, 124] and other observables more generally [130, 131]. This chapter will develop and apply both standard and novel extraction procedures in order to obtain the PDFs of the pion and nucleon from the Ioffe-time dependent distributions isolated in Chapter 4.

## 5.1 Regularization Through Model Ansätze

All partonic distributions of hadrons, such as PDFs and GPDs, are not direct physical observables. It is the application of the QCD factorization theorems to inclusive and exclusive scattering processes that splits the experimentally-measured hadronic cross sections into partonic hard contributions, and the long-distance non-perturbative parton distributions. Section 2.2.2 outlined that the global fitting community relies on well-informed PDF parameterizations in order to extract these continuous distributions from discrete measurements of the  $x$  and  $Q^2$  dependencies of the DIS structure functions and Drell-Yan cross sections. In this section, the PDF forms used by many of the leading global fitting

collaborations will be looked at in more detail. Given the many similarities to the inverse problem faced when attempting to relate LCS quantities to PDFs, we propose a novel fitting prescription that has the potential to capture and remove systematic effects from LCS data while simultaneously extracting the targeted PDF.

### 5.1.1 Phenomenology

If the DIS structure functions could be measured continuously across its independent variables  $x$  and  $Q^2$ , PDFs could be obtained straightforwardly at some order in  $\alpha_s$  by inverting the factorization relationship (2.33); numerical stability and to what order in  $\alpha_s$  the matching coefficients are computed to would then be the principal sources of potential pitfall. The extraction of PDFs from global analyses of only discretely measured (semi-)inclusive structure functions can only proceed by modeling phenomenologically the PDF in question. Selections must be made for the precise parametric form and the order of perturbative truncation in the DIS coefficient functions, or partonic cross section in the case of Drell-Yan. A parametric fit does however offer several important benefits: any parton sum rules, as well as known convergent/divergent behavior of PDFs in the  $x \rightarrow 1$  and  $x \rightarrow 0$  regimes, can be engineered into the functional form. While the truncation in  $\alpha_s$  does ultimately affect the PDF extraction<sup>1</sup>, the most serious source of bias arises from the model chosen to describe the PDF. The optimal method to understand the severity of this bias and minimize its effect is achieved by traversing the full range of functional descriptions consistent with the symmetries and sum rules of QCD. Fortunately the global fitting community implements this mantra quite well, as we now explore.

Consider the light quark sector  $\{u, d, s\}$ , the corresponding anti-quarks and gluon.

---

<sup>1</sup>The treatment of heavy quark flavors  $\{c, b, t\}$  can also heavily influence PDFs for each flavor. This complication is not discussed, but the reader is directed to any of the cited phenomenological PDF results for a thorough discussion.

Recent PDF sets in this sector at an initial scale  $Q_0^2$  published by the CJ [132] and MSTW [133] collaborations make use of functional form

$$xf_{a/h}(x, Q_0^2) = Ax^\alpha (1-x)^\beta (1 + \gamma\sqrt{x} + \delta x), \quad (5.1)$$

while the 2014 PDF set from MMHT [37] exploits a slightly modified form

$$xf_{a/h}(x, Q_0^2) = Ax^\alpha (1-x)^\beta \left( 1 + \sum_{k=1}^4 c_k T_k^{\text{Ch}}(1 - 2\sqrt{x}) \right), \quad (5.2)$$

where  $T_k^{\text{Ch}}$  are Chebyshev polynomials in the combination  $(1 - 2\sqrt{x})$ . The Chebyshev terms are clearly more sophisticated than the combination  $(1 + \gamma\sqrt{x} + \delta x)$ . Indeed the authors of the MMHT set, some of whom also authored the MSTW set, note the Chebyshev parameterization is more favorable, as the expansion coefficients  $c_k$  were found to be more stable than the  $\gamma, \delta$  terms in (5.1). Other collaborations, such as the CTEQ-TEA (CT) collaboration, have made use of the functional form

$$xf_{a/h}(x, Q_0^2) = Ax^\alpha (1-x)^\beta \sum_{k=1}^4 c_k b_k^4(\sqrt{x}) \quad (5.3)$$

in their 2018 global analysis [36], where  $b_n^m(y) = \binom{m}{n} y^n (1-y)^{m-n}$  are Bernstein polynomials. The authors note the Bernstein polynomials minimize rapid variation in the PDF in the limiting  $x \rightarrow 0/x \rightarrow 1$  regimes, and likewise cut down on correlations between the  $c_k$  parameters that would conventionally multiply fractional powers of  $x$ .

The similarities between each functional form cannot be missed. Each PDF parameterization is nominally expressed as  $xf_{a/h}(x, Q_0^2) = Ax^\alpha (1-x)^\beta P(x)$ . The  $x \rightarrow 0$  behavior is described by a Regge-like term  $x^\alpha$  [134], while the  $x \rightarrow 1$  regime is described by a  $(1-x)^\beta$  term consistent with power counting rules derived in perturbative QCD [135]. Fi-

nally, if a momentum sum rule exists for a specific parton flavor, the coefficient  $A$  ensures that the sum rule is satisfied - otherwise the parameter is left to float.

As PDFs are involved with intrinsically inelastic scattering processes, the use of the term Regge-like for the small- $x$  behavior of the PDF would seem inappropriate. The phenomenological use of *Regge* in this context stems from early efforts to understand hadronic elastic scattering amplitudes  $T(s, t)$ , with  $\{s, t\}$  the standard Mandelstam variables. In the large- $s$  regime, the amplitude scales as  $T(s, t) \sim s^{\alpha(t)}$  with the power law dictated by  $\alpha(t) = \alpha_0 + \alpha' \cdot t$ , or a *Regge trajectory* which governs the linear dependence of the invariant mass of resonances on their spin. The insistence of the global fitting community on terms like  $\sqrt{x}$  can be understood qualitatively in terms of  $q\bar{q}$  pairs produced at small- $x$ . These quark-antiquark pairs look like a  $\rho$ -meson which lies on a Regge trajectory with  $\alpha_0 \sim 0.5$  and  $\alpha' \sim 1$  [136]. These statements are given a rigorous backdrop in Ref. [137] in terms of the Veneziano dual model [138] of the strong interactions.

Returning to the global fitting forms, apart from details relevant to error estimation/propagation and fitting frameworks, the primary difference between these global fits is the smooth function  $P(x)$  used to connect the limiting PDF behaviors. Other popular PDF sets are provided by the NNPDF collaboration [139, 38], unique among the global fitting collaborations in their parameterization of  $P(x)$  using a neural network.

The different functional forms of each collaboration are subject to different systematics and fit parameter correlations. Indeed these effects may adversely affect any one particular PDF set. Taken together however, the consistency of PDFs obtained by each collaboration (cf. Fig. 2.6 and Fig. 2.7), in spite of the varied treatments of the smooth interpolating polynomial  $P(x)$ , strengthens considerably the universality of PDFs obtained from data and justifies the functional parameterization as a sound method to regulate the inverse problem.



The LCSs presented in Ch. 4 generically face an inverse problem represented by

$$L = \sum_{a=q,\bar{q},g} K_a(\alpha_s) \otimes \mathcal{F}_a(\mu^2) + h.t., \quad (5.4)$$

where  $L$  are the Ioffe-time dependent invariant amplitudes associated with the two-current or Wilson line matrix elements that factorize into perturbative kernels  $K_a$  and the PDFs up to higher-twist ( $h.t.$ ) corrections. Inspired by the phenomenological forms of the global fitting community, we will first extract PDFs of the nucleon and pion from the data in Ch. 4 using the parameterizations

$$f_{q_v/h}(x, \mu^2) = N_v x^\alpha (1-x)^\beta P(x) \quad (5.5)$$

$$f_{q_+/h}(x, \mu^2) = N_+ x^{\alpha_+} (1-x)^{\beta_+} P(x). \quad (5.6)$$

Given the limited range of Ioffe-time in our results, we will find the simplest 2-parameter ansatz with  $P(x) = 1$  cannot be rejected. Where possible, the bias of this highly-constraining choice will be studied by supplementing  $P(x)$  with additional half-integer powers of  $x$ :  $P(x) = 1 + \sum_k \lambda_k x^{(k+1)/2}$ , thereby increasing the flexibility of our parameterizations. The light valence quark PDFs of the nucleon and pion each satisfy the quark counting rule  $\int_0^1 dx f_{q_v/\{\pi, N\}}(x) = 1$ , for which we fix  $N_v^{-1} = B(\alpha + 1, \beta + 1) + \sum_k \lambda_k B(\alpha + 1 + \frac{k+1}{2}, \beta + 1)$ .<sup>2</sup> These functional forms we adopt parallel those of CJ and MSTW, and are used almost exclusively in other lattice calculations (e.g. [122, 118, 123, 114, 124, 140]). Ultimately any PDF reported from a lattice calculation should take into account the space of functions that smoothly connects the  $x \rightarrow 0$  and  $x \rightarrow 1$  limits, as is done in the global fitting community. We now turn to a more refined fitting prescription.

---

<sup>2</sup> $B(n, m) = \int_0^1 dx x^{n-1} (1-x)^{m-1}$  is the beta function or Euler integral of the first kind.

### 5.1.2 Jacobi Polynomials

The phenomenological parameterizations we have considered thus far are but one way to regulate the ill-posed inverse relating an LCS invariant to the corresponding PDF. As an alternative means to describe the valence/plus quark sectors and minimize model bias, we propose to parameterize the PDFs by a complete basis of classical orthogonal polynomials.<sup>3</sup> The leveraging of orthogonal polynomials to obtain an unknown distribution is not unique to this work. The approach we adopt parallels efforts to extract PDFs from phenomenological fits of inclusive processes [37, 141], as well as distribution amplitudes [142, 143] and inelastic scattering cross sections [144] from matrix elements calculated in lattice QCD.

Consider the Jacobi (hypergeometric) polynomials

$$P_n^{(\alpha,\beta)}(z) = \frac{\Gamma(\alpha+n+1)}{n!\Gamma(\alpha+\beta+n+1)} \sum_{j=0}^n \binom{n}{j} \frac{\Gamma(\alpha+\beta+n+j+1)}{\Gamma(\alpha+j+1)} \left(\frac{z-1}{2}\right)^j, \quad (5.7)$$

which form an orthogonal basis of polynomials on the interval  $z \in [-1, 1]$  with respect to the metric  $(1-z)^\alpha (1+z)^\beta$  for  $\alpha, \beta > -1$ :

$$\int_{-1}^1 dz (1-z)^\alpha (1+z)^\beta P_n^{(\alpha,\beta)}(z) P_m^{(\alpha,\beta)}(z) = \frac{\delta_{n,m} 2^{\alpha+\beta+1}}{2n+\alpha+\beta+1} \frac{\Gamma(\alpha+n+1)\Gamma(\beta+n+1)}{n!\Gamma(\alpha+\beta+n+1)}.$$

Under the mapping  $z \mapsto 1-2x$  the mapped Jacobi polynomials

$$\Omega_n^{(\alpha,\beta)}(x) = \sum_{j=0}^n \underbrace{\frac{\Gamma(\alpha+n+1)}{n!\Gamma(\alpha+\beta+n+1)} \binom{n}{j} \frac{(-1)^j \Gamma(\alpha+\beta+n+j+1)}{\Gamma(\alpha+j+1)}}_{\omega_{n,j}^{(\alpha,\beta)}} x^j, \quad (5.8)$$

form a complete basis of orthogonal polynomials on the interval  $x \in [0, 1]$  with respect to the metric  $x^\alpha (1-x)^\beta$ . The shifted orthogonality relation is omitted for brevity. As the

---

<sup>3</sup>A truncation of the basis will be necessary in practice.

set of polynomials  $\{\Omega_n^{(\alpha,\beta)}\}$  span the interval  $x \in [0, 1]$ , a PDF can be expressed generically as

$$f_{q/h}(x) = x^\alpha (1-x)^\beta \sum_{n=0}^{\infty} C_{q,n}^{(\alpha,\beta)} \Omega_n^{(\alpha,\beta)}(x), \quad (5.9)$$

with expansion coefficients  $C_n^{(\alpha,\beta)}$ . The parameters  $\{\alpha, \beta\}$  lose their familiar characterization of the  $x \rightarrow 0/x \rightarrow 1$  PDF behaviors in place of delineating different choices of bases. The expansion in Jacobi polynomials in Eq. (5.9) is thus entirely generic and model-independent. However, the series of Jacobi polynomials must in practice be truncated at some finite order- $n$ . By using a basis of orthogonal polynomials, it is hoped the bias introduced is less than for the phenomenological forms of Eq. 5.5 and Eq. 5.6. Two simple ways to study this bias include fixing the order of truncation and determining the optimum  $\{\alpha, \beta\}$ , or tuning  $\{\alpha, \beta\}$  to capture generic properties of a PDF and subsequently optimize the order of truncation. This prescription will be applied in Sec. 5.3, but first we turn to simple fits of the pion pseudo-structure function data.

## 5.2 Pion Valence PDF from Ioffe-time Pseudo-Structure Functions

The results for the  $T_1^\pi(\nu, z^2)$  Ioffe-time pseudo-structure functions across the four gauge ensembles considered in Sec. 4.3 allow the pion mass, lattice spacing, and volume dependence to be quantified. We only include the two-current LCS matrix elements in our analysis if  $|z| \leq 0.56$  fm, which is sufficiently smaller than  $\Lambda_{\text{QCD}}^{-1}$  and hence in the perturbative regime. These data are then assured to be in the perturbative regime where the factorization relationship is valid, and are also minimally afflicted by higher-twist effects. The reader is reminded that all matrix elements with  $z/a = 1$  have been excluded on the basis of contact terms. The data satisfying these conditions from the four ensembles

we have considered are shown in Fig. 4.6.

A global fit of these data can then be leveraged to obtain the  $T_1^\pi(\nu, z^2)$  Ioffe-time pseudo-structure function in the physical limit. As  $T_1^\pi(\nu, z^2)$  is functionally unknown and analytic in  $\nu$  (Sec. 4.2.1), we implement a flexible  $z$ -*expansion* fit

$$T_1^\pi(\nu, z^2) = \sum_{k=0}^{k_{\max}=4} \lambda_k \rho^k + b_1 (m_\pi - m_\pi^{\text{phys}}) + b_2 a + b_3 z^2 + b_4 a^2 p^2 + b_5 e^{-m_\pi(L-z)} \quad (5.10)$$

supplemented with well-informed chiral ( $b_1$ ), discretization ( $b_2, b_4$ ), higher-twist ( $b_3$ ) and finite-volume ( $b_5$ ) corrections, with  $\rho = \frac{\sqrt{\nu_{\text{cut}} + \nu} - \sqrt{\nu_{\text{cut}}}}{\sqrt{\nu_{\text{cut}} + \nu} + \sqrt{\nu_{\text{cut}}}}$ . Higher-order ( $k_{\max} > 4$ ) expansion terms have no statistical significance and are omitted. We selected  $\nu_{\text{cut}} \equiv 1$  to be consistent with Ref. [122]; although other choices are possible, they did not affect the final fit band.

The  $z$ -expansion fit is inspired by conformal mappings developed in model-independent form factor descriptions [145, 146] that must confront non-analytic behavior in the targeted distribution. Given the analyticity of  $T_1^\pi(\nu, z^2)$ , with the exception of  $\nu \rightarrow \infty$ , there is no non-analytic region of  $T_1^\pi(\nu, z^2)$  that is avoided by selecting  $\nu_{\text{cut}}$ . In this sense,  $\nu_{\text{cut}}$  does not have a physical interpretation, and is only useful here as part of the conformal mapping that provides a description of  $T_1^\pi(\nu, z^2)$  in general terms. The corrections in (5.10) are selected based on each being the dominant contribution of its type. For instance, model calculations suggest spatially non-local operators are subject to volume corrections that scale as  $e^{-m_\pi(L-z)}$  [108]. The global  $z$ -expansion fit provides an excellent description of the data with  $\chi^2/\text{d.o.f} = 1.20$ . Removing the corrections  $b_i$  (upper panel of Tab. 5.1) from the  $z$ -expansion result  $T_1^\pi(\nu, z^2)$ , one obtains the structure function  $T_1^\pi(\nu)$  in the physical limit, which is shown by the indigo band in Fig. 5.1. The statistical error of  $T_1^\pi(\nu)$  is estimated by the  $\rho_k$  covariances.

The corrections listed in the upper panel of Tab. 5.1 indeed indicate that the two-current LCS data are most sensitive to pion mass and finite-volume effects. The lack of

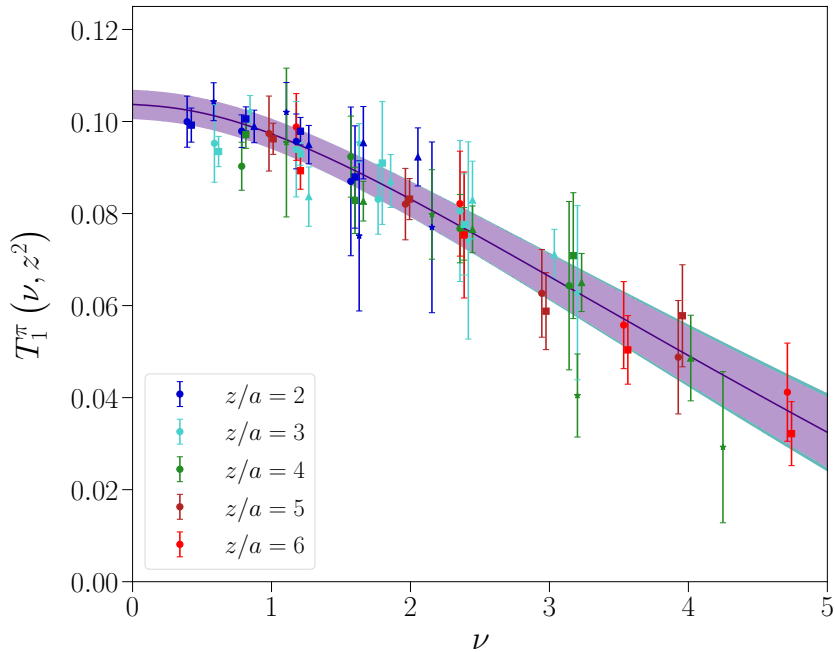


FIG. 5.1: Simultaneous and correlated  $z$ -expansion fit to the  $T_1^\pi(\nu, z^2)$  Ioffe-time pseudo-structure function computed on the  $a94m278$  ( $\circ$ ),  $a94m358$  ( $\square$ ),  $a127m413$  ( $\star$ ), and  $a127m413L$  ( $\triangle$ ) ensembles. The indigo band is  $T_1^\pi(\nu)$  in the continuum limit, having removed the lattice effects parameterized by the  $b_i$  coefficients in Eq. 5.10. The  $\rho_k$  covariances are used to determine the  $T_1^\pi(\nu)$  errorband. The outer dark cyan band is the result of combining the  $T_1^\pi(\nu)$  statistical uncertainties in quadrature with the systematic  $b_i$  uncertainties.

$z^2$ -dependence is also evident from the global fit, where the associated correction  $b_3$  is seen to be small and consistent with zero. On the one hand, this may be taken as an encouraging sign that the two-current LCS data are not affected by higher-twist effects. However, the absolute lack of any  $z^2$ -dependence translates into an inability to resolve the scale dependence of these data and hence a rigorous application of DGLAP [22, 23, 24].

Other possible correction terms included in the  $z$ -expansion, such as  $a^2$ ,  $m_\pi^2$ ,  $Le^{-m_\pi(L-z)}$ ,  $\sqrt{L}e^{-m_\pi(L-z)}$ , were also considered. Each alternate correction is given in the lower panel of Tab. 5.1. The most important observation is the independence of the  $z$ -expansion parameters  $\lambda_k$  for each alternate correction. In other words, the  $T_1^\pi(\nu)$  and ultimately  $f_{q_v/\pi}(x)$  determinations are unaffected by the alternate corrections considered. Furthermore, the fitted value of each alternate correction is seen to be sub-leading to those considered in

Correction	$b_i$	$\lambda_0$	$\lambda_1$	$\lambda_2$	$\lambda_3$	$\lambda_4$	$\chi^2/\text{d.o.f.}$
$(m_\pi - m_\pi^{\text{phys}})$	0.174(96)	0.104(3)	-0.006(3)	-0.029(9)	-0.907(404)	0.124(136)	1.20
$a$	-0.083(43)	...	...	...	...	...	...
$z^2$	-0.0004(7)	...	...	...	...	...	...
$a^2 p^2$	0.007(8)	...	...	...	...	...	...
$e^{-m_\pi(L-z)}$	0.102(51)	...	...	...	...	...	...
$a^2$	-0.049(34)	0.104(3)	-0.006(3)	-0.028(9)	-0.901(391)	0.124(135)	1.26
$(m_\pi^2 - m_\pi^{\text{phys} 2})$	0.15(12)	0.104(3)	-0.006(3)	-0.029(10)	-0.926(388)	0.118(132)	1.18
$Le^{-m_\pi(L-\xi)}$	0.007(3)	0.104(3)	-0.006(3)	-0.028(10)	-0.915(402)	0.121(136)	1.22
$\sqrt{L}e^{-m_\pi(L-\xi)}$	0.026(14)	0.104(3)	-0.006(3)	-0.029(10)	-0.914(403)	0.121(136)	1.21

TABLE 5.1: (Upper panel) Fit parameters of the  $z$ -expansion fit in Eq. 5.10 where ellipses are placeholders for the correction terms in the  $z$ -expansion fit, which all have the same  $\lambda_i$  and  $\chi^2/\text{d.o.f.}$  (Lower panel) Alternative corrections supplementing the  $z$ -expansion fit of  $T_1^\pi(\nu, z^2)$ . The alternate coefficients  $b_k$  are seen to be sub-leading relative to the adopted fit, and the  $z$ -expansion parameters are unaltered.

Eq. 5.10. We then proceed with  $T_1^\pi(\nu)$  obtained from Eq. 5.10, as the leading corrections are the greatest sources of systematic effects.

Having obtained the continuous distribution  $T_1^\pi(\nu)$  in the physical limit, it would seem the inverse problem we face to extract  $f_{q_v/\pi}(x, \mu^2)$  is now moot. Although tempting, this is not valid, as it would imply our  $z$ -expansion has garnered infinite resolution in Ioffe-time from an otherwise discrete dataset. To retain the same information content as was in  $T_1^\pi(\nu, z^2)$  across the four ensembles, we make 30 correlated and equally spaced slices of the physical  $T_1^\pi(\nu)$  in the interval  $\nu \in [0, 4.71]$ ; this number is in accordance with the 20 points determined on the *a094m278* and *a094m358* ensembles. The mean and covariance of these sampled data points are used to create 200 Gaussian pseudodata samples. We note this multi-step analysis is performed using the ROOT [147] library. Varying the number of derived pseudodata samples or increasing the number of  $T_1^\pi(\nu)$  slices cannot strongly impact the  $f_{q_v/\pi}(x, \mu^2)$  fit results, because of the highly correlated  $T_1^\pi(\nu)$  data. This was confirmed by repeating the PDF extraction now discussed.

The extraction of  $f_{q_v/\pi}(x, \mu^2)$  follows from numerically evaluating the convolution of the NLO matching kernel (4.53) with two- and three-parameter PDF functional forms (5.5),

and fitting these to bootstrap samples of the  $T_1^\pi(\nu)$  pseudodata:

$$T_1^\pi(\nu)_{\text{fit}} = \int_0^1 dx K_1^{\text{NLO}}(x\nu, z^2\mu^2) f_{q_v/\pi}(x, \mu^2). \quad (5.11)$$

Because of the lack of an observed scale dependence in these data ( $b_3$  correction of Eq. 5.10), we make the assignment  $z = 2a = 0.188$  fm, the shortest Wilson line length in this study, in the NLO matching kernel present in Eq. 5.11. The matched input scale in  $\overline{\text{MS}}$  was taken to be  $\mu_0 = 2$  GeV, for which the three-flavor value  $\alpha_s(2 \text{ GeV}) \simeq 0.303$  was taken from the LHAPDF6 library [148]. The normalization of the PDF is fixed to an appropriate reciprocal sum of beta functions due to the sum rule  $\int_0^1 dx f_{q_v/\pi}(x, \mu^2) = 1$ . Since the  $T_1^\pi(\nu)$  only exists in the limited interval  $\nu \in [0, 4.71]$ , we also supply extra physically motivated constraints  $\{\alpha \leq 0, \beta \leq 4\}$  to help stabilize the fits. The constraint  $\alpha < 0$  reflects the expected Regge behavior of the PDF at small- $x$ , while  $\beta < 4$  is a flexible range that captures the pQCD expectation of  $\beta = 2$  and surrounding values. A four-parameter fit with  $P(x) = (1 + \sigma\sqrt{x} + \delta x)$  was found to have no distinction from the three-parameter fit, as  $\sigma \simeq 0$ . This agrees with our leading-order extraction of  $f_{q_v/\pi}(x, 1 \text{ GeV}^2)$  on the  $a127m417L$  ensemble [119], as well as predictions from Dyson-Schwinger calculations [149] and global fits to experimental data. Table 5.2 summarizes the  $f_{q_v/\pi}(x, \mu_0^2)$  parameters obtained from the NLO fits to the physical  $T_1^\pi(\nu)$  structure function. A comparison is also made with our previous  $f_{q_v/\pi}(x, 1 \text{ GeV}^2)$  result computed on the  $a127m417L$  ensemble [119], which was obtained from a three-parameter LO fit of the  $T_1^\pi(\nu, z^2)$  pseudo-structure function. The pion valence quark PDFs associated with the parameters given in Tab. 5.2 are illustrated in Fig. 5.2(a).

$N_{\text{param}}$	$\alpha$	$\beta$	$\delta$	$\chi_r^2$
2	$-0.17(7)_{\text{stat}}(2)_{\text{sys}}$	$1.24(22)_{\text{stat}}(7)_{\text{sys}}$	—	1.41
3	$-0.22(11)_{\text{stat}}(3)_{\text{sys}}$	$2.12(56)_{\text{stat}}(14)_{\text{sys}}$	$4.28(1.73)_{\text{stat}}(25)_{\text{sys}}$	1.29
3	$-0.34(31)_{\text{stat}}$	$1.93(68)_{\text{stat}}$	$3.05(2.50)_{\text{stat}}$	2.2

TABLE 5.2: (Top panel) Results for  $f_{q_v/\pi}(x, \mu_0^2)$  using two- and three-parameter phenomenological ansätze convolved with the NLO matching kernel (4.53) at an initial scale of  $\mu_0 = 2$  GeV. The systematic uncertainty of each PDF fit parameter set is obtained by a 10% variation of  $\alpha_s$  from the nominal three-flavor  $\alpha_s(2 \text{ GeV}) \simeq 0.303$  value taken from LHAPDF6 [148]. (Bottom panel) Results of a leading order three-parameter fit to  $T_1^\pi(\nu, z^2)$  computed on the *a127m417L* ensemble [119], with the PDF parameterized at an initial scale  $\mu_0 = 1$  GeV. The  $z$ -expansion was not implemented in this LO analysis, so errors are statistical only and no corrections have been implemented.

### 5.2.1 Discussion of $f_{q_v/\pi}(x)$ Results

The commensurate figures-of-merit shown in Tab. 5.2 between the two- and three-parameter NLO fits to the  $T_1^\pi(\nu)$  data (5.11) limits the selection of one fit over another based solely on the goodness of fit. The NLO analysis of the vector-axial two-current matrix elements computed across the four ensembles, has however led to a statistically better determined  $(1-x)$  exponent. As seen in Fig. 5.2(a), the two-parameter NLO fit appears to favor a harder  $(1-x)$  approach to  $x$  of unity, while the three-parameter NLO fit appears to prefer a softer approach to momentum fractions of unity.

To truly distinguish between these different large- $x$  behaviors of  $f_{q_v/\pi}(x)$ , data for the  $T_1^\pi(\nu)$  ITD is required over a much larger range of Ioffe-time. This is understood quantitatively by reconstructing the  $T_1^\pi(\nu)$  ITD by convolving the NLO kernel with the PDFs obtained from the fits to the pseudodata samples. These reconstructed distributions, denoted  $K^{\text{NLO}}(\nu, z^2 \mu^2) \otimes f_{q_v/\pi} |_{N=\text{param}}$ , are compared with the true  $T_1^\pi(\nu)$  distribution in Fig. 5.2(b). The two-parameter reconstruction is seen to underestimate the uncertainty of the physical  $T_1^\pi(\nu)$  ITD by  $\sim 8 - 12\%$  for  $\nu > 4$ , and starts to deviate all together as  $\nu$  increases further. The uncertainty estimate of the three-parameter reconstruction is of



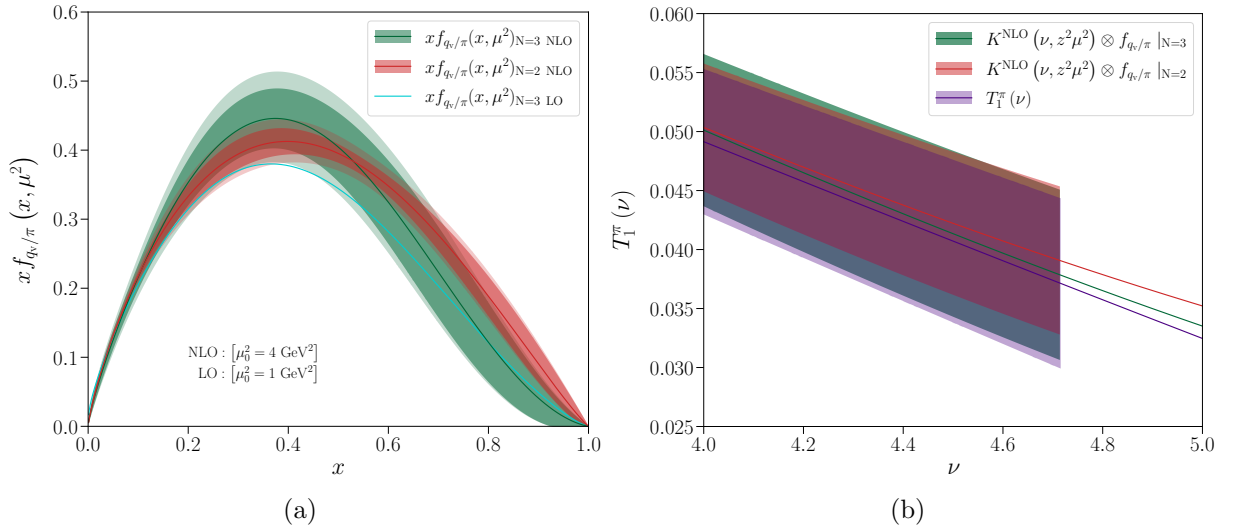


FIG. 5.2: (a) The pion valence quark distribution obtained from fitting the convolution of the NLO matching kernel (4.53) and two- and three-parameter PDF ansätze to the  $T_1^\pi(\nu)$  ITD obtained from the  $z$ -expansion fit (5.10). The two- and three-parameter PDFs are obtained from the NLO matching at an initial scale  $\mu_0^2 = 4 \text{ GeV}^2$ , and are given in red and green respectively. The same PDF obtained from a three-parameter LO matching of the *a127m413L*  $T_1^\pi(\nu, z^2)$  at  $\mu_0^2 = 1 \text{ GeV}^2$  is given in cyan - error is omitted for clarity, but may be found in Ref. [119]. (b) Comparison of  $T_1^\pi(\nu)$  with reconstructions from the PDF fits for  $4 < \nu < 5$ .

the same scale as the physical  $T_1^\pi(\nu)$  ITD, but is shifted slightly vertically. One can show that for a fixed value of  $\alpha$  in either the two- or three-parameter PDF ansätze we have considered, the ITD will decrease more rapidly as a function of  $\nu$  for smaller values of  $\beta$  relative to larger values. By extrapolating the central curve of the true and reconstructed ITDs beyond the largest Ioffe-time  $\nu = 4.71$  accessible in this calculation, it is clear were data available up to  $\nu \sim 10$  the  $T_1^\pi(\nu)$  ITD would then be able to discriminate between the two- and three-parameter forms. While PDFs can minimally be described by the  $x^\alpha(1-x)^\beta$  functional form, encompassing the Regge theory [134] and pQCD based power counting rules [135], the flexibility favored by modern global analyses [141, 37, 38] inform our decision to give higher credence to the three-parameter NLO fit. The inclusion of the, albeit simple, polynomial  $P(x) = 1 + \delta x$  that interpolates between the small- and large- $x$  regimes affords a more flexible and less biased description of the PDF.

### 5.2.2 Comparison with Experiment

The valence quark PDF of the pion is known experimentally from Drell-Yan scattering of pions from fixed-target proton rich nuclei, such as platinum and tungsten. This phenomenologically important distribution is constrained by only three experiments from the mid- to late-1980s, two at CERN [150, 151] and most recently the E615 experiment at Fermilab [152]. The shape of  $f_{q_v/\pi}(x)$  extracted in several analyses of the world data [153, 154, 155, 156, 157] are mutually in tension, and contrast sharply with expectations from perturbative QCD [158]. Various model calculations exemplify this disparity, with some favoring a harder  $\sim (1-x)$  and others a softer  $\sim (1-x)^2$  falloff as  $x \rightarrow 1$ . Although lattice calculations may one day unambiguously provide a first-principles resolution to this confusion, our goal with these calculations of  $f_{q_v/\pi}(x)$  is to establish the two-current LCS formalism as a particularly effective scheme to access the collinear momentum distributions of hadrons.

To this end, we evolve our extracted PDFs in Fig. 5.2(a) from their initial scales to  $\mu^2 = 27 \text{ GeV}^2$ , commensurate with the Fermilab E615 pionic Drell-Yan data. The evolved PDFs are shown in Fig. 5.3, and are juxtaposed with a LO factorization [152] of the E615 data and a re-analysis of the Drell-Yan data [156] where next-to-leading-logarithmic threshold soft-gluon resummation effects [121] have been included in the partonic cross section calculation. The LO experimental analysis clearly favors a harder  $(1-x)$  approach of the PDF to  $x = 1$ , while the resummation of soft-gluon logarithms leads to a softer  $(1-x)^2$  approach. In comparing our  $x f_{q_v/\pi}(x, \mu^2)$  results, the importance of an NLO matching of the two-current LCS coordinate space matrix elements is evident by the observed deviation of the LO three-parameter PDF from the experimental data and our NLO results. Both the two- and three-parameter PDF forms are remarkably consistent with experiment over the entire range of  $x$  when the NLO matching relationship is included. The

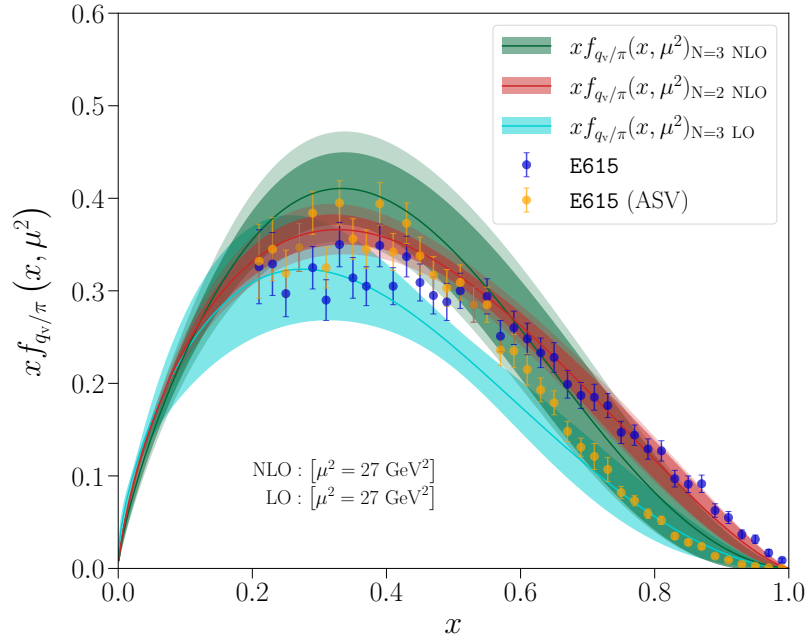


FIG. 5.3: The  $xf_{q_v/\pi}(x, \mu^2)$  distributions evolved to the scale  $\mu^2 = 27 \text{ GeV}^2$ . The PDFs resulting from the two- and three-parameter NLO analyses of the  $T_1^\pi(\nu)$  ITD are shown in red and green, respectively. The three-parameter PDF obtained from the LO analysis of  $T_1^\pi(\nu, z^2)$  on the  $a127m413L$  ensemble is given in cyan. This evolution scale was chosen to facilitate a direct comparison with a LO analysis [152] of the E615 pionic Drell-Yan data (blue points), and a re-analysis [159] accounting for the emission of soft gluons [156] (orange points).

two-parameter  $xf_{q_v/\pi}(x, \mu^2)$  obtained at NLO favors the hard approach to  $x = 1$ , while the three-parameter determination is in better agreement with the re-analyzed E615 data. Regardless, our NLO determinations evolved to  $\mu^2 = 27 \text{ GeV}^2$  are statistically consistent with each other. Future two-current LCS calculations with a greater reach in Ioffe-time and improved precision will hopefully lead to statistically meaningful differences between these NLO PDF results.

A generic feature worth noting in our LO and NLO determinations is the peak in  $xf_{q_v/\pi}(x, \mu_0^2)$  is below  $x = 0.5$  (cf. Fig. 5.2(a)) regardless of the initial scale considered. Furthermore, as these PDF sets are evolved to  $\mu^2 = 27 \text{ GeV}^2$  the peak likewise shifts towards smaller values of  $x$  and the upward concavity of each distribution in the large- $x$  regime increases. These observations are indicative of the dynamic gluonic content of the

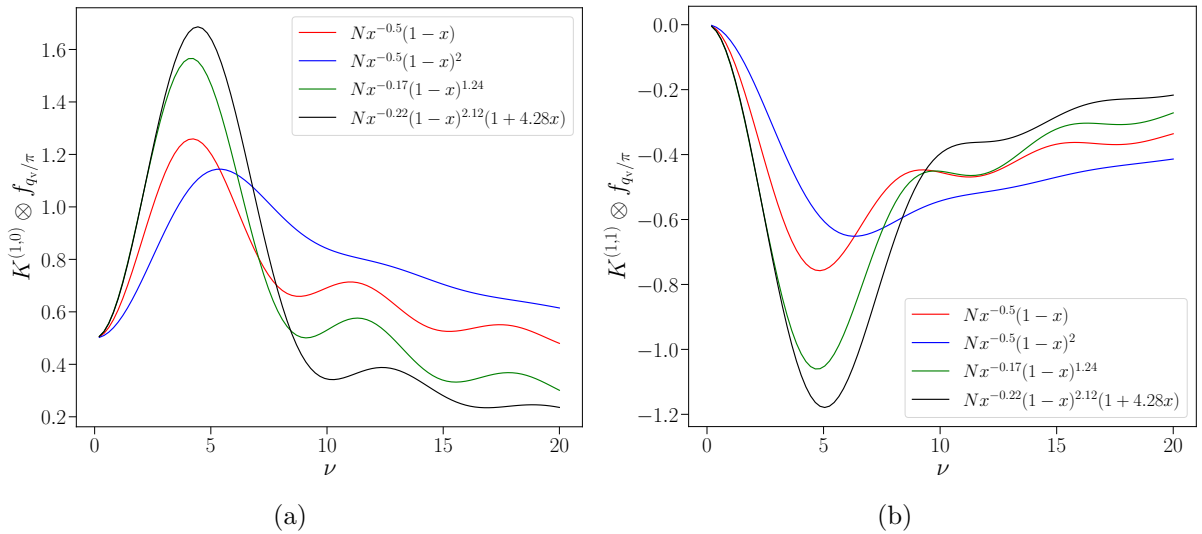


FIG. 5.4: (a) The convolution of the  $K^{(1,0)}$  kernel with model PDFs. (b) The convolution of the  $K^{(1,1)}$  kernel with model PDFs. Note the green and black model PDFs are precisely the PDF results obtained from the above global analysis of the  $T_1^\pi(\nu)$  ITD using the NLO matching kernel. The respective agreement between the green and black  $K^{(1,0)}$  and  $K^{(1,1)}$  convolutions reiterates  $T_1^\pi(\nu, z^2)$  data at larger values of  $\nu$  are needed to discriminate these PDF parameterizations.

pion; a conclusion borne out in global analyses and consistent with the pion existing as the Goldstone mode associated with dynamical chiral symmetry breaking [157].

### 5.2.3 Stability of the NLO Matching Kernel

A considerable advantage of the short-distance factorization of LCS coordinate space matrix elements into PDFs is the absence of large logarithmic corrections often encountered in the conventional QCD factorization of momentum space observables. Having discussed these details in Sec. 4.3.1, this section is dedicated to an explicit demonstration of the stability and mild impact of the NLO coordinate space matching relationship (4.53). The reader is directed to Ref. [120] for a useful comparison between the tree-level and one-loop matching kernels, wherein the ratio  $K^{(1)}/K^{(0)}$  is visualized as an asymptotic series.

To demonstrate the effect of the NLO kernels  $K^{(1,0)}$ ,  $K^{(1,1)}$ , consider their convolutions

with model pion valence quark PDFs

$$K^{(1,i)}(\nu) \otimes f_{q_v/\pi}(\mu^2) = \int_0^1 \frac{dx}{x\nu} K^{(1,i)}(x\nu) f_{q_v/\pi}(x, \mu^2), \quad (5.12)$$

with  $i \in \{0, 1\}$ . These convolutions are visualized for four different parameterizations of the pion valence quark PDF in Fig. 5.4(a) and Fig. 5.4(b), two of which are those reported in Tab. 5.2 from our NLO analysis of  $T_1^\pi(\nu)$ . These convolutions represent the difference between the  $\overline{\text{MS}}$  PDF and the two-current LCS matrix elements, and are seen to be structurally quite similar but roughly opposite in sign. Each convolution reaches an extremum around  $\nu \sim 5.0$  and begins to decay to zero at larger values of Ioffe-time. Evidently the NLO effects are most significant around the highest Ioffe-times available to our calculations ( $\nu \sim 4.71$ ). These convolutions demonstrate a reassuring feature of the position space matching. By including the one-loop prefactors  $\alpha_s$  and  $\ln(-z^2\mu^2 e^{2\gamma_E}/4)$  onto the kernels  $K^{(1,i)}$ , it is clear the full NLO term  $K^{(1)}$  is of  $\mathcal{O}(\alpha_s)$  over the entire range of Ioffe-time. Furthermore, each convolution is smooth, without cusps, and does not show any large logarithmic corrections. These behaviors are encouraging, and show the two-current LCS formalism is not subject to large perturbative corrections and has the potential to complement the well-established and modern state-of-the-art global fits of PDFs.

#### 5.2.4 Areas for Improvement in Two-current LCSs

The first and most practical means of improving the  $f_{q_v/\pi}(x)$  determination is to simultaneously analyze other current combinations that are anti-symmetric in Dirac indices. The namesake of the lattice cross section formalism solicits an even more general scenario where numerous current combinations, even those that access the CP-odd combination  $f_{q_+/\pi}(x)$ , are considered. For instance, consider a symmetric vector-vector LCS matrix

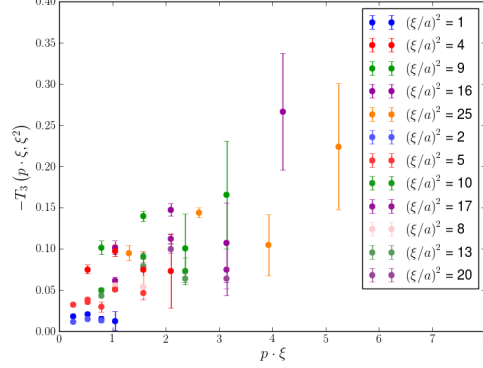


FIG. 5.5: The  $T_g^\pi(\nu, z^2)$  pseudo-structure function obtained on the *a127m413* ensemble by averaging  $\gamma_x\gamma_x$  and  $\gamma_y\gamma_y$  two-current combinations. Lack of a clear functional trend together with a floating normalization of  $f_{q_+/\pi}(x)$  accessible from these current combinations, limits a global analysis with the vector-axial currents.

element  $M_{VV}^{\mu\nu}(p, z) = z^4 \langle \pi(p) | \mathcal{J}_V^\mu(z) \mathcal{J}_V^\nu(0) | \pi(p) \rangle$ . With only four symmetric combinations of the Lorentz structures  $\{p^\mu, z^\mu\}$ , the Lorentz decomposition of  $M_{VV}^{\mu\nu}(p, z)$  is given by

$$M_{VV}^{\mu\nu}(p, z) = \frac{p^\mu p^\nu}{p^2} T_{pp}(\nu, z^2) + \frac{1}{2} \frac{(p^\mu z^\nu + z^\mu p^\nu)}{\nu} T_{pz}(\nu, z^2) + g^{\mu\nu} T_g(\nu, z^2) + \frac{z^\mu z^\nu}{z^2} T_{zz}(\nu, z^2). \quad (5.13)$$

The generic LO coordinate space quark matrix element (4.31) reduces in this case to  $M_{VV}^{\mu\nu(0)} = -\frac{2\nu x}{\pi^2} \sin(x\nu) (\nu^{-1} [p^\mu z^\nu + z^\mu p^\nu] - g^{\mu\nu})$ . The non-trivial LO matching coefficients

$$K_g^{q(0)}(x\nu, z^2) = -\frac{ix\nu}{\pi^2} (e^{ix\nu} - e^{-ix\nu}) \quad K_{pz}^{q(0)}(x\nu, z^2) = \frac{2ix\nu}{\pi^2} (e^{ix\nu} - e^{-ix\nu}) \quad (5.14)$$

follow easily and confirm the symmetric  $M_{VV}^{\mu\nu}(p, z)$  accesses  $f_{q_+/\pi}(x)$ . A global analysis of the vector-axial  $T_1^\pi(\nu, z^2)$  and vector-vector  $T_g^\pi(\nu, z^2)$  pseudo-structure functions was attempted on the *a127m413* ensemble in an effort to jointly constrain  $f_{q_+/\pi}(x)$ . This effort was fraught with numerical instability, as both  $T_1^\pi(\nu, z^2)$  and  $T_g^\pi(\nu, z^2)$  lack well-determined functional behaviors, as seen in Fig. 4.6 and Fig. 5.5. Absent any algorithmic

improvements or changes in lattice parameters, the most feasible method to improve the  $f_{q_v/\pi}(x)$  determination is simply to analyze other current channels that exclusively access this CP-even combination.

Some of these challenges are attributable to our present two-current LCS implementation, including a single measurement of the two-current matrix element per time slice, and a limited number of temporal separations used to constrain the ground-state matrix elements. The former is a consequence of having not performed a momentum projection, equivalently a volume average, on the two-current operator time slice, as this would nullify our ability to control the hard scale  $z$  needed for the short-distance factorization. The dramatic scatter seen in  $T_1^\pi(\nu, z^2)$  (Fig. 4.6) and  $T_g^\pi(\nu, z^2)$  especially for small- $\nu$  cannot be explained by poorly constrained matrix elements. The currents implemented in these two-current LCS results are local and introduce error of  $\mathcal{O}(a)$ . Many coordinate space methods with local currents are known to have the most severe discretization errors when currents are separated along lattice axes [59, 142]. By considering separations along body or facial diagonals these discretization effects can be reduced [142]. A dedicated calculation in the freefield to more rigorously assess the impact of discretization effects in these LCSs is a high priority for future work.

### 5.3 Unpolarized Nucleon PDFs from Ioffe-time Pseudo-Distributions

As PDFs are determined phenomenologically at a factorization scale  $\mu^2$  in  $\overline{\text{MS}}$  to renormalize the associated collinear divergences, the nucleon unpolarized reduced pseudo-ITD shown in Fig 4.9 must be matched to a common scale in  $\overline{\text{MS}}$  prior to any meaningful comparisons. At one-loop and without loss of generality, negating the sign of the  $\mathcal{O}(\alpha_s)$

correction and interchanging the ITD and reduced pseudo-ITD in (4.44), one obtains the factorization relationship that matches at NLO the reduced pseudo-ITD to the ITD:

$$\mathcal{Q}(\nu, \mu^2) = \mathfrak{M}(\nu, z^2) + \frac{\alpha_s C_F}{2\pi} \int_0^1 du \left[ \ln \left( \frac{e^{2\gamma_E+1} z^2 \mu^2}{4} \right) B(u) + L(u) \right] \mathfrak{M}(u\nu, z^2). \quad (5.15)$$

This relationship describes the evolution of each distinct set of  $\mathfrak{M}(\nu, z^2)$  data of constant- $z^2$  to a common scale  $\mu^2$  in  $\overline{\text{MS}}$ . Regardless of whether the evolution and matching steps are done separately or in one step, a smooth and continuous description of the reduced pseudo-ITD for each  $z^2$  is required. It is common in the literature to find polynomials in Ioffe-time fit to each set of distinct  $z^2$  data in order to build  $\mathfrak{M}(u\nu, z^2)$  [118, 123, 114, 124]. Interpolations within a range of Ioffe-time available to a calculation are also common, and when utilized have been found to be consistent with polynomial fits [118, 124].

A polynomial in  $\nu$  is perhaps a dubious choice, as it cannot capture the correct limiting behavior of the ITD at large- $\nu$ . To understand this, consider a simple nucleon valence PDF ansatz

$$f_{q_v/N}(x) = \frac{\Gamma(\alpha + \beta + 2)}{\Gamma(\alpha + 1)\Gamma(\beta + 1)} x^\alpha (1-x)^\beta. \quad (5.16)$$

The cosine transform of this ansatz with respect to Ioffe-time (Eq. 4.40) is given by

$$\Re \mathcal{Q}(\nu, \alpha, \beta) = \frac{\pi \Gamma(2 + \alpha + \beta)}{2^{1+\alpha+\beta}} {}_2F_3 \left( \frac{1+\alpha}{2}, \frac{2+\alpha}{2}; \frac{1}{2}, \frac{2+\alpha+\beta}{2}, \frac{3+\alpha+\beta}{2}; -\frac{\nu^2}{4} \right), \quad (5.17)$$

with  ${}_2F_3$  a generalized hypergeometric function and  $\alpha, \beta > -1$ . In the large Ioffe-time regime (5.17) behaves as

$$\Re \mathcal{Q}(\nu) \simeq \beta \cos \left( \frac{\pi}{2} \alpha \right) \frac{\Gamma(\alpha + 2)}{\nu^{\alpha+2}} - \sin \left( \frac{\pi}{2} \alpha \right) \frac{\Gamma(\alpha + 1)}{\nu^{\alpha+1}}. \quad (5.18)$$

For the real component of the ITD to correspond to a valence PDF with a finite sum rule,



the ITD must then vanish for asymptotically large- $\nu$  (i.e.  $\alpha > -1$ ). This suggests the usefulness of a smooth polynomial in  $\nu$  extends only so far as interpolating the discrete pseudo-ITD data, and should not be used as a measure of the moments of the pseudo-PDFs given their divergent behavior at large- $\nu$ . This motivates methods to directly extract the PDFs from the reduced pseudo-ITD, thereby obviating the need for a continuous description of  $\mathfrak{M}(\nu, z^2)$  in order to perform the evolution/matching steps. This will be developed in Sec. 5.3.2.

To get a handle on the scale dependence of our data and ground the ensuing discussion, we nonetheless start with a provisional sixth order polynomial fit in Ioffe-time to the reduced pseudo-ITD for constant  $z^2$ :

$$\mathfrak{M}(\nu, z^2) = 1 + \sum_{n=1}^3 (c_{2n}\nu^{2n} + ic_{2n-1}\nu^{2n-1}). \quad (5.19)$$

The even (odd) powers of the polynomial are applied to jackknife samples of the real (imaginary) component of  $\mathfrak{M}(\nu, z^2)$  given in Fig. 4.9. Higher order polynomials were considered, but were found to be unconstrained by the data. With the polynomial fits in hand, we perform the evolution and scheme conversion convolutions (5.15) in a single step. The matched  $\overline{\text{MS}}$  scale  $\mu = 2$  GeV was chosen, and the strong coupling  $\alpha_s(2 \text{ GeV}) \simeq 0.303$  was adopted from LHAPDF6 [148]. The scale  $\mu = 2$  GeV corresponds to the reduced pseudo-ITD being evolved to the common distance scale  $z_0^2 = 4e^{-2\gamma_E-1}(2 \text{ GeV})^{-2} \simeq 0.12 \text{ GeV}^{-2}$  or  $z_0^{-1} \simeq 2.94 \text{ GeV}$ . On this ensemble *a094m358*, this common scale then equates to  $z_0^2/a^2 \simeq 0.511$ . The computed evolution and scheme matching convolutions are depicted in Fig. 5.6 for the real and imaginary components, respectively. It is curious the evolution and matching convolutions appear to be nearly equal in magnitude but opposite in sign. This feature of the pseudo-distributions has been observed in independent calculations [123, 124] and hints that an NNLO matching relation may not be needed.

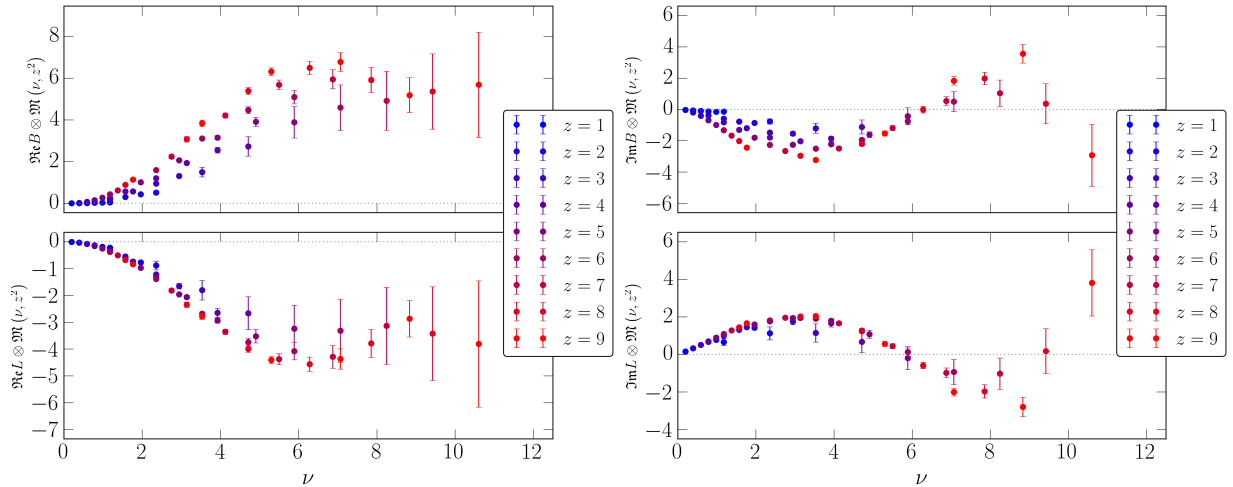


FIG. 5.6: Convolutions needed to evolve (upper) and match (lower) the reduced pseudo-ITD to a common scale of 2 GeV in  $\overline{\text{MS}}$ . The real and imaginary convolutions are shown at the left and right, respectively. The NLO prefactor  $\alpha_s C_F / 2\pi$  is included in these data, but omitted from the labels for clarity. The convolutions were performed up to  $z/a = 16$ , but data for  $z/a > 9$  are generally noisy and not shown.

When the scale and scheme conversion are incorporated, we observe in Fig. 5.7 a dramatic collapse of the reduced pseudo-ITD onto a common curve for  $z/a \lesssim 10$ . The lack of residual  $z^2$ -dependence is particularly striking in the real component of the ITD, but less so in the imaginary component. This confirms the formation of the reduced ratio (4.43) indeed cancels much of the  $z^2$ -dependence in the pseudo-ITD, with any remaining at small- $z^2$  ideally described by the coordinate-space DGLAP evolution [109].

### 5.3.1 PDF Extractions from ITDs

The effort spent evolving the reduced pseudo-ITD data to a common scale allows the simple Fourier transform relating the ITD and PDF (4.40) to be invoked. Of course the PDF defined in terms of the ITD  $f_{a/h}(x, \mu^2) = (2\pi)^{-1} \int_{-\infty}^{\infty} d\nu e^{-i\nu x} \mathcal{Q}(\nu, \mu^2)$  remains an ill-posed inverse. Regularization of the inverse problem at this stage with a PDF ansatz is however cheap and numerically stable relative to a direct matching to the reduced pseudo-ITD.

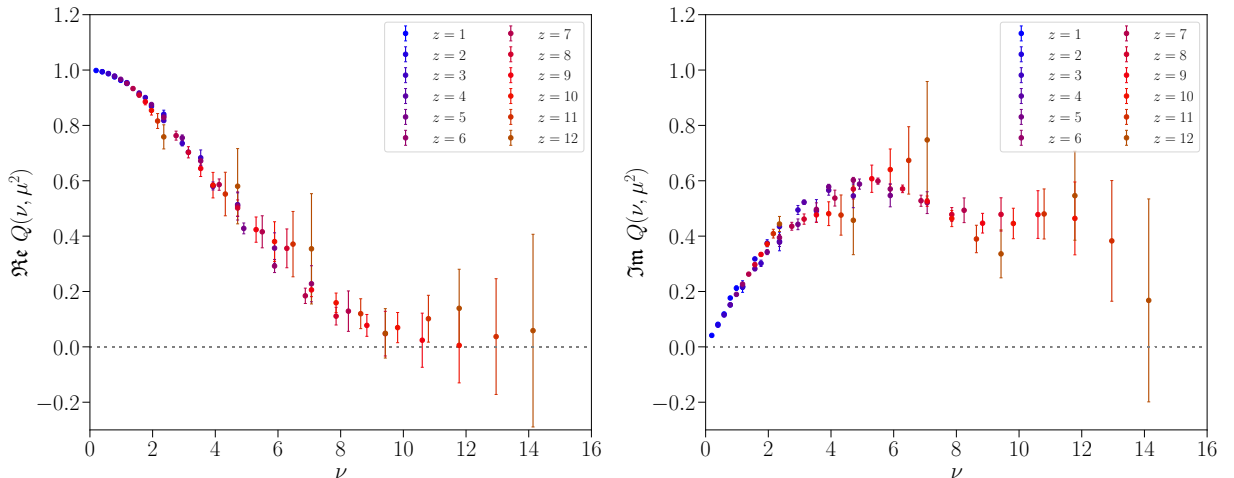


FIG. 5.7: The real (left) and imaginary (right) components of the unpolarized ITD at a scale of 2 GeV in  $\overline{\text{MS}}$  obtained from the matching relation (5.15) applied to polynomial fits of the reduced pseudo-ITD data. Data is shown for Wilson line extents  $z/a \leq 12$  - Wilson lines of  $z/a > 12$  are considerably uncertain, and thus excluded from our ensuing analysis.

To form a backdrop for the PDF extraction methods we consider, simple two- and three-parameter PDF parameterizations (Eq. 5.5 and 5.6) are our starting point. In the three-parameter case, we take  $P(x) = 1 + \delta x$ . The cosine/sine transforms of these PDF forms are fit to the real/imaginary ITD data using first an uncorrelated least-squares regression

$$\chi^2 = \sum_{\nu_{\min}}^{\nu_{\max}} \frac{[\mathcal{Q}(\nu, \mu^2) - \mathcal{Q}_{\text{fit}}(\nu, \mu^2)]^2}{\sigma_{\mathcal{Q}}^2}, \quad (5.20)$$

with  $\sigma_{\mathcal{Q}}^2$  the variance of the ITD, and  $\{\nu_{\min}, \nu_{\max}\}$  representing potential cuts on the data. These uncorrelated fits include all  $z/a \in \{1, \dots, 12\}$  and  $ap_z \in \{1, \dots, 6\} \times 2\pi/L$ . For ease of later reference, this method of extraction is denoted type-*C*. The fits to the real and imaginary components of the ITD are shown in Fig. 5.8(a) and Fig. 5.9(a). The resulting valence and plus quark PDFs are juxtaposed with phenomenological determinations in Fig. 5.8(b) and Fig. 5.9(b). The phenomenological PDFs are three flavor NLO determinations by the CJ (CJ15n1o) [132] and JAM (JAM20-SIDIS\_PDF\_proton\_nlo) [160] collaborations, and three flavor NNLO determinations of MSTW (MSTW2008nn1o68c1\_nf4) [161]

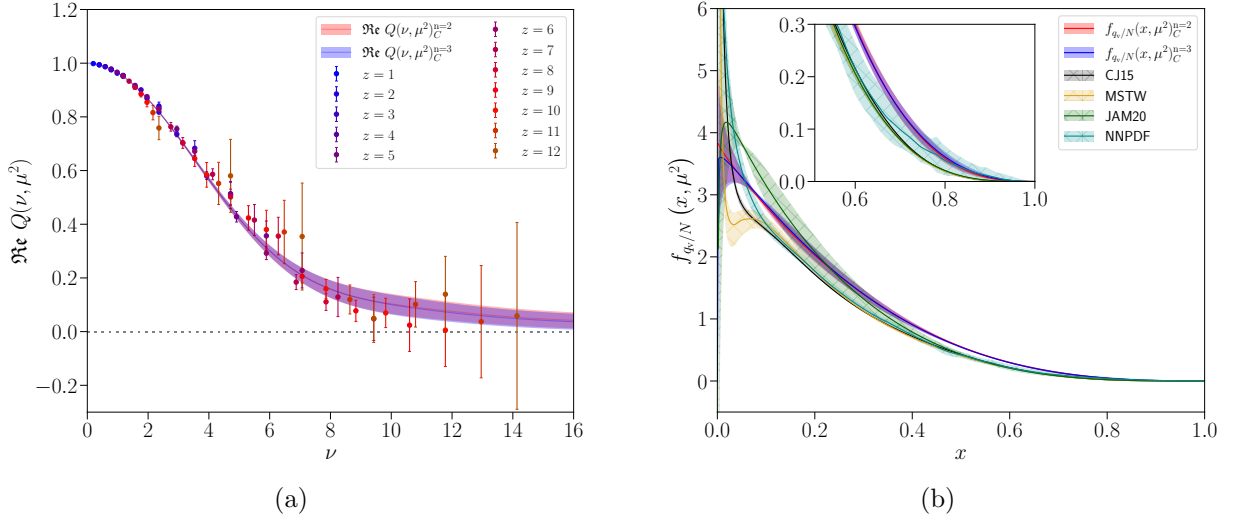


FIG. 5.8: (a) Real component of the matched ITD at  $\mu = 2$  GeV in  $\overline{\text{MS}}$  fit by cosine transforms of two- and three-parameter model PDFs (Eq. 5.5). Data have been fit for  $z/a \leq 12$ , and correlations have been neglected. The resulting PDF parameters and figure of merit are gathered in Tab. 5.3. (b) The two- and three-parameter PDF parameterizations are compared with four phenomenological determinations (noted in text) at the same scale.

$N_{\text{param}}$	$N_{v/+}$	$\alpha$	$\beta$	$\gamma$	$\delta$	$\chi_r^2$
2	–	–0.006(98)	2.754(285)	–	–	2.183(483)
3	–	0.019(98)	2.212(291)	–	–0.737(12)	2.192(490)
2	3.616(2.260)	–0.077(275)	2.983(606)	–	–	2.780(806)

TABLE 5.3: Unpolarized nucleon valence and plus quark PDF parameters obtained from performing uncorrelated cosine/sine transform fits to the real/imaginary component of the matched ITD at 2 GeV in  $\overline{\text{MS}}$ . Results for the plus quark PDF are only shown for  $N_{\text{param}} = 2$ , where the smooth polynomial  $P(x) = 1$ , as higher numbers of parameters led to uncontrolled fits. The uncorrelated figure of merit is also shown.

and NNPDF (NNPDF31\_nnlo\_pch\_as\_0118\_mc\_164) [38].

Apart from the  $z/a \geq 9$  data, such an uncorrelated fit would seem to well describe the  $\Re Q(\nu, \mu^2)$  data and lead to valence PDFs that feature many structural similarities with phenomenological determinations at the same scale. The statistically consistent figure of merit for the two- and three-parameter fits tabulated in Tab. 5.3, however indicates the data cannot distinguish between these models. The two-parameter fit to  $\Im Q(\nu, \mu^2)$  is

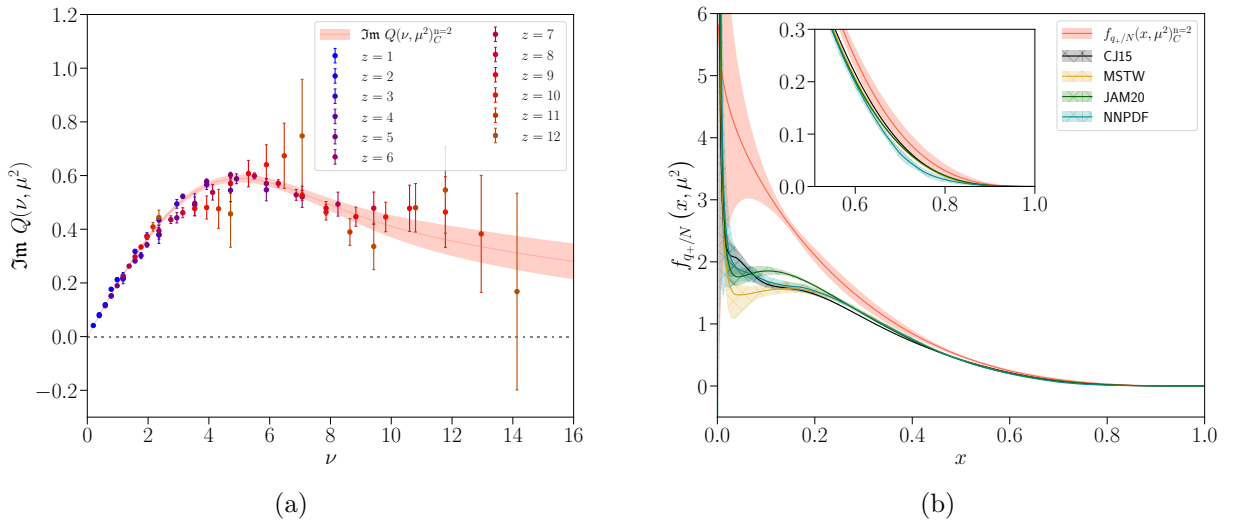


FIG. 5.9: (a) Imaginary component of the matched ITD at  $\mu = 2$  GeV in  $\overline{\text{MS}}$  fit by a sine transform of a two-parameter model PDF (Eq. 5.6). Data has been fit for  $z/a \leq 12$ , and correlations have been neglected. The resulting PDF parameters and figure of merit are gathered in Tab. 5.3. (b) The two-parameter PDF parameterization is compared with four phenomenological determinations (noted in text) at the same scale.

clearly more heavily constrained by the  $z/a \lesssim 7$  data, and all but avoids points of the ITD originating from larger separations. Above  $x \sim 0.4$  the extracted  $f_{q_+/N}(x, \mu^2)_{C^{n=2}}$  result likewise shares structural similarities with the shown phenomenological results. The lack of any large- $\nu$  constraint provided by  $\Im Q(\nu, \mu^2)$  entails a generally unconstrained fitted PDF in the small- $x$  regime, although this relation is not bijective.

### 5.3.2 Direct Extraction of PDFs from Reduced Pseudo-ITDs

A separate, though in principle equivalent, route to extract PDFs from these data is to directly apply the factorized relationship (4.44) having substituted the definition of the ITD:

$$\mathfrak{M}(\nu, z^2) = \int_{-1}^1 dx \int_0^1 du \mathcal{C}(u, z^2 \mu^2, \alpha_s(\mu^2)) e^{ix\nu} f_{q/N}(x, \mu^2) + \sum_{k=1}^{\infty} \mathcal{B}_k(\nu) (z^2)^k. \quad (5.21)$$

By assuming a PDF parameterization and performing a maximum likelihood regression of the double convolution and  $\mathfrak{M}(\nu, z^2)$ , the introduction of additional systematic errors from the evolution/matching steps and a potentially incorrect functional description of  $\mathfrak{M}(\nu, z^2)$  when interpolating its  $\nu$ -dependence (e.g. Eq. 5.19) can all be avoided. The direct matching relationship between the PDFs and the reduced pseudo-ITD is given by

$$\left\{ \begin{array}{l} \Re \\ \Im \end{array} \right\} \mathfrak{M}(\nu, z^2) = \int_0^1 dx \left\{ \begin{array}{l} \mathcal{K}_v(x\nu, z^2\mu^2) f_{q_v/N}(x, \mu^2) \\ \mathcal{K}_+(x\nu, z^2\mu^2) f_{q_+/N}(x, \mu^2) \end{array} \right\} + \sum_{k=1}^{\infty} \mathcal{B}_k(\nu) (z^2)^k, \quad (5.22)$$

where the one-loop kernels that match the  $\{x, \mu^2\}$ -dependencies of the valence/plus quark PDFs to the reduced pseudo-ITD are given by

$$\mathcal{K}_v(x\nu, z^2\mu^2) = \cos(x\nu) - \frac{\alpha_s C_F}{2\pi} \left[ \ln \left( \frac{e^{2\gamma_E+1} z^2 \mu^2}{4} \right) \tilde{B}_v(x\nu) + \tilde{D}_v(x\nu) \right] \quad (5.23)$$

$$\mathcal{K}_+(x\nu, z^2\mu^2) = \sin(x\nu) - \frac{\alpha_s C_F}{2\pi} \left[ \ln \left( \frac{e^{2\gamma_E+1} z^2 \mu^2}{4} \right) \tilde{B}_+(x\nu) + \tilde{D}_+(x\nu) \right], \quad (5.24)$$

with the Altarelli-Parisi and scheme matching kernels modified to

$$\tilde{B}_v(y) = \frac{1 - \cos(y)}{y^2} + \frac{3 - 4\gamma_E}{2} \cos(y) + 2 \sin(y) \frac{y \text{Si}(y) - 1}{y} + 2 \cos(y) [\text{Ci}(y) - \ln(y)]$$

$$\tilde{B}_+(y) = -\frac{\sin(y) + y}{y^2} + \frac{3 - 4\gamma_E}{2} \sin(y) - 2 \cos(y) \frac{y \text{Si}(y) - 1}{y} + 2 \sin(y) [\text{Ci}(y) - \ln(y)]$$

$$\tilde{D}_v(y) = -4y \Im [e^{ix} {}_3F_3(111; 222; -iy)] + \cos(y) (1 + 2/y^2) - 2/y^2$$

$$\tilde{D}_+(y) = 4y \Re [e^{ix} {}_3F_3(111; 222; -iy)] + \sin(y) (1 + 2/y^2) - 2/y,$$

and  $\text{Si}(y)/\text{Ci}(y)$  are the integral sine/cosine functions and  ${}_3F_3(111; 222; -iy)$  is a generalized hypergeometric function [162, 115]. A notable challenge of this direct approach is the multi-precision arithmetic and computational efficiency required for sufficient and timely convergence of the generalized hypergeometric function. PDFs extracted by directly

$N = 2_{v/+}$	$N_{v/+}$	$\alpha$	$\beta$	$\chi_r^2$
$2_v$	–	–0.030(96)	2.601(277)	7.364(761)
$2_+$	5.131(3.405)	0.091(299)	3.244(638)	4.536(902)

TABLE 5.4: Unpolarized nucleon valence and plus quark PDF parameters obtained from type- $K$  fits to the real/imaginary component of  $\mathfrak{M}(\nu, z^2)$ .

performing parametric fits (5.22) to the reduced pseudo-ITD data are denoted type- $K$ .

Simple two-parameter PDFs obtained from uncorrelated type- $K$  fits are shown in Fig. 5.10(a) and Fig 5.10(b), together with the same phenomenological determinations and the uncorrelated type- $C$  two-parameter PDF fits. Visually the type- $C$  and type- $K$  fits are statistically consistent. This is confirmed by comparing the type- $K$  fit results in Tab. 5.4 to the type- $C$  results in Tab. 5.3. However, the central values of the type- $K$  fits suggest that at small- $x$  the  $f_{q_v/N}(x)$  is more divergent and the  $f_{q_+/N}(x)$  is instead convergent for small- $x$  at the scale  $\mu = 2$  GeV. The factor of two or three increase in

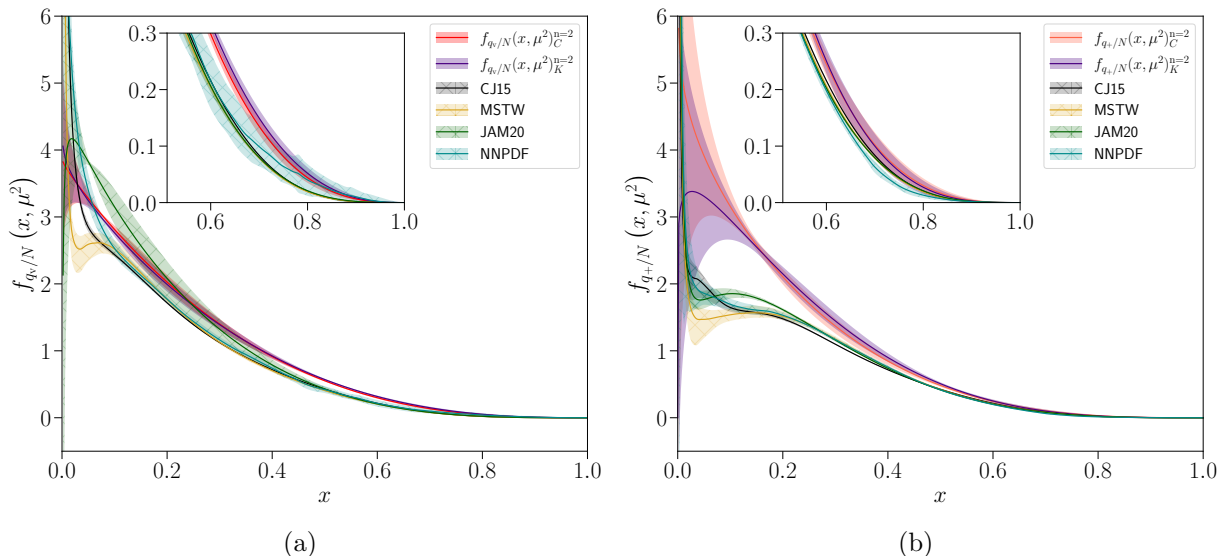


FIG. 5.10: Two-parameter valence (a) and plus (b) quark PDFs resulting from type- $C$  (red) and type- $K$  (indigo) fits to the unpolarized nucleon ITD and reduced pseudo-ITD, respectively. The direct matching fits are consistent with the cosine/sine transform of the model PDF fit to the ITD.

the figure of merit when switching from type- $C$  to type- $K$  fits is the first indication of puzzling behavior in  $\mathfrak{M}(\nu, z^2)$ . We reiterate that the naive two-parameter fits capture the known limiting regimes of the PDFs. The poor figures of merit in the type- $K$  fits hint that  $\mathfrak{M}(\nu, z^2)$  at this stage apparently does not align well with expectations from the direct matching (5.22). This is a potentially disastrous conclusion. To gain some insight, we now consider the data correlations.

### Data Correlation

The data featured in this and indeed any lattice calculation naturally are correlated. By beginning this subsection with uncorrelated fits, we highlight that without knowledge or through the simple neglect of data correlations, which appears to be common in the literature, one might incorrectly assume an adequate description of the data has been achieved. These correlations must be taken into account in order to provide a rigorous accounting of mutual fluctuations in the data and thus an agnostic PDF determination.

Simply repeating the two-parameter fit to  $\Re \mathcal{Q}(\nu, \mu^2)$ , only this time accounting for the data covariance, we arrive at a much different conclusion shown in Fig. 5.11(a). The visual discrepancy between the ITD and two-parameter fit is stark, and leads to a correlated  $\chi^2/\text{d.o.f} \sim \mathcal{O}(40)$ . Although the fit misses nearly all of the moderate to large- $z$  points, Fig. 5.11(b) illustrates that the large increase in the figure of merit is primarily due to the slight deviation from the very precise  $z/a \lesssim 4$  data. Visualizing the data covariance in the real component in Fig. 5.12(a), it is clear the low-momentum data  $ap_z \leq 4\pi/L$  are strongly correlated amongst each other and correlate weakly with the  $ap_z \geq 8\pi/L$  data; some mild correlation is visible with the  $ap_z = 6\pi/L$  data with  $z/a \leq 6$ . Within the  $ap_z \leq 4\pi/L$  channels the strongest correlation can be found in the shortest Wilson line data. These observations provide an explanation for the poor correlated two-parameter fit in Fig. 5.11(a) - the strongest correlation is with the most precise data in our calculation



causing any correlated fit to favor the small- $\nu$  data. Indeed strong correlation is also observed amongst the momentum channels  $ap_z = \{4, 5, 6\} \times 2\pi/L$ , but the signal-to-noise degradation for these high-momentum data minimizes their effect on any fit. It is curious this delineation corresponds to the transition from an unphased to phased eigenvector basis. The data covariance in the imaginary component, shown in Fig. 5.12(b), shows the strongest correlations within each momentum channel and between adjacent Wilson line lengths (e.g.  $z/a = 4$  and  $z/a = 5$ ). It is then no surprise a correlated two-parameter PDF parameterization of  $\Im \mathbf{m} \mathcal{Q}(\nu, \mu^2)$  is also met with a poor figure of merit. The non-trivial structures of correlation evident in these data are indicative of our simple PDF parameterizations (5.5) and (5.6) being inappropriate for these data. The above puzzling, and indeed worrisome, conclusions are given a deeper quantitative understanding in the following subsections.

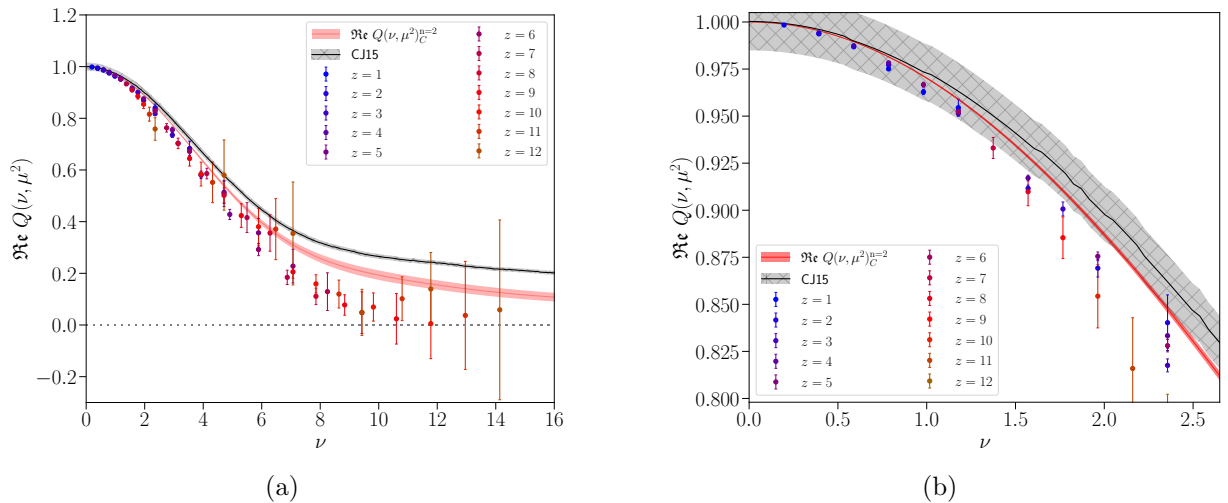


FIG. 5.11: (a) Real component of the matched ITD at  $\mu = 2$  GeV in  $\overline{\text{MS}}$  fit by the cosine transform of a two-parameter model PDF (5.5). Data has been fit for  $z/a \leq 12$  and *data correlations have been incorporated*. The fit clearly misses each point of the ITD. The derived CJ15 ITD at the same scale is shown for reference. (b) The same as panel (a), but with focus given to the small- $\nu$  region. The correlated two-parameter fit is seen to deviate appreciably from the precise small- $\nu$  data.

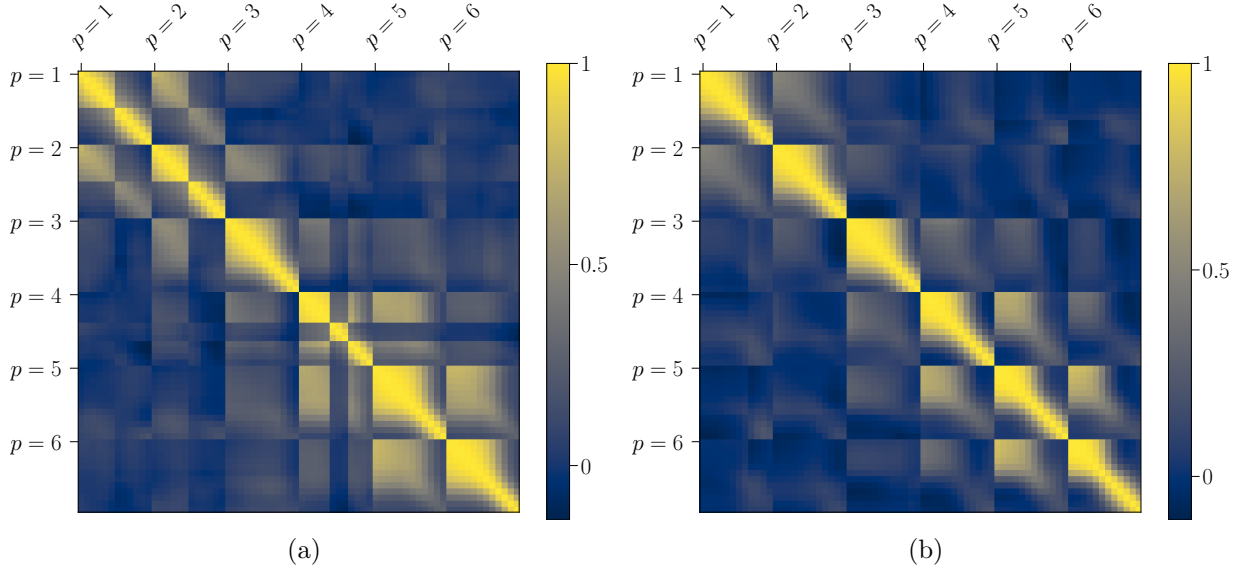


FIG. 5.12: Data covariance in the real (left) and imaginary (right) components of the matched ITD at 2 GeV, normalized according to  $\text{Cov}_{ij}/\sqrt{\text{Cov}_{ii}\text{Cov}_{jj}}$ . Within each lattice momentum block, entries are ordered in ascending Wilson line lengths.

### 5.3.3 Nucleon PDFs from Reduced Pseudo-ITDs Parameterized with Jacobi Polynomials

Our strategy to parameterize the reduced pseudo-ITD using a set of  $\Omega_n^{(\alpha,\beta)}(x)$  will be met by similar numerical difficulties as the type- $K$  fits discussed above. The numerical effort is lessened by considering a Taylor series expansion in  $\nu$  for fixed separations  $z^2$  of the direct matching kernels  $\mathcal{K}_{\nu/+}(x\nu, z^2\mu^2)$  and Eq. 5.9. The contribution of an  $n^{\text{th}}$ -order Jacobi polynomial  $\Omega_n^{(\alpha,\beta)}(x)$  to  $\Re \mathfrak{M}(\nu, z^2)$  and  $\Im \mathfrak{M}(\nu, z^2)$  is given by

$$\begin{aligned}\sigma_n^{(\alpha,\beta)}(\nu, z^2\mu^2) &\equiv \int_0^1 dx \mathcal{K}_\nu(x\nu, z^2\mu^2) x^\alpha (1-x)^\beta \Omega_n^{(\alpha,\beta)}(x) \\ \eta_n^{(\alpha,\beta)}(\nu, z^2\mu^2) &\equiv \int_0^1 dx \mathcal{K}_+(x\nu, z^2\mu^2) x^\alpha (1-x)^\beta \Omega_n^{(\alpha,\beta)}(x).\end{aligned}$$

Expanding the direct matching kernels  $\mathcal{K}_{v/+}(x\nu, z^2\mu^2)$  in even/odd powers of  $\nu$  one finds

$$\sigma_n^{(\alpha,\beta)}(\nu, z^2\mu^2) = \sum_{j=0}^n \sum_{k=0}^{\infty} \frac{(-1)^k \nu^{2k}}{(2k)!} c_{2k}(z^2\mu^2) \omega_{n,j}^{(\alpha,\beta)} B(\alpha + 2k + j + 1, \beta + 1) \quad (5.25)$$

$$\eta_n^{(\alpha,\beta)}(\nu, z^2\mu^2) = \sum_{j=0}^n \sum_{k=0}^{\infty} \frac{(-1)^k \nu^{2k+1}}{(2k+1)!} c_{2k+1}(z^2\mu^2) \omega_{n,j}^{(\alpha,\beta)} B(\alpha + 2k + j + 2, \beta + 1), \quad (5.26)$$

with  $\omega_{n,j}^{(\alpha,\beta)}$  given in Eq. 5.8 and where

$$c_n(z^2\mu^2) = 1 - \frac{\alpha_s C_F}{2\pi} \left[ \gamma_n \ln \left( \frac{e^{2\gamma_E+1}}{4} z^2\mu^2 \right) + d_n \right]. \quad (5.27)$$

The constants  $\gamma_n$  and  $d_n$  are the leading order moments of the Altarelli-Parisi and scheme matching kernels

$$\gamma_n = \int_0^1 du B(u) u^n = \frac{3}{2} - \frac{1}{1+n} - \frac{1}{2+n} - 2 \sum_{j=1}^n \frac{1}{j} \quad (5.28)$$

$$d_n = \int_0^1 du L(u) u^n = 2 \left[ \left( \sum_{j=1}^n \frac{1}{j} \right)^2 + \frac{2\pi^2 + n(n+3)(3+\pi^2)}{6(n+1)(n+2)} - \psi^{(1)}(n+1) \right] \quad (5.29)$$

derived in Ref. [163], with  $\psi^{(1)}$  the order-1 polygamma function. The sum over  $k$  is to be performed to assure convergence for a given value of  $\nu$  - we have identified  $k_{\max} = 75$  as providing more than adequate numerical precision, in reasonable computation time. With the above definitions, the leading-twist valence and plus quark PDFs describe the reduced pseudo-ITD components according to

$$\Re \mathcal{M}^{lt}(\nu, z^2) = \sum_{n=0}^{\infty} \sigma_n^{(\alpha,\beta)}(\nu, z^2\mu^2) C_{v,n}^{lt(\alpha,\beta)} \quad \Im \mathcal{M}^{lt}(\nu, z^2) = \sum_{n=0}^{\infty} \eta_n^{(\alpha,\beta)}(\nu, z^2\mu^2) C_{+,n}^{lt(\alpha,\beta)}, \quad (5.30)$$

where the  $C_{v/+,n}^{lt(\alpha,\beta)}$  are the Jacobi polynomial expansion coefficients.

The reduced pseudo-ITD is subject to discretization errors that vanish in the contin-

uum limit, and higher-twist effects that survive the continuum limit. A reliable determination of the leading-twist PDF in the continuum then depends on parameterization and removal of these effects. As the Fourier transform in  $\nu$  of the reduced pseudo-ITD only has support on the momentum fraction interval  $x \in [-1, 1]$  [110], any contaminating effects must also have support only in this interval and can be parameterized by the same basis of Jacobi polynomials. Any corrections by construction must be functions of  $\nu^2$  in the real component, and  $\nu$  in the imaginary component. Since the space-like matrix element (4.58) is on-shell, at a single lattice spacing we may account for contaminating discretization and higher-twist effects of  $\mathcal{O}(a/z)$  and  $\mathcal{O}(z^2 \Lambda_{\text{QCD}}^2)^n$ . The latter are the expected polynomial corrections to the Wilson line LCS factorization (4.44), while the discretization correction should scale based on parity. Namely, the real (imaginary) component of  $\mathfrak{M}(\nu, z^2)$  is even (odd) in  $z$ , so any discretization effect should behave in this manner as well. We will find this to be especially subtle in our data, motivating the present designation of  $\mathcal{O}(a/z)$ .

The contaminating  $x$ -space distributions are of the same form in (5.9) with distinct expansion coefficients. The coefficients of the corrections are denoted  $C_{\tau,n}^{\text{corr}(\alpha,\beta)}$  with  $\tau = \{v, +\}$  indicating whether the effect arises in the valence/plus quark PDFs. The choice of basis  $\{\alpha, \beta\}$  in (5.30) may equally be utilized to quantify these distributions. Supposing, for simplicity, these effects enter at tree-level, their contributions to the reduced pseudo-ITD signals with  $\sigma_{0,n}^{(\alpha,\beta)} \equiv \sigma_n^{(\alpha,\beta)}(\nu, z^2 \mu^2)|_{\alpha_s=0}$  and  $\eta_{0,n}^{(\alpha,\beta)} \equiv \eta_n^{(\alpha,\beta)}(\nu, z^2 \mu^2)|_{\alpha_s=0}$  are then

$$\Re \mathfrak{M}^{\text{corr}}(\nu, z^2) = \kappa_{\text{corr}} \sum_{n=1}^{\infty} \sigma_{0,n}^{(\alpha,\beta)} C_{v,n}^{\text{corr}(\alpha,\beta)} \quad (5.31)$$

$$\Im \mathfrak{M}^{\text{corr}}(\nu, z^2) = \kappa_{\text{corr}} \sum_{n=0}^{\infty} \eta_{0,n}^{(\alpha,\beta)} C_{+,n}^{\text{corr}(\alpha,\beta)}, \quad (5.32)$$

where  $\kappa_{\text{corr}}$  is a dimensionless parameter constructed from the dimensionful parameters of the calculation which describes the scaling of each correction (e.g.  $\kappa_{\text{corr}} = a/z$ ). Visualizing

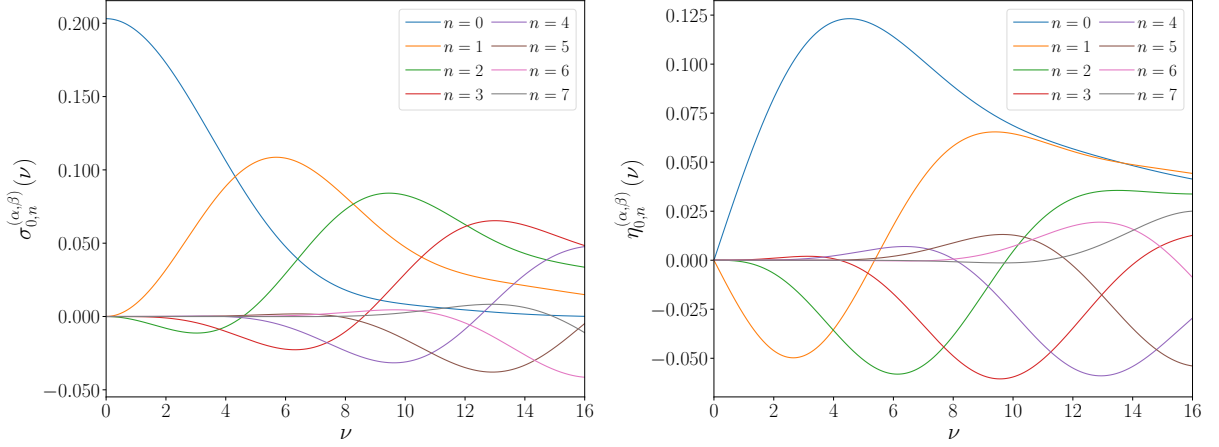


FIG. 5.13: The eight lowest-order  $\sigma_{0,n}^{(\alpha,\beta)}$  (left) and  $\eta_{0,n}^{(\alpha,\beta)}$  (right) polynomials for an arbitrarily chosen basis  $\alpha = 0.125$  and  $\beta = 2.85$ . Each polynomial features an extremum in a range of Ioffe-time accessible in our lattice calculation, and asymptotically approaches zero for  $\nu \rightarrow \infty$ .

the Taylor-expanded matching kernels (5.25) and (5.26) at tree-level across a range of Ioffe-times in Fig. 5.13, it is seen the polynomials  $\sigma_{0,n}^{(\alpha,\beta)}, \eta_{0,n}^{(\alpha,\beta)}$  reach an extremum in Ioffe-time commensurate with the polynomial order and asymptotically approach zero. This conveniently reflects the correct large- $\nu$  behavior of the ITD in the same limit (see Eq. 5.18). Since  $\mathfrak{M}(0, z^2) = 1$  by construction, all corrections must vanish at zero Ioffe-time. Of the Jacobi polynomial expanded corrections, only  $\sigma_{0,0}^{(\alpha,\beta)}(0) \neq 0$  (blue curve in left panel of Fig. 5.13). The corrections to the real component of  $\mathfrak{M}(\nu, z^2)$  (5.31) must then be restricted to order  $n \geq 1$ .

The complete functional forms we apply to each component of  $\mathfrak{M}(\nu, z^2)$  are:

$$\begin{aligned} \Re \mathfrak{M}_{\text{fit}}(\nu, z^2) &= \sum_{n=0}^{\infty} \sigma_n^{(\alpha,\beta)}(\nu, z^2 \mu^2) C_{v,n}^{lt(\alpha,\beta)} + \left(\frac{a}{z}\right) \sum_{n=1}^{\infty} \sigma_{0,n}^{(\alpha,\beta)}(\nu) C_{v,n}^{az(\alpha,\beta)} \\ &\quad + z^2 \Lambda_{\text{QCD}}^2 \sum_{n=1}^{\infty} \sigma_{0,n}^{(\alpha,\beta)}(\nu) C_{v,n}^{t4(\alpha,\beta)} + z^4 \Lambda_{\text{QCD}}^4 \sum_{n=1}^{\infty} \sigma_{0,n}^{(\alpha,\beta)}(\nu) C_{v,n}^{t6(\alpha,\beta)} \end{aligned} \quad (5.33)$$

$$\begin{aligned} \Im \mathfrak{M}_{\text{fit}}(\nu, z^2) &= \sum_{n=0}^{\infty} \eta_n^{(\alpha,\beta)}(\nu, z^2 \mu^2) C_{+,n}^{lt(\alpha,\beta)} + \left(\frac{a}{z}\right) \sum_{n=0}^{\infty} \eta_{0,n}^{(\alpha,\beta)}(\nu) C_{+,n}^{az(\alpha,\beta)} \\ &\quad + z^2 \Lambda_{\text{QCD}}^2 \sum_{n=0}^{\infty} \eta_{0,n}^{(\alpha,\beta)}(\nu) C_{+,n}^{t4(\alpha,\beta)} + z^4 \Lambda_{\text{QCD}}^4 \sum_{n=0}^{\infty} \eta_{0,n}^{(\alpha,\beta)}(\nu) C_{+,n}^{t6(\alpha,\beta)}. \end{aligned} \quad (5.34)$$

The leading-twist ( $C_{\tau,n}^{lt}$ ) and discretization ( $C_{\tau,n}^{az}$ ) corrections are accompanied by twist-4 ( $C_{\tau,n}^{t4}$ ) and twist-6 ( $C_{\tau,n}^{t6}$ ) corrections. The twist-6 corrections will almost certainly not be constraining, as their effect will be large beyond the range of Ioffe-time for which we have statistically clean data ( $\nu \sim 10$ ); they are included nonetheless for exploration purposes. We note that higher-twist corrections in a lattice calculation must arise in even powers of  $z$ , as odd powers are not hypercubic invariants.

In the fits we perform according to (5.33) and (5.34), we elect to fix the order of truncation for the leading-twist and each type of correction, and numerically search for the optimal  $\{\alpha, \beta, C_{\tau,n}^{corr}\}$ . Treating each fitted parameter as non-linear in a maximum likelihood fit leads to wildly unstable results. The way forward is to recognize that  $\alpha, \beta$  are the only fitted parameters that are truly non-linear; the correction coefficients  $C_{\tau,n}^{corr}$  are all linear. A maximum likelihood fit of the posterior distribution of the linear terms is then Gaussian and cheap to obtain. It is worth digressing for a moment to discuss separable minimization problems, and a specific algorithm for their solution.

## Variable Projection

Extremization of a posterior distribution of a correlated data set conventionally proceeds by minimizing the correlated  $\chi^2$  defined according to

$$\chi^2 = \sum_{ij} \left( y_i - \sum_k c_k \phi_k(x_i) \right) \text{Cov}_{ij}^{-1} \left( y_j - \sum_k c_k \phi_k(x_j) \right), \quad (5.35)$$

where  $y_i$  is the dependent data sampled at  $x_i$ , and a linear combination of basis functions  $\phi_k$  defines the model function:  $\sum_k c_k \phi_k(x_i)$ . As the parameters  $\{c_i\}$  appear linearly, for a given set of non-linear parameters the  $\{c_i\}$  can be determined by solving a linear least-squares regression - a numerically cheap task. This separation of linear and non-linear parameters and the *variable projection* (VarPro) algorithm as a method for its solution,

was first shown analytically by G. Golub and V. Pereyra [164]. The linear variables  $\{c_i\}$  are solved for exactly by extremizing the functional (5.35) with respect to these linear variables. As the data covariance matrix  $\text{Cov}$  is symmetric by construction, from  $\partial\chi^2/\partial c_i = 0$  it follows

$$\begin{aligned} \sum_{ij} (y_i \text{Cov}_{ij}^{-1} \phi_l(x_j) + \phi_l(x_i) \text{Cov}_{ij}^{-1} y_j) &= \sum_{ij} \sum_k \{ \phi_k(x_i) \text{Cov}_{ij}^{-1} \phi_l(x_j) + \phi_l(x_i) \text{Cov}_{ij}^{-1} \phi_k(x_j) \} c_k \\ 2 \sum_{ij} y_i \text{Cov}_{ij}^{-1} \phi_l(x_j) &= 2 \sum_k \sum_{ij} \phi_k(x_i) \text{Cov}_{ij}^{-1} \phi_l(x_j) c_k. \end{aligned}$$

Defining the vector  $\mathbf{Y}_i = \sum_{ij} y_i \text{Cov}_{ij}^{-1} \phi_l(x_j)$  and matrix  $\Phi_{kl} = \sum_{ij} \phi_k(x_i) \text{Cov}_{ij}^{-1} \phi_l(x_j)$ , a solution for  $\mathbf{C}_i = c_i$  becomes apparent:

$$\mathbf{Y} = \Phi \mathbf{C} \quad \Rightarrow \quad \mathbf{C} = \Phi^{-1} \mathbf{Y}. \quad (5.36)$$

Upon substitution of (5.36) into (5.35), the linear parameters may be swapped for the non-linear basis functions  $\phi_k$  as follows

$$\begin{aligned} \chi^2 &= \sum_{ij} y_i \text{Cov}_{ij}^{-1} y_j - \sum_k \sum_{ij} y_i \text{Cov}_{ij}^{-1} \phi_k(x_j) c_k - \sum_k c_k \sum_{ij} \phi_k(x_i) \text{Cov}_{ij}^{-1} y_j \\ &\quad + \sum_k c_k \sum_m \sum_{ij} \phi_k(x_i) \text{Cov}_{ij}^{-1} \phi_m(x_j) c_m \\ &= y^T \text{Cov}^{-1} y - \mathbf{Y}^T \mathbf{C} - \sum_k c_k \sum_{ij} y_j \text{Cov}_{ji}^{-1} \phi_k(x_i) + \mathbf{C}^T \Phi \mathbf{C} \\ &= y^T \text{Cov}^{-1} y - 2\mathbf{Y}^T \mathbf{C} + \mathbf{C}^T \Phi \mathbf{C} \\ &= y^T \text{Cov}^{-1} y - 2\mathbf{Y}^T \Phi^{-1} \mathbf{Y} + \mathbf{Y}^T (\Phi^{-1})^T \Phi \Phi^{-1} \mathbf{Y} \\ &= y^T \text{Cov}^{-1} y - \mathbf{Y}^T \left( 2\Phi^{-1} - (\Phi^{-1})^T \right) \mathbf{Y}. \end{aligned} \quad (5.37)$$

This result implies the dimensionality of an optimization in both linear and non-linear parameters can be reduced dramatically by solving exactly for the linear parameters, effectively removing them from the problem.

This result is generalized trivially in the event the linear parameters  $\{c_k\}$  are constrained. Suppose Bayesian priors of a Gaussian form are imposed for each  $c_k$ . The unconstrained functional (5.35) is then modified as

$$\chi^2 = \chi_{unconstrained}^2 + \sum_k \frac{(c_k - \bar{c}_k)^2}{\sigma_{c_k}^2}, \quad (5.38)$$

where  $\bar{c}_k$  and  $\sigma_{c_k}$  are the prior and prior widths, respectively, of the linear parameters  $c_k$ . Repeating the extremization exercise above, one finds

$$\begin{aligned} \frac{\partial \chi_{unconstrained}^2}{\partial c_l} &= -\frac{2(c_l - \bar{c}_l)}{\sigma_{c_l}^2} \\ \sum_{ij} (y_i \text{Cov}_{ij}^{-1} \phi_l(x_j) + \phi_l(x_i) \text{Cov}_{ij}^{-1} y_j) &= \sum_{ij} \sum_k \{ \phi_k(x_i) \text{Cov}_{ij}^{-1} \phi_l(x_j) \\ &\quad + \phi_l(x_i) \text{Cov}_{ij}^{-1} \phi_k(x_j) \} c_k + \frac{2(c_l - \bar{c}_l)}{\sigma_{c_l}^2} \\ \sum_{ij} y_i \text{Cov}_{ij}^{-1} \phi_l(x_j) &= \sum_k \sum_{ij} \phi_l(x_i) \text{Cov}_{ij}^{-1} \phi_k(x_j) c_k + \frac{(c_l - \bar{c}_l)}{\sigma_{c_l}^2} \\ \mathbf{Y}_l &= \mathbf{\Phi}_{lk} \mathbf{C}_k + \frac{\bar{c}_l}{\sigma_{c_l}^2} \left( \frac{1}{\bar{c}_l} \mathbf{C}_l - \mathbf{1}_l \right) \\ \mathbf{Y}_l + \frac{\bar{c}_l}{\sigma_{c_l}^2} \mathbf{1}_l &= \left( \mathbf{\Phi}_{lk} + \frac{1}{\sigma_{c_l}^2} \delta_{lk} \right) \mathbf{C}_k. \end{aligned} \quad (5.39)$$

As in the unconstrained case, the linear parameters are obtained by solving  $\mathbf{C} = \tilde{\mathbf{\Phi}}^{-1} \tilde{\mathbf{Y}}$ , where  $\tilde{\mathbf{Y}}_l = \left( \mathbf{Y}_l + \frac{\bar{c}_l}{\sigma_{c_l}^2} \mathbf{1}_l \right)$  and  $\tilde{\mathbf{\Phi}}_{lk} = \left( \mathbf{\Phi}_{lk} + \frac{1}{\sigma_{c_l}^2} \delta_{lk} \right)$ . Thus Eq. 5.38 with normally distributed Bayesian priors can be re-expressed in terms of the non-linear basis functions via

$$\chi^2 = y^T \text{Cov}^{-1} y - \tilde{\mathbf{Y}} \left( 2\tilde{\mathbf{\Phi}}^{-1} - \left( \tilde{\mathbf{\Phi}}^{-1} \right)^T \right) \tilde{\mathbf{Y}} + \sum_k \frac{\bar{c}_k^2}{\sigma_{c_k}^2}. \quad (5.40)$$



The reader is reminded that the final terms  $\frac{\bar{c}_k^2}{\sigma_k^2} \in \mathbb{R}$ , and are not varied in the optimization.

## PDF Results with Jacobi Polynomials and VarPro

The reduced pseudo-ITD fits of Eqns. 5.33 and 5.34 are implemented with the help of VarPro. This reduces the dimension of the non-linear optimization from  $d = N_{corr} + 2$  to  $d = 2$ , where  $N_{corr}$  are the number of linear correction coefficients. In our case, minimization is performed in the  $d = 2$  Jacobi polynomial basis  $\{\alpha, \beta\}$ , and any correction terms  $C_{\tau,n}^{corr(\alpha,\beta)}$  are solved for exactly in terms of the non-linear basis functions  $\{\sigma_n^{(\alpha,\beta)}, \sigma_{0,n}^{(\alpha,\beta)}, \eta_n^{(\alpha,\beta)}, \eta_{0,n}^{(\alpha,\beta)}\}$ . We note without VarPro, optimizations with  $N_{corr} \geq 4$  were numerically unstable, regardless of the type of correction included in the model.

Care needs to be taken as correction terms are included in Eqns. 5.33 and 5.34, as physical insight can quickly be replaced with over-fitting. The first sensible restriction to impose is for all  $x$ -space corrections  $\mathcal{O}(a/z)$ ,  $\mathcal{O}(z^2\Lambda_{\text{QCD}}^2)$  and  $\mathcal{O}(z^4\Lambda_{\text{QCD}}^4)$  to be sub-leading relative to the leading-twist PDF. It would be alarming to obtain, say, a twist-4 contribution that is larger than the leading-twist PDF, given that the short-distance factorization of the pseudo-distributions implies leading-twist dominance. Such disastrous scenarios are avoided with several Bayesian constraints of a Gaussian form. So as to allow the reduced pseudo-ITD to dictate the best fit results, all Bayesian priors are fixed to zero. The hierarchy we desire is realized with the following prior widths:

- Leading-twist:  $\delta C_{\tau,0}^{lt(\alpha,\beta)} = 1.1$ ,  $\delta C_{\tau,1}^{lt(\alpha,\beta)} = 0.75$ ,  $\delta C_{\tau,2}^{lt(\alpha,\beta)} = 0.5$ ,  $\delta C_{\tau,3}^{lt(\alpha,\beta)} = 0.25$ ,  
 $\delta C_{\tau,4}^{lt(\alpha,\beta)} = 0.125$ ,  $\delta C_{\tau,5}^{lt(\alpha,\beta)} = 0.1$ ,  $\delta C_{\tau,6}^{lt(\alpha,\beta)} = 0.05$ ,  $\delta C_{\tau,7}^{lt(\alpha,\beta)} = 0.025$
- Corrections:  $\delta C_{\tau,n \in \mathbb{Z}_3}^{corr(\alpha,\beta)} = 0.25$ ,  $\delta C_{\tau,n=3,4,5}^{corr(\alpha,\beta)} = 0.125$ ,  $\delta C_{\tau,n=6,7}^{corr(\alpha,\beta)} = 0.1$ .

The validity of the entire Jacobi polynomial parameterization is guaranteed using shifted log-normally distributed priors to ensure  $\alpha, \beta > -1$ . In practice, the log-normal prior on beta is shifted to  $\beta = 0$  to secure  $\beta > 0$  and hence convergent PDFs at  $x = 1$ .

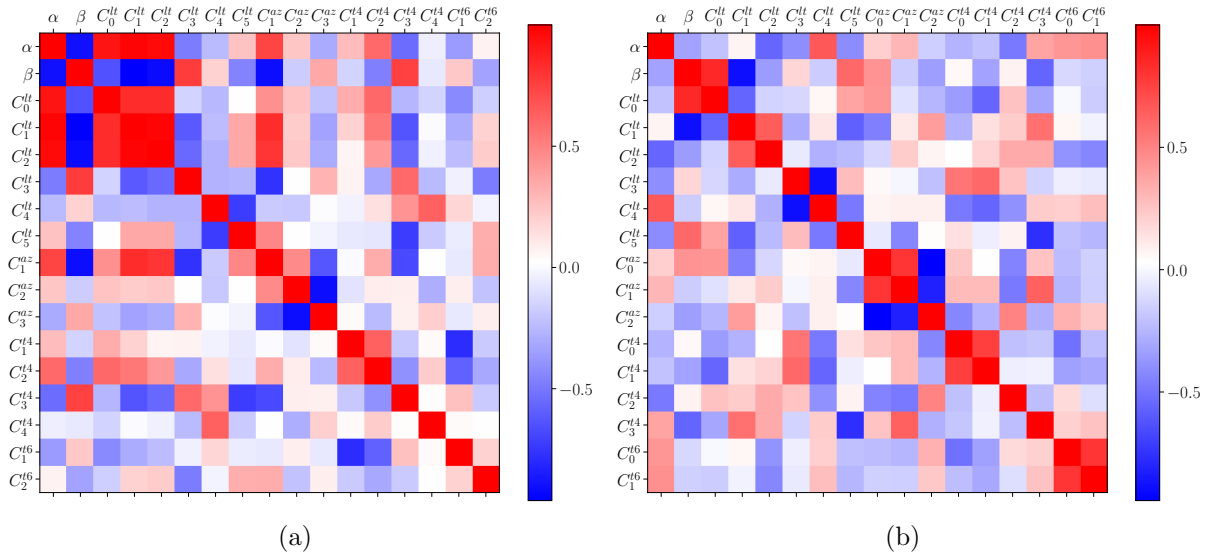


FIG. 5.14: Parameter covariances in Jacobi polynomial fits with  $[n_{lt}, n_{az}, n_{t4}, n_{t6}] = [6342]$  to the real (left) and imaginary (right) components of the unpolarized reduced pseudo-ITD for  $z/a \leq 12$ . Entries are normalized according to  $\text{Cov}_{ij}/\sqrt{\text{Cov}_{ii}\text{Cov}_{jj}}$ .

As leading-twist and correction terms are added, the question becomes at which order each series of Jacobi polynomials should be truncated. We address this by scanning over all possible combinations of truncation orders for  $n_{lt} \in \{3, 4, 5, 6\}$ ,  $n_{az} \in \mathbb{Z}_4$ ,  $n_{t4} \in \mathbb{Z}_5$ ,  $n_{t6} \in \mathbb{Z}_3$ , where  $n_*$  are the orders of truncation in the fits (5.33) and (5.34). Figure 5.14 illustrates, for a rather large number of Jacobi polynomials  $\{n_{lt}, n_{az}, n_{t4}, n_{t6}\} = \{6, 3, 4, 2\}$ , the covariances of  $\alpha, \beta$  and each linear correction term  $C_{\tau, n}^{\text{corr}(\alpha, \beta)}$  in fits to the real (5.33) and imaginary (5.34) reduced pseudo-ITD components for Wilson line lengths  $z/a \leq 12$ . The covariance of each pair of fitted parameters is estimated via jackknife resampling

$$\text{Cov}_{ij} \simeq \frac{N-1}{N} \sum_{n=1}^N (\mathbf{f}_{n,i} - \bar{\mathbf{f}}_i) (\mathbf{f}_{n,j} - \bar{\mathbf{f}}_j), \quad (5.41)$$

where fit parameters associated with jackknife sample  $n$  are denoted by  $\mathbf{f}_{n,k}$ , with jackknife average  $\bar{\mathbf{f}}_k$ . Without observing the quality of agreement between each fit and the reduced pseudo-ITD, it is clear several parameters correlate weakly or not at all with other param-

eters in the fit. This implies these weakly correlated parameters are not well-constrained by the data, and their removal will not affect the information content of the fit. For instance, the real component fit parameter covariances, shown in Fig. 5.14(a), suggest the leading-twist expansion coefficients  $C_{n_{lt}}^{lt}$  are constrained by the data for  $n_{lt} \leq 3$ , while  $C_4^{lt}, C_5^{lt}$  weakly correlate with the remaining parameters. The discretization, twist-4 and twist-6 corrections exhibit mild correlation for  $C_1^{az}, C_2^{t4}, C_3^{t4}, C_1^{t6}$ , with the remaining correction parameters largely unconstrained. In the imaginary component, the fit parameter covariances shown in Fig. 5.14(b) suggest a more nuanced pattern of correlation. Several leading-twist Jacobi polynomials appear to be well-constrained by the data, while the relative correlation between the  $C^{az}$  and  $C^{t4}, C^{t6}$  parameters is increased relative to the corresponding entries in Fig. 5.14(a).

This exercise demonstrates an important point. Although the VarPro implementation of the Jacobi polynomial fits allows for arbitrarily many leading-twist and correction coefficients, the reduced pseudo-ITD data simply do not contain enough information to constrain so many parameters. One should then expect that the likelihood function is maximized for the real component of the reduced pseudo-ITD with truncation orders  $n_{lt} \sim 3$  and  $n_{az} \sim 1 - 2$ , and  $n_{lt} \sim 3$  and  $n_{az} \sim 3$  for the imaginary component.

By scanning over the order of truncation for the leading-twist and correction terms parameterized by Jacobi polynomials, we find the likelihood of the functional (5.33) to describe  $\Re \mathfrak{M}(\nu, z^2)$  with  $z/a \leq 12$  to be maximized for  $\{n_{lt}, n_{az}, n_{t4}, n_{t6}\}_v = \{4, 1, 3, 2\}_v$ . Likewise, the likelihood of the functional (5.34) to describe  $\Im \mathfrak{M}(\nu, z^2)$  with  $z/a \leq 12$  is maximized for  $\{n_{lt}, n_{az}, n_{t4}, n_{t6}\}_+ = \{3, 3, 1, 0\}_+$ . The fit results for each and their respective figures-of-merit are given in Tab. 5.5. The Jacobi polynomial fits of orders  $\{n_{lt}, n_{az}, n_{t4}, n_{t6}\}_v = \{4, 1, 3, 2\}_v$  and  $\{n_{lt}, n_{az}, n_{t4}, n_{t6}\}_+ = \{3, 3, 1, 0\}_+$  applied to the real and imaginary components of  $\mathfrak{M}(\nu, z^2)$  are presented in Fig. 5.15 and Fig. 5.18, respectively.

$\{n_{lt}, n_{az}, n_{t4}, n_{t6}\}_{v/+}$	$\{4, 1, 3, 2\}_v$	$\{4, 0, 3, 2\}_v$	$\{3, 3, 1, 0\}_+$	$\{3, 0, 1, 0\}_+$	$\{6, 3, 4, 2\}_v$	$\{6, 3, 4, 2\}_+$
$\alpha$	-0.209(147)	-0.376(37)	-0.328(20)	-0.331(31)	-0.264(117)	-0.326(20)
$\beta$	1.330(415)	2.032(496)	2.361(243)	3.227(297)	1.438(404)	2.051(260)
$C_{\tau,0}^{lt}$	1.606(257)	1.340(165)	2.041(108)	1.156(83)	1.489(213)	1.954(107)
$C_{\tau,1}^{lt}$	0.427(752)	0.335(261)	0.123(248)	0.161(243)	0.174(620)	0.404(213)
$C_{\tau,2}^{lt}$	-0.880(409)	-0.125(100)	-0.464(121)	0.700(98)	-1.002(301)	-0.241(118)
$C_{\tau,3}^{lt}$	-0.675(122)	-0.651(140)	-	-	-0.568(118)	-0.018(79)
$C_{\tau,4}^{lt}$	-	-	-	-	0.089(28)	0.020(27)
$C_{\tau,5}^{lt}$	-	-	-	-	0.020(12)	-0.023(10)
$C_{\tau,0}^{az}$	-	-	-0.001(43)	-	-	0.054(35)
$C_{\tau,1}^{az}$	-0.279(48)	-	-0.338(39)	-	-0.226(53)	-0.219(46)
$C_{\tau,2}^{az}$	-	-	0.434(74)	-	0.209(67)	0.283(67)
$C_{\tau,3}^{az}$	-	-	-	-	-0.164(48)	-
$C_{\tau,0}^{t4}$	-	-	0.170(28)	0.391(46)	-	0.185(47)
$C_{\tau,1}^{t4}$	0.052(53)	-0.090(52)	-	-	0.060(50)	0.032(68)
$C_{\tau,2}^{t4}$	-0.371(106)	-0.112(77)	-	-	-0.341(93)	-0.200(79)
$C_{\tau,3}^{t4}$	-0.407(122)	0.274(99)	-	-	-0.397(131)	0.076(29)
$C_{\tau,4}^{t4}$	-	-	-	-	0.088(30)	-
$C_{\tau,0}^{t6}$	-	-	-	-	-	-0.067(34)
$C_{\tau,1}^{t6}$	-0.045(37)	0.011(39)	-	-	-0.045(36)	-0.079(53)
$C_{\tau,2}^{t6}$	0.228(52)	0.397(84)	-	-	0.227(53)	-
$\chi_r^2$	2.620(345)	45.68(1.72)	2.845(387)	123.16(2.73)	2.809(374)	3.110(431)

TABLE 5.5: Various Jacobi polynomial fits to the real and imaginary components of the unpolarized reduced pseudo-ITD for  $z/a \leq 12$ . Each column represents distinct orders of truncation in the Jacobi polynomial expansions to the leading-twist, discretization, twist-4 and twist-6 corrections. The real and imaginary component fits were found to have the highest likelihoods of describing the data with truncation orders  $\{4, 1, 3, 2\}_v$  and  $\{3, 3, 1, 0\}_+$ , respectively. The dramatic effect even a single discretization term has on each fit is shown in the columns  $\{4, 0, 3, 2\}_v$  and  $\{3, 0, 1, 0\}_+$ .

Considering first the real component fit, each set of  $\Re \mathcal{M}(\nu, z^2)$  for  $z/a \leq 8$  are well represented by the expansion in Jacobi polynomials. The main exception is the highest momentum point  $p_z = 6 \times (2\pi/aL) \sim 2.47$  GeV. The  $\Re \mathcal{M}(\nu, z^2)$  data for  $z/a > 8$  are also well represented, however the highest two momenta are seen to deviate. This behavior is not surprising despite the twist-4 and twist-6 corrections, which capture large- $z^2$  deviations, as the highest momentum data are subject to loss of signal in both the two- and three-point functions. The associated fit parameter covariances shown in Fig. 5.16(a) demonstrate the leading-twist, discretization and twist-4 corrections are well constrained by the  $\Re \mathcal{M}(\nu, z^2)$  data; as expected, the twist-6 corrections are only weakly constrained.

The resultant leading-twist PDF  $f_{q_v/N}(x)$  and  $x$ -space distributions corresponding to

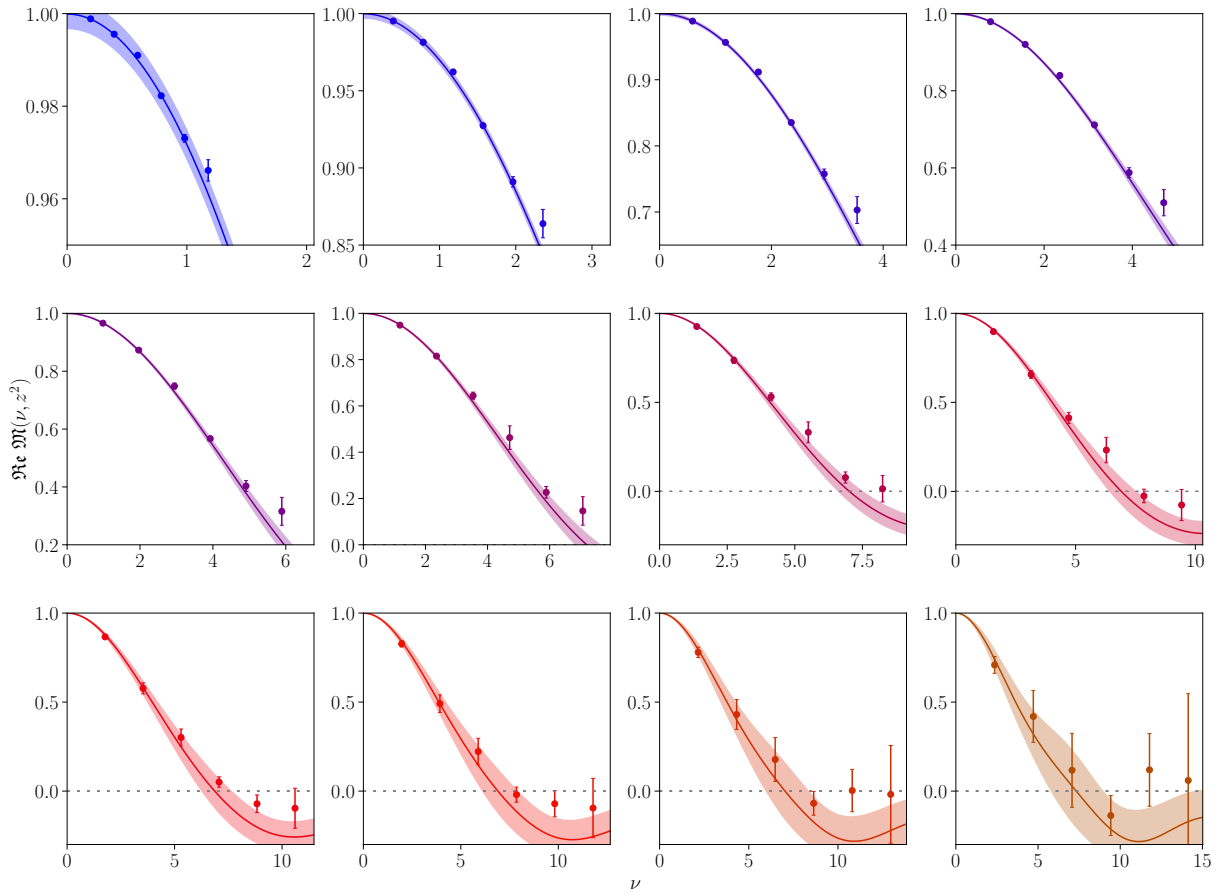


FIG. 5.15: Fit to the real component of the unpolarized reduced pseudo-ITD where the leading-twist, discretization, twist-4, and twist-6 corrections have been expanded in Jacobi polynomials up to order  $\{n_{lt}, n_{az}, n_{t4}, n_{t6}\}_v = \{4, 1, 3, 2\}_v$ . Starting from the upper left panel and traversing horizontally, the leading-twist plus corrections are shown for each  $z/a \leq 12$ .

the  $\{n_{lt}, n_{az}, n_{t4}, n_{t6}\}_v = \{4, 1, 3, 2\}_v$  Jacobi polynomial fit are gathered in Fig. 5.17(b). As expected, the corrections in  $x$ -space are sub-leading to the leading-twist PDF. The Jacobi-parameterized leading-twist PDF, however, features many structural differences with the included phenomenological PDFs and the uncorrelated two-parameter PDF fit from Sec. 5.3.1. Most evident is the softer approach to  $x = 1$ . Due to the valence quark sum rule, this enhances the low- to moderate- $x$  region and leads to further tension with the phenomenological results. By evaluating the cosine transform of the pure leading-twist component, we see in Fig. 5.17(a) that the  $z/a \gtrsim 7$  ITD data deviate successively

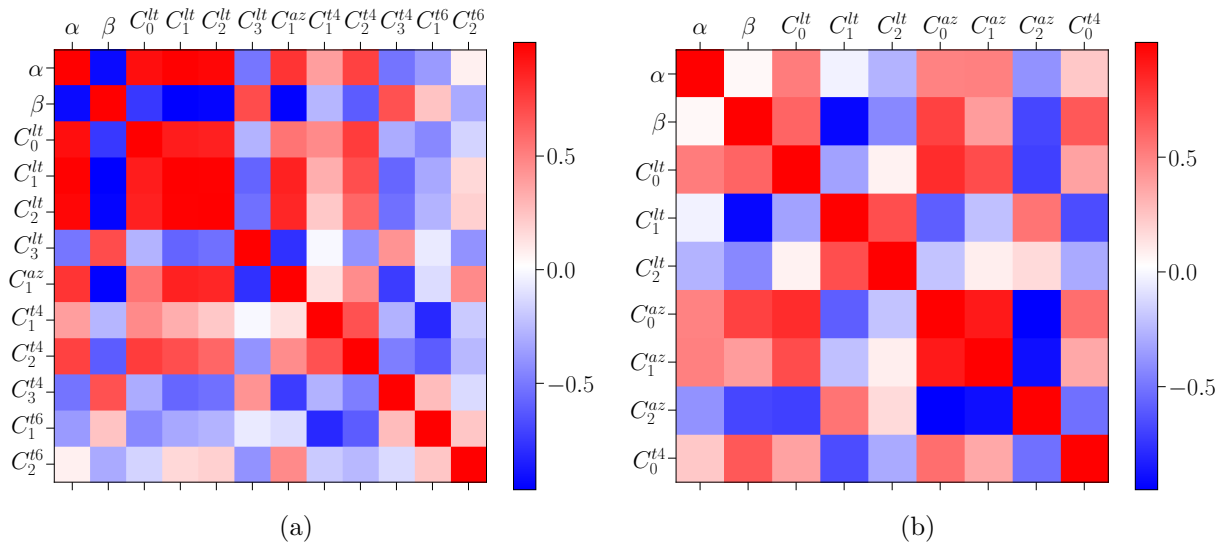


FIG. 5.16: Parameter covariances of the optimal Jacobi polynomial fits to the real (a) and imaginary (b) component of the unpolarized reduced pseudo-ITD for  $z/a \leq 12$  with truncation orders  $\{n_{lt}, n_{az}, n_{t4}, n_{t6}\}_v = \{4, 1, 3, 2\}_v$  and  $\{n_{lt}, n_{az}, n_{t4}, n_{t6}\}_+ = \{3, 3, 1, 0\}_+$ , respectively. Entries are normalized according to  $\text{Cov}_{ij}/\sqrt{\text{Cov}_{ii}\text{Cov}_{jj}}$ .

further from the derived leading-twist ITD shown in purple. Whereas the uncorrelated two-parameter ITD fit shown in red attempts to capture all the  $z/a \leq 12$  data and indeed the unwanted impact from higher-twist effects, the Jacobi polynomial parameterization has effectively isolated and removed these polynomial- $z^2$  effects, leaving the pure leading-twist contribution.

The quality of the Jacobi polynomial fit to the imaginary component of the reduced pseudo-ITD shown in Fig. 5.18 is more puzzling. The  $z/a \leq 4$  appear reasonably well represented by the expansion in Jacobi polynomials, but by  $z/a = 5$  it is evident the data for a given  $z^2$  segregate into two distinct groups - one for lattice momenta  $p_{\text{latt}} \in \{1, 2, 3\}$  and another for  $p_{\text{latt}} \in \{4, 5, 6\}$ . This distinction coincides with the switch from an unphased eigenvector basis to the phased bases  $\vec{\zeta}_{\pm}$  defined in Sec. 4.4. The fit parameter covariances shown in Fig. 5.16(b) demonstrate a milder constraint of the first and second order leading-twist Jacobi polynomials compared to the best fit of the real component. The discretization and twist-4 corrections are also seen to be well constrained by the

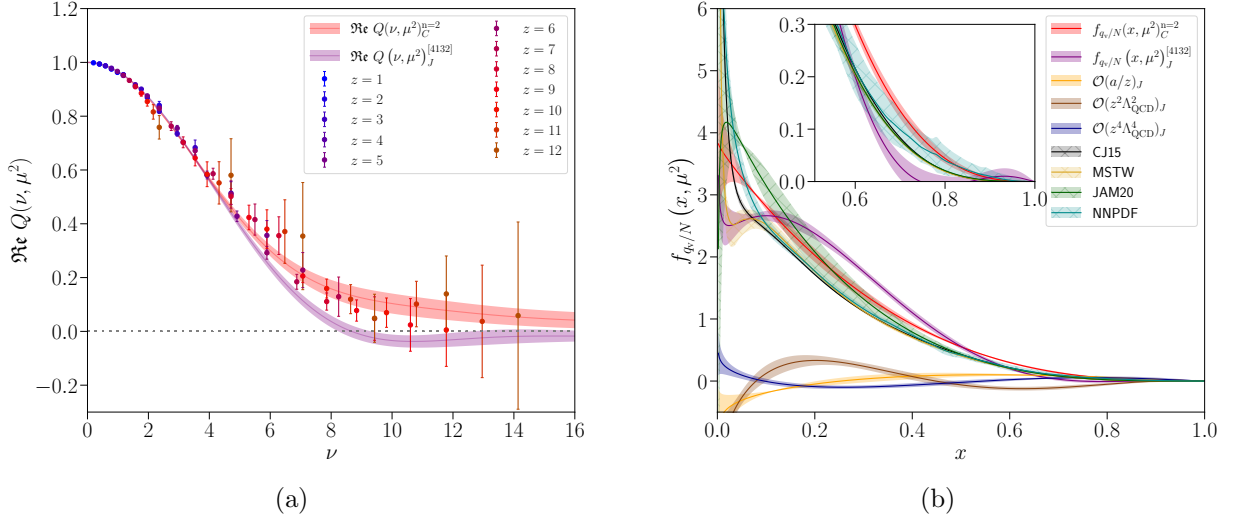


FIG. 5.17: (a) The real component of the leading-twist ITD (purple) at 2 GeV derived from the Jacobi polynomial expansion of the reduced pseudo-ITD for  $z/a \leq 12$  with  $\{n_{lt}, n_{az}, n_{t4}, n_{t6}\}_v = \{4, 1, 3, 2\}_v$ . The result is compared with the uncorrelated 2-parameter phenomenological form of Eq. 5.5 shown in red. (b) The valence quark leading-twist PDF (purple) obtained from the  $\{n_{lt}, n_{az}, n_{t4}, n_{t6}\}_v = \{4, 1, 3, 2\}_v$  Jacobi polynomial expansion of the reduced pseudo-ITD. The  $a/z$  (orange), twist-4 (brown), and twist-6 (navy)  $x$ -space distributions are also shown and seen to be sub-leading. The distributions are compared with the uncorrelated 2-parameter phenomenological fit of Eq. 5.5 (red), as well as an NLO global analyses of CJ15 [132] and JAM20 [160], and the NNLO analyses of MSTW [161] and NNPDF [38] at the same scale.

data. The resultant leading-twist plus quark PDF  $f_{q+/N}(x)$  and  $x$ -space distributions corresponding to the  $\{n_{lt}, n_{az}, n_{t4}, n_{t6}\}_+ = \{3, 3, 1, 0\}_+$  Jacobi polynomial fit are illustrated in Fig. 5.19(b). As in the real component fit, the corrections are sub-leading to the leading-twist PDF, which in this case is in agreement with the NNPDF result [38] for  $x \geq 0.5$ . At small values of  $x$ , the leading-twist PDF parameterized by Jacobi polynomials is generally consistent with the two-parameter uncorrelated PDF fit from Sec. 5.3.1. The sine transform of the pure leading-twist component is shown in Fig. 5.19(a) together with the  $\Im Q(\nu, \mu^2)$  data at 2 GeV. Unlike the real component of the derived leading-twist ITD in Fig. 5.17(a), the derived imaginary component of the leading-twist ITD does not agree with the  $\Im Q(\nu, \mu^2)$  data for any of the  $ap_z \gtrsim 4\pi/L$  data with  $z/a \gtrsim 7$ . As the imaginary component of  $\mathfrak{M}(\nu, z^2)$  is optimally fit with three discretization corrections and

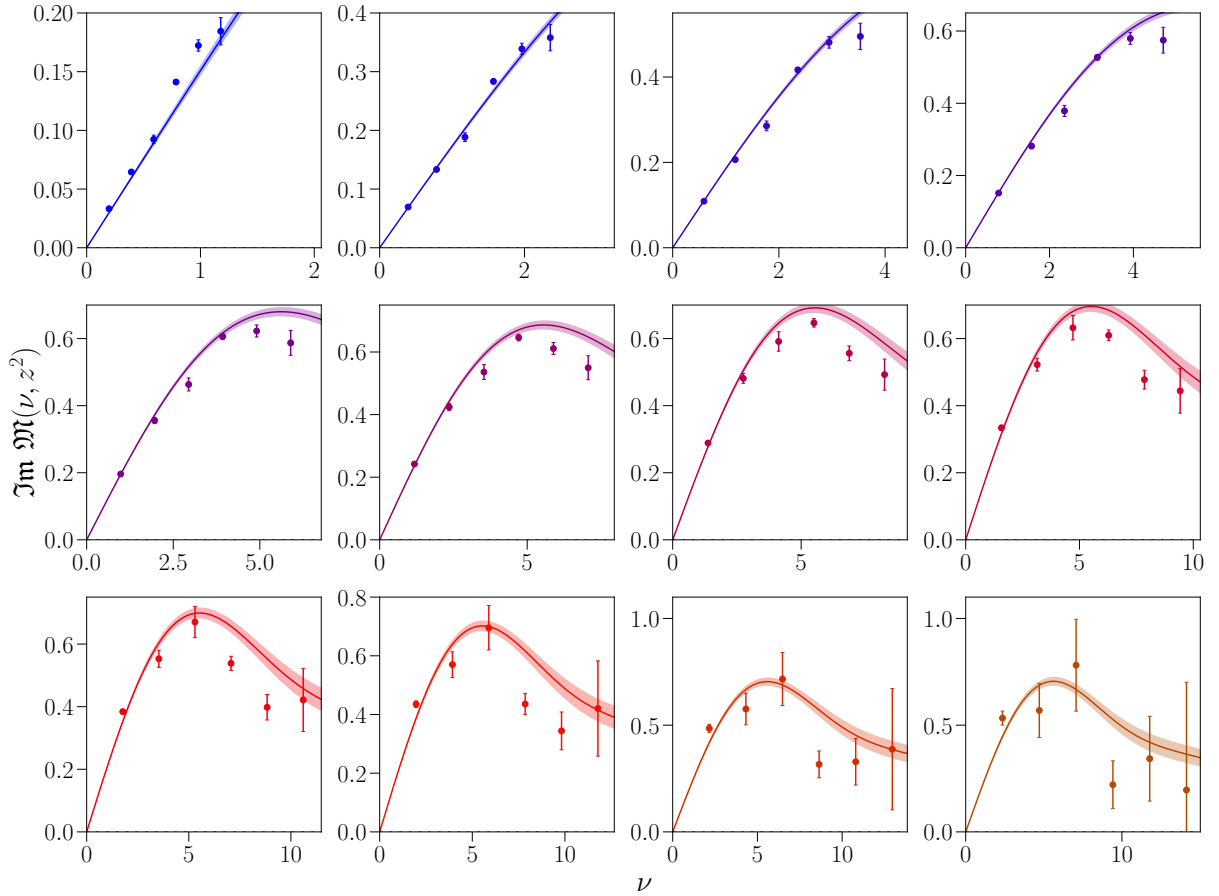


FIG. 5.18: Fit to the imaginary component of the unpolarized reduced pseudo-ITD where the leading-twist, discretization, twist-4, and twist-6 corrections have been expanded in Jacobi polynomials up to order  $\{n_{lt}, n_{az}, n_{t4}, n_{t6}\}_+ = \{3, 3, 1, 0\}_+$ . Starting from the upper left panel and traversing horizontally, the leading-twist plus corrections are shown for each  $z/a \leq 12$ .

only one higher-twist term, the  $\{n_{lt}, n_{az}, n_{t4}, n_{t6}\}_+ = \{3, 3, 1, 0\}_+$  fit would suggest the imaginary component of the ITD is susceptible to less higher-twist effects in exchange for greater discretization effects. This is a tenuous conclusion, however, in light of the segregation of the  $\text{Im } \mathfrak{M}(\nu, z^2)$  data into two distinct clusters, a low- and high-momentum set, for large Wilson line lengths. A future study exploring the side effects of phased distillation is warranted.

By far the biggest indicator of a reasonable description of the reduced pseudo-ITD data via Jacobi polynomials is a discretization term. Repeating the above Jacobi polynomial fits



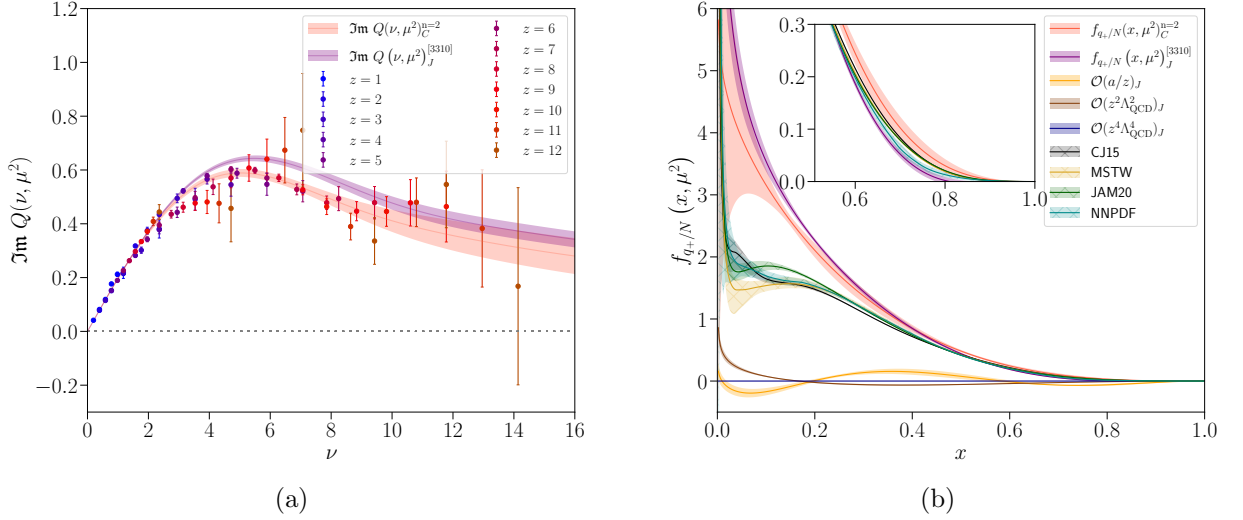


FIG. 5.19: (a) The imaginary component of the leading-twist ITD (purple) at 2 GeV derived from the Jacobi polynomial expansion of the reduced pseudo-ITD for  $z/a \leq 12$  with  $\{n_{lt}, n_{az}, n_{t4}, n_{t6}\}_+ = \{3, 3, 1, 0\}_+$ . The result is compared with the uncorrelated 2-parameter phenomenological form of Eq. 5.6 shown in red. (b) The plus quark leading-twist PDF (purple) obtained from the  $\{n_{lt}, n_{az}, n_{t4}, n_{t6}\}_+ = \{3, 3, 1, 0\}_+$  Jacobi polynomial expansion of the reduced pseudo-ITD. The  $a/z$  (orange) and twist-4 (brown)  $x$ -space distributions are also shown and seen to be sub-leading. The distributions are compared with the uncorrelated 2-parameter phenomenological fit of Eq. 5.6 (red), as well as the NLO global analyses of CJ15 [132] and JAM20 [160], and the NNLO analyses of MSTW [161] and NNPDF [38] at the same scale.

but leaving out any discretization corrections, namely  $\{n_{lt}, n_{az}, n_{t4}, n_{t6}\}_v = \{4, 0, 3, 2\}_v$  and  $\{n_{lt}, n_{az}, n_{t4}, n_{t6}\}_+ = \{3, 0, 1, 0\}_+$ , we find each correlated  $\chi^2/\text{d.o.f}$  increases considerably to an unacceptable value (see Tab. 5.5). This same conclusion is reached when cuts on momentum and Wilson line lengths are made. Since the discretization term we have included is of  $\mathcal{O}(a/z)$ , its effect is most pronounced at short distances. This is precisely the regime wherein the short distance factorization (5.15), or equivalently (5.21), is applicable. This motivates a more detailed look at the short-distance behavior of the computed reduced pseudo-ITD.

### 5.3.4 On the Numerical Consistency with DGLAP

The one-loop matching relationship between the ITD and the reduced pseudo-ITD (5.15) implies that  $\mathcal{Q}(\nu, \mu^2) = \mathfrak{M}(\nu, z^2)$  at tree-level. The scatter that exists for a given  $z^2$  should ideally be compensated at  $\mathcal{O}(\alpha_s)$  by the  $\ln z^2$ -dependence produced by the DGLAP evolution, up to large- $z^2$  higher-twist corrections. In this section we study the  $z^2$ -dependence of  $\mathfrak{M}(\nu, z^2)$  more closely, and investigate whether the observed dependence is numerically consistent with DGLAP, thus yielding a truly  $z^2$ -independent ITD.

We begin by focusing on the real component of the reduced pseudo-ITD. The dependence of  $\Re \mathfrak{M}(\nu, z^2)$  on the invariant space-like interval  $z^2$  can be most easily visualized by parameterizing the valence pseudo-PDF  $\mathcal{P}_v(x, z^2; \alpha, \beta)$  by a simple two-parameter phenomenological form

$$\mathcal{P}_v(x, z^2; \alpha, \beta) = \frac{\Gamma(2 + \alpha + \beta)}{\Gamma(1 + \alpha)\Gamma(1 + \beta)} x^\alpha (1 - x)^\beta, \quad (5.42)$$

and fitting its cosine-transform to  $\Re \mathfrak{M}(\nu, z^2)$  separately for each  $z^2$ . In order to more readily expose the role of the Altarelli-Parisi kernel, we impose the added restriction  $\beta = 3$ . This choice not only captures the naive  $x \rightarrow 1$  behavior of the nucleon's valence quark PDF [135], but also forces  $\alpha$  to reflect any  $z$ -dependence in the reduced distribution; further, this value of  $\beta$  is in statistical agreement with those obtained from the uncorrelated ITD fits (see Tab. 5.3).

Figure 5.20 illustrates the cosine-transform of the model valence pseudo-PDF (5.42) fit separately to each  $z^2$  of the real component of the reduced pseudo-ITD. The cosine-transforms of  $\mathcal{P}_v(x, z^2; \alpha, \beta = 3)$  are seen to describe  $\Re \mathfrak{M}(\nu, z^2)$  quite well for  $z/a \lesssim 10$ , with the greatest tension seen for the highest momentum point for each separation. The fits for  $z/a \geq 13$  are also shown for completeness, but are clearly noise dominated. Also noteworthy, the highest figures-of-merit are observed for the smallest separations, with a

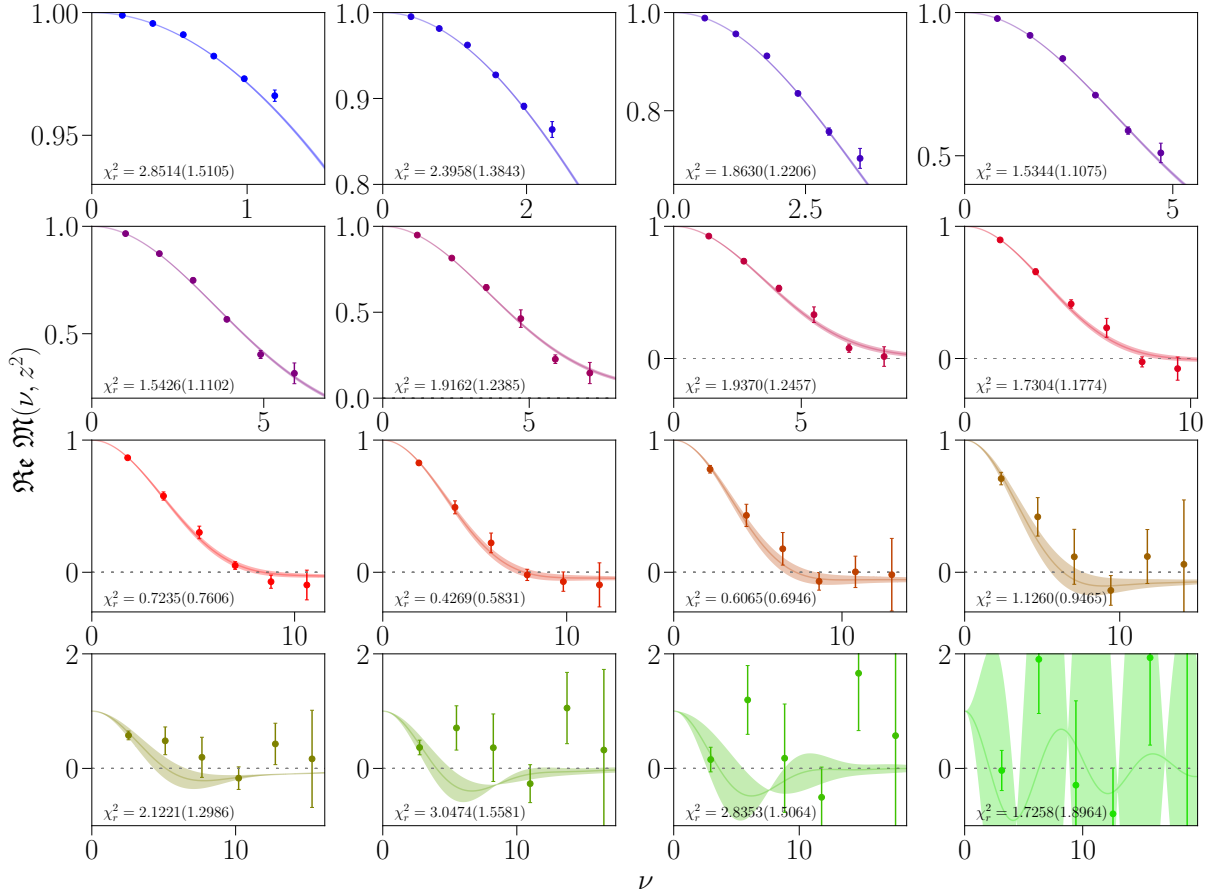


FIG. 5.20: Cosine transform of the model pseudo-PDF in Eq. 5.42 fit separately to  $\Re \mathfrak{M}(\nu, z^2)$  for distinct  $z^2$ ; data correlations have been included in each fit. Starting from the upper left panel and traversing horizontally,  $z/a$  increases from unity. The correlated figure of merit for each separate fit is also indicated.

somewhat monotonic reduction until  $z/a \simeq 11$ . The dependence of the fitted values of  $\alpha$  on the separation  $z/a$  is visualized for  $\Re \mathfrak{M}(\nu, z^2)$  in Fig. 5.21. As a function of  $z/a$ ,  $\alpha$  decreases with the Wilson line length, matching expectations from the Altarelli-Parisi evolution of the pseudo-PDF. However, it is clear  $\Re \mathfrak{M}(\nu, z^2)$  depends linearly on  $z/a$  for  $z/a \lesssim 12$ , most notably for small- $z$ .

This manifest lack of  $\ln z^2$  behavior of  $\Re \mathfrak{M}(\nu, z^2)$  at short distances immediately suggests tension with the presumed DGLAP evolution of the pseudo-PDF. To determine if this  $z^2$ -dependence in  $\Re \mathfrak{M}(\nu, z^2)$  is nevertheless numerically consistent with DGLAP, the

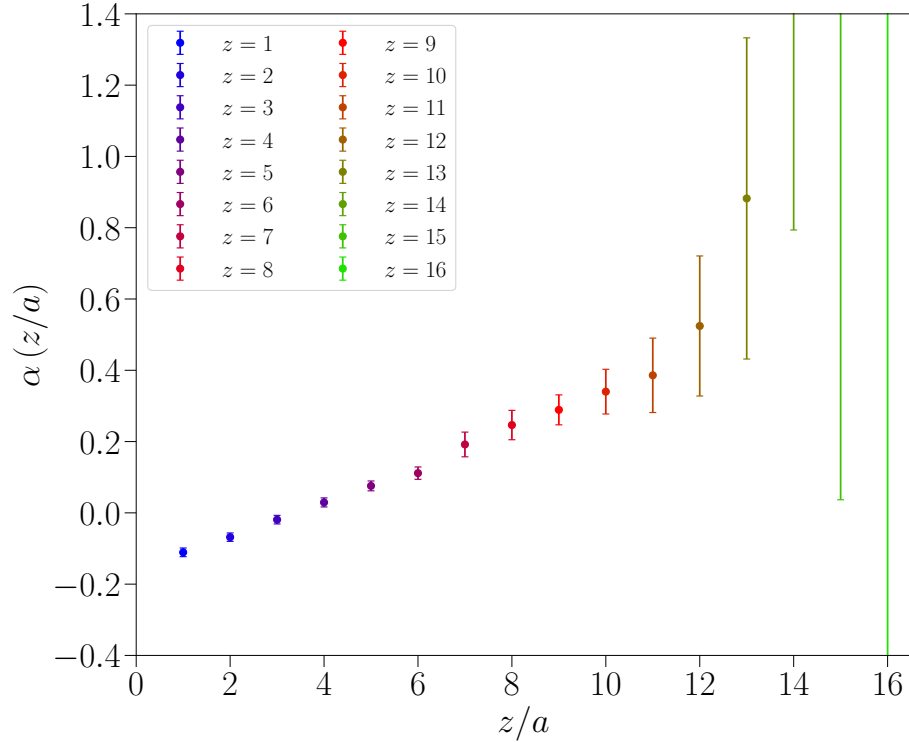


FIG. 5.21: The fitted value of  $\alpha$  as a function of  $z/a$  resulting from the cosine-transform of the model pseudo-PDF in Eq. 5.42 fit to  $\Re \mathfrak{M}(\nu, z^2)$ . The decrease of  $\alpha$  with  $z/a$  is in agreement with expectations from the Altarelli-Parisi evolution of the pseudo-PDF. This dependence is however clearly linear.

one-loop matching relationship between the reduced pseudo-ITD and ITD is applied. In the ideal scenario where the  $z^2$ -dependence of  $\Re \mathfrak{M}(\nu, z^2)$  is exactly described by DGLAP, the matched ITD will be independent of the interval  $z^2$  up to polynomial corrections for large- $z^2$ . Rather than perform the matching step to a common scale in  $\overline{\text{MS}}$  using a smooth polynomial in Ioffe-time (e.g. Eq. 5.19) as was done in Sec. 5.3.1, we leverage the cosine-transform of the model pseudo-PDF (5.42) as the smooth and continuous description of the reduced pseudo-ITD data. That is, we perform the matching of  $\Re \mathfrak{M}(\nu, z^2)$  to a common scale in  $\overline{\text{MS}}$  according to

$$\Re \mathfrak{Q}(\nu, \mu^2) = \Re \mathfrak{M}(\nu, z^2) + \frac{\alpha_s C_F}{2\pi} \int_0^1 du \mathfrak{P}(u\nu, z^2; \alpha, \beta = 3) \left[ \ln \left( \frac{z^2 \mu^2 e^{2\gamma_E + 1}}{4} \right) B(u) + L(u) \right], \quad (5.43)$$

where  $\mathfrak{P}(u\nu, z^2; \alpha, \beta = 3)$  is the cosine-transform of the model pseudo-PDF  $\mathcal{P}_\nu(x, z^2; \alpha, \beta = 3)$  expressed in a closed form by a generalized hypergeometric function

$$\mathfrak{P}(\nu, z^2; \alpha, \beta = 3) = {}_2F_3\left(\frac{1+\alpha}{2}, \frac{2+\alpha}{2}; \frac{1}{2}, \frac{5+\alpha}{2}, \frac{6+\alpha}{2}; -\frac{\nu^2}{4}\right). \quad (5.44)$$

For an explicit, albeit crude, conversion to  $\overline{\text{MS}}$ , we set  $\alpha = 0.2$  in Eq. 5.44.

Our strategy to expose any  $z$ -dependence in the ITD  $\mathcal{Q}(\nu, \mu^2)$  remains identical to the reduced distribution above. The resultant matched ITD at 2 GeV in  $\overline{\text{MS}}$  is once more

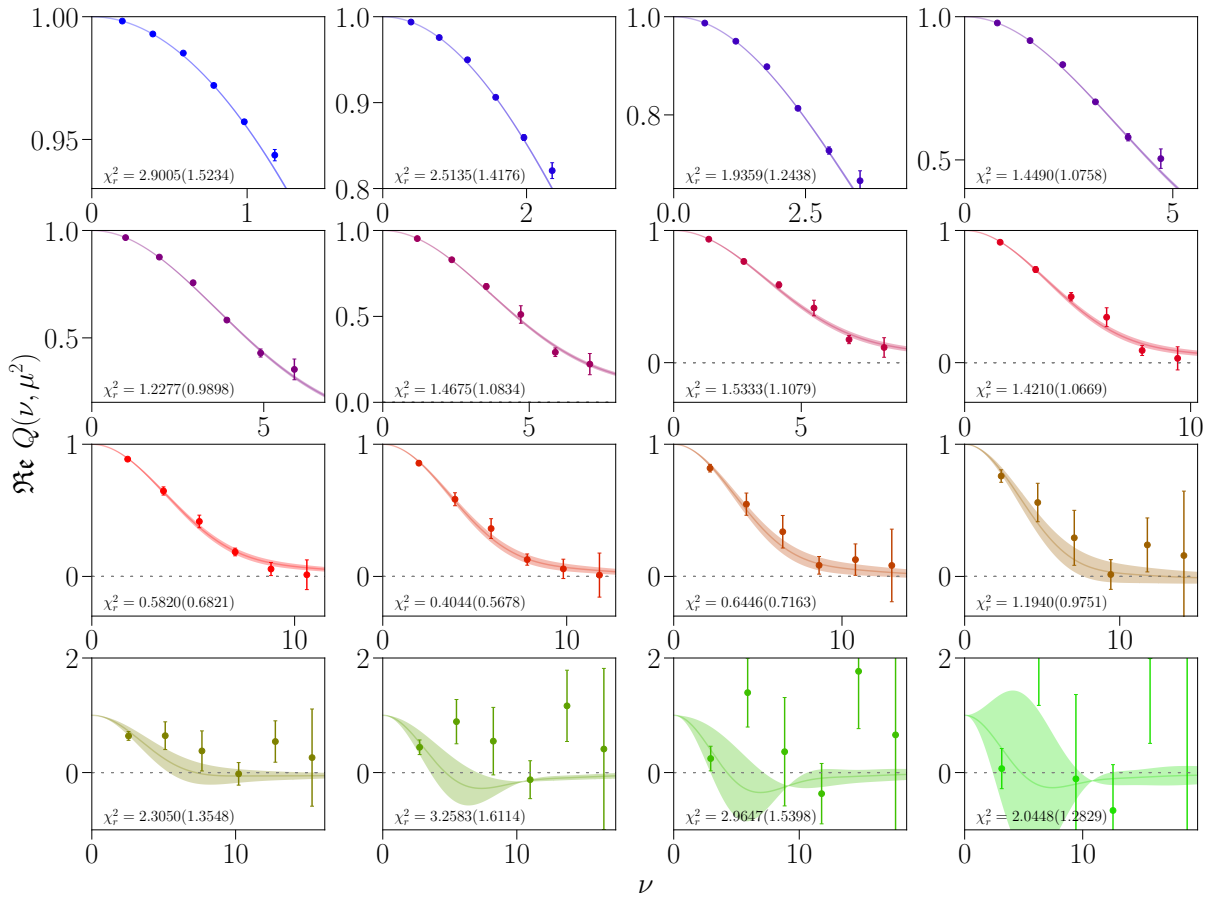


FIG. 5.22: Cosine transform of the two-parameter model PDF, with the same functional form as (5.42), fit separately to each  $z^2$  of the matched ITD. The ITD was obtained using (5.44) for the evolution/matching step. Data correlations have been included in each fit. Starting from the upper left panel and traversing horizontally,  $z/a$  increases from unity. The correlated figure of merit for each separate fit is also indicated.

fit using the two-parameter form in Eq. 5.42 independently for each  $z^2$  and with  $\beta = 3$ . The parameterized distribution in this case is of course no longer the valence pseudo-PDF, but rather the valence PDF itself. As illustrated in Fig. 5.22, each  $z^2$  of the matched ITD is well described by the simple two-parameter form. The poorest figures-of-merit are again observed for the smallest ( $z/a \lesssim 3$ ) and largest ( $z/a \gtrsim 13$ ) separations. The dependence of the fitted values of  $\alpha$  on the separation  $z/a$  for  $\Re \mathcal{Q}(\nu, \mu^2)$  is illustrated in Fig. 5.23. For  $4 \lesssim z/a \lesssim 11$  the fitted value of  $\alpha$  is observed to be independent of  $z/a$  and hence numerically consistent with DGLAP in said interval. Remarkably, however, the values of  $\alpha$  for the shortest separations, namely  $z/a \lesssim 4$ , deviate increasingly from this constancy as  $z/a \rightarrow 1$ . A subsequent analysis of the imaginary component of both the reduced pseudo-ITD and matched ITD arrived at a similar conclusion, but has been omitted for brevity.

### Jacobi Polynomial Corrections - Discretization Effects

The findings above rigorously demonstrate the reduced pseudo-ITD is numerically inconsistent with DGLAP in the small- $z$  regime. Whether matching the reduced pseudo-ITD to the light-cone ITD or directly to the light-cone PDF, the presence of the Altarelli-Parisi evolution kernel should in principle capture and remove the  $\ln z^2$  scatter that theoretically exists in  $\mathfrak{M}(\nu, z^2)$  for small- $z$ . As  $\mathfrak{M}(\nu, z^2)$  was found to depend only linearly on the separation  $z$  (Fig. 5.21), the Altarelli-Parisi kernel effectively introduces a  $\ln z^2$ -dependence into the small- $z$  ITD and thus explains the dependence of  $\alpha$  on  $z/a$  in Fig. 5.23. Despite this concerning conclusion, a broad subset of  $\mathfrak{M}(\nu, z^2)$  remains consistent with DGLAP; the statistically constant value of  $\alpha(z/a)$  observed in the ITD fits in the interval  $4 \lesssim z/a \lesssim 11$  (e.g. Fig. 5.23) validates the nice collapse of the  $\mathfrak{M}(\nu, z^2)$  data onto a common curve (Fig. 5.7) when matched to a common scale in  $\overline{MS}$ .

To gain further insight into the regions wherein DGLAP is not respected, we return to

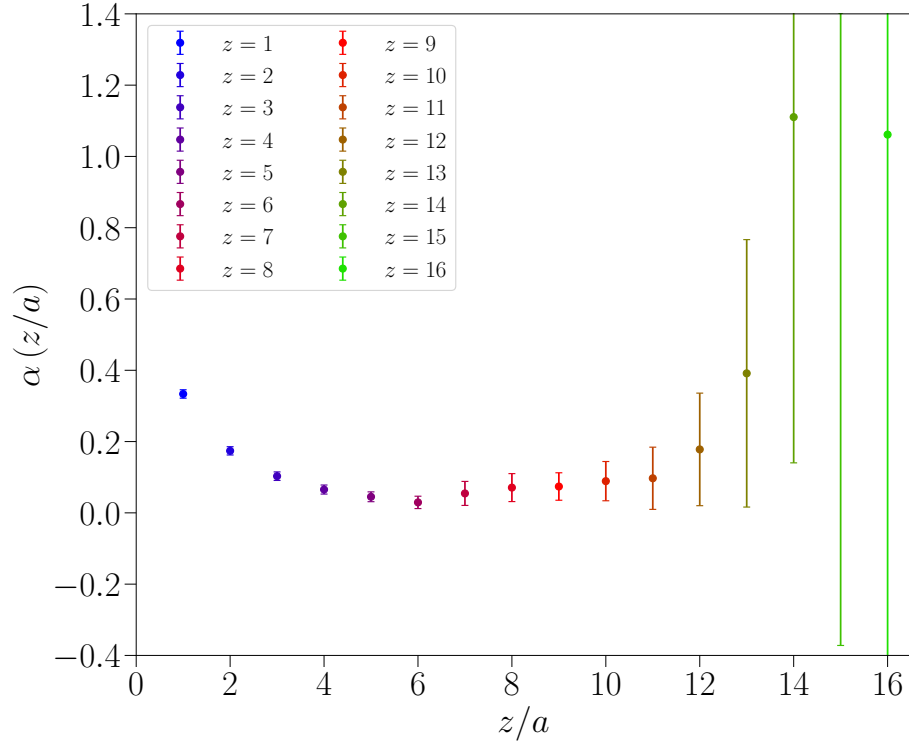


FIG. 5.23: The fitted values of  $\alpha$  from the cosine-transform of the two-parameter PDF functional form (5.42) fit to each  $z^2$  of the matched ITD. The latter was obtained using (5.44) for the evolution/matching step. The values of  $\alpha$  are statistically constant for  $4 \lesssim z/a \lesssim 11$ , with sharp deviations for small- $z/a$ .

the optimal Jacobi polynomial fits  $\{n_{lt}, n_{az}, n_{t4}, n_{t6}\}_v = \{4, 1, 3, 2\}_v$  and  $\{n_{lt}, n_{az}, n_{t4}, n_{t6}\}_+ = \{3, 3, 1, 0\}_+$ . The reader is reminded Sec. 5.3.3 concluded with the realization that a suitable description of  $\mathfrak{M}(\nu, z^2)$  was only possible with the nominal inclusion of an  $\mathcal{O}(a/z)$  correction in Eq. 5.33 and Eq. 5.34. The discretization effect parameterized by each of these fits is given by

$$\mathfrak{M}^{az}(\nu, z^2) = \frac{a}{z} \times \begin{cases} C_{v,1}^{az(\alpha,\beta)} \sigma_{0,1}^{(\alpha,\beta)}(\nu) & \text{for } \{4, 1, 3, 2\}_v \\ \sum_{n=0}^2 C_{+,n}^{az(\alpha,\beta)} \eta_{0,n}^{(\alpha,\beta)}(\nu) & \text{for } \{3, 3, 1, 0\}_+ \end{cases}, \quad (5.45)$$

and visualized in Fig. 5.24. The discretization effect  $\Re \mathfrak{M}^{az}(\nu, z^2)$  is seen to be strictly negative in the interval of Ioffe-time in which  $\mathfrak{M}(\nu, z^2)$  has been computed. By comparison,

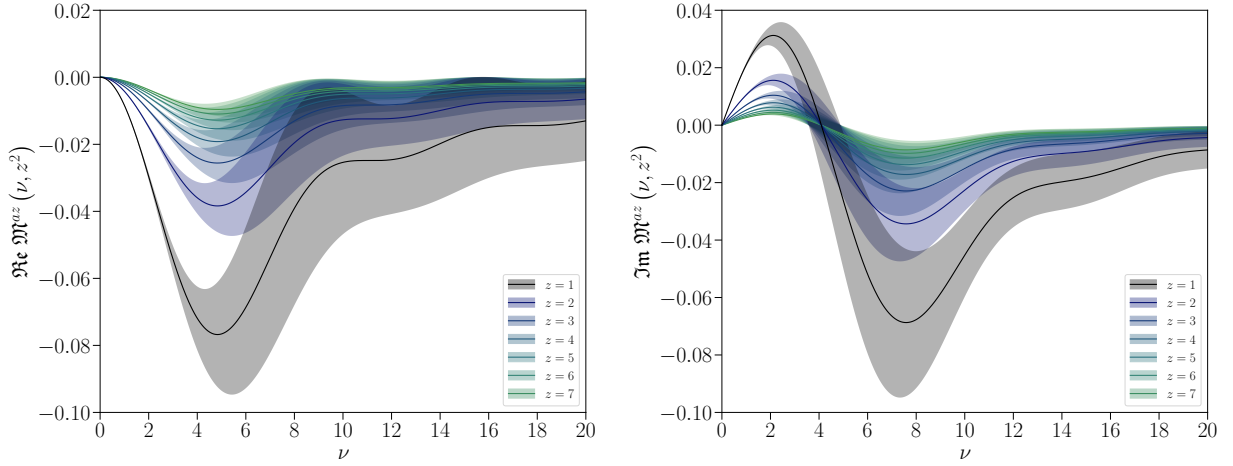


FIG. 5.24: Visualization of the discretization effects determined by the optimal Jacobi polynomial fits  $\{n_{lt}, n_{az}, n_{t4}, n_{t6}\}_v = \{4, 1, 3, 2\}_v$  (left) and  $\{n_{lt}, n_{az}, n_{t4}, n_{t6}\}_+ = \{3, 3, 1, 0\}_+$  (right) for  $z/a \leq 7$ .

the discretization effect  $\mathfrak{Im} \mathcal{M}^{az}(\nu, z^2)$  involves three Jacobi polynomials and suggests the  $\mathfrak{Im} \mathcal{M}(\nu, z^2)$  data are subject to a discretization effect that is opposite in sign at small and large values of Ioffe-time.

We now justify the necessity of the  $\mathcal{O}(a/z)$  discretization correction by considering the removal of the  $\mathfrak{Re} \mathcal{M}^{az}(\nu, z^2)$  effect from the computed  $\mathfrak{Re} \mathcal{M}(\nu, z^2)$  data, which we denote  $\mathfrak{Re} \mathcal{M}'(\nu, z^2) \equiv \mathfrak{Re} \mathcal{M}(\nu, z^2) - \mathfrak{Re} \mathcal{M}^{az}(\nu, z^2)$ . Based on the left panel of Fig. 5.24, the removal should shift the small- $z$  points of  $\mathfrak{Re} \mathcal{M}(\nu, z^2)$  to larger values, with the largest impact for  $\nu \sim 4.5$ . Figure 5.25 juxtaposes the original  $\mathfrak{Re} \mathcal{M}(\nu, z^2)$  and discretization corrected  $\mathfrak{Re} \mathcal{M}'(\nu, z^2)$  in the interval  $\nu \in [0, 2.5]$ . Although the differences are numerically small, at small Ioffe-times  $\mathfrak{Re} \mathcal{M}'(\nu, z^2)$  is noticeably larger than the uncorrected reduced pseudo-ITD. The importance of removing this discretization effect is quantitatively discerned by repeating the DGLAP investigation for  $\mathfrak{Re} \mathcal{M}'(\nu, z^2)$ .

Parameterizing the discretization corrected valence pseudo-PDF  $\mathcal{P}'_v(x, z^2)$  with the two-parameter form in Eq. 5.42 and fitting its cosine-transform to  $\mathfrak{Re} \mathcal{M}'(\nu, z^2)$  with  $\beta = 3$ , the  $z$ -dependence of  $\mathfrak{Re} \mathcal{M}'(\nu, z^2)$  is once more reflected in the variation of  $\alpha$  with  $z/a$ . As illustrated in the left panel of Fig. 5.26,  $\alpha$  now varies non-linearly with  $z/a$  for



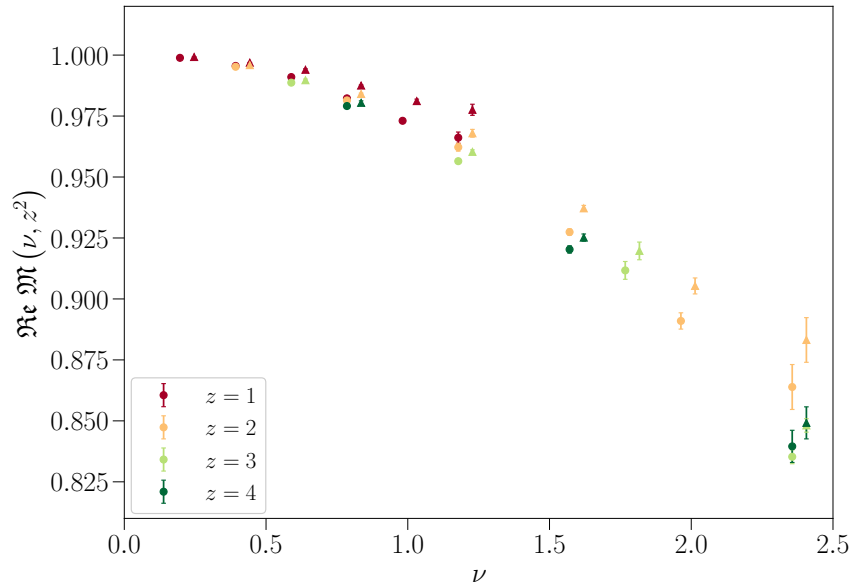


FIG. 5.25: Juxtaposition of the raw  $\Re \mathfrak{M}(\nu, z^2)$  and discretization corrected  $\Re \mathfrak{M}'(\nu, z^2)$  distributions, represented by circles and wedges respectively. The  $\Re \mathfrak{M}'(\nu, z^2)$  data is shifted horizontally for legibility.

$z/a \lesssim 4$  and linearly for  $4 \lesssim z/a \lesssim 11$ . Whether this markedly distinct  $z$ -dependence (c.f. Fig. 5.21) is numerically consistent with DGLAP is once again checked by performing the matching to a common scale in  $\overline{\text{MS}}$  using Eq. 5.44, and repeating the two-parameter fits to the discretization corrected ITD  $\Re \mathfrak{Q}'(\nu, \mu^2)$  for each  $z^2$  and with  $\beta = 3$ . The resulting fitted values of  $\alpha$  are presented in the right panel of Fig. 5.26. Relative to the  $z$ -dependence of the uncorrected ITD shown in Fig. 5.23, the variation of  $\alpha$  with  $z/a$  is considerably more constant for  $z/a \lesssim 11$ . In other words, the ITD is seen to fall into better agreement with DGLAP in the short-distance regime following removal of the  $\mathcal{O}(a/z)$  effect. That the optimal Jacobi polynomial fits  $\{n_{lt}, n_{az}, n_{t4}, n_{t6}\}_v = \{4, 1, 3, 2\}_v$  and  $\{n_{lt}, n_{az}, n_{t4}, n_{t6}\}_+ = \{3, 3, 1, 0\}_+$  provide the best description of  $\mathfrak{M}(\nu, z^2)$  can now be quantitatively explained by the compensating effect the  $\mathcal{O}(a/z)$  term provides. The poor quality of the correlated phenomenological fits to the matched ITD, as well as the

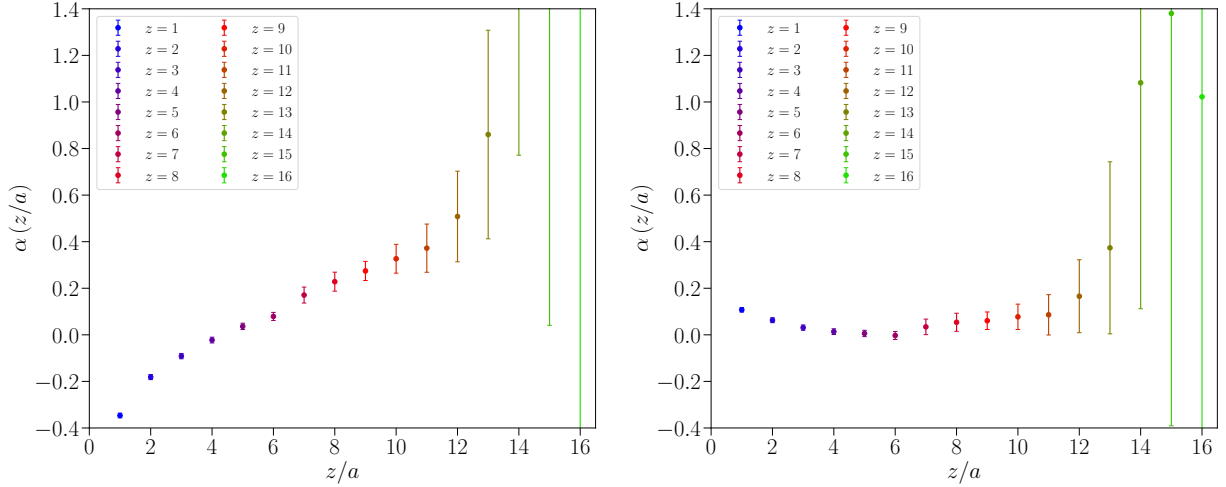


FIG. 5.26: (Left) The variation of  $\alpha$  with  $z/a$  resulting from the cosine-transform of the model pseudo-PDF in Eq. 5.42 fit to  $\Re \mathfrak{M}'(\nu, z^2)$  for each  $z^2$ . The discretization effect captured by the optimal Jacobi polynomial expansion  $\{n_{lt}, n_{az}, n_{t4}, n_{t6}\}_v = \{4, 1, 3, 2\}_v$  is subtracted from  $\Re \mathfrak{M}(\nu, z^2)$  prior to performing each fit. (Right) The variation of  $\alpha$  with  $z/a$  resulting from the cosine-transform of the two-parameter PDF form in Eq. 5.42 fit to the discretization corrected and matched ITD  $\Re \mathfrak{Q}'(\nu, z^2)$  for each  $z^2$ . The discretization corrected ITD is considerably more independent of the interval  $z^2$ .

correlated Jacobi polynomial fits to  $\mathfrak{M}(\nu, z^2)$  without any corrections, are a direct result of attempting to fit a singular function in  $z$  to data that do not exhibit singular behavior. By excluding  $z/a \lesssim 4$  and  $z/a \gtrsim 11$ , the short-distance tension and any large- $z$  polynomial effects can be removed yielding reduced pseudo-ITD or matched ITD data that are well in line with theoretical expectations. Such cuts are common in the literature, however their nominal effect is to neglect deviating behavior.

Although the DGLAP investigation has been shown for the real component of the reduced pseudo-ITD, the considerable reduction in the correlated figure-of-merit when discretization effects are included in fits to  $\Im \mathfrak{M}(\nu, z^2)$  (e.g.  $\{n_{lt}, n_{az}, n_{t4}, n_{t6}\}_+ = \{3, 3, 1, 0\}_+$  versus  $\{n_{lt}, n_{az}, n_{t4}, n_{t6}\}_+ = \{3, 0, 1, 0\}_+$  in Tab. 5.5) indicates the imaginary component of the raw reduced pseudo-ITD likewise deviates from expectations of DGLAP at short-distances. The central question left for future research is the origin of this discretization effect.

# CHAPTER 6

## Generalized Ioffe-time Pseudo-Distributions

The previous two chapters laid the theoretical foundation for the extraction of forward collinear parton distributions from lattice calculable matrix elements. The pseudo-distribution LCS formalism has recently been extended to the off-forward case, identifying suitable matrix elements that can be matched to GPDs in  $\overline{\text{MS}}$ . As of yet, no results have appeared in the literature featuring off-forward pseudo-distributions. This dissertation wraps up with some preliminary numerical results, which demonstrate the continued efficacy of the pseudo-distribution LCS formalism in frames of non-zero momentum transfer.

Consider the non-local Wilson line operator  $\hat{\mathcal{O}}_{\text{WL}}^{[\gamma^\mu]}(z)$  between nucleon states of distinct initial and final momenta:

$$\mathbb{M}^\alpha(p_f, p_i, z) = \langle N(p_f) | \bar{\psi}(z) \gamma^\alpha \Phi_z^{(f)}(\{z, 0\}) \psi(0) | N(p_i) \rangle \quad (6.1)$$

$$= \langle \langle \gamma^\alpha \rangle \rangle M(\nu_f, \nu_i, t, z^2) + z^\alpha N(\nu_f, \nu_i, t, z^2), \quad (6.2)$$

with the shorthand  $\langle\langle\Gamma\rangle\rangle = \bar{u}_N(p_f, s_f) \Gamma u_N(p_i, s_i)$ . With two distinct momenta and the Wilson line direction, the invariant amplitudes or *double Ioffe-time pseudo-distributions* depend on the Ioffe-times  $\nu_i = p_i \cdot z$  and  $\nu_f = p_f \cdot z$ , spacelike interval  $z^2$  and momentum transfer  $t = (p_i - p_f)^2$ . The unpolarized GPDs which parameterize the off-forward parton correlator (2.10) in a fast-moving hadron are again defined in light-cone coordinates with  $\alpha = +$ ,  $z^\alpha = (0, z^-, \mathbf{0}_\perp)$  and  $p_k^\alpha = \left(p_k^+, \frac{m_h^2}{2p_k^+}, \mathbf{0}_\perp\right)$ . In such a frame,  $\mathbb{M}^+$  only receives contributions from  $M(p_f^+ z^-, p_i^+ z^-, t, 0)$  and not from  $N(p_f^+ z^-, p_i^+ z^-, t, 0)$ . Introducing skewness  $\xi = \frac{(p_i z) - (p_f z)}{(p_i z) + (p_f z)}$  and average Ioffe-time  $\nu = \frac{\nu_f + \nu_i}{2}$  allows for definition of the generalized Ioffe-time pseudo-distribution (pseudo-GITD)

$$M(\nu_f, \nu_i, t, z_3^2) \mapsto \mathcal{M}(\nu, \xi, t, z^2). \quad (6.3)$$

The pseudo-GITD is subsequently parameterized by the *pseudo-GPD*  $\mathcal{G}(x, \xi, t, z^2)$

$$\widetilde{\mathcal{M}}(\nu, \xi, t, z^2) = e^{-i\xi\nu} \mathcal{M}(\nu, \xi, t, z^2) = \int_{-1}^1 dx e^{ix\nu} \mathcal{G}(x, \xi, t, z^2), \quad (6.4)$$

where the prefactor  $e^{-i\xi\nu}$  establishes a direct conjugacy with the pseudo-GPD. As in the forward case, the space-like Wilson line introduces power and logarithmic divergences that must be renormalized prior to taking the continuum limit. The reduced pseudo-GITD

$$\widetilde{\mathfrak{M}}(\nu, \xi, t, z^2) \equiv \frac{\widetilde{\mathcal{M}}(\nu, \xi, t, z^2)}{\widetilde{\mathcal{M}}(0, 0, 0, z^2)} \quad (6.5)$$

conveniently cancels this multiplicative divergent factor, and is the quantity we attempt to isolate to extract the unpolarized leading-twist GPDs.

The one-loop matching between the reduced pseudo-ITD and the ITD (4.44) is a specific case of a general one-loop matching relationship of matrix elements dependent on the non-local space-like bilinear  $\bar{\psi}(z) \gamma^\alpha \Phi_{\hat{z}}^{(f)}(\{z, 0\}) \psi(0)$  [165]. Without regards to the

external hadronic state or specific parton distribution, the reduced pseudo-GITD can be matched to the  $\overline{\text{MS}}$  Generalized Ioffe-time Distribution (GITD) to one-loop in coordinate space via [162]:

$$\begin{aligned} \tilde{\mathcal{I}}(\nu, \xi, t, \mu^2) = & \widetilde{\mathfrak{M}}(\nu, \xi, t, z^2) + \frac{\alpha_s C_F}{2\pi} \int_0^1 du \widetilde{\mathfrak{M}}(u\nu, \xi, t, z^2) \left\{ \ln \left[ \frac{e^{2\gamma_E+1}}{4} z^2 \mu^2 \right] \right. \\ & \left. \times B_G(u, \bar{u}, \xi, \nu) + L_G(u, \bar{u}, \xi, \nu) \right\} + \mathcal{O}(z^2 \Lambda_{\text{QCD}}^2), \end{aligned} \quad (6.6)$$

where the GITD is conjugate to the GPD through  $\tilde{\mathcal{I}}(\nu, \xi, t, \mu^2) = \int_{-1}^1 dx e^{ix\nu} H(x, \xi, t, \mu^2)$ . The abbreviation  $\bar{u} = 1 - u$  has been used for brevity and the kernels  $B_G(u, \bar{u}, \xi, \nu)$  and  $L_G(u, \bar{u}, \xi, \nu)$  are given by

$$B_G(u, \bar{u}, \xi, \nu) = \left[ \frac{2u}{1-u} \right]_+ \cos(\bar{u}\xi\nu) + \frac{\sin(\bar{u}\xi\nu)}{\xi\nu} - \frac{1}{2}\delta(\bar{u}) \quad (6.7)$$

$$L_G(u, \bar{u}, \xi, \nu) = 4 \left[ \frac{\ln(1-u)}{1-u} \right]_+ \cos(\bar{u}\xi\nu) - 2 \frac{\sin(\bar{u}\xi\nu)}{\xi\nu} + \delta(\bar{u}). \quad (6.8)$$

The scale dependence of  $\widetilde{\mathfrak{M}}(\nu, \xi, t, z^2)$  is then associated with the kernel  $B_G(u, \bar{u}, \xi, \nu)$ , and the scale-independent kernel  $L_G(u, \bar{u}, \xi, \nu)$  with the choice of conversion to  $\overline{\text{MS}}$ .

## 6.1 Numerical Implementation

To access the unpolarized nucleon GPDs in a frame amenable to calculation in lattice QCD, we compute the off-forward matrix element (6.1) in an isovector combination subject to the kinematics  $p_i^\alpha = (E_i, \mathbf{p}_\perp^i, p_z^i)$ ,  $p_f^\alpha = (E_f, \mathbf{p}_\perp^f, p_z^f)$  and  $z^\mu = (0, \mathbf{0}_\perp, z_3)$ . As in the forward-limit, the choice  $\alpha = 4$  removes the pure higher-twist  $N(\nu_f, \nu_i, t, z_3^2)$  pollution. The matrix elements are computed using distillation on the by now well-exercised 349 configuration subset of the *a94m358* ensemble (Tab. 3.4). The needed correlation functions, temporal parameters, interpolator and phased eigenvector constructions of this calculation

are identical to those leveraged in pursuit of the unpolarized nucleon PDFs. The reader is directed to Sec. 4.4 for these details. The principal difference here is that the distillation genprops include a non-trivial momentum projection  $\vec{q}$  at the Wilson line terminus. We consider nineteen distinct momentum transfers (given in lattice units):

$$\vec{q} = (q_x, q_y, q_z) \in \begin{cases} (0, 0, \pm 1), (0, 0, \pm 2), (0, 1, 0), (0, 1, \pm 1), (0, 1, \pm 2) \\ (1, 0, 0), (1, 1, 0), (1, 1, \pm 1), (1, 1, \pm 2) \\ (2, 0, \pm 1), (2, 0, \pm 2). \end{cases} \quad (6.9)$$

The needed correlation functions are by now standard, with the relevant two-point function given in Eq. 4.59 and the off-forward three-point function given by

$$C_3(\vec{p}_f, T; \vec{q}, \tau; \vec{p}_i; [\vec{z}]) = \sum_{\vec{z}} e^{-i\vec{q}\cdot\vec{z}} \langle \mathcal{N}(\vec{p}_f, T) \hat{\mathcal{O}}_{\text{WL}}^{[\gamma_\mu]}(\vec{z}, \tau) \bar{\mathcal{N}}(\vec{p}_i, 0) \rangle. \quad (6.10)$$

The simple ratio of three- to two-point correlation functions used in the isolation of forward matrix elements in previous chapters is no longer sufficient in the off-forward case. In order to eliminate the distinct operator-state overlaps and Euclidean time dependencies on source and sink sides of a three-point correlation function when  $p_f^\mu \neq p_i^\mu$ , we construct a more general ratio:

$$R_\Gamma(\vec{p}_f, \vec{p}_i; T, \tau) = \frac{C_\Gamma^{3pt}(\vec{p}_f, \vec{p}_i; T, \tau)}{C^{2pt}(\vec{p}_f, T)} \sqrt{\frac{C^{2pt}(\vec{p}_i; T - \tau) C^{2pt}(\vec{p}_f; \tau) C^{2pt}(\vec{p}_f; T)}{C^{2pt}(\vec{p}_f; T - \tau) C^{2pt}(\vec{p}_i; \tau) C^{2pt}(\vec{p}_i; T)}}, \quad (6.11)$$

where  $T$  is the Euclidean time separation between the source/sink nucleon interpolators and  $\tau \in (0, T)$  are the Euclidean times for which the quark bilinear is inserted. Selected ratios in the  $\Gamma = \gamma_4, \gamma_x$  channels for a mild momentum transfer of  $\vec{q} = (0, 0, -1)$  are shown in Fig. 6.1 and Fig. 6.2. A number of encouraging features can be garnered from these

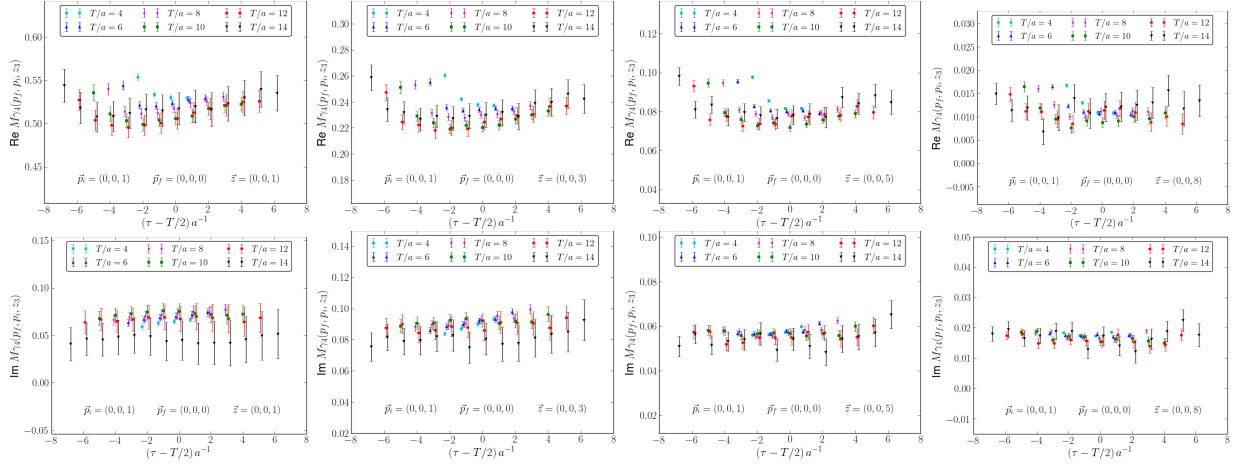


FIG. 6.1: The ratio  $R_\Gamma(\vec{p}_f, \vec{p}_i; T, \tau)$  for the  $\Gamma = \gamma_4$  insertion and  $\vec{p}_f = \vec{0}$  and  $\vec{p}_i = (0, 0, 1)$ . The top row is the real component of the ratio, and the bottom row the imaginary component. From left to right the Wilson line lengths increase monotonically in the set  $z/a \in \{1, 3, 5, 8\}$ .

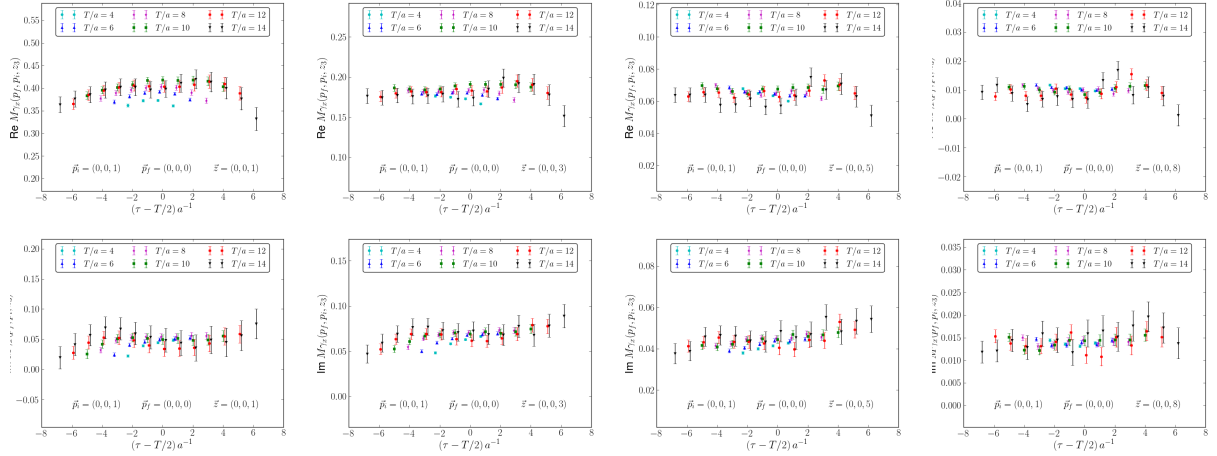


FIG. 6.2: The ratio  $R_\Gamma(\vec{p}_f, \vec{p}_i; T, \tau)$  for the  $\Gamma = \gamma_x$  insertion and  $\vec{p}_f = \vec{0}$  and  $\vec{p}_i = (0, 0, 1)$ . The top row is the real component of the ratio, and the bottom row the imaginary component. From left to right the Wilson line lengths increase monotonically in the set  $z/a \in \{1, 3, 5, 8\}$ .

very preliminary data. First, in both Dirac channels the real component ratio is seen to achieve its largest value for the shortest Wilson line lengths and gradually decreases in magnitude as the quark bilinear extent increases. Likewise in the imaginary component of both Dirac channels, the ratio starts from zero for a local quark bilinear, reaching its largest value for moderate  $z/a$  and then gradually decreases. These observations are consistent with the forward pseudo-distributions in Chapters 4 and 5, and are likewise

consistent with the Fourier transform (6.4) relating a GITD with its GPD. Furthermore, it is broadly encouraging how precise the ratios are. A great many additional ratios for several other momentum transfers and Wilson line lengths are not shown for brevity, but are likewise characterized by well-determined ratios for source/sink separations up to  $T/a \sim 10 = 0.94$  fm and have the same dependence on the Wilson line length as the forward case.

## 6.2 Outlook

The use of distillation in the computation of off-forward pseudo-GITDs has led to a tremendous amount of apparently statistically precise data. Given the nineteen distinct momentum transfers considered and nucleon momenta  $|ap_j| \in \mathbb{Z}_7 \times 2\pi/L$  collinear to the Wilson line, the coverage of a future GPD illustrated in Fig. 6.3 is quite expansive. The

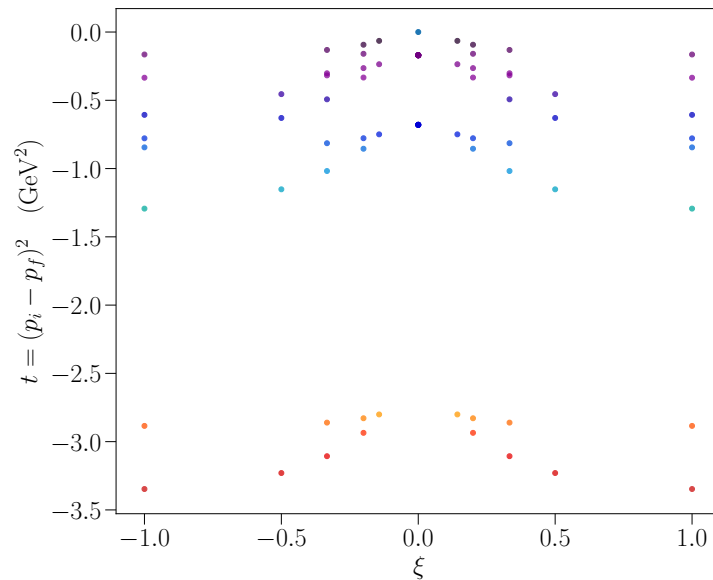


FIG. 6.3: Coverage of the unpolarized GPDs in  $\xi$  vs.  $t$  with source/sink nucleon interpolators with a component of momenta  $|ap_j| \in \mathbb{Z}_7 \times 2\pi/L$  collinear to the Wilson line and nineteen distinct momentum transfers associated with the space-like quark bilinear. The unpolarized nucleon PDFs using the pseudo-distribution that were featured in Sec. 5.3 correspond to the  $(\xi, t) = (0, 0)$  point.



analysis of these data is in its infancy at the time of this writing. However, as the analysis matures, the factorization of the relevant three-point functions provided by distillation and how they relate to the pseudo-GITDs will need to be considered more fully. In particular, for the numerous equivalent kinematic frames that will be analyzed, a given pseudo-GITD will be overconstrained by the systems of equations

$$\langle \vec{p}_f, \Lambda_f, \mu_f | j^{\Lambda_f, \mu_f} | \vec{p}_i, \Lambda_i, \mu_i \rangle = \sum_{\lambda_f, \lambda_\gamma, \lambda_i} S_{J_f, \lambda_f}^{\Lambda_f, \mu_f} \left[ S_{J_\gamma=1, \lambda_\gamma}^{\Lambda_\gamma, \mu_\gamma} \right]^* \left[ S_{J_i, \lambda_i}^{\Lambda_i, \mu_i} \right]^* \times \mathcal{K} (h_f, J_f [\lambda_f, \vec{p}_f]; h_i, J_i [\lambda_i, \vec{p}_i]) M (\nu_f, \nu_i; t; z^2), \quad (6.12)$$

where the subduction coefficients  $S_{J_k, \lambda_k}^{\Lambda_k, \mu_k}$  map continuum helicity  $\lambda_k$  eigenstates into irreps of  $O_h^D$  or its associated little groups, and the kinematic matrix  $\mathcal{K}$  captures the energy and polarization dependence of the continuum momentum channels. The extraction of the pseudo-GITDs will then proceed through matrix inversion methods well-suited for (generally) non-invertible systems.

# CHAPTER 7

## Conclusion and Outlook

The Euclidean metric of lattice QCD affords immense predictive power for the properties of the strong interaction. By discretizing the theory in a finite volume, spectral and structure information of hadronic states can be numerically computed by solving QCD from first-principles. This volume of work has unapologetically focused on hadronic matrix elements, and especially those sensitive to the light-cone structure of hadrons.

QCD factorization is the essential ingredient needed for a quantitative description of various inclusive, semi-inclusive and exclusive hadronic scattering processes. The separation of scales relies on perturbative calculation of the parton level scattering process, and on the long range non-perturbative Parton Distribution Functions (PDFs) and Generalized Parton Distributions (GPDs). The metric signature of lattice QCD complicates considerably the first-principles and non-perturbative determination of PDFs, GPDs, and any other light-like quantity. As no point in a Euclidean spacetime that is displaced from the origin has a null invariant interval, the rich light-cone structure of a hadron is inaccessible directly. A broad class of coordinate space matrix elements accessible in lattice QCD, so called Lattice Cross Sections (LCSs), fortunately factorize in a short-distance

regime into these collinear parton distributions. The specific examples of equal-time two-current correlators and space-like separated parton bilinears were developed as specific, and theoretically advantageous LCSs.

Following a global analysis of two-current correlators computed on four gauge ensembles, the valence PDF of the pion was found to agree with experiment across the entire range of  $x$  for which Drell-Yan data is available. This bolsters confidence in two-current correlations as a viable LCS. The two-current correlators were seen to suffer from several limitations including computationally existing only for mesonic systems, doing little to address short-distance discretization effects, and being plagued by relatively poor statistical quality of data due to the lack of a volume average on the non-local operator time slice. Each of these threads is actively under investigation, each promising a considerable enhancement of the already encouraging results obtained. Future studies should make full use of several current combinations to leverage the full power of the two-current LCS. A simultaneous analysis will then have the potential to constrain a number of phenomenologically interesting PDF behaviors.

The second LCS considered was the space-like parton bilinear, which when embedded between hadronic states gives rise to pseudo-distributions. The nucleon was taken as the hadron of interest, however unlike community literature the spatial smearing paradigm of distillation was implemented for the first time. To be of use, distillation was first demonstrated as an effective mechanism in the reduction of excited-states, and was later equipped with momentum smearing to access high momentum matrix elements. The use of distillation in computation of the unpolarized nucleon pseudo-distributions has led to a considerable improvement in statistical quality relative to the literature. Being valuable in its own right, the precision of these data have allowed for a rigorous quantification of systematic errors and numerical artifacts that are otherwise shrouded in statistical errors in the literature. A novel implementation of Jacobi polynomials to parameterize both the

leading-twist and any systematic artifacts is the first of its kind, and was found to be necessary for an adequate description of the data. It was found any reliable description of the reduced pseudo-ITD and determination of the leading-twist PDFs required a discretization correction. This necessity was found to be a symptom of a much larger and previously unknown deviation of the  $\mathfrak{M}(\nu, z^2)$  scale dependence from a strict  $\ln z^2$  DGLAP evolution. Whereas continuum results are not afflicted by a spacetime granularity or a finite volume, all results determined in lattice QCD are. As of this writing, the source of this discrepancy is an area of active theoretical investigation. Although the leading-twist PDFs obtained in the nucleon were seen to differ from phenomenological determinations, an expected result given the unphysical pion mass, we can have confidence in the Jacobi polynomial parameterizations of the leading-twist and corrections, and in so doing allowed the data to dictate the PDFs. Follow up calculations are underway at finer lattice spacings and ensembles of larger volumes and closer to physical light quark masses to control any other known lattice systematic.

Ultimately the coordinate space QCD factorization we have implemented, as well as the conventional momentum space variety leveraged in global analyses, is only an approximation. Power corrections to the factorization formalisms depend on the observable and in which scenarios they are applied. As systematic effects and limitations of these LCSs come into greater focus, unraveling the enigmatic structure of the pion, nucleon, and other hadrons more broadly is within closer reach. The potential is high, as some hadronic states accessible in lattice QCD, such as the  $\Delta$  baryons and the lightest pseudoscalar mesons, are especially difficult, if not impossible, to study experimentally. Moreover, these calculations of PDFs and GPDs from lattice QCD are particularly well timed given the expansive experimental efforts within the hadronic physics community. The especially ambitious plans at the future Electron Ion Collider, notably in regards to tomographic images of hadrons, solicits a synergy of increasing importance between experimental and theoretical efforts.

# APPENDIX A

## Euclidean Space Relations

The Euclidean gamma matrices are defined so as to generate a matrix representation of the Euclidean Clifford algebra  $Cl_4(\mathbb{R})$

$$\{\gamma_\mu, \gamma_\nu\} = 2\delta_{\mu\nu}. \quad (\text{A.1})$$

The Euclidean gamma matrices can be obtained from their Minkowski counterparts according to

$$\gamma_4^E = \gamma_0 \quad \gamma_j^E = -i\gamma_j. \quad (\text{A.2})$$

The “fifth” Dirac matrix is then defined as a convenient product  $\gamma_5^E = \gamma_1^E \gamma_2^E \gamma_3^E \gamma_4^E$ , which satisfies  $(\gamma_5^E)^2 = \mathbb{1}$  and anti-commutes with each other Euclidean gamma matrix. This is seen via

$$\gamma_M^5 \equiv i(\gamma^0 \gamma^1 \gamma^2 \gamma^3) = -\frac{1}{i^4}(\gamma^4 \gamma^1 \gamma^2 \gamma^3) = (\gamma^1 \gamma^2 \gamma^3 \gamma^4). \quad (\text{A.3})$$

## A.1 The Pauli-Dirac Representation

$$\gamma_M^0 = \begin{pmatrix} \mathbb{1} & 0 \\ 0 & -\mathbb{1} \end{pmatrix} \quad \gamma_M^j = \begin{pmatrix} 0 & \sigma^j \\ -\sigma^j & 0 \end{pmatrix} \quad \gamma_M^5 = \begin{pmatrix} 0 & \mathbb{1} \\ \mathbb{1} & 0 \end{pmatrix} \quad (\text{A.4})$$

$$\gamma_E^4 = \begin{pmatrix} \mathbb{1} & 0 \\ 0 & -\mathbb{1} \end{pmatrix} \quad \gamma_E^i = \begin{pmatrix} 0 & -i\sigma^j \\ i\sigma^j & 0 \end{pmatrix} \quad \gamma_E^5 = \begin{pmatrix} 0 & -\mathbb{1} \\ -\mathbb{1} & 0 \end{pmatrix} \quad (\text{A.5})$$

Spin projections:

$$u(\vec{p}, s) \bar{u}(\vec{p}, s) = (\not{p} + m) \left( \frac{1 + \gamma^5 \not{s}}{2} \right) \quad (\text{A.6})$$

$$v(\vec{p}, s) \bar{v}(\vec{p}, s) = (\not{p} - m) \left( \frac{1 + \gamma^5 \not{s}}{2} \right). \quad (\text{A.7})$$

The  $\gamma^5$  pieces become the identity when the polarization is summed over. Here  $s^\mu$  is the spin four-vector of the particle - in its rest frame  $p^\mu = (m, \vec{0})$ , the spin vector is a unit vector  $s^\mu (\vec{p} = 0) = (0, \hat{s})$  in the spin direction [166]. This then satisfies  $s^2 = -1$  and  $p \cdot s = 0$ .

## A.2 Completeness

In an infinite volume energy eigenstates satisfy the Lorentz invariant normalization

$$\langle n(\mathbf{p}, s) | m(\mathbf{q}, r) \rangle = 2E_n(\mathbf{p}) (2\pi)^3 \delta^3(\mathbf{p} - \mathbf{q}) \delta_{nm} \delta_{sr}. \quad (\text{A.8})$$

The completeness relation then takes the form:  $1 = \sum_n \int \frac{d^3k}{(2\pi)^3} \frac{1}{2E_n(k)} |n(k)\rangle \langle n(k)|$ . In a finite periodic volume momenta are quantized, and the Lorentz-invariant normalization and completeness become  $2E_n(\mathbf{p}) V_3 \delta^3(\mathbf{p} - \mathbf{q}) \delta_{nm} \delta_{sr}$  and  $1 = \frac{1}{V_3} \sum_{n,p,s} \frac{|n(k,s)\rangle \langle n(k,s)|}{2E_n(p)}$ .

# APPENDIX B

## Gell-Mann Matrices

A conventional set of  $3 \times 3$  traceless Hermitian matrices that span the fundamental representation of the  $\mathfrak{su}(3)$  algebra are given by:

$$\lambda_1 = \begin{pmatrix} 0 & 1 & 0 \\ 1 & 0 & 0 \\ 0 & 0 & 0 \end{pmatrix} \quad \lambda_2 = \begin{pmatrix} 0 & -i & 0 \\ i & 0 & 0 \\ 0 & 0 & 0 \end{pmatrix} \quad \lambda_3 = \begin{pmatrix} 1 & 0 & 0 \\ 0 & -1 & 0 \\ 0 & 0 & 0 \end{pmatrix} \quad \lambda_4 = \begin{pmatrix} 0 & 0 & 1 \\ 0 & 0 & 0 \\ 1 & 0 & 0 \end{pmatrix}$$
$$\lambda_5 = \begin{pmatrix} 0 & 0 & -i \\ 0 & 0 & 0 \\ i & 0 & 0 \end{pmatrix} \quad \lambda_6 = \begin{pmatrix} 0 & 0 & 0 \\ 0 & 0 & 1 \\ 0 & 1 & 0 \end{pmatrix} \quad \lambda_7 = \begin{pmatrix} 0 & 0 & 0 \\ 0 & 0 & -i \\ 0 & i & 0 \end{pmatrix} \quad \lambda_8 = \frac{1}{\sqrt{3}} \begin{pmatrix} 1 & 0 & 0 \\ 0 & 1 & 0 \\ 0 & 0 & -2 \end{pmatrix}.$$

First developed by Murray Gell-Mann, these matrices satisfy the orthogonality condition  $\text{Tr}(\lambda_i \lambda_j) = 2\delta_{ij}$  and are seen to generalize the Pauli spin matrices of  $\text{SU}(2)$ .

# APPENDIX C

## Grassmann Numbers

The Fermi statistics that all fermions must obey [6, 7] implies fermionic fields are anti-symmetric under interchange of their quantum numbers. That is, distinct flavors of Dirac spinors in QCD obey

$$\psi^{(f_j)}(x_j)_{\alpha_j} \psi^{(f_k)}(x_k)_{\alpha_k} = -\psi^{(f_k)}(x_k)_{\alpha_k} \psi^{(f_j)}(x_j)_{\alpha_j} \quad (\text{C.1})$$

$$\bar{\psi}^{(f_j)}(x_j)_{\alpha_j} \bar{\psi}^{(f_k)}(x_k)_{\alpha_k} = -\bar{\psi}^{(f_k)}(x_k)_{\alpha_k} \bar{\psi}^{(f_j)}(x_j)_{\alpha_j} \quad (\text{C.2})$$

$$\psi^{(f_j)}(x_j)_{\alpha_j} \bar{\psi}^{(f_k)}(x_k)_{\alpha_k} = -\bar{\psi}^{(f_k)}(x_k)_{\alpha_k} \psi^{(f_j)}(x_j)_{\alpha_j}, \quad (\text{C.3})$$

where all spacetime, flavor, Dirac and color indices have been made explicit. This behavior is described by a set of anticommuting numbers or *Grassmann numbers* defined according to

$$\theta_i \theta_j = -\theta_j \theta_i \quad \forall i, j \in \{1, \dots, N\}. \quad (\text{C.4})$$



It immediately follows any Grassmann number is nilpotent ( $\theta_i^2 = 0$ ), and polynomials are the only relevant functions of a set of  $N$  Grassmann numbers:

$$f(\{\theta_k\}) = c + \sum_i c_i \theta_i + \sum_{i < j} c_{ij} \theta_i \theta_j + \cdots + c_{12\dots N} \theta_1 \theta_2 \cdots \theta_N, \quad (\text{C.5})$$

with  $c_* \in \mathbb{C}$ . The polynomials  $f(\{\theta_k\})$  define a *Grassmann algebra*, where the individual Grassmann numbers  $\theta_i$  are generators of the algebra.

Stated without proof<sup>1</sup>, the differentiation rules of elements of a Grassmann algebra with respect to its generators are

$$\partial_{\theta_i} c = 0 \quad \partial_{\theta_i} \theta_i = 1 \quad (\text{C.6})$$

$$\partial_{\theta_i} \partial_{\theta_j} = -\partial_{\theta_j} \partial_{\theta_i} \quad \partial_{\theta_i} \theta_j = -\theta_j \partial_{\theta_i} \quad \forall i \neq j. \quad (\text{C.7})$$

The observables in lattice QCD depend on the path integrals of fermionic fields. To make sense of these, we establish “integration” rules for elements of a Grassmann algebra. Rather than define definite integrals of Grassmann variables, we need only consider the analog of a variable  $x \in \mathbb{R}$  integrated over the entire domain (i.e.  $\int_{-\infty}^{\infty} dx$ ) to define the functional integration of Grassmann variables. For a generic function of a Grassmann variable

$$\int d\theta_i f(\theta_i) = \int d\theta_i (c + c_i \theta_i), \quad (\text{C.8})$$

we demand the integral, or Berezin integral, be a complex linear functional with  $c, c_i \in \mathbb{C}$ . Furthermore, when integrated over the entire range of  $\theta_i$ , the integral must be invariant under a linear change of variables  $\theta_i \mapsto \theta_i + \eta$ . That is,

$$\int d\theta_i (c + c_i \theta_i) = \int d\theta_i (c + c_i \eta + c_i \theta). \quad (\text{C.9})$$

---

<sup>1</sup>The reader is directed to several sources [48, 167, 41] that establish these differentiation rules.

The only linear functional of  $\{c, c_i\}$  consistent with property is a constant, conventionally taken to be unity [168]. The following integral relations result:

$$\int d\theta_i (c + c_i\theta_i) = c_i \quad \int d\theta_i c = 0 \quad \int d\theta_i \theta_i = 1. \quad (\text{C.10})$$

This establishes integration and differentiation of Grassmann variables is identical! Adopting the convention

$$\int d^N\theta \theta_1 \cdots \theta_N = \int d\theta_N \cdots d\theta_1 \theta_1 \cdots \theta_N = 1 \quad (\text{C.11})$$

for several Grassmann variables, a Gaussian Berezin integral over complex-valued Grassmann variables is

$$\int d\bar{\theta} d\theta e^{-\bar{\theta}c\theta} = \int d\bar{\theta} d\theta (1 - \bar{\theta}c\theta) = \int d\bar{\theta} d\theta (1 + c\theta\bar{\theta}) = c. \quad (\text{C.12})$$

Under a linear change of variables  $\theta'_i = \sum_{j=1}^N M_{ij}\theta_j$  with  $M$  an  $N \times N$  complex matrix, the normalizing Berezin integral is modified according to

$$\begin{aligned} \int d^N\theta \theta_1 \cdots \theta_N &= \int d^N\theta' \theta'_1 \cdots \theta'_N \\ &= \int d^N\theta' \sum_{i_1, i_2, \dots, i_N} M_{1i_1} \cdots M_{Ni_N} \epsilon_{i_1 i_2 \dots i_N} \theta_1 \cdots \theta_N \\ &= (\det M) \int d^N\theta' \theta_1 \cdots \theta_N. \end{aligned} \quad (\text{C.13})$$

The totally anti-symmetric tensor emerges to capture the permutation of any two Grassmann variables, and the vanishing product if any variable is repeated. Thus under the change of variables, the integration measure behaves as  $d^N\theta = (\det M) d^N\theta'$ . These above relations can then be readily applied to establish the *Matthews-Salam* formula [169, 170]

for functional integration of generators  $\theta_i, \bar{\theta}_i$  of a  $2N$ -dimensional Grassmann algebra:

$$\left( \prod_i \int d\bar{\theta}_i d\theta_i \right) e^{-\sum_{i,j=1}^N \bar{\theta}_i M_{ij} \theta_j} = \det M, \quad (\text{C.14})$$

with  $M$  an  $N \times N$  complex matrix.

The Matthews-Salam formula (C.14) can immediately be applied to the fermionic partition function

$$Z_F[U] = \int \mathcal{D}[\psi, \bar{\psi}] e^{-S_F[\psi, \bar{\psi}, U]} \quad (\text{C.15})$$

we encounter in the fermionic expectation value of some operator in the presence of an external gauge field

$$\langle \hat{O} \rangle_F = \frac{1}{Z_F[U]} \int \mathcal{D}[\psi, \bar{\psi}] \hat{O}[\psi, \bar{\psi}, U] e^{-S_F[\psi, \bar{\psi}, U]}. \quad (\text{C.16})$$

As the fermion action is bilinear in the Grassmann-valued fields  $\{\psi, \bar{\psi}\}$  with the Dirac operator connecting the two, the fermionic partition function

$$Z_F[U] = \int \mathcal{D}[\psi, \bar{\psi}] e^{-\bar{\psi}(D[U])\psi} = \det(D[U]) \quad (\text{C.17})$$

is instead deemed the *fermion determinant*. In continuum quantum field theory, this determinant is a functional determinant and may be expressed as an infinite series of Feynman diagrams. In lattice field theory, the Dirac operator is rigorously a matrix and the determinant is defined as usual.

Inserting additional pairs of generators  $\theta_m \bar{\theta}_n$  into the Matthews-Salam integrand, one can show

$$\left( \prod_i \int d\bar{\theta}_i d\theta_i \right) \theta_m \bar{\theta}_n e^{-\sum_{i,j=1}^N \bar{\theta}_i M_{ij} \theta_j} = (\det M) (M^{-1})_{mn}. \quad (\text{C.18})$$

This conveniently captures Wick's theorem, which states the behavior of an  $n$ -point func-

tion is dictated by the inverse of the Dirac operator (quark propagators). These relationships developed in this appendix allow an observable in lattice field theory, given as a path integral over bosonic and fermionic fields, to be expressed entirely as a path integral over the bosonic degrees of freedom.

## BIBLIOGRAPHY

- [1] C. L. Bennett *et al.*, “Nine-year Wilkinson Microwave Anisotropy Probe (WMAP) Observations: Final Maps and Results,” *The Astrophysical Journal Supplement Series* **208**, 20 (2013).
- [2] Planck Collaboration, N. Aghanim, *et al.*, “Planck 2018 results. VI. Cosmological parameters,” *Astronomy & Astrophysics* **641**, A6 (2020), arXiv:1807.06209 [astro-ph.CO] .
- [3] C.-N. Yang and R. L. Mills, “Conservation of Isotopic Spin and Isotopic Gauge Invariance,” *Phys. Rev.* **96**, 191 (1954).
- [4] M. Gell-Mann, “A Schematic Model of Baryons and Mesons,” *Phys. Lett.* **8**, 214 (1964).
- [5] G. Zweig, “An SU(3) model for strong interaction symmetry and its breaking. Version 2,” in *Developments in the Quark Theory of Hadrons. vol. 1. 1964 - 1978*, edited by D. B. Lichtenberg and S. P. Rosen (1964).
- [6] M. Fierz and W. Pauli, “On relativistic wave equations for particles of arbitrary spin in an electromagnetic field,” *Proc. Roy. Soc. Lond. A* **173**, 211 (1939).
- [7] W. Pauli, “The Connection Between Spin and Statistics,” *Phys. Rev.* **58**, 716 (1940).
- [8] D. J. Gross and F. Wilczek, “Ultraviolet Behavior of Nonabelian Gauge Theories,” *Phys. Rev. Lett.* **30**, 1343 (1973).

- [9] H. D. Politzer, “Reliable Perturbative Results for Strong Interactions?” *Phys. Rev. Lett.* **30**, 1346 (1973).
- [10] K. G. Wilson, “Confinement of Quarks,” *Phys. Rev. D* **10**, 2445 (1974).
- [11] M. Diehl, “Introduction to GPDs and TMDs,” *Eur. Phys. J. A* **52**, 149 (2016), arXiv:1512.01328 [hep-ph] .
- [12] S. Meissner, A. Metz, and M. Schlegel, “Generalized parton correlation functions for a spin-1/2 hadron,” *JHEP* **08**, 056 (2009), arXiv:0906.5323 [hep-ph] .
- [13] S. Bhattacharya, A. Metz, and J. Zhou, “Generalized TMDs and the exclusive double Drell–Yan process,” *Phys. Lett. B* **771**, 396 (2017), [Erratum: *Phys.Lett.B* 810, 135866 (2020)], arXiv:1702.04387 [hep-ph] .
- [14] A. Bacchetta, D. Boer, M. Diehl, and P. J. Mulders, “Matches and mismatches in the descriptions of semi-inclusive processes at low and high transverse momentum,” *JHEP* **08**, 023 (2008), arXiv:0803.0227 [hep-ph] .
- [15] G. ’t Hooft, “Dimensional regularization and the renormalization group,” *Nucl. Phys. B* **61**, 455 (1973).
- [16] S. Weinberg, “New approach to the renormalization group,” *Phys. Rev. D* **8**, 3497 (1973).
- [17] X.-D. Ji, “Off forward parton distributions,” *J. Phys. G* **24**, 1181 (1998), arXiv:hep-ph/9807358 .
- [18] M. Diehl, “Generalized parton distributions,” *Phys. Rept.* **388**, 41 (2003), arXiv:hep-ph/0307382 .

- [19] A. Accardi *et al.*, “Electron Ion Collider: The Next QCD Frontier: Understanding the glue that binds us all,” *Eur. Phys. J. A* **52**, 268 (2016), arXiv:1212.1701 [nucl-ex] .
- [20] X.-D. Ji, “Gauge-Invariant Decomposition of Nucleon Spin,” *Phys. Rev. Lett.* **78**, 610 (1997), arXiv:hep-ph/9603249 .
- [21] J. Ashman *et al.* (European Muon), “A Measurement of the Spin Asymmetry and Determination of the Structure Function  $g(1)$  in Deep Inelastic Muon-Proton Scattering,” *Phys. Lett. B* **206**, 364 (1988).
- [22] Y. L. Dokshitzer, “Calculation of the Structure Functions for Deep Inelastic Scattering and  $e^+ e^-$  Annihilation by Perturbation Theory in Quantum Chromodynamics.” *Sov. Phys. JETP* **46**, 641 (1977).
- [23] V. N. Gribov and L. N. Lipatov, “ $e^+ e^-$  pair annihilation and deep inelastic  $e p$  scattering in perturbation theory,” *Sov. J. Nucl. Phys.* **15**, 675 (1972).
- [24] G. Altarelli and G. Parisi, “Asymptotic Freedom in Parton Language,” *Nucl. Phys. B* **126**, 298 (1977).
- [25] J. Collins, *Foundations of perturbative QCD*, Vol. 32 (Cambridge University Press, 2013).
- [26] J. Blumlein and N. Kochelev, “On the twist -2 and twist - three contributions to the spin dependent electroweak structure functions,” *Nucl. Phys. B* **498**, 285 (1997), arXiv:hep-ph/9612318 .
- [27] S. Forte, M. L. Mangano, and G. Ridolfi, “Polarized parton distributions from charged current deep inelastic scattering and future neutrino factories,” *Nucl. Phys. B* **602**, 585 (2001), arXiv:hep-ph/0101192 .

- [28] M. Anselmino, P. Gambino, and J. Kalinowski, “Polarized deep inelastic scattering at high-energies and parity violating structure functions,” *Z. Phys. C* **64**, 267 (1994), arXiv:hep-ph/9401264 .
- [29] P. Zyla *et al.* (Particle Data Group), “Review of Particle Physics,” *PTEP* **2020**, 083C01 (2020).
- [30] R. P. Feynman, *Photon-hadron Interactions*, 1st ed., Advanced Book Classics (CRC Press, 1972).
- [31] R. D. Field and R. P. Feynman, “Quark Elastic Scattering as a Source of High Transverse Momentum Mesons,” *Phys. Rev. D* **15**, 2590 (1977).
- [32] J. D. Bjorken and E. A. Paschos, “Inelastic Electron Proton and gamma Proton Scattering, and the Structure of the Nucleon,” *Phys. Rev.* **185**, 1975 (1969).
- [33] S. D. Drell, D. J. Levy, and T.-M. Yan, “A Theory of Deep Inelastic Lepton-Nucleon Scattering and Lepton Pair Annihilation Processes. 1.” *Phys. Rev.* **187**, 2159 (1969).
- [34] J. D. Bjorken, “Asymptotic Sum Rules at Infinite Momentum,” *Phys. Rev.* **179**, 1547 (1969).
- [35] J. C. Collins, D. E. Soper, and G. F. Sterman, “Factorization of Hard Processes in QCD,” *Adv. Ser. Direct. High Energy Phys.* **5**, 1 (1989), arXiv:hep-ph/0409313 .
- [36] T.-J. Hou *et al.*, “New CTEQ global analysis of quantum chromodynamics with high-precision data from the LHC,” *Phys. Rev. D* **103**, 014013 (2021), arXiv:1912.10053 [hep-ph] .
- [37] L. A. Harland-Lang, A. D. Martin, P. Motylinski, and R. S. Thorne, “Parton distributions in the LHC era: MMHT 2014 PDFs,” *Eur. Phys. J. C* **75**, 204 (2015), arXiv:1412.3989 [hep-ph] .



- [38] R. D. Ball *et al.* (NNPDF), “Parton distributions from high-precision collider data,” *Eur. Phys. J. C* **77**, 663 (2017), arXiv:1706.00428 [hep-ph] .
- [39] J. Gao, L. Harland-Lang, and J. Rojo, “The Structure of the Proton in the LHC Precision Era,” *Phys. Rept.* **742**, 1 (2018), arXiv:1709.04922 [hep-ph] .
- [40] R. P. Feynman, “Space-time approach to nonrelativistic quantum mechanics,” *Rev. Mod. Phys.* **20**, 367 (1948).
- [41] M. E. Peskin and D. V. Schroeder, *An Introduction to quantum field theory* (Addison-Wesley, Reading, USA, 1995).
- [42] K. Symanzik, “Continuum Limit and Improved Action in Lattice Theories. 1. Principles and  $\phi^4$  Theory,” *Nucl. Phys. B* **226**, 187 (1983).
- [43] K. Symanzik, “Continuum Limit and Improved Action in Lattice Theories. 2.  $O(N)$  Nonlinear Sigma Model in Perturbation Theory,” *Nucl. Phys. B* **226**, 205 (1983).
- [44] M. Luscher and P. Weisz, “On-Shell Improved Lattice Gauge Theories,” *Commun. Math. Phys.* **97**, 59 (1985), [Erratum: *Commun.Math.Phys.* 98, 433 (1985)].
- [45] G. Curci, P. Menotti, and G. Paffuti, “Symanzik’s Improved Lagrangian for Lattice Gauge Theory,” *Phys. Lett. B* **130**, 205 (1983), [Erratum: *Phys.Lett.B* 135, 516 (1984)].
- [46] W. Bietenholz *et al.*, “Flavour blindness and patterns of flavour symmetry breaking in lattice simulations of up, down and strange quarks,” *Phys. Rev. D* **84**, 054509 (2011), arXiv:1102.5300 [hep-lat] .
- [47] S. Itoh, Y. Iwasaki, Y. Oyanagi, and T. Yoshie, “Renormalization Group Improved Lattice  $SU(3)$  Gauge Action and Hadron Spectrum in Quenched QCD on a  $8^3 \times 16$  Lattice,” *Phys. Lett. B* **148**, 153 (1984).

- [48] F. Knechtli, M. Günther, and M. Peardon, *Lattice Quantum Chromodynamics: Practical Essentials*, SpringerBriefs in Physics (Springer, 2017).
- [49] G. 't Hooft, C. Itzykson, A. Jaffe, H. Lehmann, P. K. Mitter, I. M. Singer, and R. Stora, eds., *Recent Developments in Gauge Theories. Proceedings, Nato Advanced Study Institute, Cargese, France, August 26 - September 8, 1979*, Vol. 59 (1980).
- [50] M. Luscher, S. Sint, R. Sommer, and P. Weisz, “Chiral symmetry and  $O(a)$  improvement in lattice QCD,” Nucl. Phys. B **478**, 365 (1996), arXiv:hep-lat/9605038 .
- [51] B. Sheikholeslami and R. Wohlert, “Improved Continuum Limit Lattice Action for QCD with Wilson Fermions,” Nucl. Phys. B **259**, 572 (1985).
- [52] M. Luscher and P. Weisz, “ $O(a)$  improvement of the axial current in lattice QCD to one loop order of perturbation theory,” Nucl. Phys. B **479**, 429 (1996), arXiv:hep-lat/9606016 .
- [53] M. Luscher, S. Sint, R. Sommer, P. Weisz, H. Wittig, and U. Wolff, “Some new results in  $O(a)$  improved lattice QCD,” Nucl. Phys. B Proc. Suppl. **53**, 905 (1997), arXiv:hep-lat/9608049 .
- [54] G. Heatlie, G. Martinelli, C. Pittori, G. C. Rossi, and C. T. Sachrajda, “The improvement of hadronic matrix elements in lattice QCD,” Nucl. Phys. B **352**, 266 (1991).
- [55] J. Liang, Y.-B. Yang, K.-F. Liu, A. Alexandru, T. Draper, and R. S. Sufian, “Lattice Calculation of Nucleon Isovector Axial Charge with Improved Currents,” Phys. Rev. D **96**, 034519 (2017), arXiv:1612.04388 [hep-lat] .

- [56] C. R. Allton *et al.* (UKQCD), “Gauge invariant smearing and matrix correlators using Wilson fermions at Beta = 6.2,” *Phys. Rev.* **D47**, 5128 (1993), arXiv:hep-lat/9303009 [hep-lat] .
- [57] B. Blossier, M. Della Morte, G. von Hippel, T. Mendes, and R. Sommer, “On the generalized eigenvalue method for energies and matrix elements in lattice field theory,” *JHEP* **04**, 094 (2009), arXiv:0902.1265 [hep-lat] .
- [58] M. Peardon, J. Bulava, J. Foley, C. Morningstar, J. Dudek, R. G. Edwards, B. Joó, H.-W. Lin, D. G. Richards, and K. J. Juge (Hadron Spectrum), “A Novel quark-field creation operator construction for hadronic physics in lattice QCD,” *Phys. Rev.* **D80**, 054506 (2009), arXiv:0905.2160 [hep-lat] .
- [59] G. S. Bali, B. Lang, B. U. Musch, and A. Schäfer, “Novel quark smearing for hadrons with high momenta in lattice QCD,” *Phys. Rev.* **D93**, 094515 (2016), arXiv:1602.05525 [hep-lat] .
- [60] J. D. Sullivan, “One pion exchange and deep inelastic electron - nucleon scattering,” *Phys. Rev. D* **5**, 1732 (1972).
- [61] C. J. Shultz, J. J. Dudek, and R. G. Edwards, “Excited meson radiative transitions from lattice QCD using variationally optimized operators,” *Phys. Rev. D* **91**, 114501 (2015), arXiv:1501.07457 [hep-lat] .
- [62] R. A. Briceño, J. J. Dudek, R. G. Edwards, C. J. Shultz, C. E. Thomas, and D. J. Wilson, “The resonant  $\pi^+\gamma \rightarrow \pi^+\pi^0$  amplitude from Quantum Chromodynamics,” *Phys. Rev. Lett.* **115**, 242001 (2015), arXiv:1507.06622 [hep-ph] .
- [63] R. A. Briceño, J. J. Dudek, R. G. Edwards, C. J. Shultz, C. E. Thomas, and D. J.

- Wilson, “The  $\pi\pi \rightarrow \pi\gamma^*$  amplitude and the resonant  $\rho \rightarrow \pi\gamma^*$  transition from lattice QCD,” *Phys. Rev. D* **93**, 114508 (2016), arXiv:1604.03530 [hep-ph] .
- [64] G. K. C. Cheung, C. O’Hara, G. Moir, M. Peardon, S. M. Ryan, C. E. Thomas, and D. Tims (Hadron Spectrum), “Excited and exotic charmonium,  $D_s$  and  $D$  meson spectra for two light quark masses from lattice QCD,” *JHEP* **12**, 089 (2016), arXiv:1610.01073 [hep-lat] .
- [65] J. J. Dudek, R. G. Edwards, P. Guo, and C. E. Thomas (Hadron Spectrum), “Toward the excited isoscalar meson spectrum from lattice QCD,” *Phys. Rev. D* **88**, 094505 (2013), arXiv:1309.2608 [hep-lat] .
- [66] L. Liu, G. Moir, M. Peardon, S. M. Ryan, C. E. Thomas, P. Vilaseca, J. J. Dudek, R. G. Edwards, B. Joo, and D. G. Richards (Hadron Spectrum), “Excited and exotic charmonium spectroscopy from lattice QCD,” *JHEP* **07**, 126 (2012), arXiv:1204.5425 [hep-ph] .
- [67] J. J. Dudek, R. G. Edwards, B. Joo, M. J. Peardon, D. G. Richards, and C. E. Thomas, “Isoscalar meson spectroscopy from lattice QCD,” *Phys. Rev. D* **83**, 111502 (2011), arXiv:1102.4299 [hep-lat] .
- [68] M. Padmanath, R. G. Edwards, N. Mathur, and M. Peardon, “Spectroscopy of doubly-charmed baryons from lattice QCD,” *Phys. Rev. D* **91**, 094502 (2015), arXiv:1502.01845 [hep-lat] .
- [69] R. G. Edwards, J. J. Dudek, D. G. Richards, and S. J. Wallace, “Excited state baryon spectroscopy from lattice QCD,” *Phys. Rev. D* **84**, 074508 (2011), arXiv:1104.5152 [hep-ph] .

- [70] C. C. Chang *et al.*, “A per-cent-level determination of the nucleon axial coupling from quantum chromodynamics,” *Nature* **558**, 91 (2018), arXiv:1805.12130 [hep-lat] .
- [71] G. S. Bali, S. Collins, B. Glässle, M. Göckeler, J. Najjar, R. H. Rödl, A. Schäfer, R. W. Schiel, W. Söldner, and A. Sternbeck, “Nucleon isovector couplings from  $N_f = 2$  lattice QCD,” *Phys. Rev. D* **91**, 054501 (2015), arXiv:1412.7336 [hep-lat] .
- [72] R. Horsley, Y. Nakamura, A. Nobile, P. E. L. Rakow, G. Schierholz, and J. M. Zanotti, “Nucleon axial charge and pion decay constant from two-flavor lattice QCD,” *Phys. Lett. B* **732**, 41 (2014), arXiv:1302.2233 [hep-lat] .
- [73] T. Bhattacharya, V. Cirigliano, S. D. Cohen, A. Filipuzzi, M. Gonzalez-Alonso, M. L. Graesser, R. Gupta, and H.-W. Lin, “Probing Novel Scalar and Tensor Interactions from (Ultra)Cold Neutrons to the LHC,” *Phys. Rev. D* **85**, 054512 (2012), arXiv:1110.6448 [hep-ph] .
- [74] R. Gupta, Y.-C. Jang, B. Yoon, H.-W. Lin, V. Cirigliano, and T. Bhattacharya, “Isovector Charges of the Nucleon from 2+1+1-flavor Lattice QCD,” *Phys. Rev. D* **98**, 034503 (2018), arXiv:1806.09006 [hep-lat] .
- [75] R. Edwards, B. Joó, K. Orginos, D. Richards, and F. Winter, “U.S. 2+1 flavor clover lattice generation program,” (2016), unpublished.
- [76] S. Borsanyi *et al.*, “High-precision scale setting in lattice QCD,” *JHEP* **09**, 010 (2012), arXiv:1203.4469 [hep-lat] .
- [77] B. Yoon *et al.*, “Controlling Excited-State Contamination in Nucleon Matrix Elements,” *Phys. Rev. D* **93**, 114506 (2016), arXiv:1602.07737 [hep-lat] .

- [78] B. Yoon *et al.*, “Isovector charges of the nucleon from 2+1-flavor QCD with clover fermions,” *Phys. Rev.* **D95**, 074508 (2017), arXiv:1611.07452 [hep-lat] .
- [79] J. J. Dudek and R. G. Edwards, “Hybrid Baryons in QCD,” *Phys. Rev.* **D85**, 054016 (2012), arXiv:1201.2349 [hep-ph] .
- [80] C. Egerer, D. Richards, and F. Winter, “Controlling excited-state contributions with distillation in lattice QCD calculations of nucleon isovector charges  $g_S^{u-d}$ ,  $g_A^{u-d}$ ,  $g_T^{u-d}$ ,” *Phys. Rev. D* **99**, 034506 (2019), arXiv:1810.09991 [hep-lat] .
- [81] D. J. Wilson, R. A. Briceño, J. J. Dudek, R. G. Edwards, and C. E. Thomas, “The quark-mass dependence of elastic  $\pi K$  scattering from QCD,” *Phys. Rev. Lett.* **123**, 042002 (2019), arXiv:1904.03188 [hep-lat] .
- [82] A. J. Woss, C. E. Thomas, J. J. Dudek, R. G. Edwards, and D. J. Wilson, “ $b_1$  resonance in coupled  $\pi\omega$ ,  $\pi\phi$  scattering from lattice QCD,” *Phys. Rev. D* **100**, 054506 (2019), arXiv:1904.04136 [hep-lat] .
- [83] D. C. Moore and G. T. Fleming, “Angular momentum on the lattice: The Case of non-zero linear momentum,” *Phys. Rev. D* **73**, 014504 (2006), [Erratum: *Phys. Rev. D* **74**, 079905 (2006)], arXiv:hep-lat/0507018 .
- [84] C. E. Thomas, R. G. Edwards, and J. J. Dudek, “Helicity operators for mesons in flight on the lattice,” *Phys. Rev.* **D85**, 014507 (2012), arXiv:1107.1930 [hep-lat] .
- [85] C. Egerer, R. G. Edwards, K. Orginos, and D. G. Richards, “Distillation at High-Momentum,” *Phys. Rev. D* **103**, 034502 (2021), arXiv:2009.10691 [hep-lat] .
- [86] Y.-C. Jang, R. Gupta, B. Yoon, and T. Bhattacharya, “Axial Vector Form Factors from Lattice QCD that Satisfy the PCAC Relation,” *Phys. Rev. Lett.* **124**, 072002 (2020), arXiv:1905.06470 [hep-lat] .

- [87] J. Bulava, M. Donnellan, and R. Sommer, “On the computation of hadron-to-hadron transition matrix elements in lattice QCD,” *JHEP* **01**, 140 (2012), arXiv:1108.3774 [hep-lat] .
- [88] K. G. Wilson, “Nonlagrangian models of current algebra,” *Phys. Rev.* **179**, 1499 (1969).
- [89] W. Detmold and C. J. D. Lin, “Deep-inelastic scattering and the operator product expansion in lattice QCD,” *Phys. Rev. D* **73**, 014501 (2006), arXiv:hep-lat/0507007 .
- [90] K.-F. Liu and S.-J. Dong, “Origin of difference between anti-d and anti-u partons in the nucleon,” *Phys. Rev. Lett.* **72**, 1790 (1994), arXiv:hep-ph/9306299 .
- [91] K.-F. Liu, “Parton degrees of freedom from the path integral formalism,” *Phys. Rev. D* **62**, 074501 (2000), arXiv:hep-ph/9910306 .
- [92] V. Braun and D. Müller, “Exclusive processes in position space and the pion distribution amplitude,” *Eur. Phys. J. C* **55**, 349 (2008), arXiv:0709.1348 [hep-ph] .
- [93] X. Ji, “Parton Physics on a Euclidean Lattice,” *Phys. Rev. Lett.* **110**, 262002 (2013), arXiv:1305.1539 [hep-ph] .
- [94] M. Constantinou and H. Panagopoulos, “Perturbative renormalization of quasi-parton distribution functions,” *Phys. Rev. D* **96**, 054506 (2017), arXiv:1705.11193 [hep-lat] .
- [95] X. Ji, “Parton Physics from Large-Momentum Effective Field Theory,” *Sci. China Phys. Mech. Astron.* **57**, 1407 (2014), arXiv:1404.6680 [hep-ph] .

- [96] R. A. Briceño, M. T. Hansen, and C. J. Monahan, “Role of the Euclidean signature in lattice calculations of quasidistributions and other nonlocal matrix elements,” *Phys. Rev. D* **96**, 014502 (2017), arXiv:1703.06072 [hep-lat] .
- [97] C. Alexandrou, K. Cichy, M. Constantinou, K. Hadjiyiannakou, K. Jansen, A. Scapellato, and F. Steffens, “Systematic uncertainties in parton distribution functions from lattice QCD simulations at the physical point,” *Phys. Rev. D* **99**, 114504 (2019), arXiv:1902.00587 [hep-lat] .
- [98] A. M. Polyakov, “Gauge Fields as Rings of Glue,” *Nucl. Phys. B* **164**, 171 (1980).
- [99] V. S. Dotsenko and S. N. Vergeles, “Renormalizability of Phase Factors in the Non-abelian Gauge Theory,” *Nucl. Phys. B* **169**, 527 (1980).
- [100] T. Ishikawa, Y.-Q. Ma, J.-W. Qiu, and S. Yoshida, “Renormalizability of quasi-parton distribution functions,” *Phys. Rev. D* **96**, 094019 (2017), arXiv:1707.03107 [hep-ph] .
- [101] X. Ji, J.-H. Zhang, and Y. Zhao, “Renormalization in Large Momentum Effective Theory of Parton Physics,” *Phys. Rev. Lett.* **120**, 112001 (2018), arXiv:1706.08962 [hep-ph] .
- [102] J. Green, K. Jansen, and F. Steffens, “Nonperturbative Renormalization of Nonlocal Quark Bilinears for Parton Quasidistribution Functions on the Lattice Using an Auxiliary Field,” *Phys. Rev. Lett.* **121**, 022004 (2018), arXiv:1707.07152 [hep-lat] .
- [103] Y.-Q. Ma and J.-W. Qiu, “Extracting Parton Distribution Functions from Lattice QCD Calculations,” *Phys. Rev. D* **98**, 074021 (2018), arXiv:1404.6860 [hep-ph] .
- [104] Y.-Q. Ma and J.-W. Qiu, “Exploring Partonic Structure of Hadrons Using ab initio



- Lattice QCD Calculations,” *Phys. Rev. Lett.* **120**, 022003 (2018), arXiv:1709.03018 [hep-ph] .
- [105] B. Ioffe, “Space-time picture of photon and neutrino scattering and electroproduction cross-section asymptotics,” *Phys. Lett. B* **30**, 123 (1969).
- [106] V. Braun, P. Gornicki, and L. Mankiewicz, “Ioffe - time distributions instead of parton momentum distributions in description of deep inelastic scattering,” *Phys. Rev. D* **51**, 6036 (1995), arXiv:hep-ph/9410318 .
- [107] H. Georgi and H. D. Politzer, “Freedom at Moderate Energies: Masses in Color Dynamics,” *Phys. Rev. D* **14**, 1829 (1976).
- [108] R. A. Briceño, J. V. Guerrero, M. T. Hansen, and C. J. Monahan, “Finite-volume effects due to spatially nonlocal operators,” *Phys. Rev. D* **98**, 014511 (2018), arXiv:1805.01034 [hep-lat] .
- [109] A. V. Radyushkin, “Quasi-parton distribution functions, momentum distributions, and pseudo-parton distribution functions,” *Phys. Rev. D* **96**, 034025 (2017), arXiv:1705.01488 [hep-ph] .
- [110] A. Radyushkin, “Nonperturbative Evolution of Parton Quasi-Distributions,” *Phys. Lett. B* **767**, 314 (2017), arXiv:1612.05170 [hep-ph] .
- [111] M. Anselmino, M. Boglione, J. O. Gonzalez Hernandez, S. Melis, and A. Prokudin, “Unpolarised Transverse Momentum Dependent Distribution and Fragmentation Functions from SIDIS Multiplicities,” *JHEP* **04**, 005 (2014), arXiv:1312.6261 [hep-ph] .
- [112] K. Orginos, A. Radyushkin, J. Karpie, and S. Zafeiropoulos, “Lattice QCD explo-

- ration of parton pseudo-distribution functions,” *Phys. Rev. D* **96**, 094503 (2017), arXiv:1706.05373 [hep-ph] .
- [113] V. M. Braun, A. Vladimirov, and J.-H. Zhang, “Power corrections and renormalons in parton quasidistributions,” *Phys. Rev. D* **99**, 014013 (2019), arXiv:1810.00048 [hep-ph] .
- [114] X. Gao, L. Jin, C. Kallidonis, N. Karthik, S. Mukherjee, P. Petreczky, C. Shugert, S. Syritsyn, and Y. Zhao, “Valence parton distribution of the pion from lattice QCD: Approaching the continuum limit,” *Phys. Rev. D* **102**, 094513 (2020), arXiv:2007.06590 [hep-lat] .
- [115] T. Izubuchi, X. Ji, L. Jin, I. W. Stewart, and Y. Zhao, “Factorization Theorem Relating Euclidean and Light-Cone Parton Distributions,” *Phys. Rev. D* **98**, 056004 (2018), arXiv:1801.03917 [hep-ph] .
- [116] A. Radyushkin, “One-loop evolution of parton pseudo-distribution functions on the lattice,” *Phys. Rev. D* **98**, 014019 (2018), arXiv:1801.02427 [hep-ph] .
- [117] J.-H. Zhang, J.-W. Chen, and C. Monahan, “Parton distribution functions from reduced Ioffe-time distributions,” *Phys. Rev. D* **97**, 074508 (2018), arXiv:1801.03023 [hep-ph] .
- [118] B. Joó, J. Karpie, K. Orginos, A. Radyushkin, D. Richards, and S. Zafeiropoulos, “Parton Distribution Functions from Ioffe time pseudo-distributions,” *JHEP* **12**, 081 (2019), arXiv:1908.09771 [hep-lat] .
- [119] R. S. Sufian, J. Karpie, C. Egerer, K. Orginos, J.-W. Qiu, and D. G. Richards, “Pion Valence Quark Distribution from Matrix Element Calculated in Lattice QCD,” *Phys. Rev. D* **99**, 074507 (2019), arXiv:1901.03921 [hep-lat] .

- [120] R. S. Sufian, C. Egerer, J. Karpie, R. G. Edwards, B. Joó, Y.-Q. Ma, K. Orginos, J.-W. Qiu, and D. G. Richards, “Pion Valence Quark Distribution from Current-Current Correlation in Lattice QCD,” *Phys. Rev. D* **102**, 054508 (2020), arXiv:2001.04960 [hep-lat] .
- [121] G. F. Sterman, “Summation of Large Corrections to Short Distance Hadronic Cross-Sections,” *Nucl. Phys. B* **281**, 310 (1987).
- [122] B. Joó, J. Karpie, K. Orginos, A. V. Radyushkin, D. G. Richards, R. S. Sufian, and S. Zafeiropoulos, “Pion valence structure from Ioffe-time parton pseudodistribution functions,” *Phys. Rev. D* **100**, 114512 (2019), arXiv:1909.08517 [hep-lat] .
- [123] B. Joó, J. Karpie, K. Orginos, A. V. Radyushkin, D. G. Richards, and S. Zafeiropoulos, “Parton Distribution Functions from Ioffe Time Pseudodistributions from Lattice Calculations: Approaching the Physical Point,” *Phys. Rev. Lett.* **125**, 232003 (2020), arXiv:2004.01687 [hep-lat] .
- [124] M. Bhat, K. Cichy, M. Constantinou, and A. Scapellato, “Flavor nonsinglet parton distribution functions from lattice QCD at physical quark masses via the pseudodistribution approach,” *Phys. Rev. D* **103**, 034510 (2021), arXiv:2005.02102 [hep-lat] .
- [125] Z. Fan, R. Zhang, and H.-W. Lin, “Nucleon Gluon Distribution Function from 2+1+1-Flavor Lattice QCD,” (2020), arXiv:2007.16113 [hep-lat] .
- [126] L. Maiani, G. Martinelli, M. L. Paciello, and B. Taglienti, “Scalar Densities and Baryon Mass Differences in Lattice QCD With Wilson Fermions,” *Nucl. Phys. B* **293**, 420 (1987).

- [127] S. Capitani, M. Della Morte, G. von Hippel, B. Jager, A. Juttner, B. Knippschild, H. B. Meyer, and H. Wittig, “The nucleon axial charge from lattice QCD with controlled errors,” *Phys. Rev. D* **86**, 074502 (2012), arXiv:1205.0180 [hep-lat] .
- [128] K. Akiyama *et al.* (Event Horizon Telescope), “First M87 Event Horizon Telescope Results. IV. Imaging the Central Supermassive Black Hole,” *Astrophys. J. Lett.* **875**, L4 (2019), arXiv:1906.11241 [astro-ph.GA] .
- [129] J. Karpie, K. Orginos, A. Rothkopf, and S. Zafeiropoulos, “Reconstructing parton distribution functions from Ioffe time data: from Bayesian methods to Neural Networks,” *JHEP* **04**, 057 (2019), arXiv:1901.05408 [hep-lat] .
- [130] J. Liang, T. Draper, K.-F. Liu, A. Rothkopf, and Y.-B. Yang (XQCD), “Towards the nucleon hadronic tensor from lattice QCD,” *Phys. Rev. D* **101**, 114503 (2020), arXiv:1906.05312 [hep-ph] .
- [131] M. T. Hansen, H. B. Meyer, and D. Robaina, “From deep inelastic scattering to heavy-flavor semileptonic decays: Total rates into multihadron final states from lattice QCD,” *Phys. Rev. D* **96**, 094513 (2017), arXiv:1704.08993 [hep-lat] .
- [132] A. Accardi, L. T. Brady, W. Melnitchouk, J. F. Owens, and N. Sato, “Constraints on large- $x$  parton distributions from new weak boson production and deep-inelastic scattering data,” *Phys. Rev. D* **93**, 114017 (2016), arXiv:1602.03154 [hep-ph] .
- [133] A. D. Martin, W. J. Stirling, R. S. Thorne, and G. Watt, “Parton distributions for the LHC,” *Eur. Phys. J. C* **63**, 189 (2009), arXiv:0901.0002 [hep-ph] .
- [134] T. Regge, “Introduction to complex orbital momenta,” *Nuovo Cim.* **14**, 951 (1959).
- [135] S. J. Brodsky and G. R. Farrar, “Scaling Laws at Large Transverse Momentum,” *Phys. Rev. Lett.* **31**, 1153 (1973).

- [136] D. Ebert, R. N. Faustov, and V. O. Galkin, “Mass spectra and Regge trajectories of light mesons in the relativistic quark model,” *Phys. Rev. D* **79**, 114029 (2009), arXiv:0903.5183 [hep-ph] .
- [137] L. Zou and H. G. Dosch, “A very Practical Guide to Light Front Holographic QCD,” (2018), arXiv:1801.00607 [hep-ph] .
- [138] G. Veneziano, “Construction of a crossing - symmetric, Regge behaved amplitude for linearly rising trajectories,” *Nuovo Cim. A* **57**, 190 (1968).
- [139] R. D. Ball *et al.* (NNPDF), “Parton distributions for the LHC Run II,” *JHEP* **04**, 040 (2015), arXiv:1410.8849 [hep-ph] .
- [140] T. Izubuchi, L. Jin, C. Kallidonis, N. Karthik, S. Mukherjee, P. Petreczky, C. Shugert, and S. Syritsyn, “Valence parton distribution function of pion from fine lattice,” *Phys. Rev. D* **100**, 034516 (2019), arXiv:1905.06349 [hep-lat] .
- [141] S. Dulat, T.-J. Hou, J. Gao, M. Guzzi, J. Huston, P. Nadolsky, J. Pumplin, C. Schmidt, D. Stump, and C. P. Yuan, “New parton distribution functions from a global analysis of quantum chromodynamics,” *Phys. Rev. D* **93**, 033006 (2016), arXiv:1506.07443 [hep-ph] .
- [142] G. S. Bali, V. M. Braun, B. Gläbke, M. Göckeler, M. Gruber, F. Hutzler, P. Korcyl, A. Schäfer, P. Wein, and J.-H. Zhang, “Pion distribution amplitude from Euclidean correlation functions: Exploring universality and higher-twist effects,” *Phys. Rev. D* **98**, 094507 (2018), arXiv:1807.06671 [hep-lat] .
- [143] G. S. Bali, V. M. Braun, S. Bürger, M. Göckeler, M. Gruber, F. Hutzler, P. Korcyl, A. Schäfer, A. Sternbeck, and P. Wein (RQCD), “Light-cone distribution amplitudes

- of pseudoscalar mesons from lattice QCD,” JHEP **08**, 065 (2019), [Addendum: JHEP **11**, 037 (2020)], arXiv:1903.08038 [hep-lat] .
- [144] H. Fukaya, S. Hashimoto, T. Kaneko, and H. Ohki, “Towards fully nonperturbative computations of inelastic  $\ell N$  scattering cross sections from lattice QCD,” Phys. Rev. D **102**, 114516 (2020), arXiv:2010.01253 [hep-lat] .
- [145] C. G. Boyd, B. Grinstein, and R. F. Lebed, “Constraints on form-factors for exclusive semileptonic heavy to light meson decays,” Phys. Rev. Lett. **74**, 4603 (1995), arXiv:hep-ph/9412324 .
- [146] C. Bourrely, I. Caprini, and L. Lellouch, “Model-independent description of  $B \rightarrow \pi l \nu$  decays and a determination of  $|V(ub)|$ ,” Phys. Rev. D **79**, 013008 (2009), [Erratum: Phys.Rev.D **82**, 099902 (2010)], arXiv:0807.2722 [hep-ph] .
- [147] R. Brun and F. Rademakers, “ROOT: An object oriented data analysis framework,” Nucl. Instrum. Meth. A **389**, 81 (1997).
- [148] A. Buckley, J. Ferrando, S. Lloyd, K. Nordström, B. Page, M. Rüfenacht, M. Schönherr, and G. Watt, “LHAPDF6: parton density access in the LHC precision era,” Eur. Phys. J. C **75**, 132 (2015), arXiv:1412.7420 [hep-ph] .
- [149] C. Chen, L. Chang, C. D. Roberts, S. Wan, and H.-S. Zong, “Valence-quark distribution functions in the kaon and pion,” Phys. Rev. D **93**, 074021 (2016), arXiv:1602.01502 [nucl-th] .
- [150] J. Badier *et al.* (NA3), “Experimental Determination of the  $\pi$  Meson Structure Functions by the Drell-Yan Mechanism,” Z. Phys. C **18**, 281 (1983).
- [151] B. Betev *et al.* (NA10), “Differential Cross-section of High Mass Muon Pairs Produced by a 194-GeV/ $c\pi^-$  Beam on a Tungsten Target,” Z. Phys. C **28**, 9 (1985).

- [152] J. S. Conway *et al.*, “Experimental Study of Muon Pairs Produced by 252-GeV Pions on Tungsten,” *Phys. Rev. D* **39**, 92 (1989).
- [153] J. F. Owens, “ $Q^2$  Dependent Parametrizations of Pion Parton Distribution Functions,” *Phys. Rev. D* **30**, 943 (1984).
- [154] P. J. Sutton, A. D. Martin, R. G. Roberts, and W. J. Stirling, “Parton distributions for the pion extracted from Drell-Yan and prompt photon experiments,” *Phys. Rev. D* **45**, 2349 (1992).
- [155] K. Wijesooriya, P. E. Reimer, and R. J. Holt, “The pion parton distribution function in the valence region,” *Phys. Rev. C* **72**, 065203 (2005), arXiv:nucl-ex/0509012 .
- [156] M. Aicher, A. Schafer, and W. Vogelsang, “Soft-gluon resummation and the valence parton distribution function of the pion,” *Phys. Rev. Lett.* **105**, 252003 (2010), arXiv:1009.2481 [hep-ph] .
- [157] P. C. Barry, N. Sato, W. Melnitchouk, and C.-R. Ji, “First Monte Carlo Global QCD Analysis of Pion Parton Distributions,” *Phys. Rev. Lett.* **121**, 152001 (2018), arXiv:1804.01965 [hep-ph] .
- [158] E. L. Berger and S. J. Brodsky, “Quark Structure Functions of Mesons and the Drell-Yan Process,” *Phys. Rev. Lett.* **42**, 940 (1979).
- [159] L. Chang, C. Mezrag, H. Moutarde, C. D. Roberts, J. Rodríguez-Quintero, and P. C. Tandy, “Basic features of the pion valence-quark distribution function,” *Phys. Lett. B* **737**, 23 (2014), arXiv:1406.5450 [nucl-th] .
- [160] E. Moffat, W. Melnitchouk, T. Rogers, and N. Sato, “Simultaneous Monte Carlo analysis of parton densities and fragmentation functions,” (2021), arXiv:2101.04664 [hep-ph] .

- [161] A. D. Martin, W. J. Stirling, R. S. Thorne, and G. Watt, “Heavy-quark mass dependence in global PDF analyses and 3- and 4-flavour parton distributions,” *Eur. Phys. J. C* **70**, 51 (2010), arXiv:1007.2624 [hep-ph] .
- [162] A. V. Radyushkin, “Generalized parton distributions and pseudodistributions,” *Phys. Rev. D* **100**, 116011 (2019), arXiv:1909.08474 [hep-ph] .
- [163] J. Karpie, K. Orginos, and S. Zafeiropoulos, “Moments of Ioffe time parton distribution functions from non-local matrix elements,” *JHEP* **11**, 178 (2018), arXiv:1807.10933 [hep-lat] .
- [164] G. H. Golub and V. Pereyra, “The Differentiation of Pseudo-Inverses and Nonlinear Least Squares Problems Whose Variables Separate,” *SIAM Journal on Numerical Analysis* **10**, 413 (1973).
- [165] A. V. Radyushkin, “Quark pseudodistributions at short distances,” *Phys. Lett. B* **781**, 433 (2018), arXiv:1710.08813 [hep-ph] .
- [166] P. Langacker, *The standard model and beyond* (CRC Press, Boca Raton, USA, 2010) p. 663.
- [167] C. Gattringer and C. B. Lang, *Quantum chromodynamics on the lattice*, Vol. 788 (Springer, Berlin, 2010).
- [168] F. A. Berezin, “The method of second quantization,” *Pure Appl. Phys.* **24**, 1 (1966).
- [169] P. T. Matthews and A. Salam, “The Green’s functions of quantized fields,” *Nuovo Cim.* **12**, 563 (1954).
- [170] P. T. Matthews and A. Salam, “Propagators of quantized field,” *Nuovo Cim.* **2**, 120 (1955).